A rapid flow assessment tool for automated dry fibre preforms – a numerical and experimental study

<u>Usman Shafique</u>

<u>MSc</u>

Thesis submitted to the University of Nottingham
for the degree of Doctor of Philosophy

Abstract

Automated dry fibre placement (ADFP) has gained the attention of the aerospace industry in the past few years. The preforms produced by ADFP are manufactured into composite parts by liquid composite moulding (LCM) processes. In contrast to manual preforming, this automated process reduces the required time and improves quality of layup. Whereas, LCM offers low cost manufacturing, making it an excellent selection when producing large parts. Due to high compaction of unidirectional fibres during the deposition process and binder presence, the preforms are produced with high fibre volume fractions. This decreases the permeability of these preforms and effects the overall fill time during LCM. During the deposition process defects are induced into the preforms from machine inaccuracy, variability in material and poor adhesion. This results in the formation of inter-tow or inter-course gaps and overlaps.

Since gaps are inevitable in ADFP preforms, they have sometimes been intentionally programmed and placed into preform to avoid overlaps. These gaps form a vascular network of gaps within the preform and act as flow channels. This effects the overall permeability of ADFP preforms by enhancing the flow during LCM.

In this thesis, conventional methods employed to predict permeability of such preforms are compared with the experimental results on meso-scale and macro-scale level. The results showed that the percentage difference between experimental and analytical results is increased up to 165% on macro-scale and lowest in case of the only tow results (45%). In either cases the difference between results are significant. Therefore a novel method to characterize flow behaviour in a preform with gap networks of any complexity is developed. This is achieved by producing a gap network based on real preform data acquired from the deposition rig, development of numerical model based on pipe network approach to compute flow rates across

the network and visualization of flow behaviour in preform through homogenised velocity mapping.

This approach facilitated the successful reconstruction of geometries of preform reported in literature. Lower difference in comparison to the experimental permeability was found: 50% for nominal model where 1mm gap width is assigned across the preform and 19% for averaged model where 0.8mm averaged gap width was used. The numerical model was able to process 4300 gaps in under 6 minutes and enables a user to execute the network model as soon as the preform data file is ready and predict the averaged preform permeability while the preform is being prepared for LCM and make the relevant changes to achieve lower fill times. Moreover, the low computational times for this numerical model enables flow characterization of each preform produced. This eliminates the need of conventional time consuming and expensive steps such as XCT, microscopy to accesses limited preform data and produce a working mesh to enable 2D or 3D flow simulation.

Acknowledgements

Table of Contents

Chapter 1 Introduction

Composite materials were developed in the middle of twentieth century [1]. Composite materials consist of two or more constituents which are combined together without dissolving into each other forming a new component with combined properties of all its constituents. Typically, there are two constituents: fibre reinforcement, such as carbon or glass fibre, and a matrix, usually polymers such as epoxy [2-5]. Composite materials offer great design flexibility as they can be manufactured by tailoring the layers into any orientations which then directly influences the mechanical performance of the part [6]. Composite materials generally offer high specific moduli and strengths [6-8]. This can reduce the weight of a component up-to 20% - 30% compared to aluminium[6], which makes automobiles and aircrafts fuel efficient. In addition, composites also provide comparable structural strength to metallic alloys [9]. Composite materials are increasing in use in the aerospace industry. For example, in 1990 Airbus manufactured the first aircraft with a composite fin box (A310) and A320 was the first aircraft with an all-composite tail [10]. As of 2000, Airbus manufactured their first carbon fibre keel beam in a large commercial plane A340-600 [10] , while glass fibre was used in the manufacturing of Boeing 707 (1957)[11] but with a total percentage of only 2% [12, 13]. However, 50% - 60% metallic alloys have been replaced by composites materials in the Boeing 787 Dreamliner (2007) as shown in Figure 1 and Airbus A380 in (2006) [8, 13, 14]. The increase in the use of the composite materials in Airbus aircraft over times can be observed in Figure 2.The weight of the composite components is also reduced by 20% such as in the case of Dreamliner [15, 16], which will result in up to 18% energy savings throughout its lifetime [17, 18] .
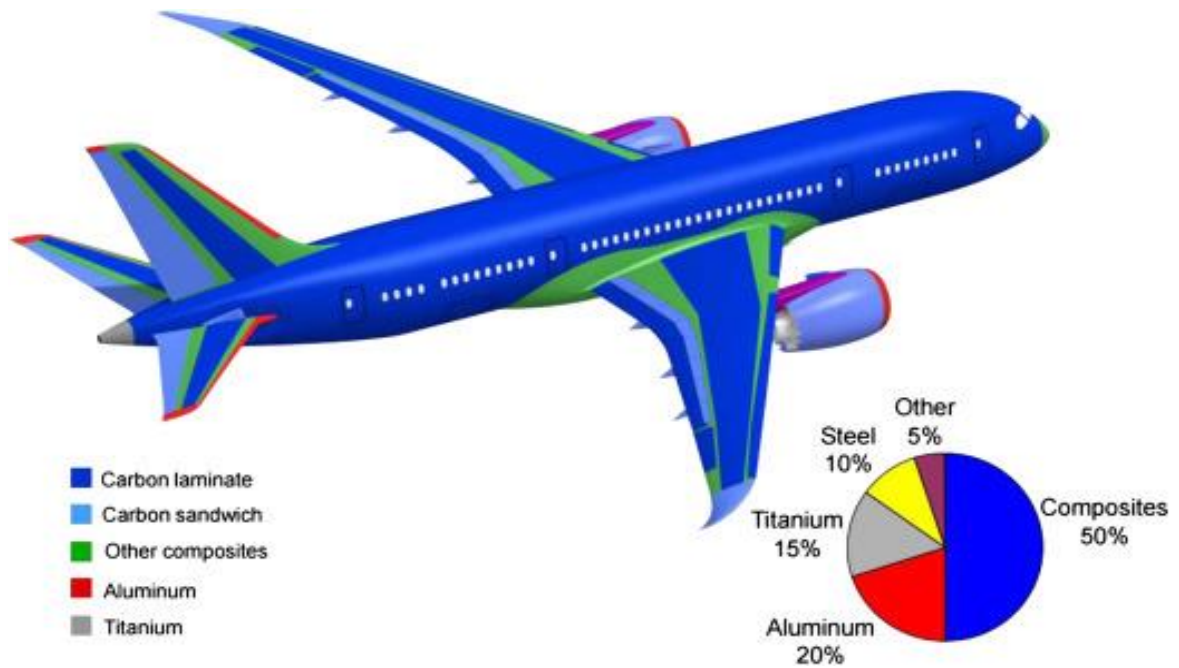
Figure 1 - Percentage usage of various materials in the Boeing 787 Dreamliner [8]. The percentage of composites is expected to further increase in future and will require advance methods to improve the production rate of composites parts.

.
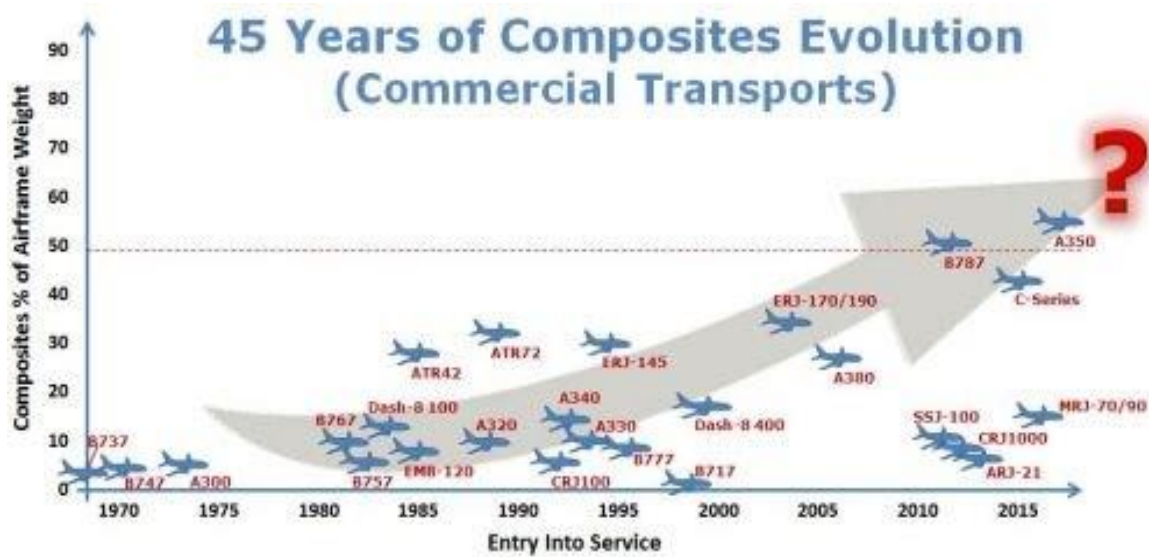
Figure 2 – Total weight percentage to composite parts in Airbus aircraft designed over time shows increasing demand of composites[19]. The increase in demand of composite materials requires modern methods to overcome limitations in conventional analytical and simulation approaches.

The use of composites is also increasing in other areas such as automotive and renewable energy [20]. Due to high increase in demand of composite parts in many industries, the production rate and economy of composites manufacturing needs to be improved. Manufacturing of a composite part consists of two main stages, preforming and impregnation/consolidation. In these two stages the cost of composites needs to be reduced in comparison to their metallic counter parts [14]. Automation has been in the spotlight for that reason and various methods have been developed to assist in preforming stage of complex mule-layered preforms. Automated dry fibre placement (ADFP) is one of the methods that have facilitated advancement of the composites manufacturing and the use of AFP systems have been continuously increasing over the past few years as show in Figure 3. In the chapter 2, details of different automated deposition processes are reviewed.
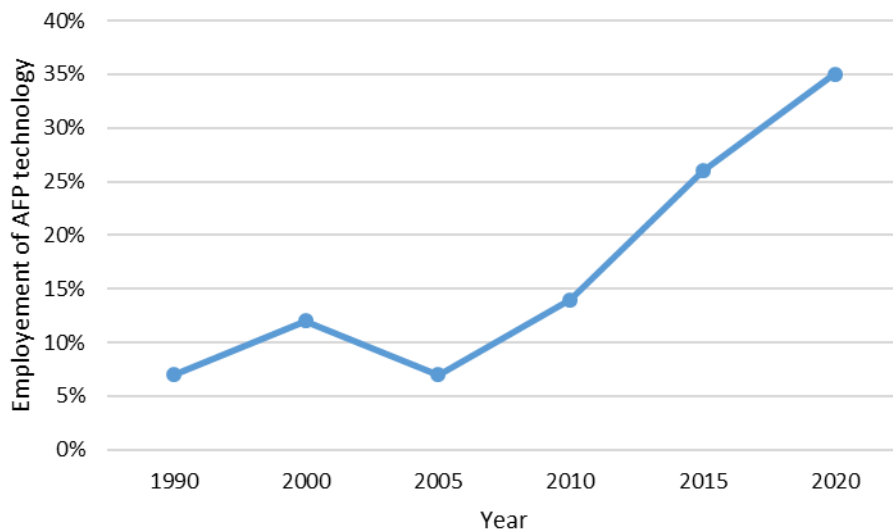
Figure 3 – Employment of AFP system over time [18]

The preforms produced by such automated process are required to be further processed to manufacture into a final composite part. Different methods have been developed with the aim of manufacturing cost-effective aerospace grade composites [21, 22]. These methods are known as liquid composite moulding (LCM). During the LCM processes, resin is injected into the preform. As the preforms are produced by use the automated processes, the layers are highly

compacted and results into lower preform permeability during the LCM process. The typical permeability of materials in comparison to ADFP preforms are given below in *Table 1* & Table 2. ADFP preforms exhibits lower permeability in comparison with woven fabrics due to fewer inter-ply resin channels and presence of binder effect [23]. It can be observed that ADFP preform exhibits lowest preform permeabilities in comparison with other materials. This is further discussed in detail in Chapter 2.

Material	V_f (%)	K_x, m^2	K_y, m^2
Carbon HT Twill 2 X 2 [24]	41%	2.01E-10	4.77E-11
E-glass twill 2 x 2 [24]	46%	4.23E-10	2.13E-10
E-glass twill 2 x 2 [24]	51%	3.41E-11	2.47E-11
Carbon HT Twill 2 X 2 [24]	51%	2.02E-11	6.30E-12
Biaxial glass fibre fabric [25]	52%	2.86E-11	2.17E-11
ADFP preform [26]	54%	1.44E-12	1.44E-12
ADFP preform with gaps [27]	54%	1.46E-11	1.44E-11

Table 1 - In-plane permeability values for different materials from literature shows ADFP preform permeability is lower than conventional materials by an order of magnitude

Material	V_f (%)	K_z, m^2
E glass woven fabric [28]	40%	1.00E-12
E-glass non-crimp fabric [29]	48%	3.60E-12
Carbon fibre woven fabric [29]	49%	7.68E-13
E-glass fabric [29]	50%	9.41E-13
E-glass non-crimp fabric [30]	55%	1.40E-12
ADFP 6.35 mm tape [31]	58%	8.51E-14
ADFP 12.7 mm tape [31]	58%	2.52E-13

Table 2 –ADFP preform exhibits the lowest transverse permeability in comparison with other materials

4

The main limitations of ADFP are the variability induced by either the material or the deposition process. These variabilities include gaps, overlaps, tape misalignment, tape twists, tape buckling and regions of poor adhesion. [14, 27, 32]. The variability induced depends on the complexity of the part design and processing parameters such as layup speed, tape width and tape steering. Gap and/or overlaps are induced mainly due to misalignments at the band edges and their occurrence can be frequent in complex shapes and results into variable flow behaviour of the preform during the LCM process [27, 31, 33]. This directly affects the reliability of analytical solution employed to measure permeability of such preforms. This is due to some model assumptions such as the fibres are arranged parallel to each other, and the shape of tow or gap is perfect rectangular. [34-45]. Furthermore, the variability in preforms also limits the applicability of conventional simulation approaches. The mesh geometry required to execute simulation requires real preform data to incorporate local variability in gap specifications. This is achieved by different methods, for example, variability in gap width or thickness is usually measured by microscopy, X-CT, SEM[46] and microscopy scans[47] which is usually done post infusion. These methods are usually time consuming, costly and can only produce limited number of sample. Since each preform produced contain different level of variability, such procedures cannot be repeated for each preform. Therefore, limiting the use of 3D simulation models. Further details about conventional simulation models are discussed in detail in chapter 2 and chapter 4.

In this project a detailed review is conducted in chapter 2 to identify gaps in research and limitations in current methods that results into unreliable permeability predictions. Such research gaps and limitations have derived the aim and objective of this project that are given in the next section.

1.1 Aims and Objectives

Aims

- Reduce production time for large composite structures by characterization of flow during LCM process through the introduction of engineered flow channels in ADFP preforms and enable rapid flow assessment via development of numerical model based on deposition process parameters to overcome limitations in conventional simulation and analytical methods.

Objectives

- To understand the limitations of conventional analytical and simulation due to manufacturing and material variability via macro-scale and meso-scale experimental investigation of permeability distribution within an ADFP preform.

- Investigate the reliability of conventional meso-scale analytical model predictions in comparison with experimental results.

- Develop a numerical model that uses real variability data to produce a graph network for complex preforms, whereby the planar and through-thickness position, size and orientation of gaps are obtained online during ADFP.

- Identify a method to characterize flow rates across the network of gaps within the ADFP preform and develop a numerical model that achieves the objective in shorter time than conventional approaches.

- Development of numerical model to homogenise local and global velocity using data from the gap network flow rates and produce velocity maps which identify regions of poor flow in a preform.

Chapter 2 Literature review

2.1 Materials

The reinforcement material can be constructed in various formats (such as woven, unidirectional, non-crimp, etc) but also may be pre-impregnated, known as prepreg, or dry fabrics.

2.1.1 Prepreg

Prepreg sheets are impregnated with polymer resins, prior to laminating onto a mould tool. For thermoset prepregs, the reaction during impregnation is intercepted by cooling or freezing, resulting prevent the material from aging beyond its gel point, this stage of material is known as B-stage material [48]. This makes the material tacky, however as a result of the resin aging they need to be stored at relatively low temperature (-18°C) [5, 49]. Alternatively, thermoplastic prepregs can be produced by melting the prepreg material before cooling below the melt temperature [50]

Working with prepregs requires planning to have the material defrosted and needs to be formed into the desired shape in their limited shelf life. The storing requirements highly increases the energy cost from transportation to in-site storage. Furthermore, material wastage is higher due to their limitations in terms of long term process-ability. If the prepregs are stored at warmer temperature it will reduce their shelf life and the prepregs with unknown shelf life or close to end of their shelf life are often disposed[49]. However, prepregs are easier to form manually (by hand) into complex shapes as the tackiness hold the fibres together in position on the mould. The curing temperature for prepregs are typically between 60ºC and 180ºC [51]. As a result of the material processing prior to distribution, the cost of prepreg is typically between 80 – 200 £/kg [52].

2.1.2 Dry Carbon Fibre

Dry carbon fibre is usually provided in a roll or a reel (Figure 4 [53, 54]). A carbon fabric is generally preformed manually, whereas carbon tow roving is used for automated processes. The preform produced is than impregnated with resin within a mould. The cost of aerospace grade virgin carbon fibre is £41.77/kg [52, 55], which is significantly lower than prepregs (up to 18.8% in case of non-crimp prepreg carbon fabric[56]), although the matrix material and consumables need to be purchased and processed separately for impregnation. The dry carbon fibre does not need any special storage environment and has clear advantage over shelf-life and energy cost in comparison with prepregs. Although dry carbon fibre has a disadvantage in handling as it can incorporate variability into the fibre sheet (waviness, twists, gaps). To avoid any handling/lay-up induced inaccuracy, usually a binder material is added to the carbon fibre tows which is melted during deposition and holds the fibre tows in position.
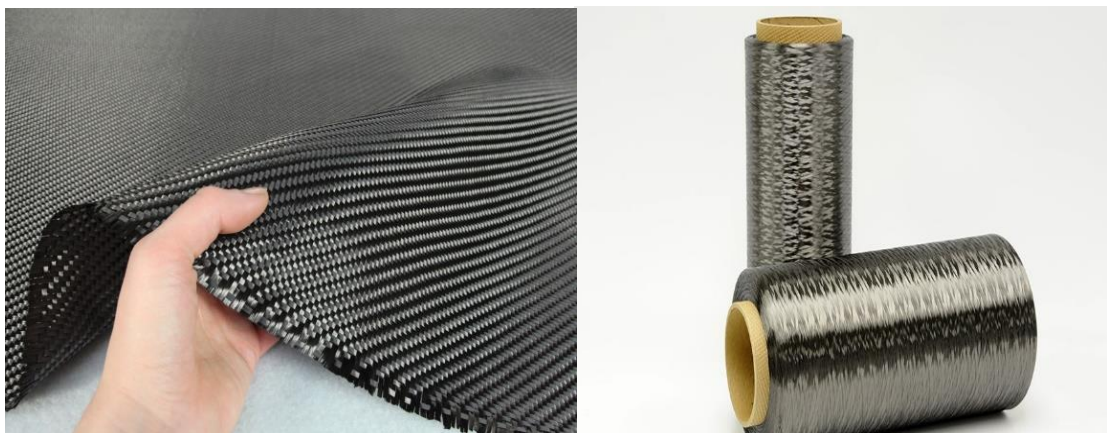
Figure 4 - Dry carbon fabric (left), Dry carbon fibre tow roving (right).

2.2 Preforming

Preforming is the first stage where dry reinforcement material is cut and formed using different methods into final designed shape of the part.

2.2.1 Hand-lay up

Hand lay-up is the most traditional composites fabricating technique [57-59]. Each ply is trimmed and handled by hand. Dry fabric in the form of woven, stitched or knitted fabrics are placed into the mould, and a brush is used to distribute/apply the matrix material. This process is repeated ply by ply until the required number of plies have been deposited. To achieve a uniform resin distribution, hand rollers are used to roll and wet out the layers thoroughly and ensure enhanced interaction between reinforcement and matrix.

Similarly, this method is also used for prepregs. It involves multiplying each ply into the designed shape by hand and firmly sticks to previous layer or mould surface without leaving any air pockets/voids.

This is a manual process and contains many limitations such as the production limit in terms of manufacturing big scale structures in aircraft industry[59]. The quality of composite part is directly dependent on the skill/experience level of the person such as laminating the reinforcement, resin mixing [58-60]. The laminate produced by hand-layup usually contains excessive void quantities [59]. Therefore the process is highly labour intensive with lower production rates and higher production costs [60, 61].

2.2.2 Automated Tape Lay-Up (ATL)

To overcome the limitations such as low productivity and quality effecting the hand lay-up process, various methods have been developed with the aim to automate the lay-up process and improving the lay-up speed and reduce the material wastage while maintaining the high volume production and quality of preforms. Many methods have been developed for automated lay-up

to improve productivity over time [62-64]. Automated Tape Lay-up, Automated Fibre Placement and Automated Dry Fibre Placement are the three main technologies that are employed today to manufacture carbon fibre laminates.

Automated tape laying (ATL) is well established automated lay-up process for composites [65]. This process is adopted to manufacture variety of parts such as wing skins [66-68] and the centre wing box of A380 [67, 69]. ATL can lay-up UD tapes (typically $75 - 300$mm wide [14]) at higher speeds, produce larger parts with greater process control [66]. Gantry or robot machines are used to deposit carbon fibre tapes directly on to the mould using a silicone head to deposit the material [62]. Generally, the material is stored in the head directly as shown in Figure 5. For automated process, the prepregs materials can be modified by changing the degree of impregnation and backing paper. Preform is manufactured by depositing multiple layers of prepregs on to the mould. In each layer, material is deposited course by course and between each course a gap of 0.5- 1mm is programmed to accommodate for any machine induced variabilities such as overlaps [14]. At the end of the course, the head deaccelerates and cuts the tape feed once reached the end point of the course using pinching or rotating blades [14]. ATL systems can reach a maximum linear speed of $0.83 - 1 \, ^m/_{s^2}$ and accelerate at 0.5 ms^{-1} [14] . A basic ATL system costs ~US$3.5M [70], an example of gantry ATL machine is shown in Figure 6. ATL process can reduce material waste (less than 6% by weight) in comparison to hand lay-up [14] . However like another system, ATL systems contain limitations such as high initial capital expenditure is required and the machines are unable to manufacture preforms with complex geometry [14].
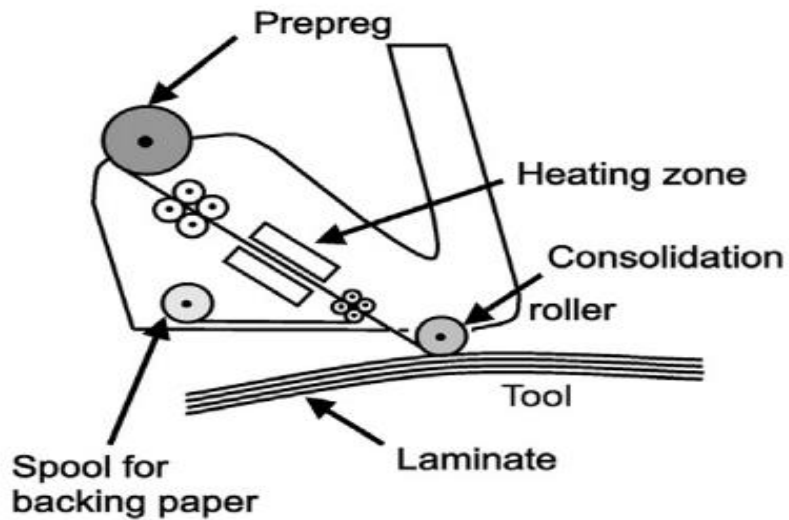
Figure 5 - Schematic of ATL machine head [71]

Figure 6 - Gantry style ATL machine [14]

2.2.3 Automated Fibre Placement (AFP)

Automated Fibre Placement (AFP) was designed to produce composite parts by directly depositing narrow prepreg slit tapes or impregnated tows to a tool using a gantry such as in Figure 7 (Left), or a robot arm such as in Figure 7 (Right) while applying heat and consolidating the tow with a roller. The difference between Automated Fibre Placement (AFP) system and

ATL is the width of the material that the system uses for depositing fibre on to the tool. The typical widths of a tow used in AFP machines are 3.2mm, 6.4mm and 12.7mm. The material is either stored in the machine head or creel cabinet as shown in Figure 7 (right). Unlike in ATL, AFP is capable of delivering several in a sequence known as bands tows as shown in the Figure 7 (left) [72]. A band then forms a course and a sequence of multiple courses is called a ply (layer). AFP machines are capable of delivering up to 32 tows within a single course [14, 72]. The tows are heated at machine head using different technologies such as laser assisted heating [73], flash lamp heat [74], and joule heating [75]. The width of the material and number of tows used can be different for each preform design and depends on complexity of the preform design. The capability of AFP machine to clamp, cut and restart during manufacturing allows to deliver each tow at individual speed [72, 76]. Such features of AFP enables layup over complex tool geometry and some degree of tow steering. AFP can deliver at linear speed of up to $1ms^{-1}$ [14, 72].

Figure 7 - Automated Fibre placement Machine – Gantry MTorres fibre layup (left), Coriolis Robot Arm (right)

AFP system have not only improved the quality, accuracy and production rates [77] but also significantly reduced the labour and material cost [78]. Due to the capability of manufacturing complex structures, AFP have enabled wider scope of lightweight manufacturing for many industries such as turbine blades for wind energy [20] . AFP has also been adopted by some of the major aerospace organisations such as Airbus, Boeing and NASA for manufacturing of light weight and precise components such as wing skins, nose cones fuselages and load-bearing propellant in space-crafts [79-81].

2.2.4 Automated Dry Fibre Placement (ADFP)

Automated Dry Fibre Placement (ADFP) is built upon the same entering concept as AFP except the material. Instead of using thermoset or thermoset matrix material ADFP uses binder material on dry fibre to retain the fibre in position. Binder is applied on dry fibre in two different ways:

- Tow/tapes already containing binder which is activated using heat application usually at the head of deposition rig such as Solvay PRISM TX1100 shown in Figure 8 [82].

Figure 8- PRISM TX1100 Dry Tape schematic

- Online binder (liquid or solid) is sprayed as the dry fibre is being deposited onto the mould surface [23] and binder is activated using heat application. Such example is shown in Figure 9.
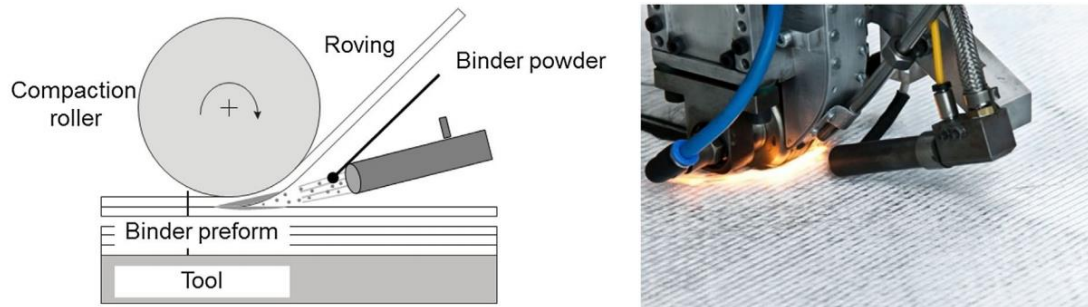
Figure 9 - Schematic and picture of online binder application tool [26]

Each ply is delivered in the similar way as AFP. The machine specification (lay up speed, maximum number of tow delivered) are also similar to AFP machine. ADFP technology is developed to manufacture a composite part in conjunction with Liquid Composite Moulding process (LCM). Once a preform is manufactured using ADFP, LCM process is used to impregnate the preform with resin. Different types of LCM processes will be discussed in the next section. Automated Dry Fibre placement (ADFP) has been attracting industrial interest due to its potential of reducing cost further than AFP. This offers improved control over the preforming process by recording online data, enables to use matrix material of choice and enables different types and volume content of binder to be used [23]. Therefore, cost is significantly reduced (43%) in comparison to hand layup, no special storage facilities are required by keeping material and preform at room temperature with unlimited shelf life [14] and no oven/high pressure (autoclave) curing required. ADFP based composite parts have already been adapted by aircrafts industry. In Russian MS21 aircraft, the critical primary structures such as wing spars, wing skins and six section panels for the centre wing box was manufactured by ADFP technology [83, 84].

2.3 Impregnation and Consolidation

Once the preform is manufactured, it is impregnated or consolidated using different techniques. Prepreg based preforms are consolidated using heat and pressure while dry carbon fibre preforms are impregnated with matrix material. This section will briefly describe the different methods of impregnation and consolidation and highlight advantages and disadvantages of each.

2.3.1 Autoclave Moulding Technique

Autoclave is high pressure chamber (Figure 10) and autoclave moulding is one to the techniques where a preform is cured by applying vacuum, heat and pressure. The preform is placed onto a mould, and it is sealed by covering it with a plastic bag and using tacky tape to create a sealing. Vacuum pump is then used to exhaust air out of the chamber. The mould is placed into the autoclave where heat and inert gas pressure (up to 10 bar) are applied for curing and densification of the composite part. A detailed schematic of moulding in autoclave is show in Figure 10.
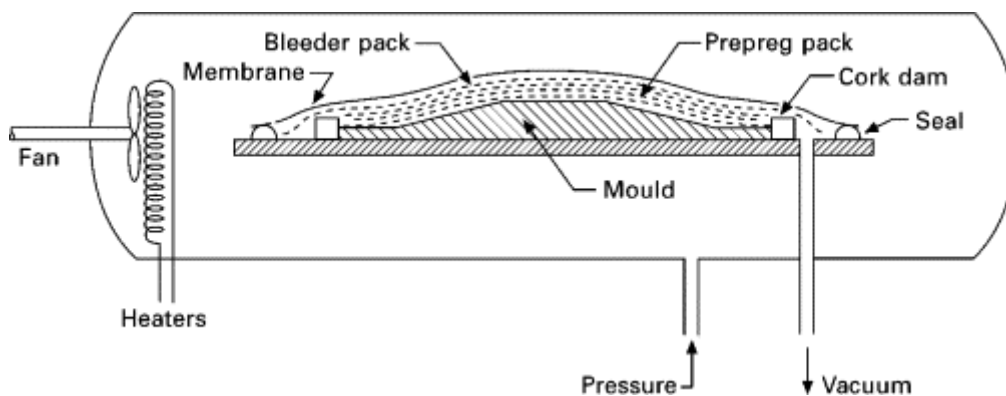
Figure 10 - Schematic of Autoclave melding process [85]

Preforms produced by ATL or AFP can be cured using this process. Due to the application of vacuum, heat and pressure, the process produces composite parts with closer control of thickness and lower void percentage [86, 87]. The parts produced by autoclave provides high level of uniformity and quality [87]. However consistent high quality composite parts can be

produced using this process, high capital investment [85, 87], operation and tooling cost is required to set up autoclave process [21]. Additionally, design of a part is limited to the size of autoclave and restricted processing schedules [21], resulting into large autoclaves that are used for manufacturing of small parts consuming excessive energy from heating and pressure [88]. Therefore, the use of autoclave processing is not sustainable and can limit the growth of composites manufacturing [89].

2.3.2 Liquid Composite Moulding Processes (LCM)

Alternative manufacturing techniques have been developed with the aim of manufacturing cost-effective aerospace grade composites [21, 22]. These processes are termed as Liquid Composite Moulding (LCM) processes. LCM has gained much attention due to the advantages, such as low-pressure requirements, lower tooling cost, less energy consumption, flexibility in part size and is less harmful to the environment [90-92]. LCM is used for dry fibre preforms such as preforms produced by ADFP technology. Preforms are impregnated with matrix material (RTM6, Epoxy, IN-2 etc.) using one of the liquid composite moulding (LCM) techniques such as Resin Transfer Moulding (RTM), Compression Resin Transfer Moulding (CRTM) or Vacuum Assisted Resin Infusion (VARI). Only RTM and VARI are relevant in this project and their procedure is explained below.

2.3.2.1 Resin Transfer Moulding (RTM)

A preform is placed onto the mould and a matching top mould is closed and sealed with bolts and nuts, or a hydraulic press. An example of RTM mould is shown in Figure 11. Resin is then injected into the mould cavity through the injection gates. There are two variations of RTM, low pressure (<10 bar) and high pressure (up to 150 bar) (HP-RTM). Resin advances through the preform pushing the air out through vents. After the preform is completely impregnated, the resin starts to flow out from the vent and the injection port is closed. The resin then undergoes a chemical reaction to form a fully cured composite part.
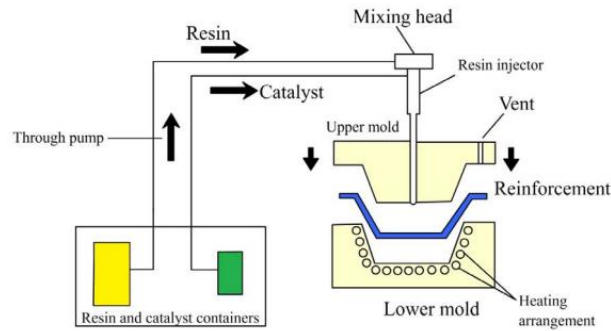
Figure 11 - Schematic example of RTM process [93]

2.3.2.2 Vacuum Assisted Resin Infusion (VARI)

Whereby the RTM is a closed-mould process, In VARI preforms are placed onto the mould and covered with vacuum bag instead of a rigid tool. The bag is sealed using tacky tape and air inside the mould is removed using vacuum pump prior to the infusion. Once resin is released through the inlet gate, the pressure gradient caused by the vacuum draws the resin through the preform, such as shown in Figure 12.
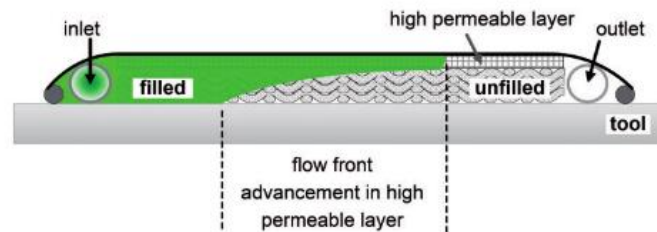
Figure 12 - Schematic example of VARI [94]

Additional compaction force is applied onto the preform in VARI which could causes nesting of fibres. V_f increase rapidly at low compaction force therefore compaction behaviour of material affects the final V_f of the part. Meanwhile in RTM no additional compaction force is applied. However, preform dimensions shall be carefully considered before impregnation. If the preform is cut too small comparing to mould surface, preform can displace due to applied

pressure by the resin. If the preform is big, fibre tow will face compressive forces upon mould closure and affect the final V_f of the part.

Despite the advantages in cost reduction, hand lay-up-based LCM process exhibit concerning disadvantages of low efficiency, poor reproducibility and difficulty in quality control. Additionally, the preform in impregnated under one vacuum pressure in VARI, the cured composite part exhibits high porosity and low fibre volume fraction. This results into a composted part with poor quality than those cured in autoclave. Therefore Aero-space industry have long limited the use of LCM process in manufacturing of secondary structures rather than primary structures [90, 95, 96].

Although ADFP technology in conjunction with LCM process have resolved the issue of low fibre volume fraction in hand layup-based LCM through compaction process during deposition process. Therefore, this process enables manufacturing of high-quality part composite parts with equivalent performance to autoclave based composite part [26, 97, 98]. This approach was used in Russian MS21 aircraft (2.2.4), the critical primary structures such as wing spars, wing skins and six section panels for the centre wing box was manufactured by ADFP technology and impregnated using VARI process [83, 84]. However, the characteristics of ADFP preforms and its influence on the infusion process are still not clear. This requires research that will further expand the application of ADFP based composite parts in aerospace industry by improving the production rate whilst marinating the quality of ADFP based composites parts.

2.3.3 Flow Characteristics during impregnation process

Permeability is one of the most important factors which affects the production time and quality of the composite parts. It is an intrinsic property of fibres that determines how easily fluid/resin can pass through it. Permeability is the dominant characteristic of resin flow during infusion and affects the quality of final composite part [99]. Permeability is defined by the well-known Darcy's law[100]

$$v = \frac{1}{\mu}[K]\Delta P \tag{1}$$

Where v is the superficial velocity(m/s) , [K] is permeability tensor of the porous medium where permeability units are m^2, μ is the resin viscosity$(Pa.s)$ and Δp is the pressure gradient. Pressure gradient is expressed as

$$\Delta P = (P_1 - P_2)/L \tag{2}$$

Where P_1 is the high pressure point (Pa) and P_2 is the low pressure point(Pa) and L = length (m) up to which flow front has reached. The equation is eligible in case of 1D flow only. To experimentally measure the permeability of a fibrous, preform, either rectilinear rig is used to generate 1D flow Figure 13 (Top) or a radial rig where a 2D flow is generated Figure 13 (Bottom). Permeability can be calculated in two different states, saturated and unsaturated. For unsaturated permeability, preform is impregnated in a sealed mould with resin and flow front is recorded either by data provided by pressure transducers [101] or by using camera for visualization [102]. The saturated permeability is obtained after the preform is fully impregnated with test fluid/resin. Once pressure and flow rate (Q) in the mould has reached a steady state, measurements are taken, and a graph can be plotted between the Q(m^3/s) and ΔP and permeability can be obtained. It has been reported that saturated and unsaturated fabrics do not exhibit the same permeabilities. Ratio of unsaturated to saturated permeabilities varies

from 0.25 to 4 [103, 104]. Meanwhile in some cases saturated permeability was recorded higher than unsaturated permeability [24, 103, 104].
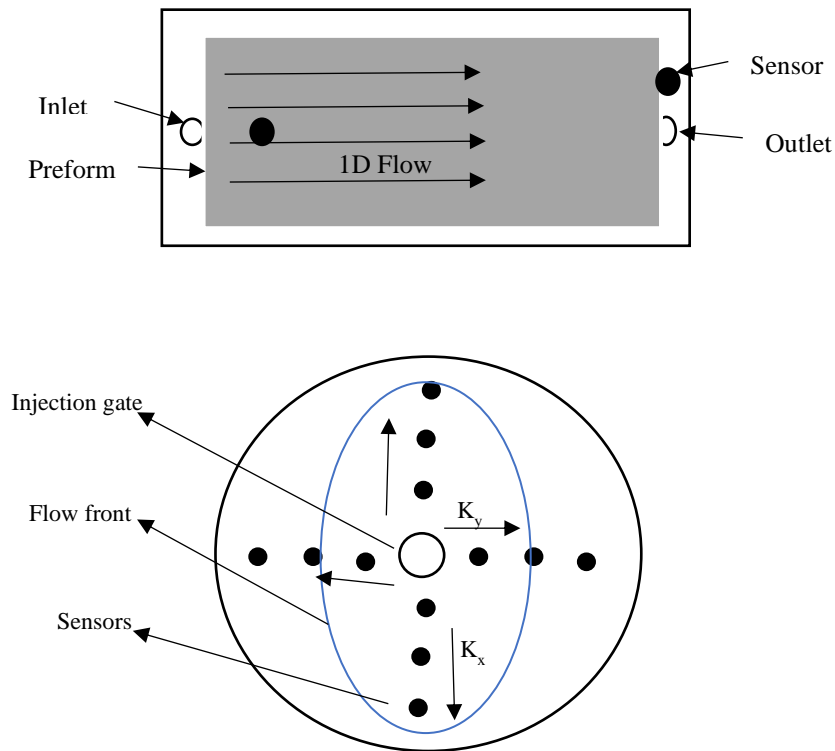
Figure 13 - Example of 1 directional flow (Top) and two dimensional flow (Bottom) experimental permeability rigs

Furthermore, two approaches can be used to measure unsaturated permeability.

1) Constant injection pressure

Resin or model fluid is injected into the mould at constant injection pressure. During the experiment the flow front position is recorded as a function of time and permeability is obtained from equation (3) [101, 105]

$$x_f = \sqrt{\frac{2\,k\,\Delta P\,t}{\mu\,\phi}} \tag{3}$$

X(f) is the flow front position and ϕ is the porosity, $\phi = 1 - V_f$.

2) Constant flow rate experiments

Constant flow rate is maintained by pressurizing test fluid/resin in the hydraulic chamber. Flow front position as a function of time can be used to obtain flow rate.

$$x_f = \frac{Qt}{\phi A}$$

(4)

Where Q is the flow rate and A is cross-sectional area of the cavity.

2.4 Previous work on permeability

This section will illuminate the repeatability problems in permeability measurement, highlight the approaches and key findings of previous work by a few researchers. Many researchers have used various approaches to characterize in-plane permeability. Few focused on analytical approach to estimate in-plane permeability before validating experimentally [27, 34, 94, 106-108] . Others have started to utilize modern simulation capabilities to predict the local permeability within in a preform [28, 109-111]. Research equipment has been developed to determine k_x permeability via 1D experiments [106, 107, 112], k_y via 2D experiments [112, 113], or k_z via 3D experiments [31, 94, 109, 114-116].

Small variances in deposition of fibres, ply orientation, resin viscosity and overall experimental conditions can affect the permeability of fluid through the preform. Since, permeability measurement method is not standardised in the composites industry, it generally results in to large scatter/variation between measurements taken for the same material from different methods and in different laboratories. This is being addressed by various institutes in a collaborated benchmark exercise [24, 29, 117]. A first benchmark exercise was carried out where eleven institutes participated and agreed to determine permeability for two different fabrics [24]. A 2 X 2 twill weave E-glass fabric and a 2 X 2 twill weave carbon fibre. Participants were free to use any technique to measure permeability at 50% V_f and the results reported are given in Figure 14.
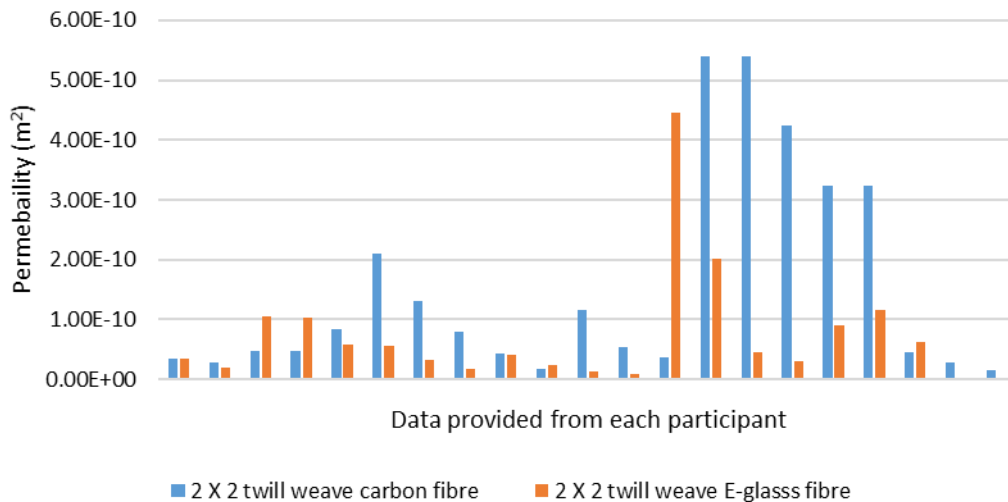
Figure 14 - Experimentally obtained permeability by eleven participant institutes -

Benchmark 1 [24]

A large degree of scatter in data was found. The Figure 14 clearly shows the difference the difference in highest and lowest value for the same fabric. It was concluded that human factor was the cause of scatter in results since independent decisions were made on processing parameters for test. Whereas "Benchmark 2" was conducted a few years later (2014) with aim to obtain the result in more controlled environment [117]. Aim for this benchmarking study was to produce less scatter in data by minimizing the human errors. Guidelines were established in [118] and 15 institutions participated in this study. Two analytical approaches were used, one is based on interpolation of flow front position against time. Figure 15 below shows the permeability values only in wrap direction.
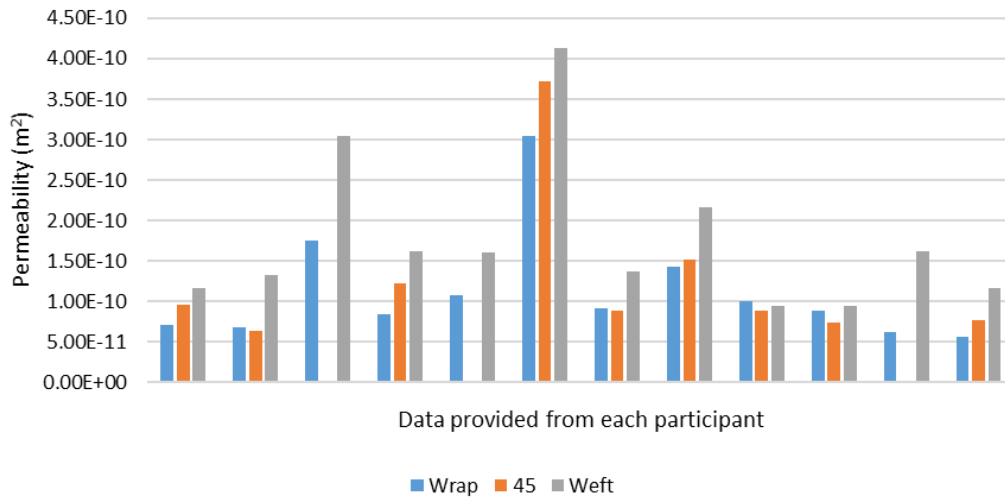
Figure 15 - Experimentally obtained permeability by 15 participant institutes - Benchmark 2 [117]

Scatter was more than one order of magnitude for V_f in range of 45% to 50% in benchmark 1 [29]. This was reduced to 25% when the participants followed guidelines in [117]. Conducting a study with various institute involved will require extremely careful control of parameters/experimental conditions in order to minimize human factors. Mishandling of 2 X 2 twill carbon fabric can lead to shearing of tow within the preform and hence will produce varying gaps in-between the weft and wrap direction such as in Figure 16. It will distribute the flow in transverse direction (k_z) and effect the in permeability on through the thickness. To characterize the permeability and generate reproducible results it will be worth to start from less complex materials.
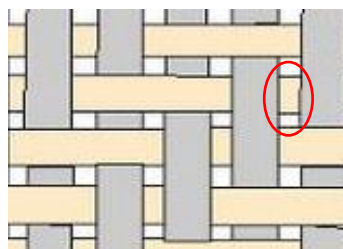
Figure 16 - Twill weave and the gap regions that encourages flow in transverse direction (z)

One of the in-plane permeability measurement device was developed by the Centre of Lightweight structures [112] which measures the permeability while the fluid is in steady state (saturated flow experiment). The results were compared with data acquired by visual flow tracking. It was concluded that the steady state permeability measurement is sufficient to model unsaturated filling process by neglecting interfacial phenomena (impregnation) which contradicts with findings in [103, 105, 117] which showed unsaturated permeability is lower comparing to saturated permeability. It was also claimed that permeability measurements by visual flow front tracking of resin are questionable due to the high sensitivity of flow on multi-scale. Therefore pressure transducers should be used to produce more accurate data by recording the exact arrival time of resin/model fluid as used in [26, 27, 31]. On the other hand, 25% scatter was found in reported results when pressure transducers were used [24, 117].

The majority of the techniques developed for permeability measurements are based on experimental methods. But some have developed analytical and numerical methods to characterise the permeability. In rectilinear mould resin quickly propagates from the edges of the mould towards the outlet and triggers the sensor even the mould is partially filled [119]. A lot of experiments were discarded due to such effects in [27]. In [107, 119], Wang et al. and Lawrence et al showed race tracking can be incorporated into the predictions by using analytical relationship. The analytical model was tested by comparing experimental and simulation results, similar fill times, flow front progression and void formations was predicted by the proposed models. On the other hand, Di Fratta et al. [106] proposed a semi-analytical approach to measure permeability as a function of fibre volume fraction with a single unidirectional experiment. Two pressure transducers, located at the inlet X_{in} and within the cavity X_s, may then be used to calculate permeability as a function of time under constant injection pressure from *[106]*. A recursive algorithm is then used to create an online profile of permeability. These algorithm requires pressure data from two transducers and allow real time

estimation of permeability. Figure 17 shows the working principle of the algorithm. The algorithm finds the permeability K_i between previous X_{i-1} and current X_i flow front position and creates a profile of permeability at different flow front position using pressure data. The algorithm does not consist of any limitation of fibre volume fraction and permeability may be estimated for different fibre volume fractions in one experiment. This approach was experimentally validated, and permeability was estimated for 3 zones (zone A = 6 layers of fabric, zone B = 7 layers and zone c = 8 layers) creating different V_f sections in a single preform. Flow front was visualized using acrylic mould top to validate the equations. If fibre wash or race-tracking happened during mid-experiment sudden pressure drop will notify the defect using this approach.
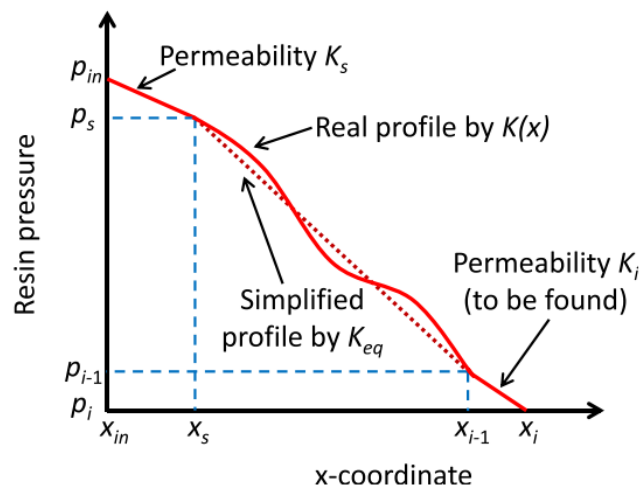
Figure 17 - Working principal of the reclusive algorithm [106]

Within LCM processing, an overall constraint is the maximum processing time which usually depends on the resin being used. Through-thickness permeability (K_z) is when the fluid flows in the z-direction of a preform. It is usually neglected in preforms with smaller thickness [105]. But it is important to incorporate K_z for predictions in preforms with larger thicknesses [31].

Measuring through-thickness permeability of a preform is more complex unlike the in-plane permeability experiments, visualization of flow front within the preform is not possible.

Therefore, alternative approaches have been taken by the researchers to track the flow front position by various techniques like, ultra sound measuring technique [29], smart weave sensing [120], flow front detection through fibre optics [121] and electrical sensors technique[122]. For large and thick parts, impregnation of textile is often desired in the through-thickness direction by the use of flow enhancing media to reduce the overall flow distance through low permeability regions. A flow enhancing media has lower permeability compared to preform material, enabling the resin to travel quickly along the surface of the preform with low resistance before encouraging flow through the thickness of the preform [31]. Through thickness permeability of ADFP preforms is usually 1-2 order of magnitudes lower as compared to conventional style fabrics such as woven or non-crimps (Table 2). Also comparing with In-plane permeability values in *Table 1*, through thickness permeability (Table 2) is approximately one-order of magnitude lower. This is because resin/fluid travels faster in fibre direction [105] and at a microscale, the compaction causes the filaments to nest, blocking or restricting the flow between the filaments. However, at a mesoscale, the tows spread, closing gaps between neighbouring tows, blocking the flow path around. A continuous technique was developed by Scholz et al. [123] to measure transverse permeability of a preform during compaction. They conducted experiments by injecting gas or a Newtonian fluid through the preform. They concluded that the both gas and liquid experimentation shows same through-thickness permeability values.
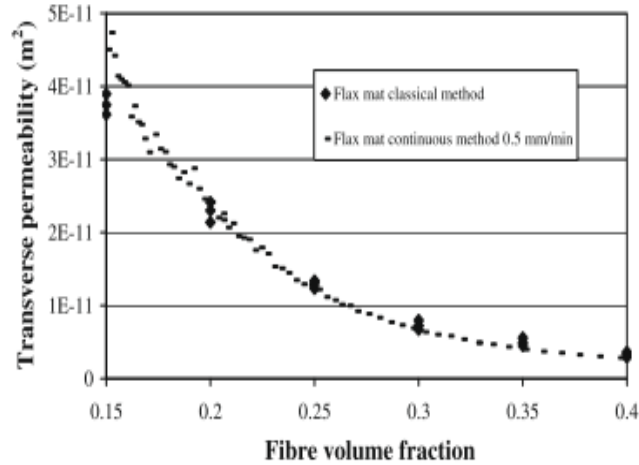
Figure 18 - Continuous vs classical transverse permeability of flax mat [124]

Ouagne et al. [124] used both, classical method and continuous method to measure through-thickness permeability of preforms. They developed a device with adjustable cavity height to measure permeability at different V_f. [112] also used an adjustable cavity height system to measure through-thickness permeability of preform at different V_f. In classical method, desired flow rate is applied to a V_f and rise of pressure by fluid flow across the preform is measured. Four different materials showed very similar results. They noticed a sudden decrease in permeability at lower fibre volume fraction and the decrease slows down as the V_f increases. They concluded that similarity between results is due to the fibres and bundles has time to rearrange within the preform during compression. Rearrangement of the fibres and bundles into a steadier position will result penetration of drop in permeability and reduction in measured pressure values. However, Becker, D et al. [30] reported. $K_z = 2.6 \times 10^{-12}$ m^2 measured at lowest pressure gradient was found to be an order of magnitude higher than the $K_z = 3.93 \times 10^{-13}$ m^2 measured at highest pressure gradient. This shows that the through-thickness permeability is dependent on fibre volume fraction but also on the pressure gradient. The effect of preforming technologies on through-thickness permeability of woven glass fabric was also investigated [114]. This investigation discussed the few different preforming methods given below:

27

- Stitching

  manually stitched woven glass fabric was compared to a non-stitched reference material and found clear increase in out-of-plane permeability 2.05 x 10^{-12} m^2 of stitched textile [23, 114]. The size of the sewing needle also effects the permeability. They had a needle of 5mm diameter and thickness of thread was only 1.2mm. This left big channel for resin and increased the permeability. Thread thickness also effects the V_f. higher volume fractions were achieved with smaller thickness of thread as compared to reference and resistance to compaction decreases due to pre-compaction. Conversely, higher thickness of thread gave smaller V_f as compared to the reference material and achieved increased resistance to compaction due to pre-compaction.

- Binder

  Samples of activated binder showed lower K_z = 8.81 x 10^{-13} m^2 as compared to samples with not activated binder K_z = 1.02 x 10^{-12} m^2. Binder is an additional volume to the layup which blocks the resin channels after activation resulting in lower permeability in comparison with non-activated samples. Within the measured pressure range, sample with non-activated binder showed no additional compaction. K_z of reference textile = 1.51 x 10^{-12} m^2 was found to be higher as compared to samples with activated or not activated binder. At higher pressure drops (>1.5 bar) permeability increase of 18% was found in sample with not activated binder.

- Shearing

  An average of K_3 of textiles at 0⁰, 10⁰ and 20⁰ was found to be 10% lower as compared to the reference material. This was because shearing creates small channel in crossing region but also narrowed the main channels. Meanwhile shearing of higher angles (45⁰,90⁰) in successive plies increased the permeability by 87% in comparison with sample with no shearing [125].

Fibre architecture or ply orientation can create flow channels at multiscale and encourage the flow through the thickness. Hatic et all. [125] numerically and experimentally studied the effect of relative ply orientation and small misalignments on through thickness permeability of a preform. Numerical permeability was estimated by modelling of unit cell models in the software FLUENT and compared with experimental results. This uses the same equipment as [102]. Five different layup sequence were investigated. Layup sequence and their relative permeability is shown in the Table 3.

Case	1	2	3	4	5
Layup	Angle 0º	Angle 5º	Increment of 5º for each layer	Increment of 45º for each layer	Increment of 90º for each layer
Experimental $K_z \times 10^{-11}, m^2$	0.277	0.317	0.295	0.938	1.733
Numerical $K_z \times 10^{-11}, m^2$	0.377	0.3995	0.498	0.898	1.810

Table 3 - Lay-up sequence and respective permeability in experimental and numerical analysis

In their study, the 1st, 2nd and 3rd case was related to any minor misalignment and variabilities during layup. Case 4 and 5 showed an excessive increase in k_z. This increase in permeability was attributed to lower resistance in resin path and this behaviour was confirmed with numerical simulation. In general opinion, if less resistance was the only cause of this excessive increase in k_z, Case 1 and 2 should have highest k_z as all plies are unidirectional and offer more direct flow channels in z-direction as compared to case 3 & 4 where every next ply is incrementing to a certain angle. As k_{xz} and k_{yz} were found to be slightly higher in [28] and shifted the ellipse centre, in these cases these skew term might have played a role in collaboration with in-plane permeability resulting into overall increase of k_z.

2.5 ADFP Preform Characteristics

As mentioned in chapter 1, the main limitations of ADFP is induced by either the material or the deposition process. These variabilities can be in form of gaps, overlaps, tape misalignment, tape twists, tape buckling and regions of poor adhesion. [14, 27, 32]. Gap and/or overlaps are induced mainly due to misalignments at the band edges and their occurrence can be frequent in complex shapes [33]. Defects such as tow buckling, tape pull-up induced by tape steering. tape misalignment may be induced due to tape steering if the radius is too small [14]. Additionally, increasing the lay-up speed is accompanied by poor adhesion between the layers and formation of voids. This is because of insufficient time for the heat to melt the binder.

The tape to tape gaps and overlaps are the most notable defect with highest occurrence [126]. Because they are typically induced on a very small scale comparing to component size (i.e. 0.8 mm tow to tape gap in an aircraft part), this increases the difficulty in inspection stage. An inspector may be able to spot a gap or overlap in a preform, but to inspect a full scale preform for a microscale defect entails high level discretion and a significant time commitment [126]. This is required through-out the time-sensitive manufacturing process. Moreover, the formation of gaps and overlaps is directly related to machine and material tolerances [127] and it is not possible to minimize machine inaccuracy to 0%. Therefore, gaps presence in ADFP produced preforms cannot be avoided. But some researchers have accepted the presence of gap and used it for avoid other defects. As overlaps are forbidden by aerospace industry as they alter the local geometry and effect the overall thickness, one of the techniques used to avoid formation of overlaps is introducing a gap of 0.5mm between the bands [127] as shown in Figure 19 . This gap allows space for any machine inaccuracies. The width of the gap is defined according to the machine tolerances.
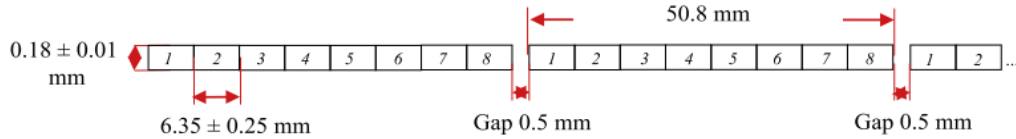
Figure 19 – Rule used by aircraft manufacturers for avoid overlaps [127]

Such discontinuities in the lay-up highly effect the flow characteristics during the LCM process. The gaps behave as microscopic channels and enhance the flow. On the other hand overlaps are high fibre volume fraction (V_f) regions which take longer to impregnate. This affects the local permeability of the preform and results into uneven flow front position throughout the LCM process. Such phenomenon leads to incorrect process parameters prediction by analytical or numerical models. Moreover, when the resin travels through a channel, it starts impregnating the neighbouring tapes in perpendicular to the flow direction (K_y). This may lead to higher percentage of voids in the final part. Also gaps are resin rich zones which ultimately act as crack initiating zones [126]. These characteristics affect the overall quality and performance of the composites part. Hence it is vital to understand such characteristics and incorporate them into analytical and numerical modelling.

As described in above, ADFP preform generally contains variabilities in comparison to as designed models [27, 31, 32]. Such differences at the meso-scale of ADFP produced preforms has been studied by [27]. In this work, cross-ply preforms were produced by ADFP, with a target inter-tape gap width of 1mm. To predict the permeability of the preforms through analytical models, the geometry of reinforcements was divided into elementary volumes and channels, which are then reconnected assuming series and/or parallel flow. The geometry at the meso-scale was viewed as a layered structure with each layer consisting of homogeneous tapes with rectangular gaps between them. For each region with different properties (gaps and fibres) a model was assigned to predict their corresponding permeabilities by using Gebart's model [34] and Cornish's model [44]. The global analytical permeability of preforms was

predicted by homogenization technique. The same approach is chosen here given the simple mesoscale geometry of the ADFP preform.

The layer permeability is calculated by weighted averaging technique. Permeability for layers in perpendicular direction was calculated by using the rotation matrix. Whereas the experimental permeability was measured using a rectilinear rig consisting of two pressure sensors to trigger resin/oil arrival time. Gap heights and widths were assessed using Matlab tools the results of which are shown in Figure 20.
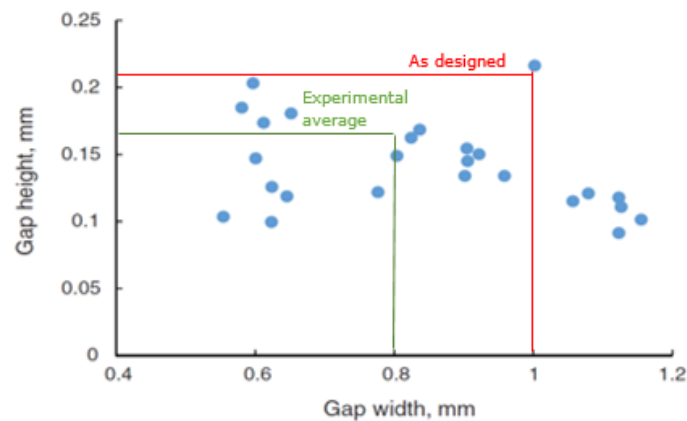
Figure 20 - Example variabilities in gap heights and widths (from [27]). Each data point represents one gap in the cross-section

The designed gap width 1.0 mm had an average gap width of 0.8 mm and designed gap height 0.2mm showed an average gap height of 0.16 mm [27]. Both vary up to 20% compared to the target gap dimensions as shown in Figure 20. The experimentally observed permeability of 1.56 x 10^{-11} m^{2}was half of the predicted value for a designed preform (2.81 x 10^{-11} m^2). The analytical model showed only 15% difference from experimental results when averaged parameters were used for predictions. Aziz et al. [31] provided further insight towards importance of variability for permeability prediction. Two 4-layer preforms with 0.2mm intentionally placed gaps between two tape widths 12.7mm (Preform A) and 6.35mm (Preform B) were studied by X-CT scanning. An ideal model of preform geometry was built in TexGen

and compared with a model reconstructed using the geometry captured by X-CT scanning. Through-thickness permeability of the material was measured in adjustable cavity equipment and compared with the permeability estimated by a numerical model built in ANYSYS. Preforms were produced by VARI and microscopic analysis was used to study their structure and any variability in gaps in the final part. Gaps in preform A were found to be smaller than the designed value of 0.2mm. The average gap width in each layer was 0.14, 0.14, 0.15 and 0.15mm. Meanwhile Preform B had gaps larger than 0.2mm. The average gap in each layer was found to be 0.59, 0.58, 0.25 and 0.26mm. The ANSYS model was reconstructed using this data and permeability was estimated. Table 6 shows the results, Analytical results showed high difference (up to 80%) from experimental under designed conditions in both [27] & [31] and the difference was minimized to only 15% and 10% once the variability data was incorporated into the adopted numerical models.

Preform	Tape width (mm)	Experimental K_3 m^2	CFD K_3 m^2 (as-designed preform)	CFD K_3 m^2 (X-CT scan data)	Error (Exp vs. Design)	Error (Exp vs. reconstructed)
A	6.35	8.31×10^{-14}	3.87×10^{-13}	7.47×10^{-14}	366%	10%
B	12.7	1.85×10^{-13}	3.65×10^{-14}	2.04×10^{-13}	80%	10%

Table 4 - Comparison was designed and actually transverse permeability of ADFP manufactured preform [95].

Another important observation was that while the robot arm failed to achieve absolute accuracy, it was significantly worsened by the increase in tape width from 6.35mm to 12.7mm [31]. Further study on the relationship between tapes with different widths and same inter-tape gap width is needed but the results observed in this paper may be machine specific. This demonstrated that the CFD and homogenization approach employed in [27, 31] can provide accurate estimates of permeability but only if the true gap and tow dimensions across the preforms are known.

Another study [32] investigated the effect of gaps on a 26 plies thick complex preforms with lay up of [(- 45, + 45, 0, 90)s, 0, (- 45, + 45, 0, 90)]s was manufactured. Preforms had a gap of (1mm to 4mm) placed after every course and VARI process was used to infuse the preforms and flow front was tracked using a camera. The results from the investigation are presented in Figure 21.
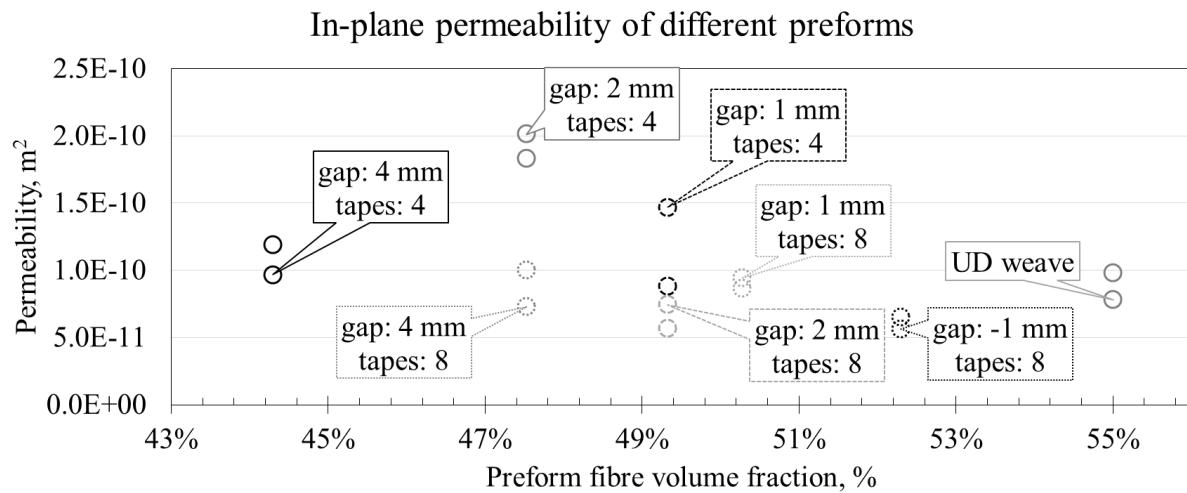
Figure 21 - Permeability results for different preforms produced by ADFP in [32]

From the results above the study rigorously concluded that gap does not have any effect on the in-plane and through thickness permeability of preforms which directly contradicts with [27, 31, 128].Figure 22 below shows a micrographs from [32], where it was displayed (in red) as if a perfect as designed preform was produced using an industrial size AFP Coriolis machine. However the yellows marked areas (marked for this literature review) were avoided where variability in gap dimensions and preform can be observed by naked eye.
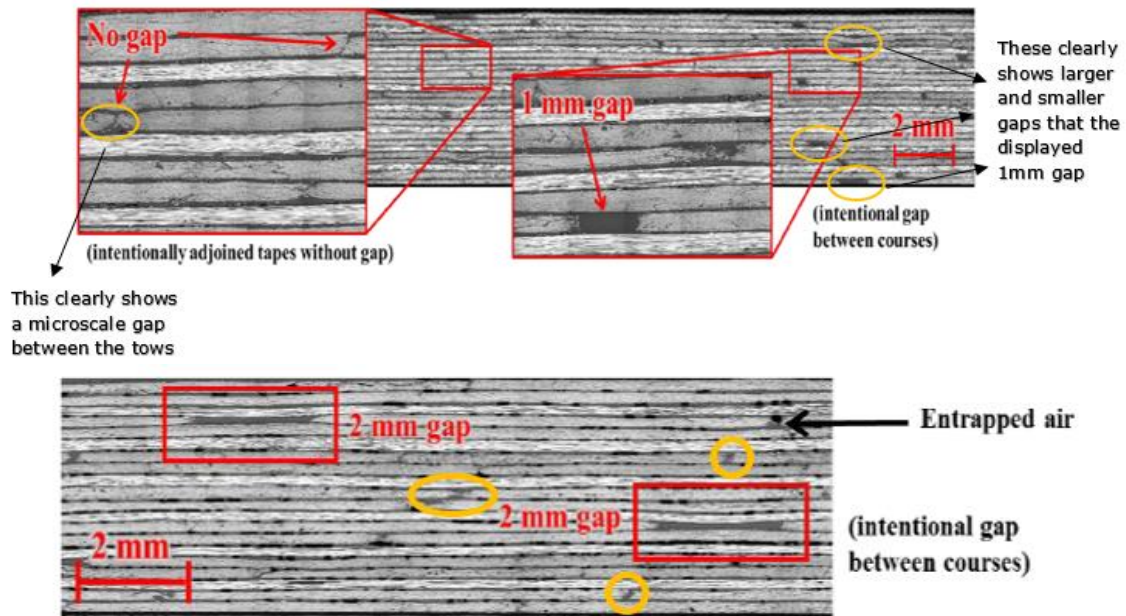
Figure 22 - Micrograph of preform with 1mm (Top) & 2mm (Bottom) intentionally placed gaps [32].

It was also reported that the gaps with wider widths (2mm, and 4mm) tend to be highly affected by roller compaction and completely close off the gaps from neighbouring layers as shown in Figure 22 (Bottom) also reported by [27]. To some extent this explains why the acquired permeability values did not exhibit much difference. Similar experimental results were reported by [26]. For different preform arrangements; inter-ply gaps/open arrangement, overlaps and nominal layup. A quasi-isotropic laminate negated any orientation bias during the experiments and 2mm gaps and overlaps were used after every 5th tape.

As expected, due to high fibre volume fraction and more resistance to flow, permeability of preforms with the overlapping pattern had the lowest value of $K1 = 3.15 \times 10^{-12}$ m^2. However, the nominal and open preforms had almost the same K_x values of 5.15×10^{-12} m^2 and 5.21×10^{-12} m^2. Based on the results it was concluded that gaps have no effect on preforms permeability. This is in contrast to through-thickness permeability experiments on preforms with intentionally placed gaps [31], which showed that gaps encourage through thickness flow in a preform. Gaps act as flow channels and should enhance the permeability of a preform but in this case the same K was obtained for both arrangements. This could be due to compression

during the deposition process causing tow from successive layers to bend and decreases the gap height significantly such as reported by [27, 32] .

Rimmel et al. [23] studied the effect of preforming methods on through-thickness permeability of ADFP produced preforms. Since reducing cost is one aim of ADFP technology compared to AFP [14], applying online binder is becoming more popular. The effect of binder particle sizes and its effects on permeability is of interest. Sieve analysis was done on powdered binder provided by the manufacturer and the binder was split into three different groups. The groups contained large particles (>250µm), medium particles (125-250µm) and fines. Samples with medium, large, and mixed (as supplied) binders were manufactured. The change in out-of-plane permeability because of using different binder particle sizes is not decisive. But since manufactured mixed of binder showed lowest permeability, this means a slight variability in out-of-plane permeability can be expected from online application of binder under similar forming conditions. NCFs shows good out-of-plane permeability due to resin channels introduced by the stitching process [129, 130].

The effect of tufting on ADFP preforms has also been studied by [23]. The V_f of preform was not highly affected by tufting. A total of 1070 stitches were applied in a rectangular pattern which increased the permeability by factor of 30 compared to the reference preform. Tufting was stated to be the most effective way of enhancing permeability of a preform despite this involving an extra step in the preforming stage. From the investigations above it can be identified that a clear gap is present in current available research in understanding of meso-scale flow behaviour under experimental conditions. This gap in research has also been highlighted by [131]. In most of the numerical investigations the permeability has been numerically obtained without validating it against the experimental permeability [131]. In their research, they investigated glass fibre permeability at three different fibre volume fractions. They developed a new experimental technique to measure tow level permeability and

compared with the analytical models most used in the research such as Gebart's and Kozeny-Carman.
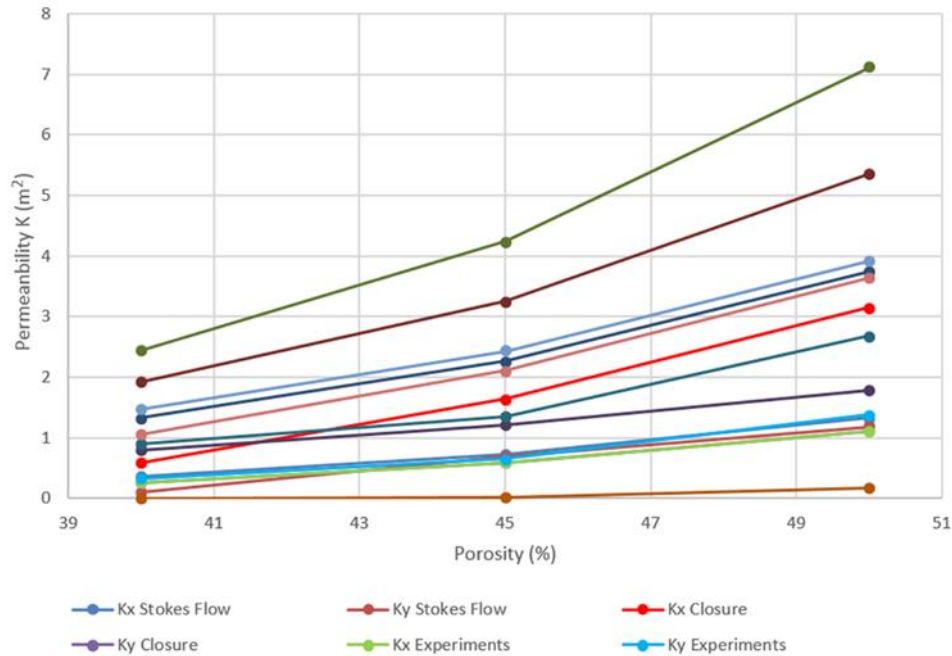
Figure 23 – Experimental permeability in comparison with analytical and numerical results [131].

They found that the permeability calculated by Gebart, Kuwabara, and Berdichevski and Cai was an order of magnitude less than the experimental values show in Figure 23. The investigation on glass fibre at tow level by [131] clearly shows the scatter between the results using different analytical models. No such investigation has been conducted on carbon fibre tows or tapes and gap models which are adopted to incorporate the gap effect in ADFP produced preform.

In conclusion, [27] showed that gaps can be adopted to enhance permeability of ADFP preform and homogenization approach can be adopted measure permeability of preforms containing complex gap networks but it failed to investigate the meso-scale permeability and compared experimental permeability with final homogenised permeability of a preform. It has also been understood that compactions force of roller can play a vital role and change gap specifications

and increase the difference from nominal permeability [27, 32]. The findings from [27, 31] showed that the error in experimental permeability can be minimized by using real preform data but the method adopted (Microscopy & XCT scanning) is expensive and requires each preform produced to be scanned preforms to be scanned. It was reported in [26, 32] that gaps have no effect on preform permeability directly contradicting with [27, 31]. They investigated only experimental permeability and ignored the effect of variability in preforms. And finally, results in [131] clearly showed the importance of validating the analytical models at meso-scale before comparing the macro-scale experimental results.

In conclusion, a clear gap in the research can be identified from studies discussed above. three level experimental validations are required before comparing the analytical obtained permeability to macro-scale experimental permeability. The three level validations are:

1- Tow, Gap, Tow and Gap

2- Layer level permeability

3- Multi-layer permeability

Moreover, it has been understood that the scatter in numerically obtained permeability can be minimized by incorporating the real preform architecture into a numerical model [31]. However, the current methods to enable that are rather expensive such as XCT scans and it is not cost effective to scan every single preform produced. Therefore, a modern method is required which could enable to scan every single preform during the deposition process and provide the real preform data. A cost and time effective numerical tool is also required which can incorporate the real preform data for each preform produced into the model and measures its permeability.

2.6 Prediction and modelling

Modern techniques of flow simulation are highly useful. Simulation software, such as PAM-RTM, Fluent and LIMS are used to predict the flow behaviour during moulding to determine parameters such as fill time, resin rich zones, air entrapment, locations of air bubbles risks, permeability profile across the component. This enables optimization of LCM processes by introducing vents or gates or changing ply-orientation to ensure complete impregnation [125]. The accuracy of the flow simulations is sensitive to in-plane as well as through thickness permeability. K_z can be very crucial depending upon the geometry of the component and impregnation direction of resin [109].

A simulation approach was used to study the effects of distribution media permeability and its effects on through thickness flow and void formation during vacuum assisted resin transfer moulding (VARTM) on woven glass fabric [109]. Woven fabric contains regions of gaps around the junctions of fibre tows. These gaps act as resin channels and enhance the through thickness permeability. It is essential to include these regions with higher permeability into the simulation for reliable results. They included these region as 1-directional cylinders surrounded by 3-Directional fibre tow. With the assumption of these regions as cylinder, permeability was estimated using the formula for permeability of a cylindrical tube as shown below:

$$k_{pin} = C\frac{R^2}{8}$$

(5)

Where R is the radius of the pinhole, C is the correction factor (hydraulic radius) which accounts for porous wall and non-circular pinhole geometry. Over 500 hundred simulations were done and compared with the numerical model developed. Distribution media with low, medium, and high permeability was tested. It was found that the percentage of voids increases with the increase in permeability of distribution media. Simulation was experimentally validated, and fair agreement was found between the results shown in Figure 24.
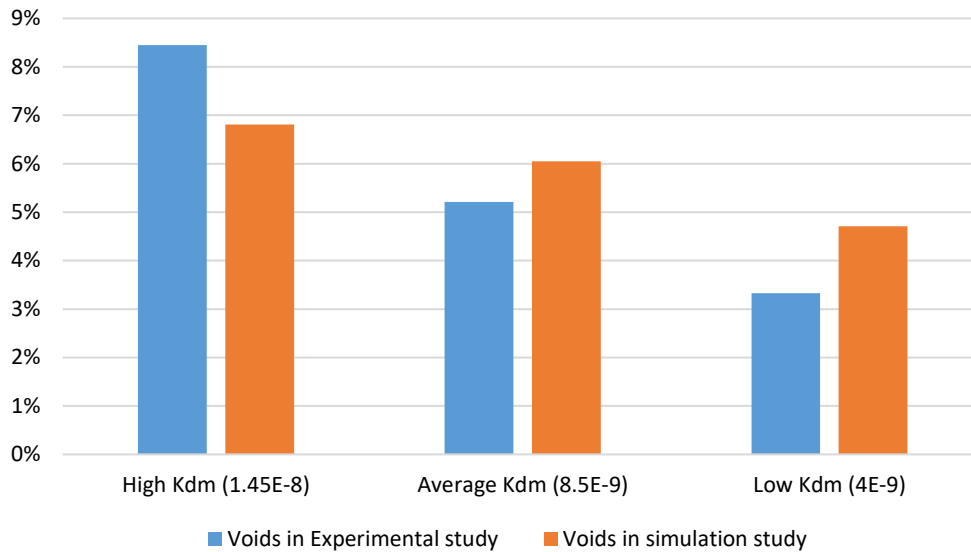
Figure 24. Effect of distribution media permeability on void formations (experimental vs simulation results) [109]

Okonkwo et al. [102] developed an optimization algorithm to estimate four components of permeability tensor in one experiment. Through-thickness permeability was estimated assuming that preforms have lower permeability in the z-direction than x and y-direction. The sensor in bottom of mould will get triggered first, resin will impregnate through the preform and triggers the sensor on top of mould. This data was used to reconstruct the 3D nature of the flow and predict the through thickness permeability. The simulation software required the permeability components. Mesh was created to reflect the exact coordinates of the mould sensors. Each component was estimated step by step. The data from sensors was used to consistently manipulate the permeability tensor. A layer of distribution media was used around the inlet gate to increase the injection radius. Effect of distribution media (DM) was included by considering 4 different scenarios and the most accurate values were predicted when DM was used in both simulation and experiments. Two components of permeability K_{xz} & K_{yz} were still not addressed in this study.

Whereas, Advani et al. [28] addressed the skew term in the permeability tensor. In radial injection, if resin is injected from the bottom of a thick preform the ellipse shape will slightly move as compared to its principal direction. A mould with transparent top and bottom plate was used to conduct the experiment. Initial in-plane permeability set was measured by processing images from the camera and initial transverse permeability set was measured by grid method and image information. Similar to [102], initial values were feed into simulation software to predict flow front and compared with the experimentally obtained flow front. Residual Sums of Square was calculated for flow front at top and bottom. Great agreement between simulation and experimental flow front was achieved. The shift of centre of ellipse at the top as shown in Figure 25 confirmed the influence of skew terms in thick parts and was found to be same order of magnitude as K_z.
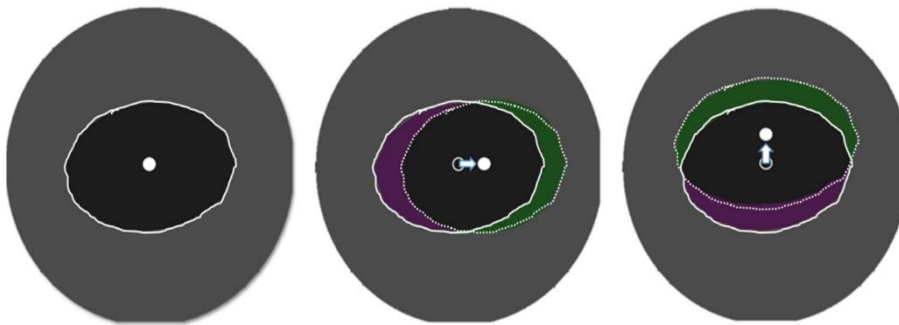
Figure 25 - Shift of ellipse due to influence of skew terms [28]

The k_{xz} and k_{yz} was found to be slightly higher as compared to k_z shown in Table 10. It helps to understand the shift of the ellipse and also the complexity to compute accurate permeability.

K_x	K_y	K_z	K_{xy}	K_{xz}	K_{yz}
1.97e-10 m^2	9.8e-10 m^2	9.9e-13 m^2	1e-11 m^2	5.01e-12 m^2	4.98e-12 m^2

Table 5 - Experimentally found skew terms of permeability tensor by [30]

The investigations discussed previously looked at the micro-scale effect on permeability, while [45] investigated the sensitivity of resin flow through inter-yarn gaps in fibrous reinforcements

to yarn cross-sectional shapes. A layer was represented by a repeated unit cell shown in Figure 26.
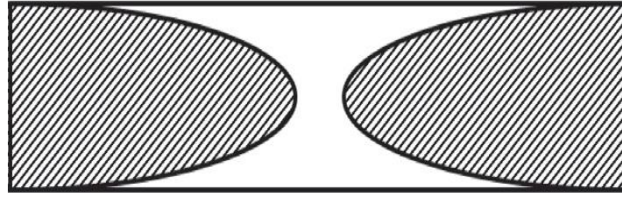
Figure 26 - Unit cell cross-section with yarns (blank) and gaps (shaded)

Similar to [27], a weighted average approach is adopted to calculate layer permeability [45] where axial layer permeability K_{layer} is given by,.

$$K_{layer} = \emptyset \, K_g + (1 - \emptyset)K_y \tag{6}$$

Where K_g is gap permeability, $\emptyset$ gap volume fraction and K_y is the axial yarn permeability. Unlike in [27] where the properties of fibre tow was incorporated into the model, [45, 132] analytically established that the contribution of the axial yarn permeability to the layer permeability is generally small compared to the contribution of the equivalent gap permeability and therefore it can be neglected.

$$K_{layer} \approx \emptyset K_g$$

The cross-sectional shape of a yarn in a preform is affected by effect of compression and it can be approximated by generalised power ellipse given in the Figure 27.

$n = 0.25$	
$n = 0.75$	
$n = 1.00$	
$n = 1.50$	
$n = 2.00$	
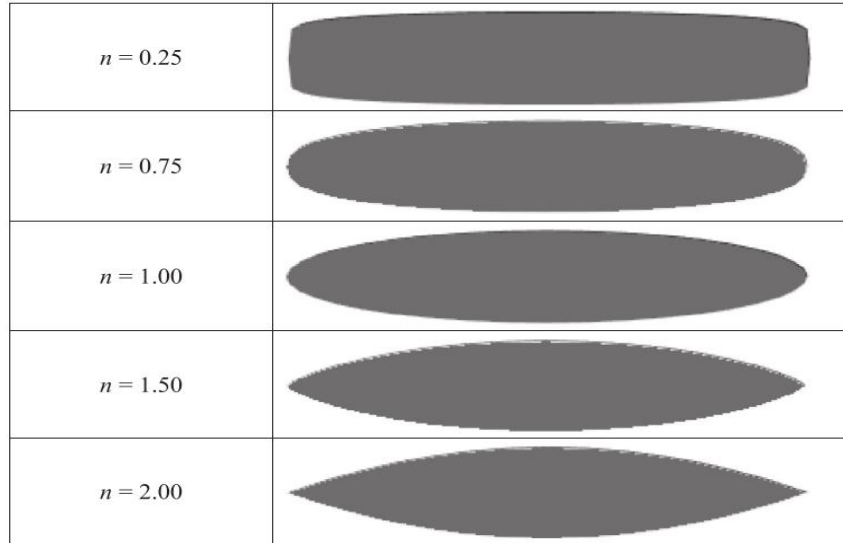
Figure 27 – Cross-section shape estimation of yarn using generalized power ellipse method [45].

The gap permeability was predicted using an analytical model [44] which is a solution of the Navier-Stokes equation for flow through a rectangular duct with no-slip boundary conditions on all walls. It was reported that gap permeability decreases with decreasing $\emptyset$ at given s and n, since the total gap cross-sectional area decreases.
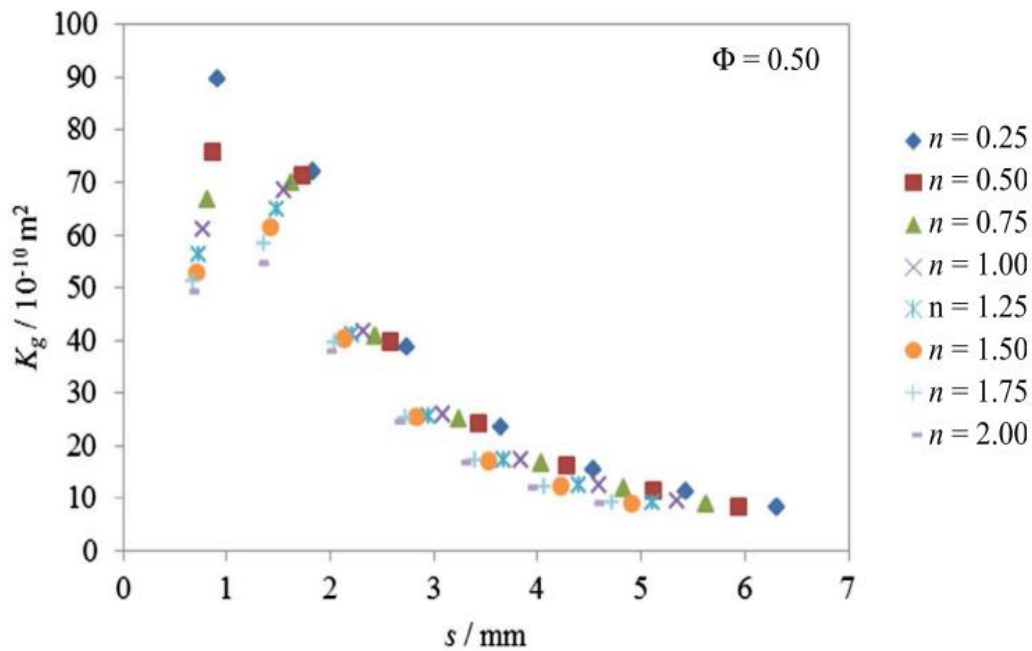
Figure 28 - Effect on gap permeability due to different cross-sectional shape of yarns in a unit cell

The importance of effect of micro-scale fibre and gap cross sectional shape is understood from this study [45]. A trend can be observed in Figure 28 which shows gap permeability decreases as the n is increased. This showed that gap permeability is higher if the yarn cross section is rectangular comparing to other cross-sectional shapes. This also implies that changing/increasing the duct cross sectional area will not enhance the equivalent unit cell permeability. Although like previous studies, this model is based on ideal straight architecture of the yarn which is never the case in a real preform. Despite this investigation provide an insight to ideal behaviour of gap flow and effect of yarn shapes on unit cell permeability, it may not estimate reliable parameters for a full scale real preform. Therefore, it can be established that simulation approach can produce reliable parameters and provide an insight into preform flow behaviour. At the same time, the accuracy of this approach depends on the construction of preform architecture representing the mesoscopic structure of a real preform. There are different types of simulation models that can be adopted and highlights and limitation of each of them is discussed below.

2.6.1 3D simulation models

A 3D model requires solid tetrahedral elements to execute flow simulation [133-135]. For a multi-layered preforms, each element should be connected to neighbouring layer to ensure reliable process parameters are predicted. The advantage of a 3D model includes visualization of meso-scale and macroscale flow pattern and void regions can be identified in multi-layer preform [136]. A 3D model enable user to assign different properties of each layer. This enables simulation based of real preform geometry to predict reliable flow pattern and process parameters such as global permeability and fill times.

While there are clear advantages of a 3D simulation model, the process to generate a 3D simulation is equally complex. A 3D model requires longer computational time (depending on the complexation of geometry) [133, 137] and creating a fully connected 3D tetrahedral mesh

mode requires highly skilled user to ensure each node in each layer is connected to the neighbouring layers [133-135]. Moreover, each preform produced consist of variability [27, 31], meso-scale architecture information is required to produce unique mesh for each preform produced to predict corresponding process parameters.

2.6.2 Unit cell models

Unit cell model is adopted by identifying a representative elementary volume in a layer and used to predict process parameter for a unit cell (Figure 29), which is then averaged out to a full-scale model.
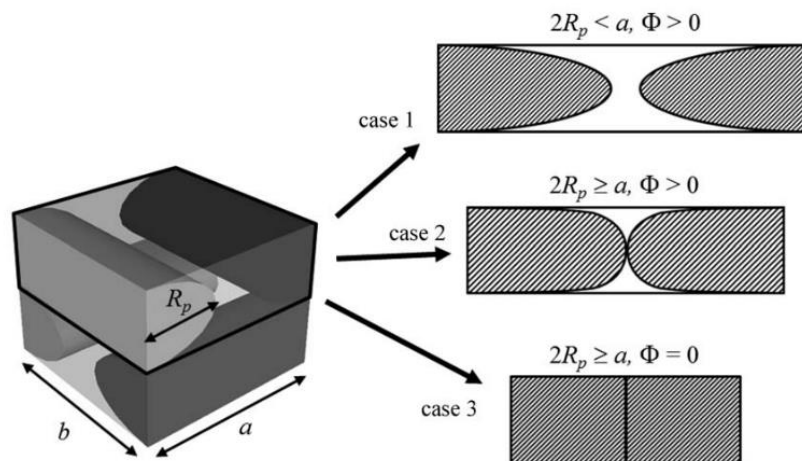
Figure 29 - Unit cell model example and how different conditions can be applied to investigate effect of different fibre architecture

The unit cell models offer lower computational time comparing to 3D model[138] and displays micro-scale flow behaviour for the developed geometry [45]. However, the main disadvantages of unit cell model is a representative elementary volume (REV) needs to be identified for each design and averaging out the flow behaviour from meso-scale to macro-scale ignores any variability across the preform and this will more likely yield unreliable process parameters.

2.6.3 2D simulation models

A 2D models consist of a shell mesh which can be generated for any complex design show in Figure 30. Parameters can assigned for a multilayer and usually a software packed such as

PAM-RTM [139] homogenises the parameters across the shell mesh before allowing the user to execute a simulation.
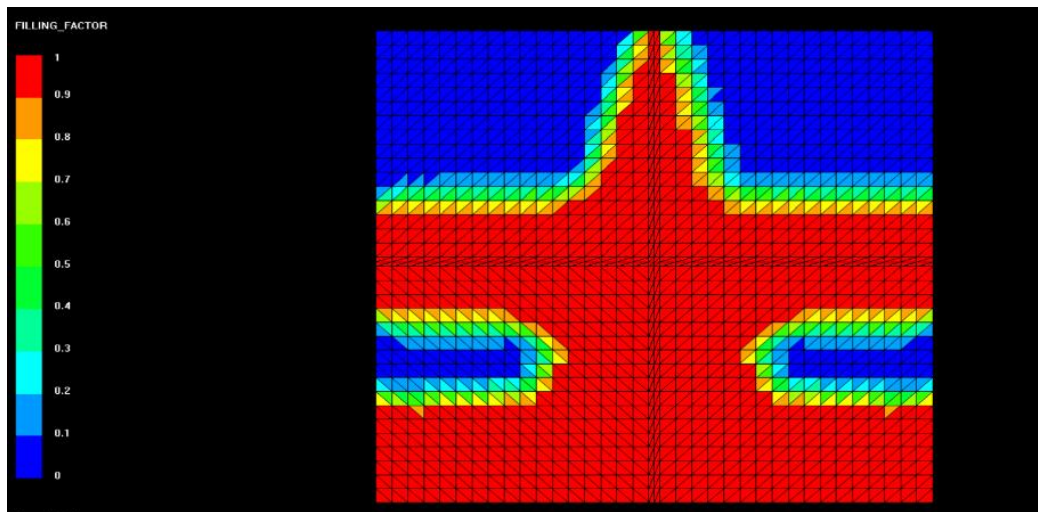
Figure 30 - 2D model simulation in APM - RTM. Global flow behaviour can be observed but through thickness and inter layer flow behaviour is not accessible

Low computation time is required to produce a shell mesh and execute a 2D simulation comparing to the 3D modelling approach. This enables users to produce a rapid simulation to predict a global flow pattern and fill times[140].

Similar to a unit cell model, a 2D model does not provide any information about inter layer or intra-layer flow behaviour. A fully connected model can be created layer by layer as a conventional way but it requires longer time. This approach is not feasible with the aims of this project as numerous model need to be created based on real deposition data. Moreover, it can be difficult and time consuming to produce a shell mesh for preforms containing high level of gaps such as in ADFP preforms or woven fabrics etc.

This shows each of the method has its advantages and limitations. In terms of ADFP preforms, it has been shown by [23, 27, 31-33, 126, 128] that ADFP preforms consist of high percentage of variability and instead of intending to avoid gaps, they can be adopted and used to enhance the process parameters. It will be difficult to adopt current available simulations tools for such

complex preforms. Placement of gaps will produce a vascular network of gaps and high level of variability within the meso-scale dimensions of gaps challenges the ability of all three conventional simulation methods directly. A 3D model for such a complex preform will require excessive time. If ADFP produced preforms, unit cells cannot even be identified at micro-scale as the dimensions can vary across the length of the gap, across the layer and finally across the preform. A 2D model can be adopted for a layer model but will lack the ability to incorporate complex geometry into a single shell. Hence more effective ways are required which can utilize modern computational capabilities and enables the following:

a.   Incorporate the variability of the preform within the model

b.   Investigate various gap strategies

c.   Identifies the strategy with the most effective permeability

d.   Less/acceptable computational time

e.   Easier to amend

One of the approaches is adopted to quantify the flow across vascular network of pipes in a city or a country in civil engineering know as pipe network flow modelling. This concept offers the potential to be applied on to ADFP preforms. The details are discussed in the next section.

2.7 Pipe network flow modelling

2.7.1 Introduction

A water distribution system across a city consists of complex interconnected pipes. This delivers water from the treatment plant to the consumer directly. Water distribution systems can be very complex infra-structures built underground shown in Figure 31 [141]. The network is designed to keep the water supply constant to highly variable demands. To ensure the supply is constant throughout the pipe network, pipe network analysis approach is adopted by the

designers. Pipe network analysis is method where pipe flow rates and pressure heads are determined through iterative process to minimize error. The pressure heads and pipe flow rates must satisfy the continuity and energy equations within the network. In other words, the fundamental relationship of conservations of mass and energy mathematically describe the flow and pressure distribution within a pipe network under steady state conditions.

Figure 31 - Example of a complexity of pipe network across a town [141]

2.7.2 Linear Theory/Linear Graph Theory

Pipe network analysis involves the process of determining/predicting of discharge and associated pressure at every node. A significant fraction of the entire set of equations consists of the nonlinear equation and a large number of these equations must be solved simultaneously in which the flow resistance relates pipe head loss to discharge. These equations become non-linear by substitution of constitutive relation when the solution of these equations is obtained through the iterative process. A numerical model was proposed by [142] where a system of equations were introduced to for flow analysis.

1. Writing energy equation for each pipe

2. Identify loops in the network

3. Formulation of system equations

a. Assigning arbitrary direction of flow for each edge and writing equation of continuity for each node

b. Extracting loops equation for each loop in the network and extract the direction of flow

4. A solution algorithm – (Wood [142])

   a. Hazen-Williams to estimate initial pressure head

   b. Coefficients of [A] n x n matrix is defined. Matrix [A] is a diagonal matrix where each resistance of each pipe is calculated. The size of matrix is equal to total number of pipes (n) in the network.

   c. [A]*[Q] = [B], (where vector [B] is equal of value of discharge at the corresponding node)

   d. Estimated flow rates are obtained by successive iteration where pressure value is updated for each iteration

The model was further developed and using a graph network by placing an arbitrary node connecting to all inlet nodes and outlet nodes was proposed by Gupta and Prasad [143] for analysis of pipe networks. The linear graph is drawn by creating a separate reference node and connecting all the nodes of the network to it. An example of a pipe network (a) and its linear graph (b) is shown in Figure 32. All of the branches connecting the nodes of the network and the reference node are included in the tree.
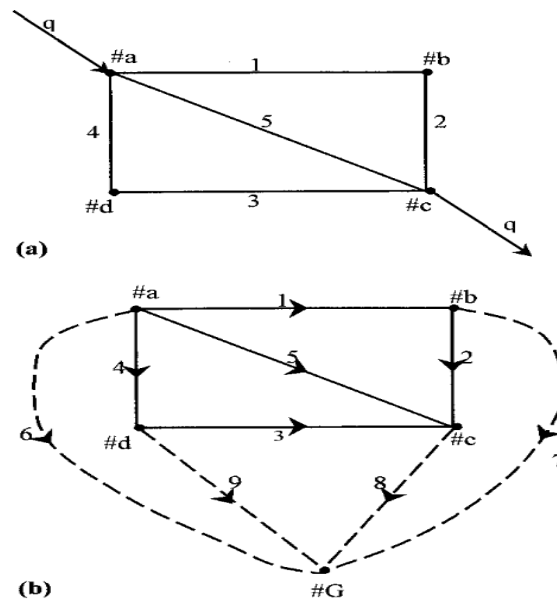
Figure 32 - Pipe network (a) and its linear graph (b) (Gupta and Prasad, 2000)

This technique has been recently used by [144] by further extending the algorithm to include valve and tanks into the equations. It is not within the scope of this project. But results obtained by [145] is compared with flow rates obtained by EPA-net extended period simulation of hydraulic behaviour within the pipe network. Technique proposed by [143] is validated by comparing its relative error with other techniques used for the analysis of pipe network as shown in *Figure 33* below. This authenticates the use of this technique for analysis of flow in complex gap network. It has been shown by both [142, 143] that linear theory can be used to analyse the flow in the network, but the main limitation of this approach is to identify the loops within the network. For a water pipe network, the identification of loops can be relatively straight forward however in case of ADFP preforms where each layer can be in different orientation, it can generate numerous loops and therefore increase the number of mass equations which needs to be balanced across the network before solving them. Moreover, by replacing the Hazen-William equation with equation more suitable to resin as fluid, it will acquire a pressure drop across each pipe instead of pressure drop across the network. Therefore, this approach is less attractive for assessing the flow behaviour in gaps of an ADFP preform.

50
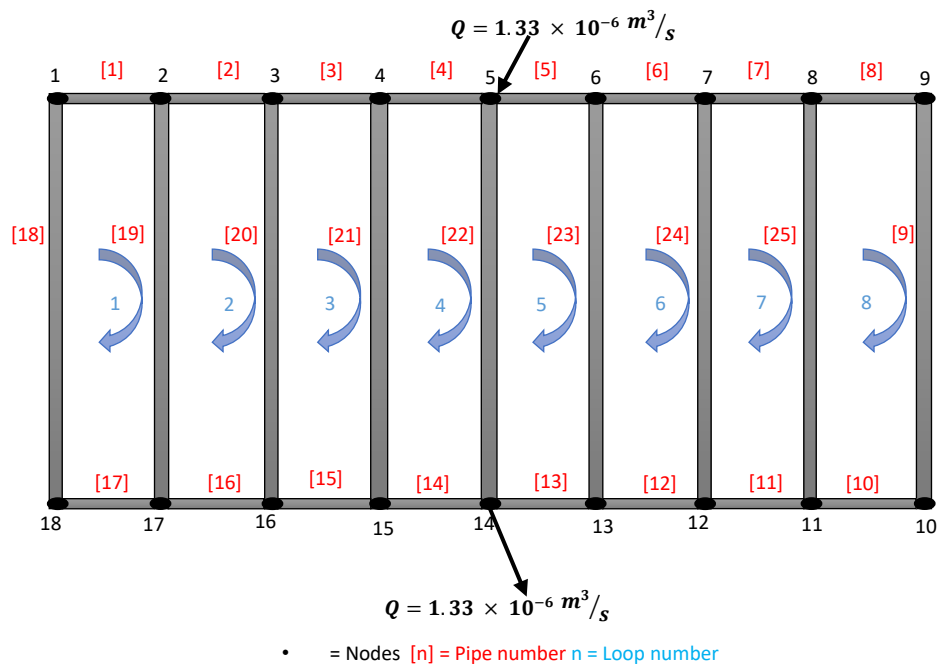
Figure 33 - Example network using Network modelling approach for a unit cell ADFP layer

2.7.3 The Global Gradient Analysis

Initially the method was proposed by [146] in 1972 for gas networks which was further developed by [147] in 1987 for water networks. This algorithm provides a simultaneous solution by combining mass balance equations and energy loss equations. This method is partially similar to linear graph method in terms of linear conservations of mass equations for each junction/node. The difference is non-linear equations are written for each pipe rather than each path or loop. By applying a Taylor series expansion to both sets of equations, linear system of N (number of nodes) equations are solved to calculate updated heads. Thereafter, scalar equation for each pipe P in the network is solved to calculate the updated flows. The main advantage of GGA over the graph network theory is that it does not require fundamental set of loops or paths to be identified. This effectively decreases the complexity of equations in a large network by enabling writing continuity equations for each node without a sequence. The core equation of the model is given below.

$$[A]^{n \times n} = \begin{bmatrix} A_{11} & A_{12} \\ A_{21} & A_{22} \end{bmatrix}$$

$$[A]^{n \times n} \begin{bmatrix} \Delta Q \\ \Delta H \end{bmatrix} = \begin{bmatrix} -dE \\ -dq \end{bmatrix}$$

Where A matrix consists of submatrices, A_{11} is the diagonal matrix consisting of pipe parameters multiplies by flow rate, A_{12} is the connectivity matrix consisting of junction information in the network, A_{21} is the transpose of connectivity matrix, A_{22} is a null matrix, ΔQ is change in flow rates, ΔH is change in heads, $-dE$ is the energy equations and $-dq$ is the conservations of mass equations. The summary of overall procedure to run this model is

1. Write energy equation for each pipe

2. Write conservation of mass equations for each node

3. Formulation of system equations

4. Form matrix **nA₁₁** using the data (pipe parameters and assumed flow rates)

5. Compute the nodal balance error **(-dq)** and pipe balance error **(-dF).**

6. Solve the system of equations as shown above in Equation for $\Delta \boldsymbol{H}$ and $\Delta \boldsymbol{Q}$.

7. Update the nodal heads and pipe flows for the next iteration.

8. Check if the difference between acquired heads and flows comparing to their values in previous iteration is negligible. If satisfies, stop. Or not continue to next iteration.

This approach [146, 147] is commonly used as a standard/most effective for water distribution network modelling (WDM) [148] and also adopted by a well-known open-source program EPANET [149, 150] for WDM.

$$Q = 1.33 \times 10^{-6} \, m^3/s$$
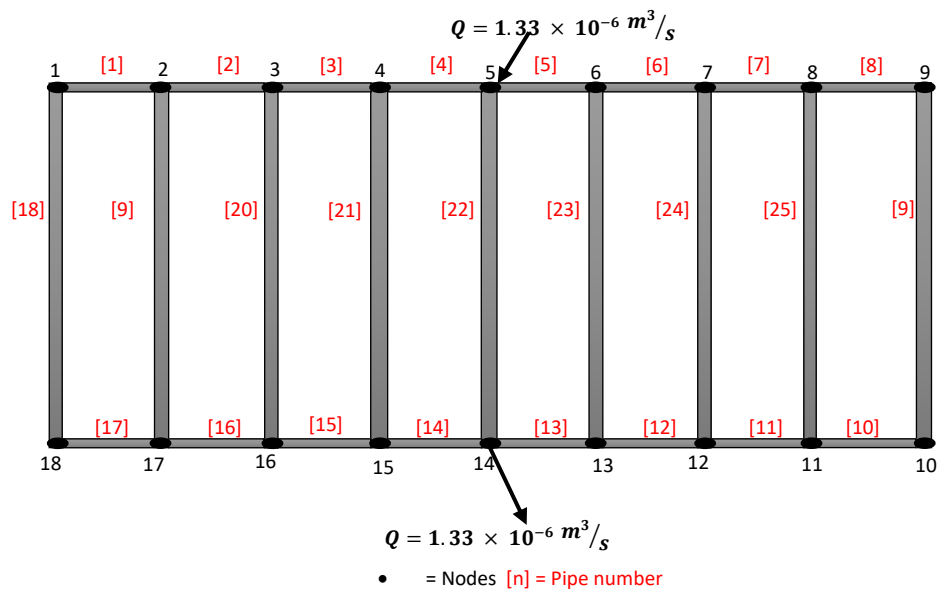
Figure 34 - Example network using GGA modelling approach for a unit cell ADFP layer.

The Global Gradient Algorithm offers less complicated method of formulation comparing to the other network models used for water distribution systems. This method also does not require the loop identification and therefore makes it simpler to solve complex networks. Moreover, it provides a head value at each node instead of a head difference in linear network model. If the equations are exchanged for pressure instead of head, pressure at both ends and flow rate in a gap will be calculated therefore corresponding permeability of a gap can be acquired. Similarly, the pressure drop across the network can be calculated and global layer/multi-layer permeability can be acquired. Therefore, GGA can be identified as an adoptable model to quantify flow behaviour in gap of ADFP produced preform. More precise details of formulation of system equations will be given in Chapter 4.

2.8 Conclusions

A critical review of literature helped to bring forward many factors affecting reproducibility of permeability measurements and potential ways to enhance permeability of a preform. Main governing issues observed in this review that requires attention for further improvement of ADFP procedure are discussed below.

Flow enhancement – To enhance flow in ADFP produced preform, a few papers have investigated effect of gaps on preform permeability [23, 26, 27, 31]. No significant difference between nominal and open (with gaps) preforms was shown by [26]. 66% difference in through thickness permeability between two preforms with percentage gap of 3.5% and 1.5% was shown by [31]. It can be concluded that gaps can enhance flow in a preform but a modern approach is required to characterize the effect of gaps in preforms produced by ADFP technology.

Meso-scale permeability - It has been observed in [26, 32] that the conclusion in each of the studies are drawn based on experimental macro-scale flow behaviour. Where [32] ignored the meso-scale variability in geometry which was clearly visible in the images provided in the paper. While [27] used the homogenization approach to estimate the permeability of a preform and compared with macro-scale experimental permeability. Only [131] shed some light on experimental permeability of glass fibre tow and compared with analytical models and found differences up to an order of magnitude between experimental and analytical tow permeability. This clearly shows the need of further validation of analytical models commonly adopted to measure gap permeability such a Cornish's model and fabric permeability by Gebart's model to be validated at tow and gap level, layer level and preform level to identify the source of error.

ADFP lay-up inaccuracy – It has been understood that deposition variabilities during ADFP affects the flow behaviour and results into over or underestimation of permeability value. Designed permeability was overestimated by half (1.56×10^{-11} m^2) in comparison with experimentally obtain value (2.81×10^{-11} m^2) due to 20% variability in gap sizes [27]. In-plane permeability, K_x, K_y was found in range of (1.44×10^{-12} - 1.49×10^{-12} m^2) of an ADFP of $V_f = 54\%$ produced preform was found for Nominal and preform consisting 2 mm gap after every 5th tow [26]. An error of 366% found between CFD designed (8.31×10^{-14} m^2) and experimentally (3.87×10^{-13} m^2) obtained through thickness K_z permeability. Error was reduced to 10% by capturing meso-scale preform specifications and rebuilding CFD model [31]. In conclusion reliable permeability cannot be predicted based on designed geometry of a component/preform. The difference between designed and experimental permeability results can be minimized if permeability is measured using actual geometry data of a preform after deposition. This was shown by minimizing 356% error in case of K_z [31] and 20% error in case of K_x [27]. Similarly [32] showed the gap with higher gap width tends to have lower gap height and in case of 2mm gap width, the gap was almost blocked by neighbouring layers compressed in between. Real deposition data will be used, and actual geometry of preform/component will be used to predict the permeability.

Reproducibility of permeability – A scatter in data was found due to different equipment being used in benchmark exercise [24, 117] and proved that scatter can be minimized if similar procedure is followed [117, 118] different preforming techniques effected permeability of preform on multi-scale [114] on through thickness permeability, skew terms were found to consist higher permeability values as compared to through thickness permeability and shifted the centre of ellipse [28]. By providing a good agreement between and experimental and simulated flow behaviour [28, 31, 102, 107, 109], accuracy of simulation approach is reliable.

However, simulation requires precise geometry of a component and permeability of the material. This can be achieved by addressing local variabilities [31, 109].

Simulation limitations – It has been understood that the conventional 2D and 3D simulation approach will have limitations if preform contains high gap volume fraction. The preforms will comprise of a vascular gap network. To run a 3D simulation for such preform will require excessive time from developing fully interconnected mesh to running a simulation. A 2D simulation will have increased complications for a multi-layer model and will require a homogenised layer permeability to be assigned to each layer for simplification. Because of this user will not be able to investigate the effect of through thickness flow through interconnected gap junctions between layers. Therefore a novel approach (Network modelling) has been identified that is applicable to gap network in an ADFP preform [147]. The modelling approach also offers simplification to change any parameters (gap width, gap length, gap height), develop any complex multi-layer gap network and offers the potential to run a simulation and calculate the local (gap level), layer and global (multi-layer) permeability faster than any other conventional simulation approaches. Unlike the unit cell modelling approach which is based on averaging out the local flow behaviour to global level GGA method will also allow to assign real preform data (in <2 minutes) and predict permeability (<10 minutes) for each part produced without consuming excessive user time. The main limitation associated with this approach revolves around the flow in fibre tows. This approach by itself will neglect the flow in tows/tapes. This can be justified as a few researchers successfully developed numerical models to predict reliable permeability and neglected the tow/tape permeability by analytically showing the contribution of the tow/tape to the layer permeability is generally smaller compared to the contribution of the equivalent gap permeability [45, 132]. However, the significance of effect of flow in tow on the global permeability in presence of vascular gap network will have to be experimentally investigated to show the reliability of GGA method.

Chapter 3 Effect of gaps on meso-scale and macro-scale permeability and comparison of experimental and analytical results

3.1 Introduction

It is understood from the literature review that an ADFP produced preform exhibits very low permeability and high level of variability. Researchers have utilised this variability by intentionally incorporating gap into the preforms which act as flow enhancing channels with intention of encouraging flow and permeability in an ADFP preform. Predicting permeability of such preforms can be difficult and researchers have used theoretical models such as Gebart's model[34] and Cornish's model[44] for this purpose. These models have some basic assumptions such as either the fibres are arranged parallel to each other and the shape of tow or gap is perfect square, rectangular, oval or randomly arranged [34-45]. These models are often used for permeability predictions but only tested in [131] for unidirectional glass fibre by Owen Corning. The permeability of such dry material is not similar to carbon fibre tows used in ADFP technology. A binder materials is used to contain the carbon fibre together for ADFP application. This binder material can create additional friction at microscale level and affect the global flow behaviour. Therefore each material acquired through different manufacturer will have different micro-scale structure depending on the process used and it is necessary to investigate their flow response experimentally. The results from their investigations have been discussed in the previous chapter. These micro- and meso-scale permeability models have never been tested for their accuracy for carbon fibre tows and gaps by directly comparing their predictions with experimental permeability measurements. Instead, predictions from such models are typically compared with results from macro-scale preform level experiments e.g. [27, 34, 45]. In [131] Zarandi et al. compared range of studies and highlighted how most of the investigations in the past validated the adopted models by comparing their results with either previously reported large lab-scale results or their own macro-scale experiments [26, 27, 32].

A large scatter is found in most of the studies and usually human factors and experimental conditions are stated as the source of error. The difference between the analytical and experimental results raises a question of whether these models are predicting a reliable permeability at all. This chapter will investigate such models by conducting permeability experiments at three different levels: tow level, layer level, and preform level. For the first time, the effect of different gap widths on tow permeability is investigated experimentally using a meso-scale permeability rig. Different methods of processing the data, different flow regions (tows and gaps) and flow fronts are identified. Results from all three stages are compared with the analytical results for the given configuration. The results derived from all these methods have been compared to find the accuracy and degree of agreement among them. The main purpose of the present study is to evaluate the accuracy of the considered theoretical models for the three realistic tow fibre volume fractions of 40% 50% and 60%.

3.2 Methodology

Different analytical models are required in order to predict permeability of fabric region and gap regions. The mostly used models are selected to compute analytical permeabilities. The details are discussed later in the section. To experimentally test these models, a table top meso-scale permeability rig was designed for different gap width specifications. Permeability was experimentally measured at tow level, layer level and a preform level to observe the percentage difference from analytical solutions. The details of the procedures adopted are discussed in this section.

3.2.1 Material

A dry carbon fibre tow TX1100 IMS65-24K-UDU194-6.35 from Cytec Solvay Group has been used to the experiments. The material consists of 5-10 wt. % of epoxy-based binder on the lower side and a veil of carbon fibre on the surface [32]. The rest of the parameters of the material are given in the Table 6.

Parameters	
Density of fibre	1800 kg/m^3
Nominal weight	194 gsm
Diameter of Fibre	7.0E-06 m

Table 6 - TX1100 material specifications

Figure 35 – Post deposition example of the material *TX1100 IMS65-24K-UDU194-6.35*

3.2.2 Analytical Modelling

A representative layer permeability is achieved by a homogenization which starts by defining the permeabilities of the basic substructure of a preform as shown in Figure 36. A preform can consist of nf layers in different orientations. If gap is placed after every i-th tow, each layer will consist of multiple tows and gaps. Different analytical models are adopted for the two regions (gap & fabric). A three-step procedure is followed to estimate a layer permeability.
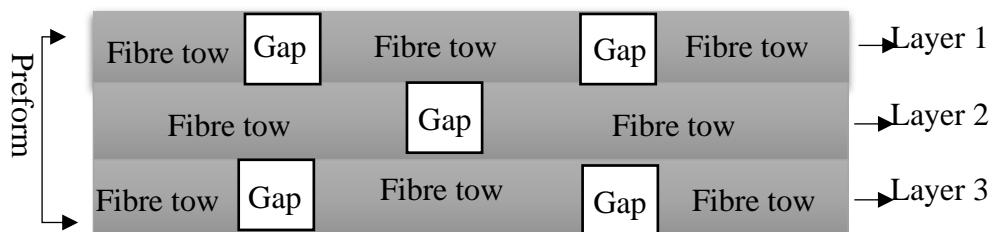

Figure 36 – Example of cross-sectional view of preform substructures.

3.2.2.1 A – Tow permeability

The model developed by Gebart [34] is used to calculate the fibre tow permeability. This model has also been used in many other studies such as [27, 131]. Gebart [34], by simplifying and reducing the general form of the Navier-Stokes equation, developed two different sets of permeability models for in-plane flow along the length of fibres and transverse flow across the length fibres. The effect of different parameter for each direction was investigated. For the in-plane permeability along the length of fibres, the effect of opening size on the permeability in terms of the ratio of opening size (a) to the fibre radius was considered. It was found that this ratio plays its role as a function of fibre volume fraction (or porosity). However the spacing of the fibres may vary as a function of fibre volume fraction. In case of this study, meso-scale is viewed as a single tow and a gap where each tow used for ADFP technology is rectangular in shape and assumed to be homogeneous along it length.

K_x can be given by,

$$K_x = \frac{8R^2}{c} \frac{\left(1 - V_f\right)^3}{V_f^2} \tag{7}$$

Where R is the fibre radius (given in Table 6), V_f is the fibre volume fraction within the tow, c is the fibre packing constant by Gebart's model and k is Kozeny constant which is a correction factor that accounts for the orientation of the pore system and tortuosity.

Fibre packing	$V_{f\,max}$	c	k
Quadratic	$\dfrac{\pi}{4}$	57	1.78
Hexagonal	$\dfrac{\pi}{2\sqrt{3}}$	53	1.66

Table 7- Quadratic and Hexagonal fibre packing constants for Gebart's model [34]

3.2.2.2 B – Gap permeability

Similarly, to fabric permeability model, another model is required to define the flow with in the gap regions. The gap regions are empty channels where flow can progress through faster comparing to fabric regions. A simple pipe model can be adopted to describe the flow in the gap depending on its geometric parameters. Such a model was given by White [151] and later further derived and used by Cornish [44] and has been used in [27, 45] for defining the flow in the inter-tow or inter yarn gaps in a layer/unit cell. It is the solution of the Navier–Stokes equation for flow through a rectangular duct with no-slip boundary conditions. In case of this study, rectangular gaps with different widths are placed next to a carbon fibre tow. It is assumed that the gap height and width is homogeneous along it length. The permeability of these rectangular gaps is computed using the following equation.

$$K_{gap} = \frac{b^2}{12}\left(1 - \frac{192}{\pi^5}\frac{b}{a}\sum_{i=1}^{\infty} \frac{\tanh\left(\frac{(2i-1)\pi a}{2b}\right)}{(2i-1)^5} \right) \tag{8}$$

*W*here a, is the gap width and b is the gap height as shown in

Figure 37. The infinite series will be reduced to 10 terms, which has been shown to give less than 1% errors [27]
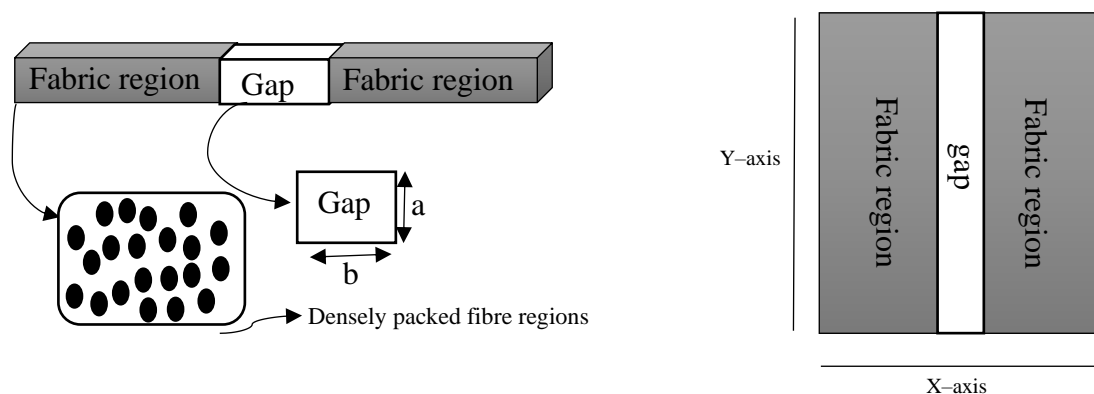

Figure 37 - Micro-scale geometry of tow and gap region in a layer

3.2.2.3 C – Weighted averaging approach

Once the permeability for each sub-region is calculated using the equations given above, the layer permeability can be estimated using a weighted averaging approach [27, 152] assuming only in-plane flow in the tows and the gaps. Homogenisation approach has been proved to be effective in many cases and materials. Such as UD multi layered preforms [153], plain weaves [154]and multi-layer triaxial braid[155]

$$K_{xlayer} = \left(K_{gap}\; \emptyset\right) + \left(K_{xtow}\; (1 - \emptyset)\right) \tag{9}$$

*W*here $\emptyset$ is the gap volume fraction. The assumption certainly means that through thickness flow and the flow sinking from the gaps into the fibrous tow is neglected. Similarly, assuming that flow is parallel in both sub-regions and flow is not exchanged between the two regions, making no contribution to the global flow therefore it is neglected.

3.2.3 Experimental details

A total of three experimental rigs with target fibre volume fraction of 40%, 50% and 60% within the tow have been designed to investigate the results acquired from the analytical models at meso-scale. Each rig is made of aluminium plate at the bottom in which cavities are machined to desired thickness to achieve the desired fibre volume fraction. Each rig consists of 10 cavities (Figure 38). Cavity 1 is designed to test only one tow and no gap to measure the tow permeability, cavities 2-5 have one tow and a gap starting from 0.25mm, 0.5mm, 1mm and

2mm. Cavities 6 – 9 are repeated in terms of gaps but consist of two tows and a gap starting from 2mm, 1mm, 0.5mm, 0.25mm and only two tows without any gap in cavity 10.
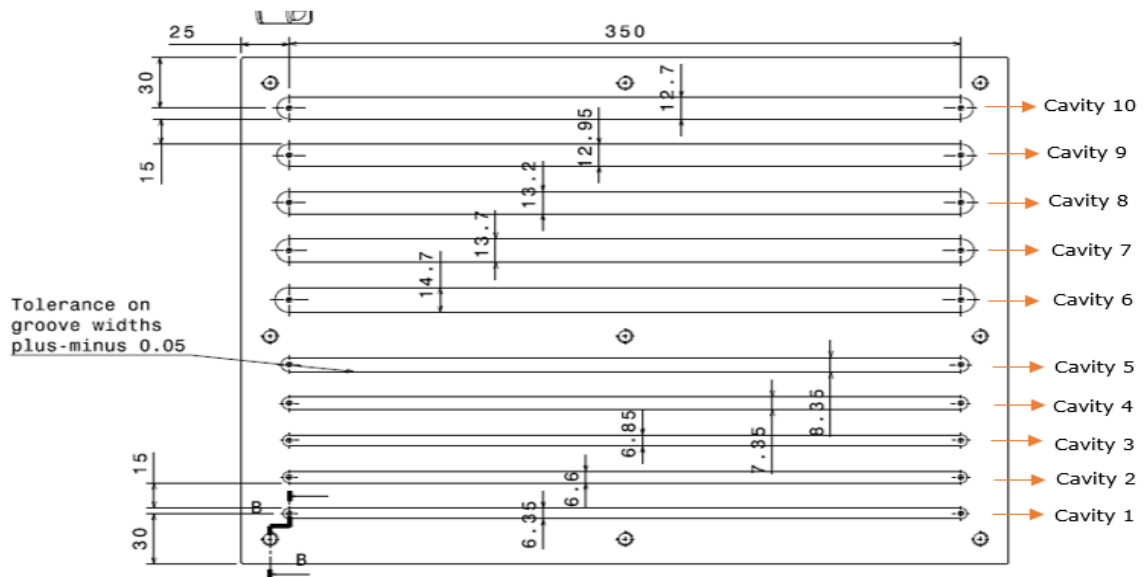
Figure 38 - Width specification of the designed tool for tow and gap permeability experiments. Cavity 1- 5 is designed for one tow and a gap and cavity 6-10 is designed to hold two tows and a gap in the middle. The gap widths varies from 0.25mm,0.5mm,1mm and 2mm for both cases.

To ensure the testing fluid flows through the cavity only without any leaks, the tows are placed into the cavity and sealed using a transparent self-adhesive tape. The tows are then compressed into the cavity by the mould top which is made of clear acrylic plastic which is held into position by use 9 screws. Use of fewer position holding points can cause deflection of the mould top and result into varying cavity thickness and tow fibre volume fraction causing a scatter in the recorded data. Reynolds number is usually used to determine the degree of laminar or turbulent fluid flow. It is the ratio of inertial forces to vicious forces. It can exhibit the effect of fluid viscosity in controlling the flow pattern or velocity of fluid. However, for this project, the injected flow is always laminar and therefore the viscous forces are dominant at low Reynolds number, and the fluid viscosity is more of interest as the viscosity of different resin system and fluids are usually provided by the manufacturers. Moreover, to calculate the Reynolds number requires kinetic as well as absolute or dynamic viscosity of the fluid. The

viscosity of the fluid can also be directly assigned to the model. Engine oil was used as a testing fluid as it represents similar viscosity to the resin materials. To compute/interpolate the viscosity value, the temperature of the fluid is checked before each experiment using a RS51 K input wired digital thermometer. The pressure of the testing fluid was measured near the inlet by using a Digitron 2000P digital pressure meter with maximum 10bar pressure measurement capacity. The rig is shown in Figure 38 and a full drawing is attached in appendix A. The only difference in three rigs is the cavity thickness and is shown in Table 8.

Test Rig Number	Target V_f (%)	Thickness (mm)
1	40	0.27
2	50	0.22
3	60	0.18

Table 8 - Cavity thickness and corresponding tow fibre volume fractions in three experimental rigs

3.2.3.1 Experimental procedure

The length of each cavity is 350mm. A tripod is placed on top on the mould and a camera is used to record the progression of the flow from the start of the experiment till the fluid reaches the outlet. Time is recorded when the fluid travels every 50mm. This will give seven data points along the length of the cavity. At least 5 sets of identical experiments are conducted per cavity in all three moulds for the purpose of statistical averaging. A full step by step process guide is shown in Figure 39 below shows the procedural steps for an experiment.
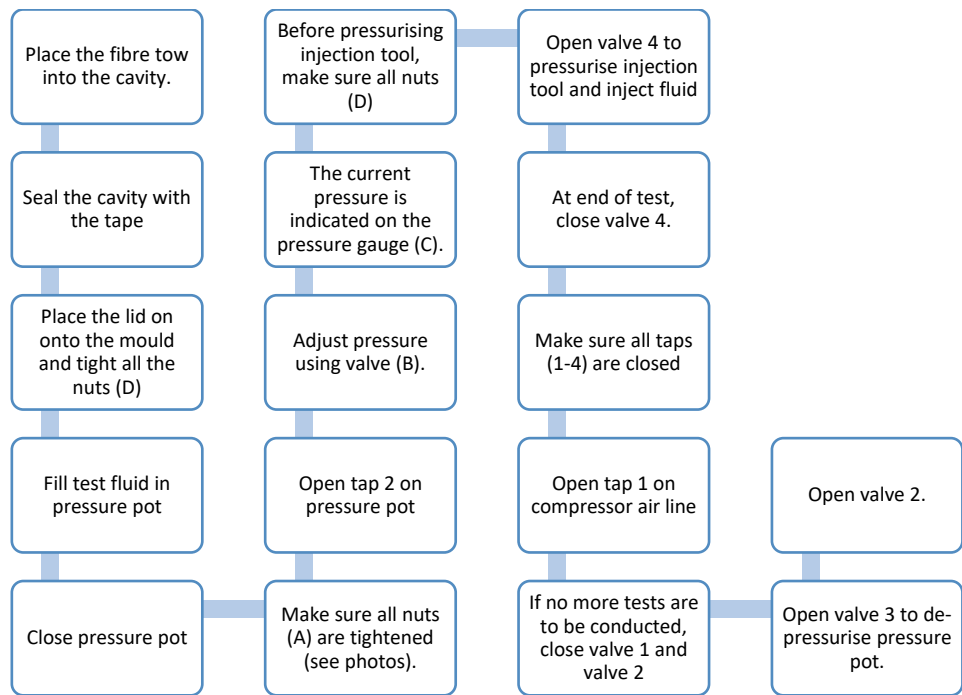
Figure 39 - Tow and gap permeability experiments - A step guide


Figure 40 - A 2mm gap can be observed in cavity 6. The cavity 1 is designed to contain single tow (bound) and no gap while cavity 10 is designed for two tows (bounded) and no gaps.

3.2.3.2 Computing methods used to process data

To obtain the permeability, flow front over time recorded during the infusion can be processed using different methods. The methods adopted may produce different overall results. It is important to identify the most suitable computing method depending on flow behaviour during infusion. Two types of methods have been used to process meso-scale permeability experimental data. Details of the two processes are given in this section.

1 – Squared flow front method

For data processing, a well-established Squared Flow Front (K_{sff}) approach can be adopted [24, 117, 118, 156]. In a constant injection test, the one-dimensional permeability should be plotted versus time and a typical graph under constant injection pressure condition should look like Figure 41.
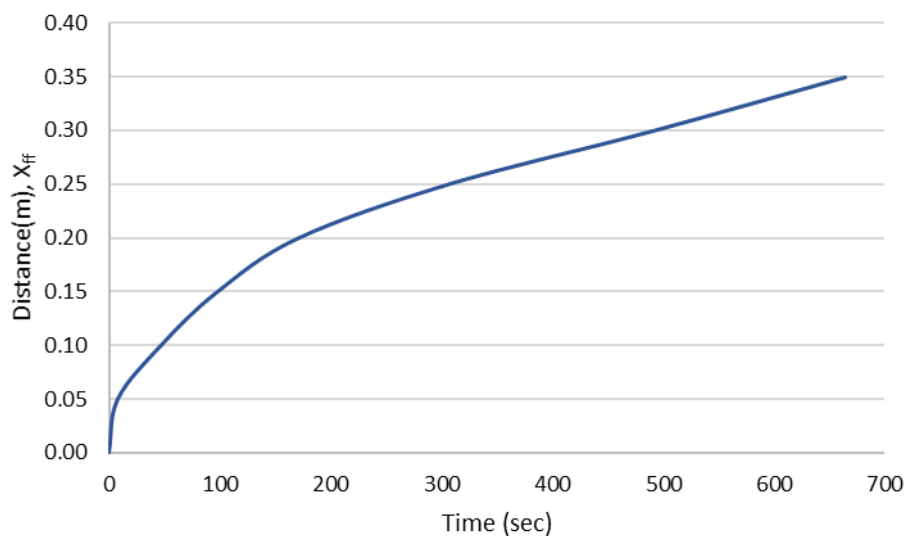
Figure 41 – A typical flow front position versus time graph under constant injection pressure condition.

The distance of flow front from the inlet should be squared and once plotted versus time should yield a straight line according to Darcy's law [24, 100, 117, 118, 156]. A linear trend can obtained from this processed data and slope of this straight line, m, can be calculated. For a

one-dimensional constant pressure injection, the permeability the fibrous reinforcement can be evaluated based on Darcy's law

$$K_{sff} = \frac{x_f^2}{2 \ P_{in} \ t} \ \emptyset . \mu \tag{10}$$

Where $\emptyset$ = porosity, μ = viscosity and P_{in} = Pressure at injection port. Using the equation above, the slope of the graph shown in Figure 42, the experimental permeability can be calculated as follows:

$$K_{sff \ 1-n} = \frac{m \ \emptyset \ \mu}{2 \ P_{in}} \tag{11}$$

The layer K_x can be calculated by taking the average of the measurements as follows:

$$K_{x \ layer} = \frac{\sum_{i=1}^{n} K_{sff(i)}}{n} \tag{12}$$

$$m = \frac{x_{f \ n}^2 - x_{f \ n-1}^2}{t_n - t_{n-1}}$$
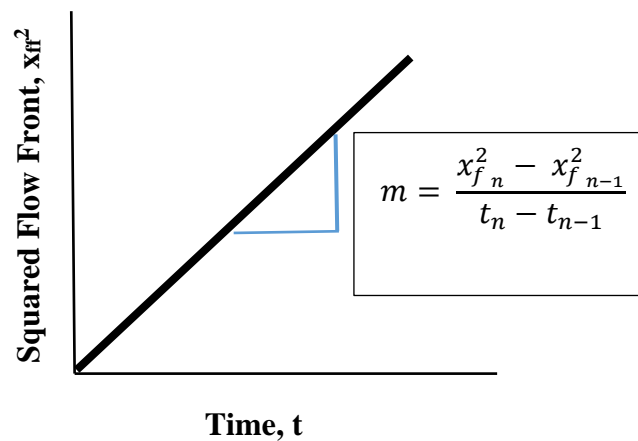
Figure 42 - A graph of squared flow front versus time under constant injection pressure conditions. The slop (m) can be calculated by taking the difference between each data point

2 – Direct method

In this method, permeability is calculated directly by taking the single measurement of time taken by fluid to reach the outlet and average of five measurement of pressure at inlet during the experiment.

$$K_x = \frac{l^2 \ \emptyset \ \mu}{2 \ t \ P_{in}} \tag{13}$$

3.3 Results and discussion

The preliminary investigation was conducted with the aim to understand the magnitude of effect of single or multiple gaps in a layer (280mm x 280mm x 0.22mm) permeability while global gap volume fraction (V_{gf}) in a layer is kept constant. Gap widths from 1mm till 5mm was analytically investigated under fibre volume fraction from 40% up to 70%. For each global gap width, the number of gaps were changed from only one gap in a layer up to 500 smaller gaps giving an equal V_{gf} as having one corresponding width in a layer as shown in Table 9. Figure 43 below shows the results from one of the cases (one gap width = 5mm).

Global V_{gf}	0.0179					
Number of gap	1	2	10	50	100	500
Gap width	5	2.5	0.5	0.1	0.05	0.025

Table 9 - Changing gap width and number of gaps by keeping same gap volume fraction in a layer
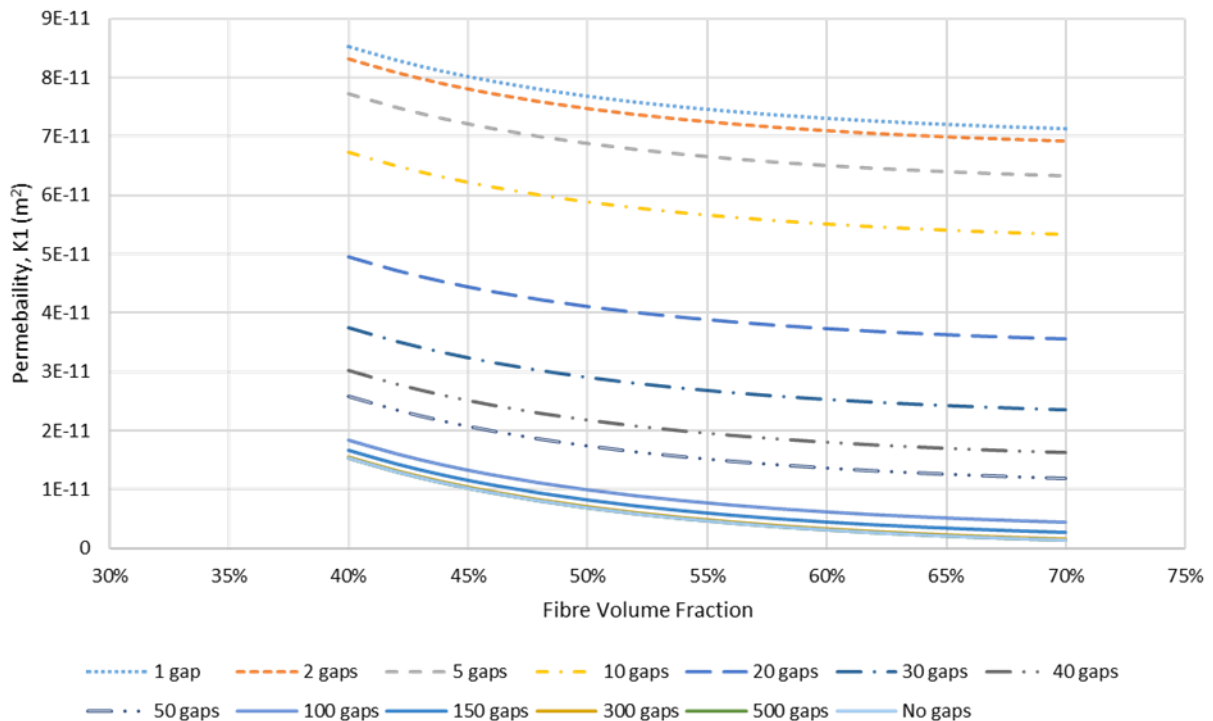

Figure 43 - Analytical calculated layer permeability with respects to fibre volume fraction and the number of gaps for a constant gap volume fraction in a single layer

It can be observed that the as gap width decreases, the permeability becomes closer to the nominal permeability of layer indicated by no gaps. Highest permeability of a layer can be achieved by placing a single gap. Changing the number of gaps from 1 to 500 shows a very high percentage decrease in permeability and the magnitude of the percentage change in permeability decreases till there is no or negligible contribution to layer permeability from gaps. This shows that even if the global gap volume fraction is kept similar in a layer under nominal conditions, gap width can still highly affect the overall permeability. Similarly, when analytical permeability of rectangular channels/gaps is observed, it shows a similar trend of higher magnitude of permeability increase for smaller gap widths (0.25mm – 2.5mm). Only 3% percentage change can be observed when gap widths are increased from 2.5mm to 5mm and the trend shows asymptotic behaviour. Therefore, magnitude of increase in permeability is higher when smaller gap widths and higher number of gaps are adopted in a layer comparing to higher gap width and lower number of gaps in Figure 43.

This exercise has highlighted that even if the overall V_{gf} is similar in a layer, gap width variation within the layer can greatly affect the overall permeability. Therefore, it is essential to investigate the gap widths individually. Figure 44 showed the analytical overview of change in permeability due to change in gap width, but this raises a question of whether the predictions given through this analytical model are reliable when the channel is surrounded by permeable fibrous material. Particularly when the investigation above has established that the magnitude of change in permeability is higher for lower gap widths. Studies mentioned in the literature review have adopted such model to calculate a global permeability of preforms but did not provide any insight towards flow behaviour in a single gap itself as it shown in Figure 44. Therefore, it is essential to investigate the effect of different gap widths on tow permeability at meso-scale. The following section will focus on investigating the reliability of analytical models by using the meso-scale permeability rig shown in methodology section which enables

experimental measurement of meso-scale permeability of tow in presence of different gap widths.
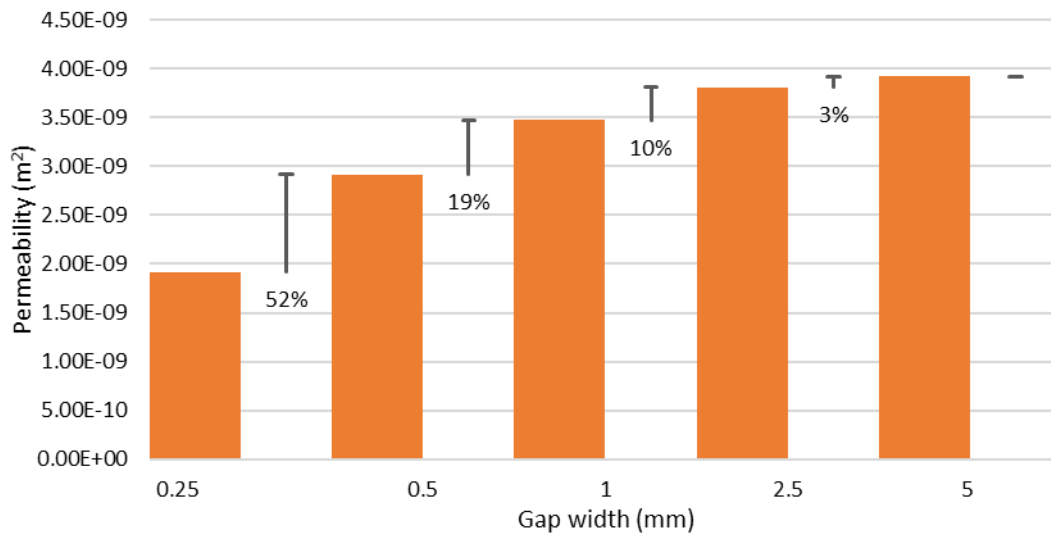
Figure 44 – Change and percentage increase in permeability of rectangular channels/gaps calculated by Cornish's model

3.3.1 Difference in results from using different computing methods

Unlike Macro-scale experiments the two methods known as direct method and squared flow front method have not been investigated for meso-scale tow level experiments. The methods can produce different results. Hence it is important to compare results acquired from both methods. Analytical permeability is calculated assuming nominal condition such as perfect rectangular channel with constant cavity thickness of 0.22mm and as designed gap width. The analytical permeability will be used as a reference to compare the experimental data. If the results acquired by both methods are similar, it will highlight that the data processing can be made easier by adopting the first method, if the results are different, the approach best representing the experimental conditions will need to be identified.

The details of both methods have been given in the methodology section. As this section is only focused on comparison between the two calculation methods and choose the most reliable

method to process the experimental results, only tool 2 (V_f = 50%) was used to perform the analysis.

Gap widths (mm)	0	0.25	0.5	1	2
Case A	1.70%	41.85%	24.85%	8.64%	10.93%
Case B	4.63%	32.12%	23.08%	24.57%	11.07%
Degree of freedom (Df)	6	8	8	8	8
T-value	0.114	2.04	0.85	0.56	0.38

Table 10 - Percentage difference of results computed using direct method and squared flow front method, where case A represent a tow and a gap and case B represents two tows and a gap. The T value was calculated by using the equation (14).

T-test was conducted on all of the samples. The T value was calculated by using the equation (*14*).

$$t = \frac{x_1 - x_2}{\sqrt{S^2 \left(\frac{1}{n_1} + \frac{1}{n_2}\right)}}$$

(14)

t is the t-value, *x*1 and *x*2 are the means of the two groups being compared, S^2 is the pooled standard error of the two groups, and n^1 and n^2 are the number of observations in each of the groups. Degrees of freedom is related to your sample size, and shows how many 'free' data points are available in your test for making comparisons. The greater the degrees of freedom, the better your statistical test will work.

The results acquired by the two methods showed a small difference (1.70% and 4.63%) given in Table 10 in both cases, A & B when there are no gaps in the cavity. The results showed difference is not statistically significant. However, in case of presence of gaps, the percentage difference is highest (41.85% - Case A, 32.12% - Case B) in case of smallest gap width (0.25mm). The difference decreases as the gap width increases from 0.25mm to 2mm as the trend shows in Figure 45. Even though the direct method results are much closer to the

analytically acquired results, the error bars in the two methods in Figure 45 are overlapping. This indicates higher errors should be expected from the permeability values acquired by the direct method as it neglects any local variability. On the other hand, from Figure 45 it is understood that the permeability is more sensitive to local configurations in presence of gaps with smaller width. Therefore, any magnitude of variability in smaller gap widths could induce much higher errors in the final results. Since the squared flow front method provides more data and any variability in the results can be highlighted, the SFF method is adopted from here onwards to process the experimental data.
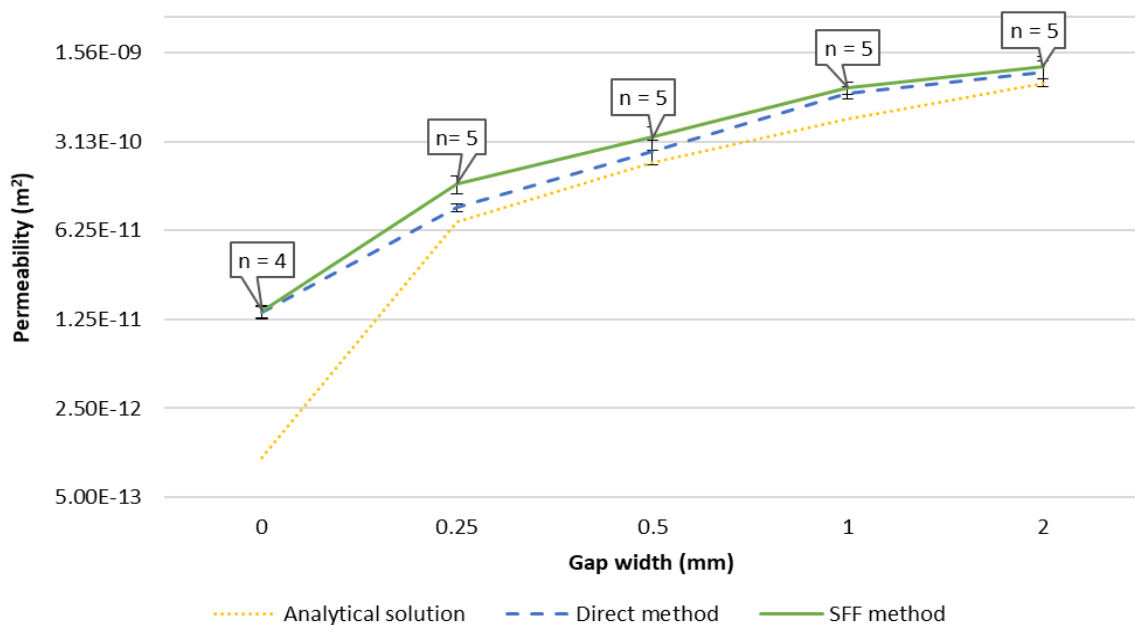
Figure 45 - Logarithmic scale graph of permeability obtained for V_f =50%, case A (Tow – Gap) experiments using: (A) Analytical solution, (B) The Direct method and (C) The SFF method.

3.3.2 Simultaneous flow front in two distinct region (Fibre tow and a gap)

Once the computing method was decided, another analyses was required before all the experimental results are processed. A phenomenon that occurs during progression of flow in a presence of gaps is formation of two flow fronts as shown in Figure 46. One flow front is in the zone with least resistance (gap) hereafter called as fastest point (fp) where the resin/test liquid racetracks towards the outlet, and the second flow front is in the fibre zone (tow)

hereafter referred to as slowest point (sp) where the resin/test liquid travels through a densely

packed fibre tow causing more resistance in the flow path.
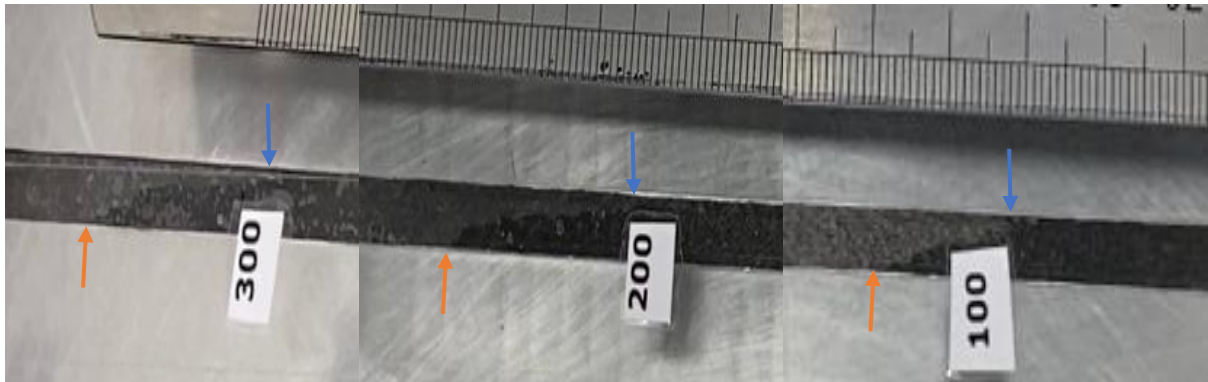
Figure 46 - Flow front progression in presence of a 0.25mm gap. Orange arrow pointing at flow front in gap region and blue arrow pointing at gap in tow region.

As the gap width is increased, the faster flow in the gaps becomes a more dominant factor

resulting into increased distance between the two flow front points (slowest and fastest) as

shown in Table 11. For example, the distance between the flow front positions in Figure 46 is

18.64mm in the 0.25mm gap which is more than doubled to 56.94mm when the gap width is

increased to 5mm. This will result in different fill times depending on which part of the flow

front is selected. Since the equation used to compute permeability requires the flow front

position, selection of flow front position will yield different permeability results. Therefore, in

this section permeability is calculated using flow front data from both regions (fabric & gap)

and results are compared for both cases A & B.

Gap Width (mm)	Distance (mm)
0.25	18.64
0.5	42.12
1	56.25
2	56.94

Table 11 - Distance measured in ImageJ between the two flow fronts (in gap & fibre) taken once the fluid reached 100mm distance from inlet in Case A at V_f =50%.

Once the videos were processed to identify the flow front in the tow region, a number of issues were encountered. It was observed that as the V_f of tow is increased to 60%, either the flow in gap starts impregnating the tow in the y-direction or flow patches appear well ahead of the visible flow front in tow. Similar phenomena of gap flow impregnating the tow in y-direction was only observed in case of $V_f = 50\%$ when gap widths was increased to 5mm. The flow front formation was clear, consistent and easily identified in case of $V_f = 40\%$.
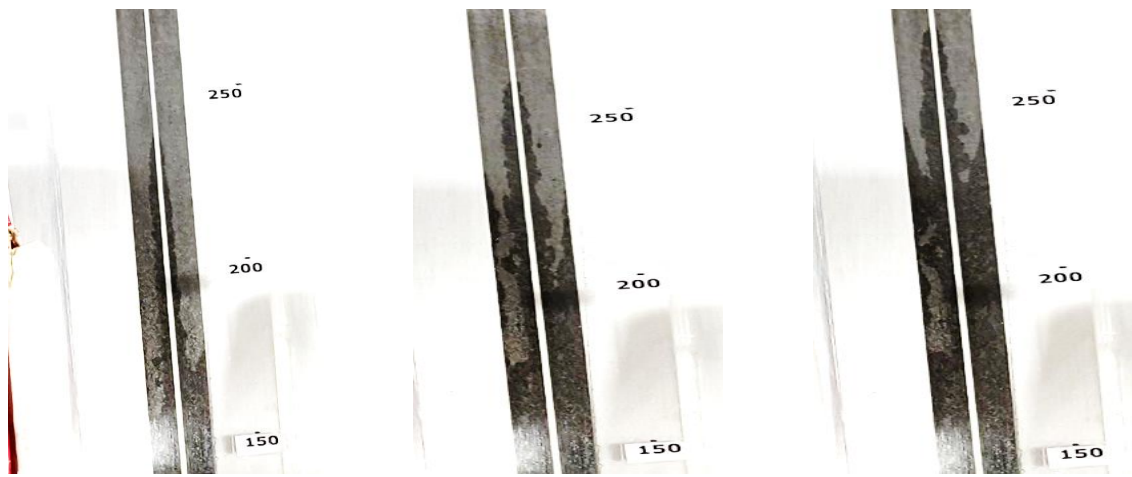
Figure 47 - Tow impregnation in y-direction from flow in gap and void formations

For Case A (single tow & a gap) experiments, the graph in Figure 48 exhibits those results acquired by using slow point is in good agreement with analytical results for both cases of V_f = 40% and 50% for gap widths of 0.25mm to 1mm. The graph slightly deviates away from analytical results and towards the fastest point results as the gap width is increased to 2mm in case of $V_f = 40\%$. However, for Case B slowest point experiments of $V_f = 50\%$ showed a similar trend to Case A experiments, $V_f = 40\%$ is in agreement with analytical results in case of 0.25mm & 5mm gap widths but deviates away from analytical results for all the other gap widths (0.5mm and 1mm). The graph for case B experiments can be found in appendix A.
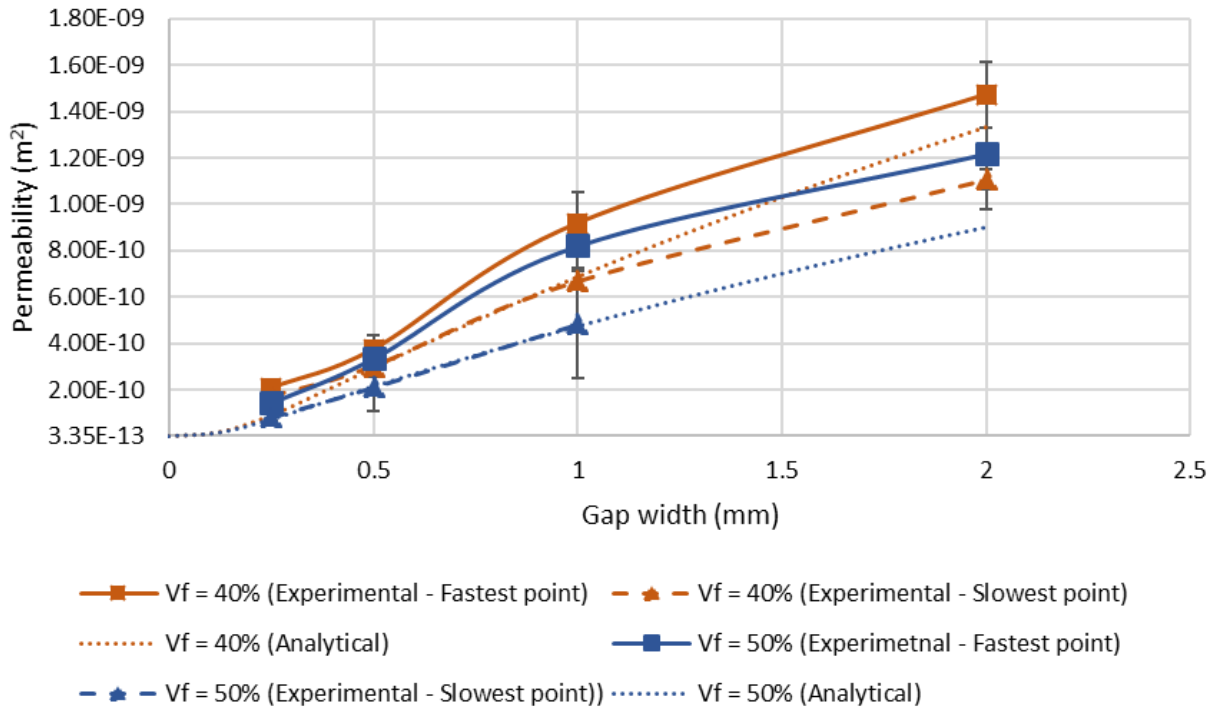
Figure 48 – Correlation between permeability computed for Case A) using fastest and slowest flow front point shows permeability acquired by using slowest point is in closer agreement with the analytical results

The experiments made it clear that for tows at high fibre volume fractions, using the slowest point is not practical as it is more likely to be affected due to impregnation of tow in y direction from gap flow such as in case of $V_f = 60\%$ shown in Figure 47. The results of 5mm gap width at $V_f = 50\%$ also indicated that a similar phenomenon can occur at higher gap widths. This means that while higher tow V_f affects the flow behaviour and progression in the fibre region, it also enhances the flow in the region and reduces the distance between the two flow fronts of gap and fibre region. Moreover, the slowest point can be affected due to more parameters (material variability, binder etc.), than the flow in gap itself. While the slowest point results are in more agreement with analytical results, the accuracy of the experiments at higher V_f due to difficulty in flow front tracking can contribute towards higher error in experimentally calculated permeability. Also, it is essential to highlight that most of ADFP preform produced consists of higher fibre volume fraction (>50%) resulting into flow enhancement in tow region

and spreading the slowest point across the length and making it unidentifiable. For reliable and realistic permeability results for layer/parts with higher V_f flow front in gap regions (fastest point) should be used to compute the permeability.

3.3.3 Detailed analysis of effect of gaps on meso-scale tow permeability using the methods employed in the previous sections

The rest of the experimental data is process based on the method sections (SFF and FP) made in previous sections. The experiments were successfully repeated five time for each cavity other than only tow experiments at $V_f = 60\%$ due to random distributed flow appearance along the tow lengths. The synthetic test oil temperature was checked before each test using a probe thermometer. The temperature value was then used to interpolate the viscosity of oil using the viscosity values at known temperatures provided by the manufacturer. The viscosity data table is provided in the Appendix A. The permeability estimated for case A & B for only tows using Gebart's model was $2.52 \times 10^{-12} m^2, 1.03 \times 10^{-12} m^2 \ and \ 3.35 \times 10^{-13} m^2$ at 40%, 50% and 60% V_f. The computed results given in Figure 49 & Figure 50 revealed that the Gebart's model under predicted the permeability of tows, however the results for both cases A & B showed highest permeability $2.95 \times 10^{-11} m^2$ & $3.97 \times 10^{-11} m^2$ at $V_f = 40\%$ and lowest $1.44 \times 10^{-11} m^2$ & $6.34 \times 10^{-12} m^2$ at $V_f = 50\%$. This was expected from the cavities with no gap, as the tow with densely packed fibres ($V_f = 50\%$) will generate more resistance to the flow and therefore a lower permeability comparing to tows tested at $V_f = 40\%$.

In the presence of gaps, the analytical models consistently under predicted the permeabilities of layers with different configurations. It is important to highlight that the analytically results are calculated under the designed conditions and the main assumption is that the geometry of channel/gap is consistent/rectangular, and fibres are perfectly aligned. For both cases A & B, it can be observed in Figure 49 (Bottom) & Figure 50 (Bottom) the difference is highest (>140%) in case of only tow only experiments, the difference is then decreased as the gaps are

introduced in the cavities but overall difference remains high for smallest gap width (0.25mm). The difference further decreases as the gap widths is increased and can be seen lowest (20%) for highest gap width. The remaining results from all conducted experiments processed using SFF method and FP as flow front are added into the Figure 48 and given in Figure 49.

Figure 49 - Comparison between analytically and experimentally computed permeability for Case - A at different fibre volume fractions (Top), Percentage difference between analytical and experimental results computed for Case A (Bottom), shows magnitude of difference of analytical model is higher in presence of smaller gap widths.
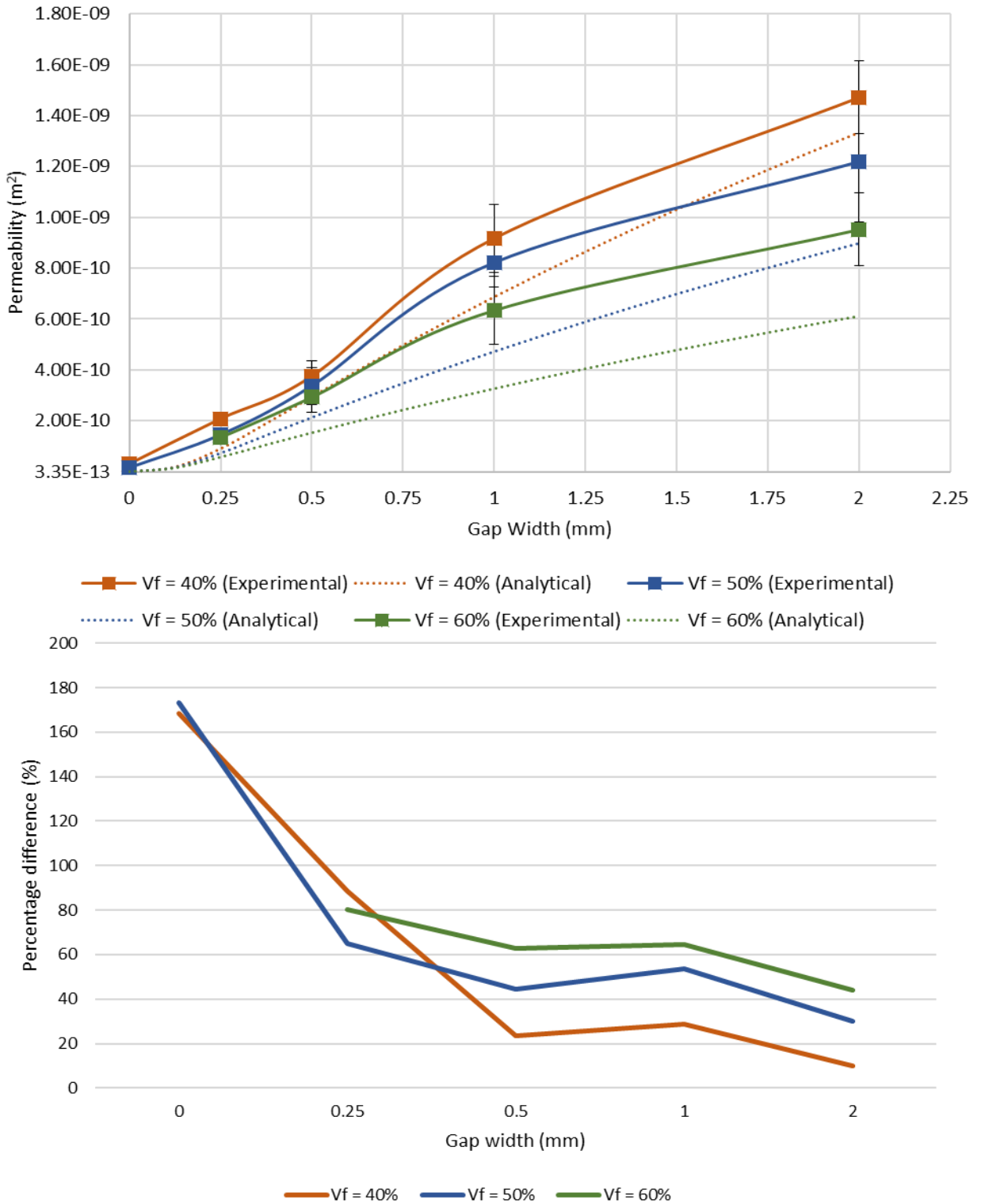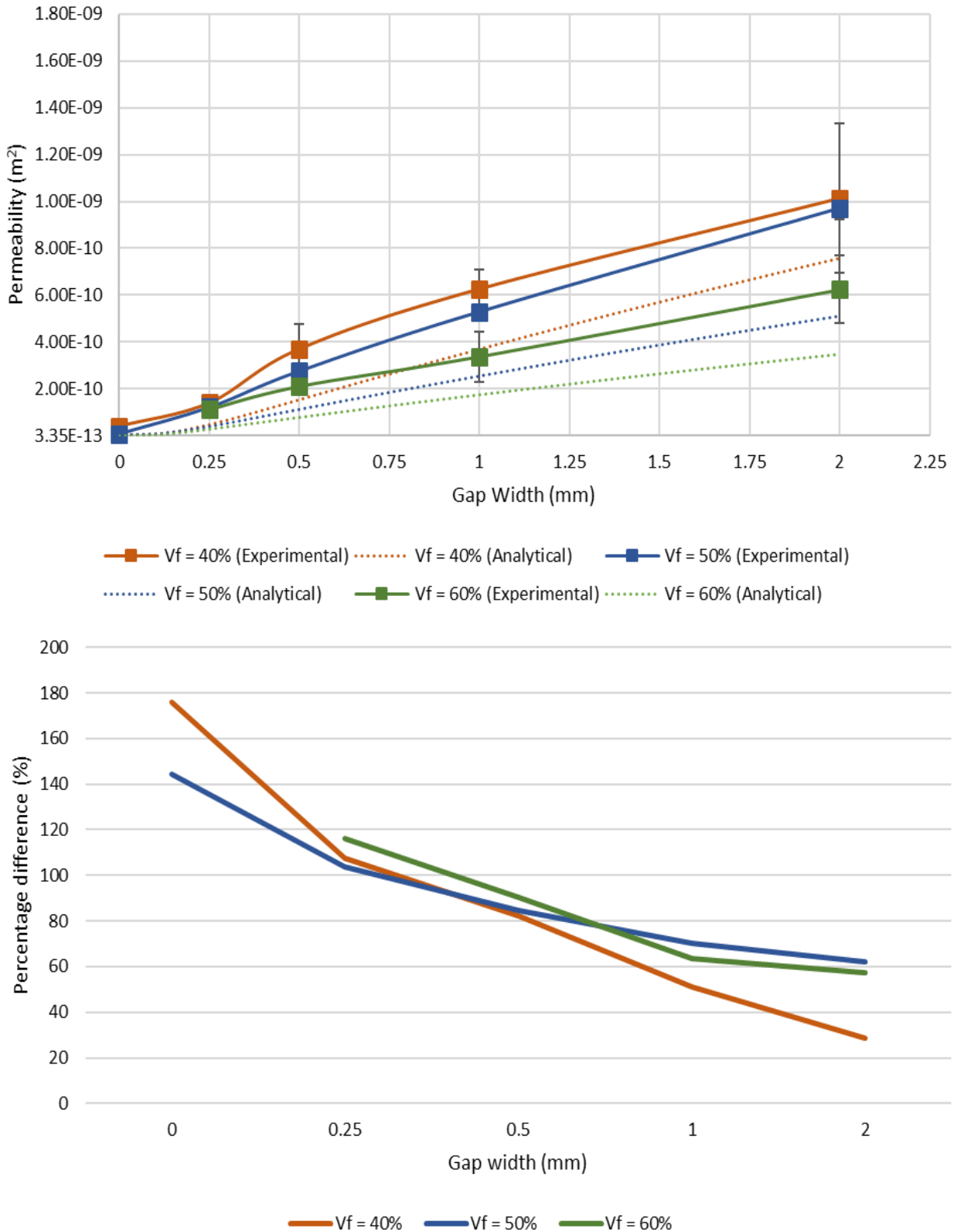
Figure 50 – Comparison between analytically and experimentally computed permeability for Case – B at different fibre volume fractions (Top), Percentage difference between analytical and experimental results computed for Case B (Bottom) shows magnitude of difference of analytical model is higher in presence of smaller gap widths.

As the experiments were conducted in lab conditions, and such conditions will incorporate some degree of variability such as inconsistent thickness of cavity, mould deflection, variability in material effecting the gap width etc. Therefore, it is not possible to maintain as-designed conditions during the experiments. This means that using these analytical models under as designed assumptions will exhibit some degree of scatter compared to experimental results.

Two cases are used to demonstrate the repeatability of results when conditions are scaled up. In one case, smaller gap width (0.25mm,0.5mm and 1mm) at lower V_f of 40% is compared with results from wider gaps (0.5mm, 1mm and 2mm) at higher V_f of 60%. The V_f in Case A is equal to V_f in Case B as shown in Table 12. The results are like previous results and exhibited highest difference (up to 62.3%) between the two cases as the gap widths are smallest. Similarly, the difference decreases to as low as 1.7% when Case A with 1mm is scaled up to 2mm Case B. This establishes that the results are highly affected for smaller gap widths and smaller error can be expected for wider gaps as after a certain increase in gap width, it will exhibit asymptotic behaviour. The Table 12 displays the smallest error is found when Case A results at V_f = 40% is compared against Case B results at V_f = 60%. This also exhibits that ideally lowest permeability cases (V_f = 60%) under Case B configuration are catching up to highest permeability cases (V_f = 40%) under Case A configuration. This point towards the fact that how quickly and significantly permeability is affected due to change in configurations. This casts doubts upon towards the previous studies using analytical predictions derived from models based on meso-scale configurations and comparing it with macro-scale full preform experimental results. This investigation requires another clarification of magnitude of scatter when a layer is investigated.

Case A - ($V_f = 40\%$)		Case B - ($V_f = 60\%$)		Percentage error (%)
Gap width (mm)	Permeability (m^2)	Gap width (mm)	Permeability (m^2)	
0.25	2.07E-10	0.5	2.11E-10	2%
0.5	3.74E-10	1	3.38E-10	10%
1	9.17E-10	2	6.25E-10	38%

Table 12 – High scatter in difference can be observed between case A and case B

3.3.4 Macro-scale flow behaviour due to high gap volume fraction

The results in the previous section showed the effect of gaps on meso-scale tow permeability under different configurations. It was established that smaller gaps imposes higher effect on overall permeability and at the same time smaller gaps are prone to higher scatter and similar results were reported by [27]. In this section, macro-scale flow behaviour in a layer and a preform with high gap volume fraction will be investigated and compared with analytical findings.

3.3.4.1 Flow response in a single layer

A layer was produced with 21 gaps after every two tows. The layer was prepared using a conventional approach by hand layup. A nominal gap width of 0.5mm was aimed at by marking the distance after layup of each band (two tows) with the best accuracy possible by hand as shown in **Figure 51**. The band width was equal to width of two tows (12.7mm), the total width of the layer is 302.6mm, length is 300mm and thickness is 0.22mm. These nominal parameters are used to predict the analytical permeability of the layer.
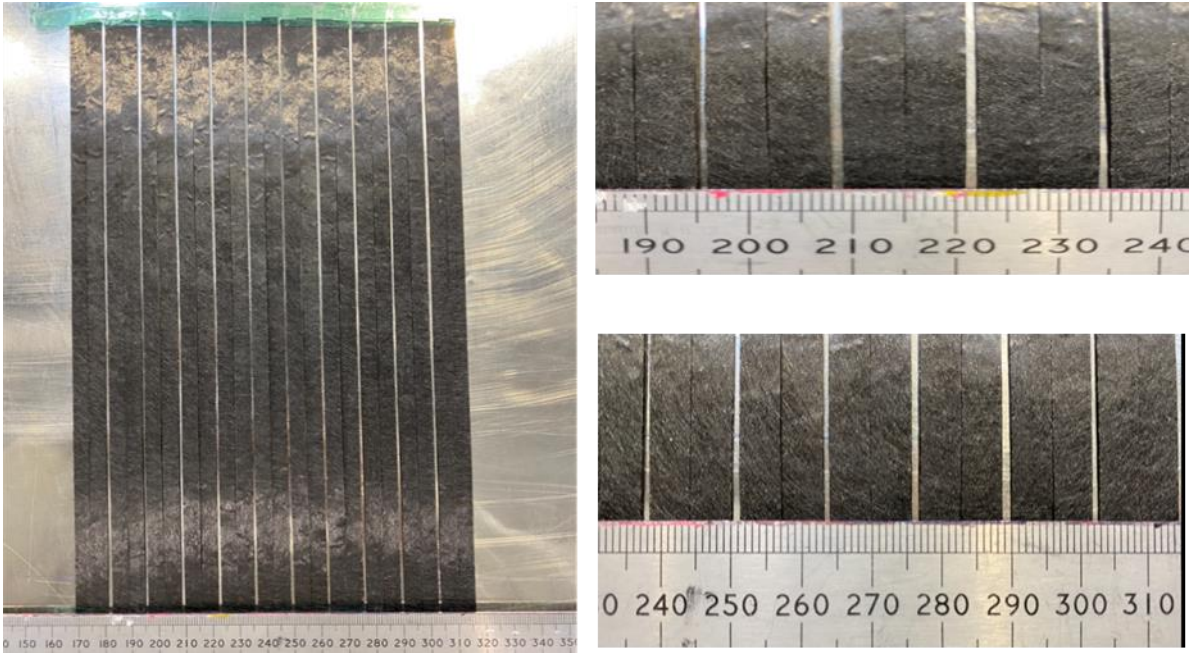
Figure 51 - Layer formed with nominal gap width of 1mm after every two tows.

A thin aluminium plate covered with release film was used to cover the layer to avoid the plastic bag blocking the gaps and to replicate multilayer conditions. The layer was performed under vacuum at $160°C$ for 20 minutes to activate the binder.
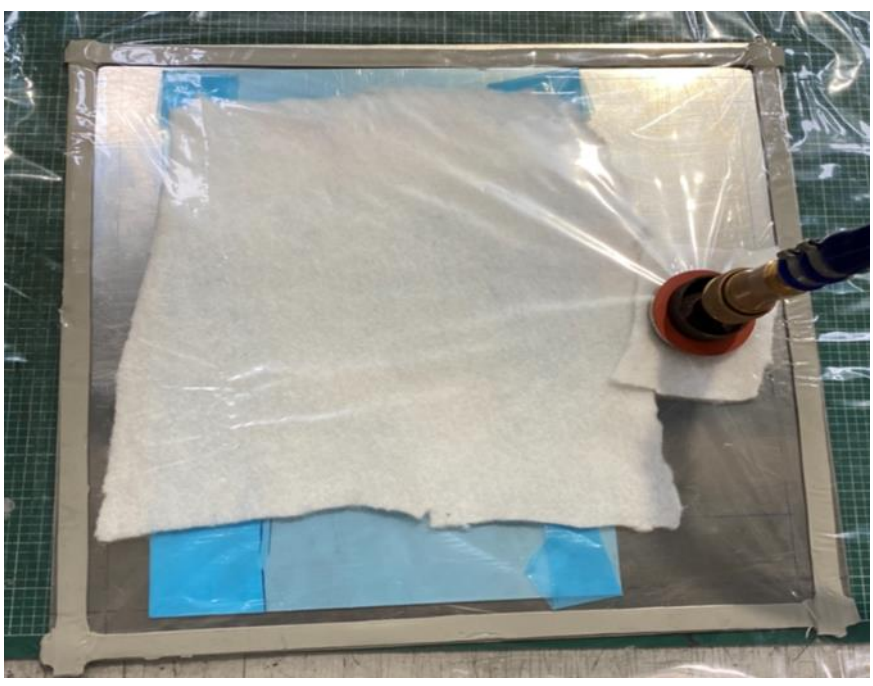
Figure 52 – Activation of binder material in tow under vacuum at 160°C to replicate the real condition of an ADFP produced layer

After the preforming, the mould was left out of the oven to cool down and the vacuum bag was removed carefully. At this stage a clear toughened glass plate was used to cover the preformed layer to enable visibility of flow front under infusion. An infusion mesh was used to distribute flow evenly across the width of the layer. Prime 20 LV resin was used for infusion. The infusion was conducted at room temperature (24ºC) and viscosity of Prime 20 LV is between 214 – 228 cP as per manufacturer (Gurit) data sheet. The value of viscosity was assumed to be 219 cP. The infusion was recorded using a camera. The fastest flow front position was used to post process the video and record length once the resin travels every 50mm up to 300mm.

The V_f of the layer was 47% which was measured by checking the thickness of the panel. The difference in analytical permeability at tow and gap level was found to be 84.64% at nominal $V_f = 50\%$ and the magnitude of difference showed significant increase of 140% in layer results shown in Figure 53. As it has been understood earlier that the error in analytical results are lowest in wider gaps (>1mm), this means similar or higher error can be expected as a result of having smaller gaps (0.25mm or 0.5mm etc.). In case of a layer experiment, hand layup technique was used which increased the magnitude of variability in gap widths. Also the layer was formed by VARI therefore the cavity thickness was not fixed. Gap width and thickness are the two parameters that can affect the overall analytical results. Therefore, for the next stage the real parameters are measured to understand their effect on analytical predictions. The gap widths are measured by scanning the fully consolidated layer and measuring the distance between pixels in ImageJ software. A totally of three measurements from top, centre and end of the gap were taken for each gap. A table of measurements is given in appendix A.

Parts produced using VARI usually have one smooth surface from the mould and one rough surface due to the presence of peel ply, release film, and vacuum bag. But in this case the top of the layer was covered with glass plate which results in very smooth surfaces on both sides of the final part. Therefore, the 0.19mm thickness was measured directly by Vernier callipers

by taking an average of 6 measurements. This means V_f of the layer is changed from 47% to 55%. The variability data is incorporated one by one in the analytical and experimental results to understand the effect due to change in each parameter. The models are as follows:

1- Nominal where only nominal (as-designed) parameters are used.

2- Nominal gap widths are used but the thickness is updated to real thickness.

3- The gap width is updated to one averaged gap value using all the width data collected.

4- An average is calculated for each gap and applied to each gap in the layer, this means all gaps are assigned a unique averaged width

5- The three measurements per gap are used to assign a variable gap width per gap along its length.

One of corner gaps in the layer was completely closed off by the neighbouring tows therefore total number of 23 bands and 21 gaps were present in the layer. In model 2 as the thickness is corrected from the nominal value of 0.22mm to 0.19mm, the V_f is increased from 47% to 55% while the gap volume fraction $V_{gf} = 3.47\%$ remains same for both models 1 & 2 . Due to higher V_f, the corresponding permeability of layer is reduced in the graph. In the next step, as the gap width is updated from nominal 0.05mm to averaged value of gap widths measured in ImageJ 0.701mm. As the gap width is changed, global V_{gf} is increased to 4.82%. Applying a unique average value per gap in Model 4 or an averaged value globally in Model 5 does not affect the permeability, V_f, and V_{gf}. Despite incorporating variability in gap widths in form of an averaged value, the percentage error between the experimental and analytical permeabilities was found to be 76.12% for model 3, 4 & 5.
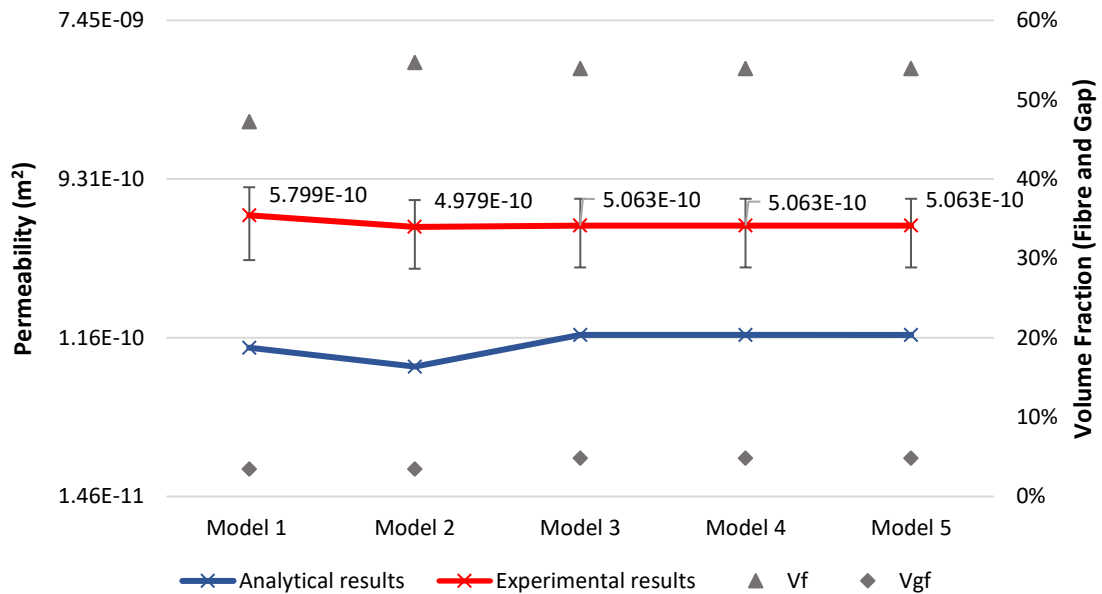
Figure 53 - Layer permeability results show difference between analytical and experimental permeabilities can be minimized by incorporating real gap widths and part thickness into the computations

This establishes that incorporating the variability in gap widths into the analytical model does reduce the permeability from 140% to 123% but the difference remains very high. The difference between analytical results was lowest in Case A (44.59% for 0.5mm gap and V_f = 50%), which increased to 59.11% in Case B (for 1mm and V_f = 59%) and once a layer was examined the difference was significantly increased to 122%.

Even though variability was incorporated into the layer result, the method used showed that the analytical permeability still did not yield results close to the experimental result. Considering [32] reported that gaps did not affected the permeability of complex preforms [[(- 45, + 45, 0, 90)s, 0, (- 45, + 45, 0, 90)]s] significantly, while [27] showed a significant change in permeability in a 0/90 preform and showed the discrepancy between analytical and experimental permeability can be decreased by incorporating variability. Therefore, it is essential to establish that similar agreement can be found on tow, layer and preform level and any complex design of preform does not minimize the effect of gaps on global permeability.

In the next stage a full industrial style preform is produced to investigate the agreement established above for tow and layer level.

3.3.4.2 Flow response in multi-layer preforms with different gap volume fractions

Two 44/44/12 laminates with different gap configurations were produced using an industrial scale ADFP machine with lay-up speed of 500mm/s, feed speed of 200mm/s, cutting speed 400mm/s and compaction force of 450N. A 0.5mm gap was designed after every course (8 tows) in each layer for a Preform 1 & 1mm course to course gap was designed in each layer for preform 2 shown in Figure 54.
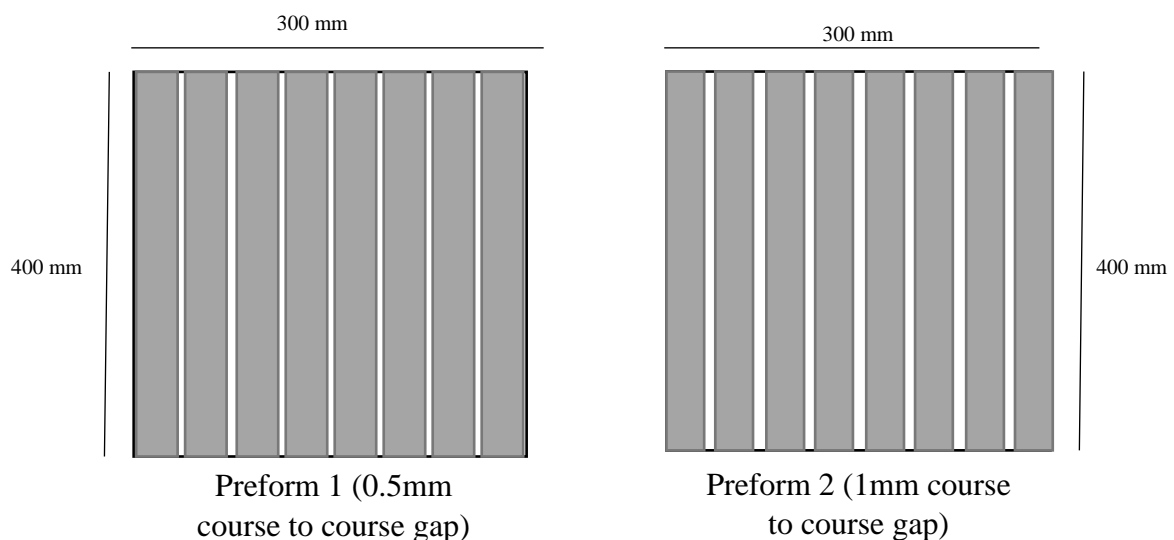
Figure 54 - Schematic of industrial grade preforms

HexFlow RTM6 mono-component resin system [157] was used for the infusion. RTM6 is the aerospace industry standard resin and is preferred due to its high glass transition temperatures and flexibility in injection and cure cycle parameters. The resin was preheated to 80ºC and the preform was preheated to 120ºC using a hotplate. A thermal blanket was used to ensure the preform reaches the required infusion temperature. A thermocouple was used to continuously monitor the temperature of the preform and a thermocouple was used to check the temperature of the resin. An additional hot plate was used to keep the resin at 80ºC. Patches of high-temperature infusion mesh was used at inlet and outlet to ensure an even distribution of the

flow. As the temperature was consistently checked, the viscosity of 33cP from manufacturer data sheet.
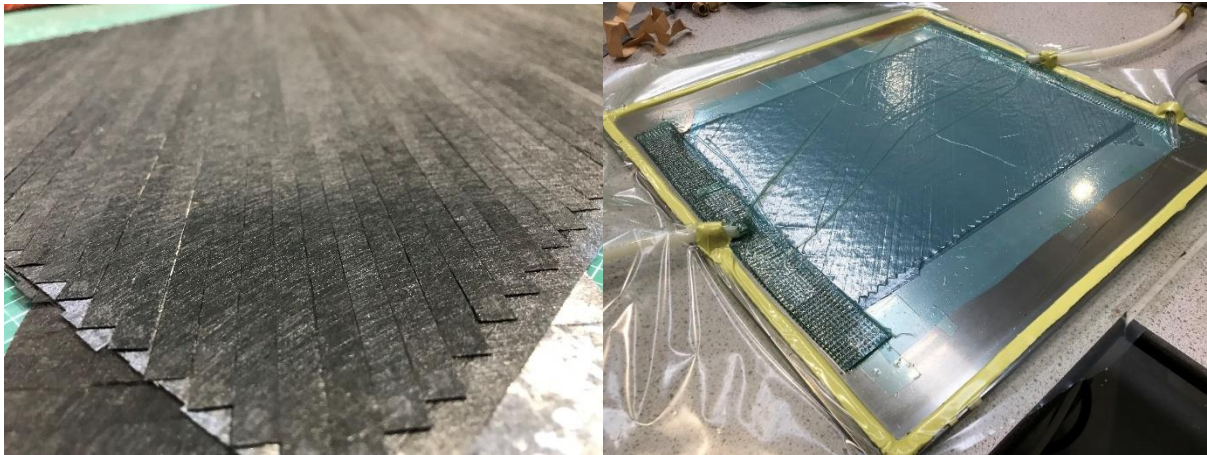
Figure 55 - ADFP preform (left) and infusion setup (right)

Flow front was recorded using a video camera. Due to the presence of gaps in each layer in different direction, an uneven spikey flow front was formed during the impregnation of the preform. Preform 1 containing 0.5mm course to course gap was filled in more than 2.5 hours. Whereas Preform 2 containing 1mm course to course gap was filled in 20mins. This shows gaps specifications can affect the influence fill time of a composite part. A total of 16 measurements were included in SFF method using fastest point. Figure 56 shows the flow front progression captured at different time during VARI. The laminate top layer is in 45° orientation and flow in the top layer is race tracking ahead. In some regions, flow from gaps in 0° orientation can be seen impregnating the layer through the thickness. This results into formation of bristly type flow front shape during VARI.
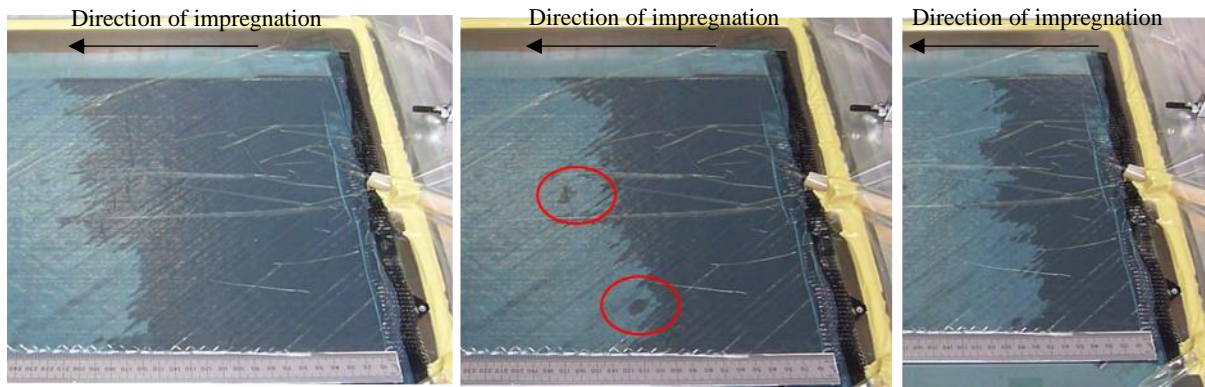
Figure 56 - Flow front progression during VARI shows a spikey flow front formation exhibiting the flow in gaps are ahead of flow in fibre regions

The random appearance of wet spots well ahead of the visible flow front highlighted in red circles can be seen in figure above. The spots were noticed in different regions of both preforms throughout the infusion. This demonstrates that the gaps placed in each layer have formed a network within the preform. At the intersection points of these gaps the flow start impregnating the neighbouring layer. This results into formation of wet spots across the preform. There were no macroscale visible voids in the final part after demoulding. However increasing the gaps widths or overall V_{gf} may results into high void formations. The orientation of layers in the preform can also effect the void formation. This was taken as one of the aim to during the development of numerical tool later explained in thesis.

The analytical model predicted a percentage increase of 54% from preform 1 and preform 2. However the experimental results (Preform $1 = 1.24 \times 10^{-12} \text{m}^2$ & Preform $2 = 7.08 \times 10^{-12} \text{m}^2$) showed higher increase of 83%. The percentage difference between the analytical and experimental results further increases to 165% in comparison to layer level in case of preform 1 with 0.5mm gap. The results also showed that the analytical results under predicted the increase (54%) of permeability as gap widths are increased from 0.5mm to 1mm and actual increase calculated from experimental results was much higher (83%). The preform results showed the highest percentage difference in comparison to the analytical predictions.

The main source of this increase in difference was revealed in Figure 56, that gaps within the preform are behaving as a network for flow and the flow front in gap within the preform can be well ahead of the flow front in the top layer. Even when the analytical predictions were based on gap and fibre models and flow in both regions were incorporated to estimate the permeability, higher errors were found when preform results were compared to analytical predictions, similar to [27].

3.4 Conclusions

The effect of gaps on the permeability of dry carbon fibre tow has been investigated (both analytically and experimentally) at different V_f. A tabletop experimental rig was designed which successfully carried out meso-scale permeability experiments in presence of different gap widths. A preliminary analytical investigation of a layer showed that even if the total number of gaps and gap widths vary but a constant V_{gf} is maintained, the permeability of the layer directly depends on the gap widths and number of gaps. Higher gap widths with fewer gaps will result in a higher layer permeability and vice versa.

Two different methods (Direct and K_{sff}) were used to analyse the experimental data from meso-scale permeability experiments. In case of only tow experiments, the results showed only 1.7% and 4.63% difference from analytical results. However, in case of presence of gaps, the percentage difference is highest (41.85% - Case A, 32.12% - Case B) in case of smallest gap width (0.25mm). T-test conducted on data computed using both methods showed no statistically significant difference. The direct method yielded results closer to analytical results however the K_{sff} method was selected to process the results as it included any change in pressure during the experiments and showed any change in local permeability.

In meso-scale experiments, two flow fronts are formed in presence of gaps, one in gap region and second in the tow region. Both were used to compute the permeability and the comparison

showed the permeability calculated using the flow front in tow was in better agreement with the analytical results. However, it can be difficult to track flow front position in the tow region such as in case of V_f =60% experiments, the flow front progression was random since the permeability using slowest point could not be computed. Also, if normal permeability testing methods/rig is used, it will be difficult to identify the last point of fluid arrival at certain point in presence of cavity in-built sensors. For such reason it is ideal to use the fast point to compute permeability. Highest percentage difference (176%) between experimental and analytical results was found in only tow experiments. As the V_{gf} is increased in the cavity the percentage difference decreases as low as below 20% in case of $V_f = 40\%$.

An increase in permeability was observed as the experiments were scaled up from single tow to two tows. Similarly, the results showed that by upscaling from meso-scale to layer level, percentage difference between the two approaches (experimental and analytical) increases up to 120%. A step-by-step method to incorporated variability clarified that using few data point to assign a mean average value per gap or globally in a layer will not reduce the error between experimental and analytical results. It clarifies the necessity of accessing local gap width data to enable assessing more reliable mean value and incorporating them into analytical model will potentially minimize the error between experimental and analytical measurements further. As the Gebart's model assumes a perfect square or hexagonal shape for fibre tows, similarly the gap models assume a perfect rectangular shape of the gap and both models does not take fluid properties such as viscosity into account, the overall error remained very high (51.35%).

Furthermore, the difference between the analytical and experimental permeability showed further increment in percentage difference of 165% in case of a 44/44/12 ADFP produced preform. Figure 56 shows the reason behind this high percentage difference, where forming flow patches can be seen at random position. These patches were formed due to resin propagating quickly through the channels while impregnating the tows in the surrounding

regions. This showed that the gaps behave as a network within the preform and the actual flow front can be well ahead than the visible flow front on the top layer. Therefore **Error! Reference s ource not found.** shows a high difference in analytical and experimental results. Similar delayed reading can be expected when permeability rig with embedded sensors are being used. The variability in gap width and gap positioning data was not accessible as the preform was produced by industrial partner therefore only as designed parameters were adopted in analytical models which contributes towards the high difference to some extent but overall higher difference from layer level is inevitable. The preform data (gap width and positioning) is identified as one of the main factors that can cause higher error in permeability prediction from analytical solutions and experimental results.

The preforms tested in this work did not show any visible void formation in the final parts. However, only two preforms with 0.5mm and 1mm gap specifications were tested for the analysis. It was observed during meso-scale experiments at 60% V_f, the flow is much more dominant in the gap compared to the fibre regions and reaches the outlet much before the flow in tow, leaving non-impregnated regions in the tow. Therefore it can be established that high V_{gf} can lead to void formations in the part. This will be taken into account in the development of the numerical tool to identify regions of poor flow to make relevant changes to ensure full impregnation of the preform.

This presented work clarified that if permeability is computed by using averaged gap parameters (calculated by taking limited measurements such as in [27]) will not highly affect the overall results. Moreover, using meso-scale models and taking a weighted averaging approach to homogenise will cause higher scatter in results at a preform level. Therefore, the analytical models failed over all different stages (tow level, layer level, and preform level) to predict reliable permeability. The models maybe accurate under the as designed assumptions, however the real experimental conditions are usually very different from as designed and

permeability is sensitive to such conditions. Therefore, it is essential to test analytical models predicting micro- and meso-scale permeabilities at different scale to understand if predictions from such models can be used as benchmarks.

Gap widths can highly vary from beginning to the end point and taking only a few measurements along the length is not enough to adopt a gap width which can be applied globally across a layer or preform. These models also neglect any interlayer flow and in presence of gaps through thickness flow should not be neglected as the flow in gap travels with much higher velocity and is likely to reach the junction with other gap and pass the flow across the layer. In order to measure reliable permeability such models will require local gap width data which can be challenging to obtain. One possible and economic way of accessing such complex information for each layer in an ADFP preform can be by using a laser scanner during the deposition process. However, with such information, a different/novel technique will be required to compute permeability numerically. A technique which can incorporate such changes in gap widths across the preform and does not neglect the flow interchange at the gap junctions. A method that does not only depend on the shape of gap but also pressure drop. This way more reliable permeability can be predicted. In the next chapter of this project, a numerical model was developed to overcome the current limitations in conventional simulation methods. A novel method has been identified to enable flow characterization of ADFP performs with high V_{gf} based on real preform data.

3.5 Appendix A
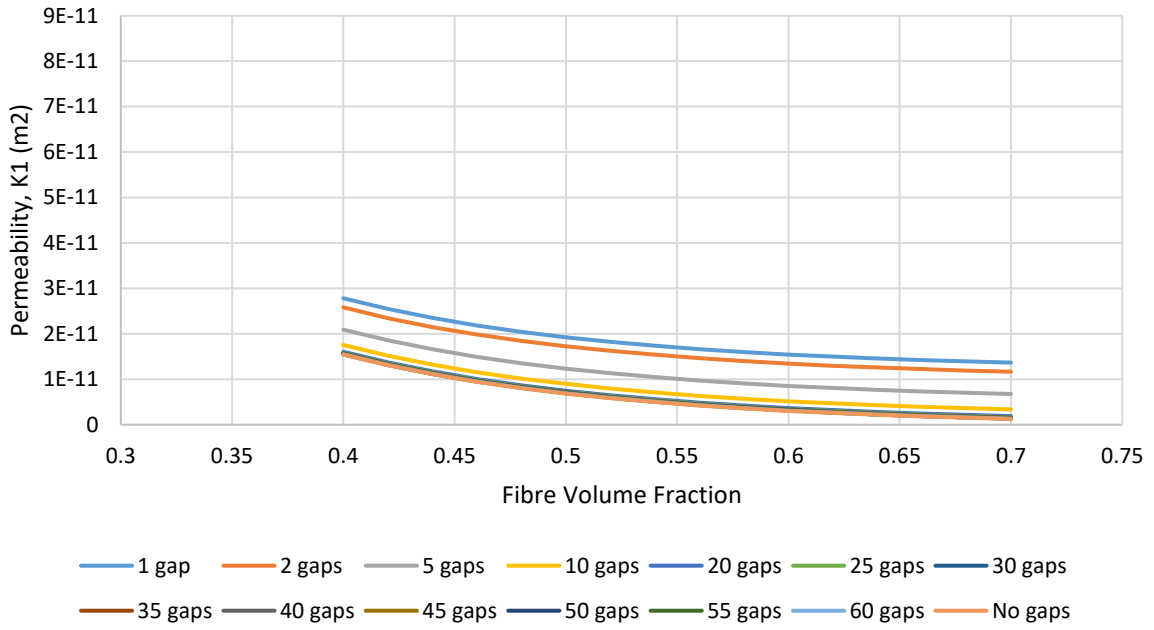
Effect on permeability due to varying gap widths (V_{gf}= 0.00357)
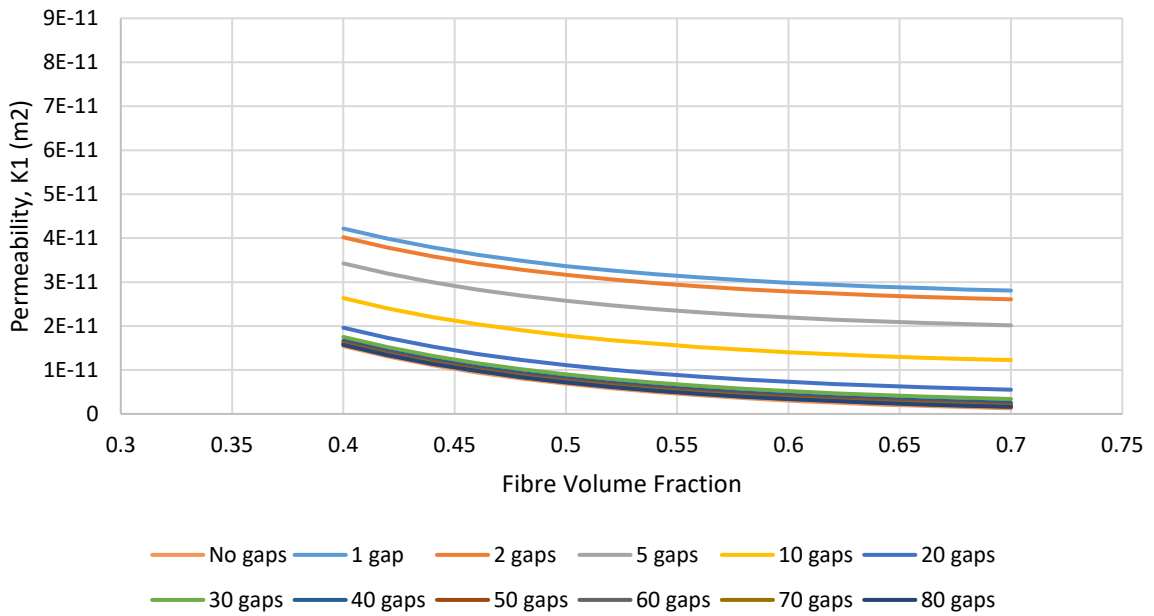
Effect on permeability due to varying gap widths (V_{gf} = 0.00714)
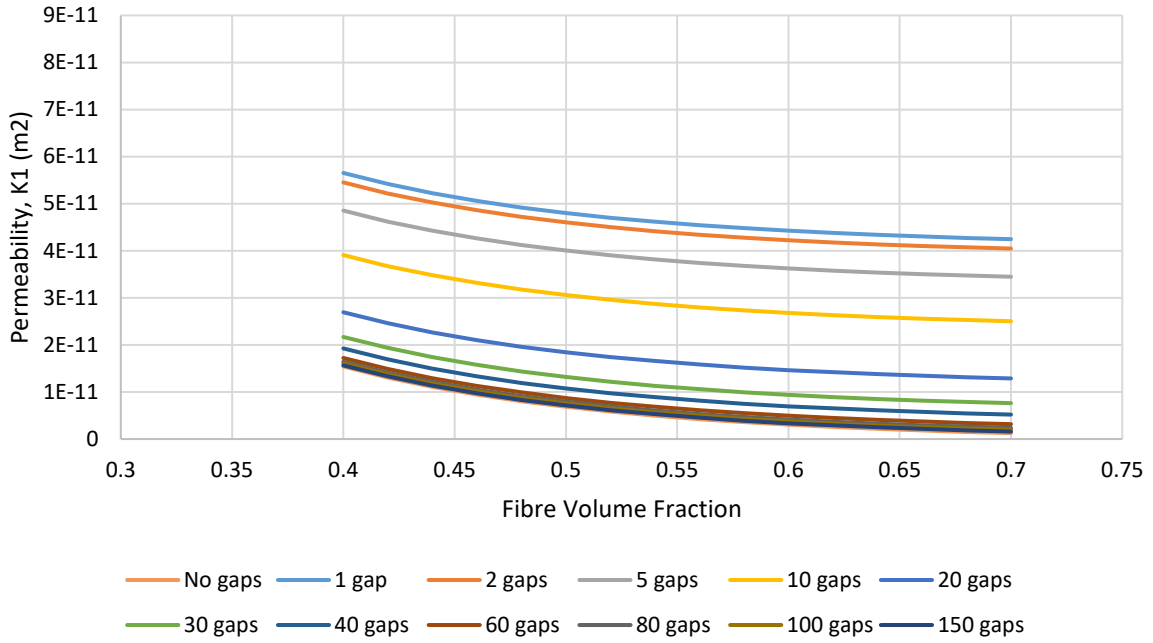
Effect on permeability due to varying gap widths ($V_{gf} = 0.0107$)
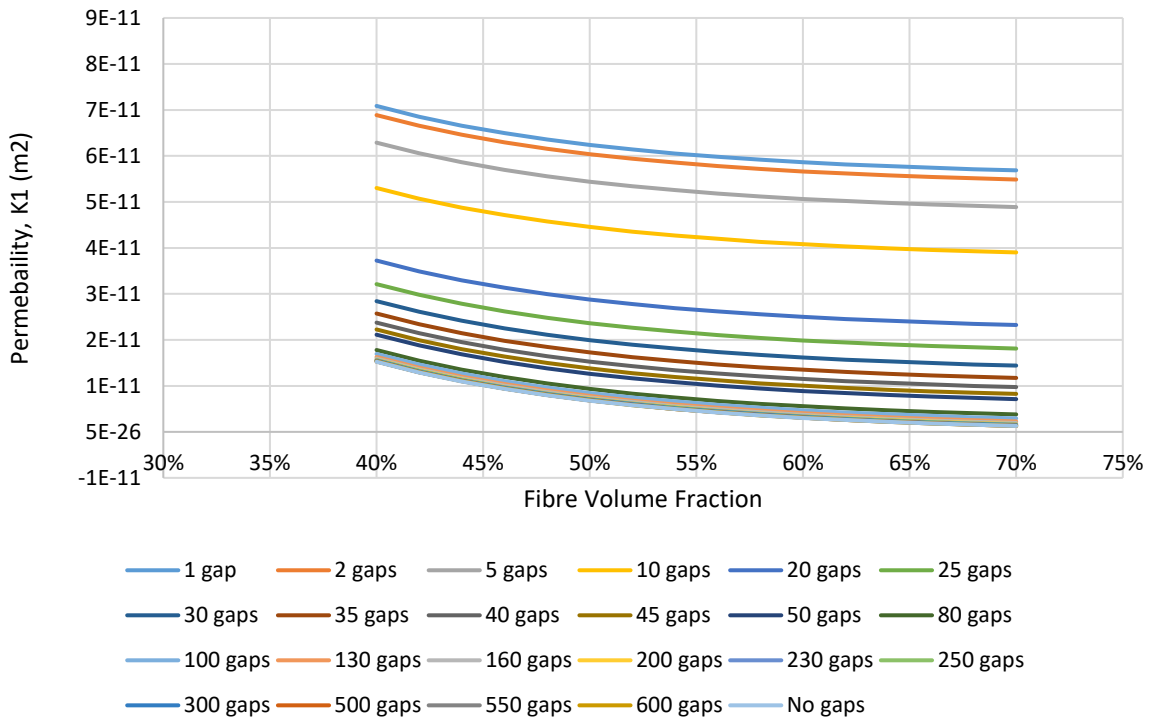
Effect on permeability due to varying gap widths ($V_{gf} = 0.0143$)

94
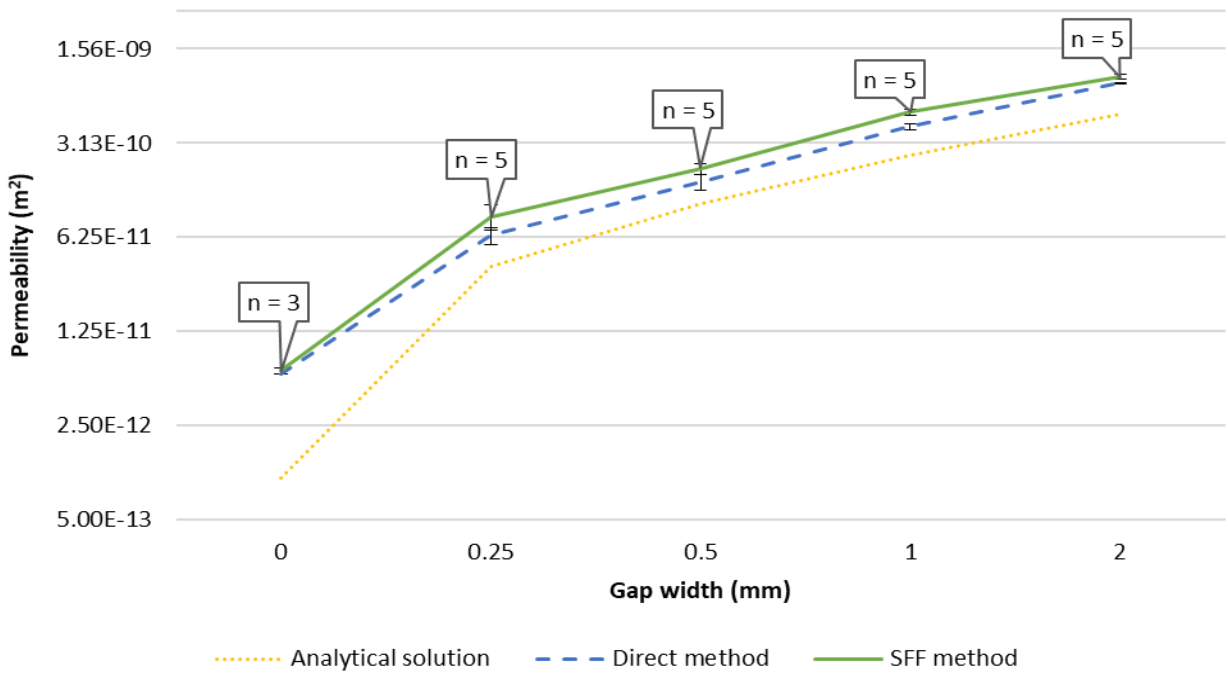
Logarithmic scale graph of permeability obtained for V_f=50%, case B (Tow – Gap - Tow) experiments using: (A) Analytical solution, (B) The Direct method and (C) The SFF method
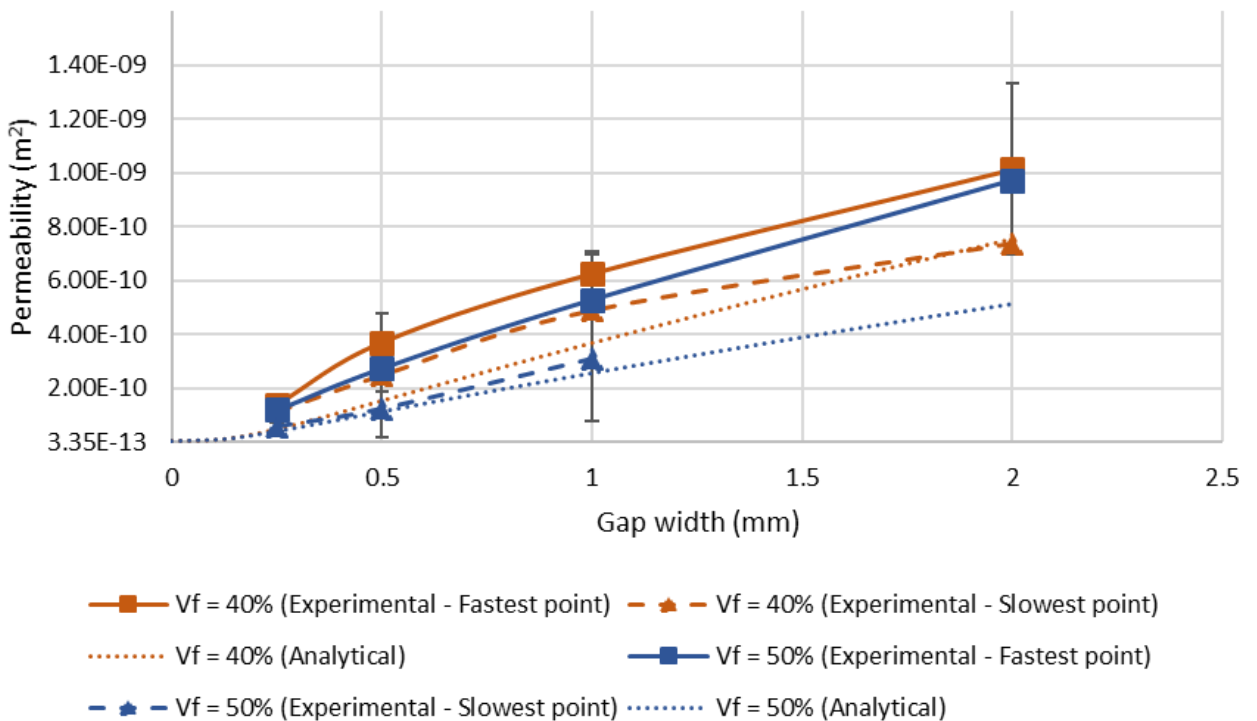
Correlation between permeability computed for Case A (Top) & Case B (Bottom) using fastest and slowest flow front point shows permeability acquired by using slowest point is in closer agreement with the analytical results

Variability in gap widths

Measurement	1	2	3	Average
Gap 1 (mm)	0.588	0.656	0.511	0.585
Gap 2 (mm)	1.002	0.512	0.505	0.673
Gap 3 (mm)	0.746	0.836	0.76	0.780667
Gap 4 (mm)	0.829	0.85	0.843	0.840667
Gap 5 (mm)	1.009	1.168	1.175	1.117333
Gap 6 (mm)	0.4728	0.518	0.732	0.574267
Gap 7 (mm)	0.843	0.761	0.594	0.732667
Gap 8 (mm)	0.843	0.67	0.829	0.780667
Gap 9 (mm)	0.912	0.663	0.566	0.713667
Gap 10 (mm)	0.753	0.504	0.67	0.642333
Gap 11 (mm)	0.988	0.587	0.594	0.723
Gap 12 (mm)	0.912	0.594	0.49	0.665333
Gap 13 (mm)	0.67	0.836	1.154	0.886667
Gap 14 (mm)	0.421	0.408	0.574	0.467667
Gap 15 (mm)	0.829	0.829	0.843	0.833667
Gap 16 (mm)	0.497	0.573	0.739	0.603
Gap 17 (mm)	0.587	0.573	0.671	0.610333
Gap 18 (mm)	0.566	0.905	0.753	0.741333
Gap 19 (mm)	0.256	0.339	0.414	0.336333
Gap 20 (mm)	0.573	0.815	0.829	0.739
Gap 21 (mm)	0.843	0.594	0.836	0.757667

Permeability calculations of full preform.

Time (sec)	Xf1			Xf2		
	xf1(cm)	Xf^2 / time - slope (m)	K(SSF), (m^2)	xf2(cm)	Xf^2 / time - slope (m)	K(SSF) , (m^2)
600	70	8.17E-06	6.20E-13	100	1.67E-05	1.27E-12
1200	110	1.20E-05	9.11E-13	145	1.84E-05	1.39E-12
1680	146	1.92E-05	1.46E-12	180	2.37E-05	1.80E-12
2100	160	1.02E-05	7.74E-13	194	1.25E-05	9.46E-13
2700	180	1.13E-05	8.60E-13	215	1.43E-05	1.09E-12
3330	205	1.53E-05	1.16E-12	245	2.19E-05	1.66E-12
3900	233	2.15E-05	1.63E-12	257	1.06E-05	8.02E-13
4500	248	1.20E-05	9.13E-13	275	1.60E-05	1.21E-12
5100	270	1.90E-05	1.44E-12	289	1.32E-05	9.99E-13
5700	292	2.06E-05	1.56E-12	310	2.10E-05	1.59E-12

6300	300	7.89E-06	5.99E-13	320	1.05E-05	7.97E-13
6900	305	5.04E-06	3.83E-13	332	1.30E-05	9.90E-13
7500	316	1.14E-05	8.64E-13	360	3.23E-05	2.45E-12
8100	325	9.62E-06	7.30E-13	369	1.09E-05	8.30E-13
8700	335	1.10E-05	8.35E-13	377	9.95E-06	7.55E-13
Average, (m^2)			9.82E-13			1.24E-12
Standard deviation			3.81E-13			4.73E-13
Variance			1.45E-25			2.23E-25

Effective permeability of Preform 1 containing 0.5mm course to course target gap width

Time (sec)	Xf1			Xf2		
	Xf1 (cm)	Xf2 / time - slope (m)	K(SFF), (m^2)	Xf2 (cm)	Xf2 / time - slope (m)	K (SFF), (m^2)
62	2.5	0.000010	7.83E-13	4	0.000026	2.01E-12
120	5.5	0.000041	3.22E-12	8	0.000083	6.43E-12
180	7.5	0.000043	3.37E-12	9	0.000028	2.20E-12
240	10	0.000073	5.67E-12	12	0.000105	8.16E-12
300	11.5	0.000054	4.18E-12	14.9	0.000130	1.01E-11
360	13	0.000061	4.76E-12	16.4	0.000078	6.08E-12
420	15	0.000093	7.25E-12	18	0.000092	7.13E-12
480	17	0.000107	8.29E-12	19.2	0.000074	5.78E-12
540	19.2	0.000133	1.03E-11	21.2	0.000135	1.05E-11
600	21	0.000121	9.37E-12	22.7	0.000110	8.53E-12
720	22.6	0.000058	4.52E-12	24.3	0.000063	4.87E-12
840	24.1	0.000058	4.54E-12	26.4	0.000089	6.90E-12
960	26.6	0.000106	8.21E-12	29.4	0.000140	1.08E-11
1080	27.8	0.000054	4.23E-12	31.1	0.000086	6.66E-12
1200	28.9	0.000052	4.04E-12	33.5	0.000129	1.00E-11
Average, (m^2)			5.52E-12			7.08E-12
Standard deviation			2.62E-12			2.73E-12
Variance			6.88E-24			7.47E-24

Effective permeability of Preform 2 containing 1mm course to course target gap width

T / °C	η / mPa×s
14	143.2
14.2	141.6
15.5	131.9
15.5	131.9
16.0	128.3
16.5	124.8
17.0	121.4
17.6	117.5
18.0	114.9
18.5	111.8
19.0	108.8
19.5	105.8
20.0	103.0
20.5	100.2
21.0	97.4
21.5	94.8
22.0	92.2
22.5	89.7
23.0	87.3
23.5	84.9
24.0	82.6
24.5	80.4
25.0	78.2

Viscosity of supreme synthetic 5W20 test oil (raw data)
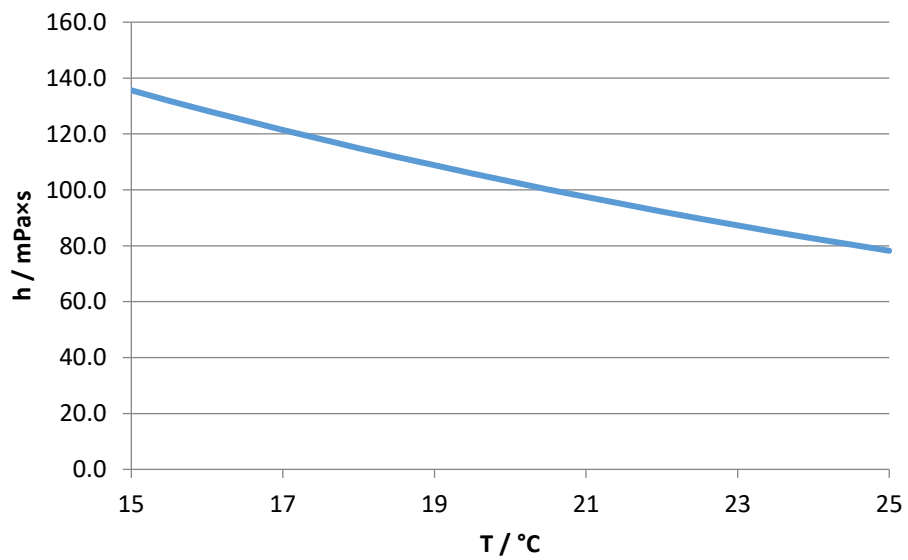
Viscosity of supreme synthetic 5W20 test oil (graph)
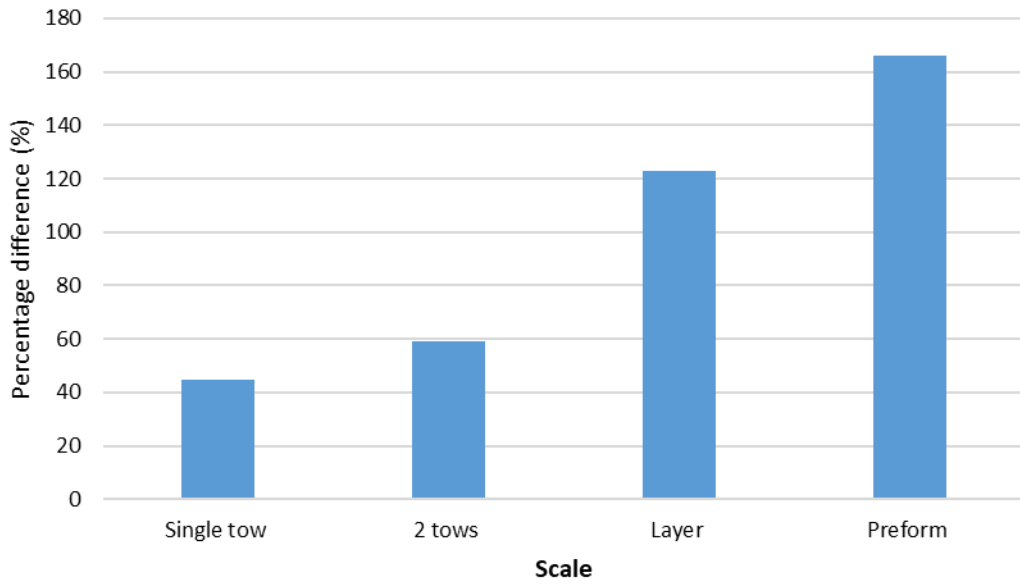
Percentage difference between analytical and experimental results shows how it increases from tow level to full preform level

# Chapter 4 A novel approach to calculate flow rates and permeability of ADFP produced preforms using network analysis

4.1 Introduction

The meso-scale results (both analytical and experimental) showed the limitations of conventional techniques to characterize ADFP produced preforms with high gap volume fraction. It is understood from the previous results that even smaller gap widths can highly influence the global permeability and a higher difference between analytical and experimental results is a consequence of a few main factors. Disregarding the variability of gap widths in analytical models, disregarding the through thickness flow at interlayer gap junctions and incorporating the variability in gap widths based on very few measurements are identified as the most influential factors. Similarly, modern computational capability has enabled both 2D and 3D flow simulations. This can help to visualize the flow progression during infusion and predict the fill times and identify regions of poor permeability causing dry spot formation or increasing the overall fill time. The 3D simulation approach can incorporate the interlayer flow exchange, but the accuracy of results directly depends on the element size. Element size plays a vital role in a 3D simulation. While a higher number of elements can provide details of meso-scale flow behaviour, the element count is directly proportional to both the time required to produce a fully connected 3D mesh and to actually run the simulation. This process can be difficult for the ADFP produced preforms with a higher gap volume fraction, such as the one examined in previous section 3.3.4. Such preforms require users to produce a geometry mesh containing different regions for gaps and tows. To connect the mesh of different regions in each layer, it will need the same number of nodes at their boundaries and desirably coincident nodes in the neighbouring regions as shown in Figure 57 (Middle). This complicates the mesh when the layers are in different orientations. To enable realistic flow simulation by incorporating the variability in the gap widths, the user will be required to access the preform data in each layer

of a preform and generate a CAD file of geometry based on real data which is then used to produce a fully connected mesh. This mesh will then be imported into a different simulation software and run a flow simulation such as shown for a simple geometry in Figure 57 (Right). This means every-time a new preform is produced a user will need to go through all the steps to run a simulation and discard the mesh the next preform will have always have different specifications. This limits the adoption of 3D simulation for an ADFP produced preform. Figure 58 shows run time of different number of elements for a same geometry. It can be observed that for element size of 10cm, PAM-RTM produced the simulation in 13.3 hours. To be able to observe the local behaviour and flow front progression in an ADFP preform with high V_{gf}, much smaller element size will be required as the gap widths are usually smaller by an order of magnitude than 10 cm.
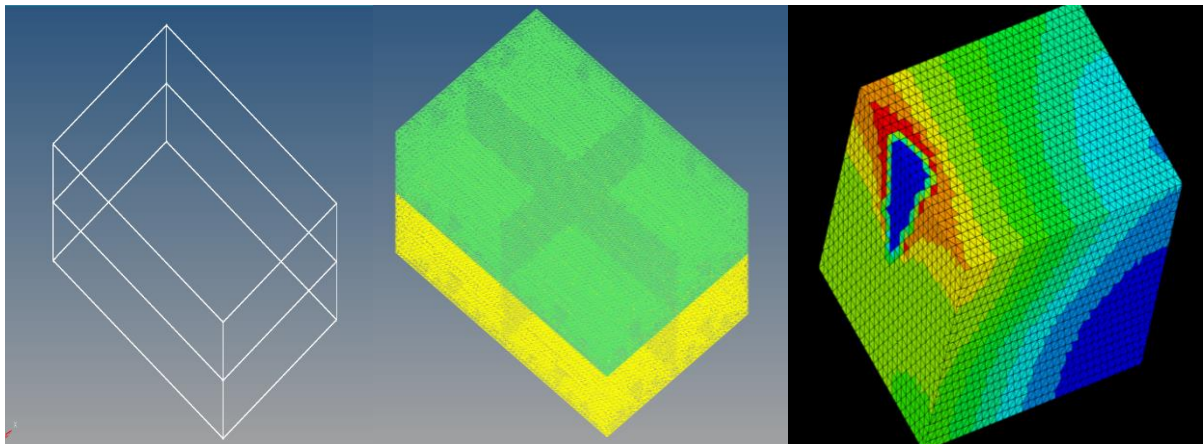

Figure 57 - 3D CAD file of an example geometry used to create a fully connected mesh with tetrahedral elements of two regions in HYPERMESH (Middle). The mesh is imported to PAM-RTM to produce a flow simulation (Right).
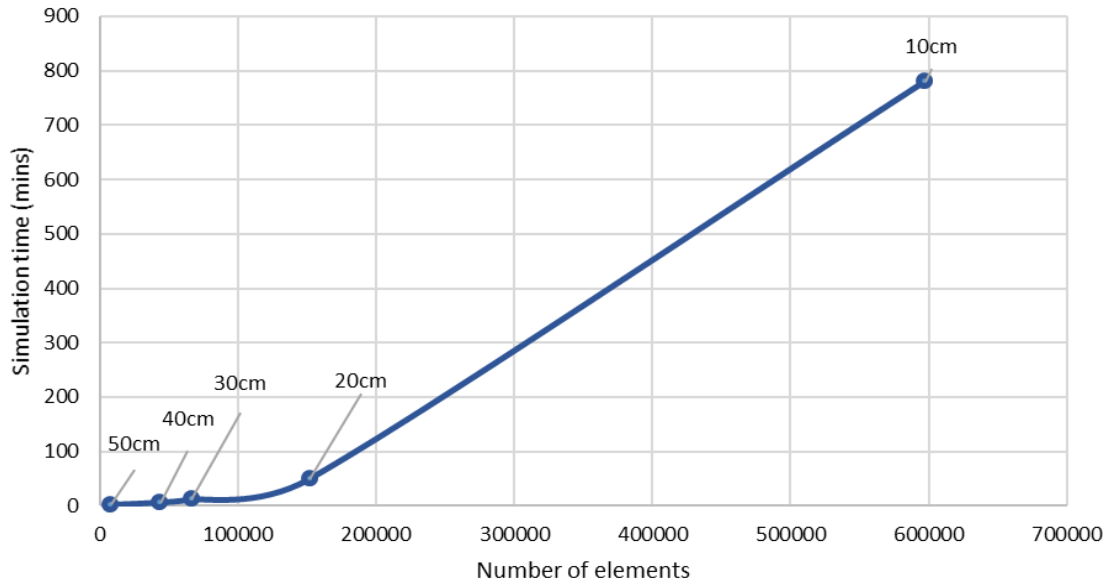
Figure 58 - Expected simulation time by PAM-RTM for a 3D model with different element sizes shows more than 13 hours will be required to simulate 600,000 elements even when the element size is as big as 10cm

The other option is 2D simulation where all the layers are homogenised into a 2D model. Figure 59 shows the run time simulated using different number of elements in PAM-RTM. The graph shows a 2D model can process more number of elements 700,000 in less than 2 hours. The lower run times of 2D model, less complications and less user time required in generating a shell mesh, user time required to assign properties and limited 2D visualization of flow behaviour comparing to a 3D model makes them a lot more favourable for flow simulations. Despite it being relatively easier to produce a 2D mesh for an ADFP produced preform and their lower run times, the production of mesh along with running a simulation still has challenges. In a 2D mesh, different regions of flow can be assigned for different layers. It requires identifying regions with similar flow properties. This is possible for preforms with consistent geometries. The process becomes complicated for preforms with higher gap volume fractions due to their high variability. Therefore, a common assumption is mostly made based on few measurements that the geometry of each layer in a preform is consistent and hence a homogenised permeability value is computed for each layer. The simulation software further homogenises the interlayer permeabilities together and computes a global homogenised

permeability. The main disadvantage of such approach is when the gap widths between each layers are different in a preform, the simulation may produce results which does not show realistic flow behaviour. In such case, the simulation does not provide any insight towards local flow behaviours and does not provide any visual to local flow behaviour. These complications require a different approach that enables a user to overcome all the above-mentioned limitations and analyse the flow characteristics of an ADFP preform quicker than the conventional 2D or 3D simulation approaches. This approach should bring the speed of analysis into the same order as moving the preform from the preforming station to the moulding station. This can enable the user to make the required changes to achieve the fastest fill time. Hence this approach should enable formation of any preform geometry from scratch and not be time expensive. It should be capable of incorporating any level of preform variability without requiring the user to access the information from individual layers and retrieve data through expensive means of microscopy, SEM, or XCT etc. This should also aid towards visualizing the local and global flow behaviour in a preform. Different computer software are required to run a simulation. One software is usually used to produces the preform geometry mesh, such as Hyper-Mesh and the other which is employed to perform the numerical flow simulation such as PAM-RTM, LIMS etc.
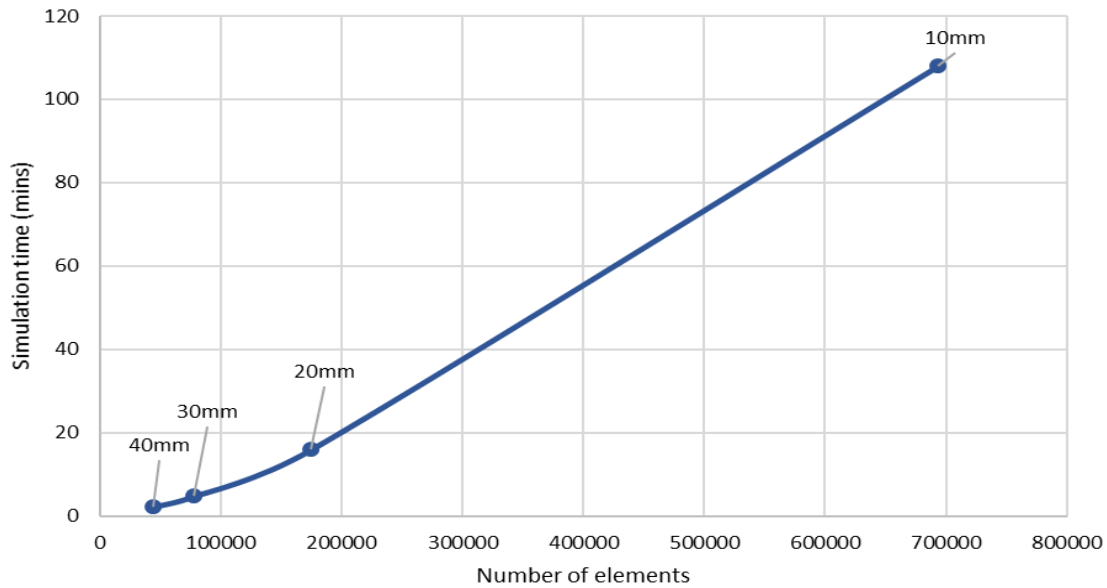
Figure 59 - Expected simulation time by PAM-RTM for a 2D model with different element sizes shows only 1.8 hours are required to simulate 700,000 elements even when the element size is as small as 10mm

In this chapter, a novel network method has been proposed which addresses all of the previously mentioned limitations of using conventional 2D and 3D approaches. This numerical code produces a vascular structure of gap network based on real gap width data which is acquired directly from the deposition rig through laser profilometry, and performs a flow analysis by using a network analysis method that is usually used for analysing flow in pipe networks in Civil Engineering. The whole code is capable of processing preforms with a layer in any direction and offers significantly lower run time compared to producing a 3D mesh and simulation. However the proposed model calculates the flow rates based on the gaps in the network only and assumes the tows are impermeable. This assumption, further details and comparisons of rum times will be discussed later in the chapter.

4.2 Methodology

This section will focus on the methods that have been adopted in order to execute the network analysis. The Global Gradient Analysis (GCA) for numerical simulation has been identified in the literature review that yields the desired outputs (pressure drop across the network, flow

rates in gaps, etc) to calculate the layer/preform permeability. However, the model needs to be further developed in order to make it applicable for use when assessing ADFP preforms' flow behaviour. This involves replacing pressure relations that are applicable for different resins systems and using the output from the network model to generate preform permeability. This approach will predict the flow behaviour in steady state. During saturation of preform the fluid will sink into the fibre tows in transverse direction causing a sink effect. However this phenomena will be neglected at this stage of model development and no sink effect will be assumed. This section will explain the mathematical procedure involved in GGA, details of equations and its application to ADFP produced preforms.

4.2.1 Formulation

Todini and Pilati (1987) [147] formulated a system of equations for water networks by writing conservation of energy for each pipe, resulting in a set of *npipe* equations containing *npipe* flow and *nnode* nodal heads as unknowns. They coupled these equations with the node equations (conservation of mass) written in terms of pipe flow to form a set of *npipe* together with *nnode* equations for an equal number of unknowns. The method is known as the gradient method approach. This method is also used for gas networks by Hamam and Brameller (1972) [146] and Osiadacz (1991).

Example network
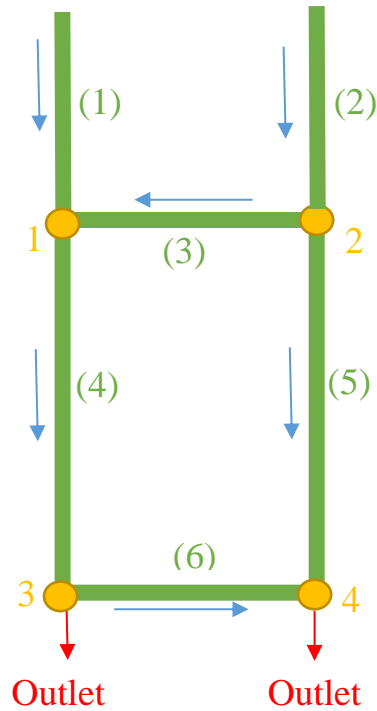
Figure 60 - Schematic of simple gap network

For the six-pipe network shown in the Figure 60, the set of equations includes one equation for each node and each pipe. Initially the direction of pipe flow can be arbitrarily assumed, and a system of equations are derived from two fundamental physical laws that are used to determine the unknowns in a network.

1. Conservations of Mass (Kirchhoff's 1st law)

   The sum of all the flows (known or unknown) at each junction within the network must be equal to zero (ie no fluid can be lost or acquired).

   $$\text{Node 1: } Q_1 + Q_3 - Q_4 - q_1 = 0$$

   $$\text{Node 2: } Q_2 - Q_3 - Q_5 - q_2 = 0$$

   $$\text{Node 3: } Q_4 - Q_6 - q_3 = 0$$

   $$\text{Node 4: } Q_5 + Q_6 - q_4 = 0$$

The pipe equations can be written for each pipe with the nodal heads and pipe flow. The friction loss equation is given a positive sign, so the node has a negative sign for the upstream source node and positive for the downstream node of the pipe.

2. Conservation of Energy (Kirchhoff's 2nd law)

   the net change in energy around any closed loop must equal zero.

   3. Pipe 1: $K_1|Q_1|^n + H_1 - H_{source} = 0$

   4. Pipe 2: $K_2|Q_2|^n + H_2 - H_{source} = 0$

   5. Pipe 3: $K_3|Q_3|^n + H_1 - H_2 = 0$

   6. Pipe 4: $K_4|Q_4|^n + H_3 - H_1 = 0$

   7. Pipe 5: $K_5|Q_5|^n + H_4 - H_2 = 0$

   8. Pipe 6: $K_6|Q_6|^n + H_4 - H_3 = 0$

Where all the K and H_{source} are known, $|Q_1|^n$ represents the absolute value of the pipe flow 1.. The sign of the flow direction is applied to the head loss term. The flow signs are applied in the node equations as well. Thus, the solution will yield a negative flow and defines a flow is in the opposite direction rather than the initial assumption. Therefore, in the example given above, conservation of mass and energy comprise seven equations written with respect to six pipe flows and four nodal heads.

Todini and Pilati (1987) generalized this formulation into a matrix form. Conservation of energy (in the pipes) and mass (at the nodes) equations can be written matrix form as:

$$[A]^{n \times n} \begin{bmatrix} \Delta Q \\ \Delta H \end{bmatrix} = \begin{bmatrix} -dE \\ -dq \end{bmatrix} \tag{15}$$

Where (A) matrix consists of four sub matrices,

$$[A]^{n \times n} = \begin{bmatrix} A_{11} & A_{12} \\ A_{21} & A_{22} \end{bmatrix} \tag{16}$$

A_{11} Is a diagonal matrix and defined as,

$$A_{11} = \begin{bmatrix} nK_1|Q_1|^{n-1} & \cdots & 0 \\ \vdots & \ddots & \vdots \\ 0 & \cdots & nK_{npipe}|Q_{npipe}|^{n-1} \end{bmatrix} \quad (17)$$

A_{21} Is the connectivity matrix representing the connection of pipes in the network and each column in the matrix corresponds to a pipe and row to a node. If the fluid is flowing towards the node, 1 is assigned and if the fluid is flowing away from the node -1 is assigned. If the pipe is not connected to a specific node, 0 is assigned to it. For the six-pipe network shown in the Figure 60 above, A_{21} should look as follows:

$$Pipe1 \quad Pipe2 \quad Pipe3 \quad Pipe4 \quad Pipe5 \quad Pipe6$$

$$A_{21} = \begin{matrix} Node\ 1 \\ Node\ 2 \\ Node\ 3 \\ Node\ 4 \end{matrix} \begin{bmatrix} 1 & 0 & 1 & -1 & 0 & 0 \\ 0 & 1 & -1 & 0 & -1 & 0 \\ 0 & 0 & 0 & 1 & 0 & 1 \\ 0 & 0 & 0 & 0 & 1 & 1 \end{bmatrix}$$

$$A_{21} = \begin{bmatrix} 1 & 0 & 1 & -1 & 0 & 0 \\ 0 & 1 & -1 & 0 & -1 & 0 \\ 0 & 0 & 0 & 1 & 0 & 1 \\ 0 & 0 & 0 & 0 & 1 & 1 \end{bmatrix} \; and \; A_{12} = A_{21}^T = \begin{bmatrix} 1 & 0 & 0 & 0 \\ 0 & 1 & 0 & 0 \\ 1 & -1 & 0 & 0 \\ -1 & 0 & 1 & 0 \\ 0 & -1 & 0 & 1 \\ 0 & 0 & 1 & 1 \end{bmatrix}$$

A_{22} Is a null matrix.

A Newton-type solution scheme is applied to the system of equations yielding:

$$n\, A_{11}\, \Delta Q^{(m)} + A_{12}\, \Delta H^{(m)} = -dE$$

$$A_{21}\, \Delta Q^{(m)} = \text{-dq}$$

$$(18)$$

This set of equations is solved for ΔQ and ΔH. Where, $H^{(m)}$ and $Q^{(m)}$ for the following iteration is updated by:

$$H^{(m)} = H^{(m-1)} + \Delta H^{(m)}$$

$$Q^{(m)} = Q^{(m-1)} + \Delta Q^{(m)}$$

(19)

4.2.1.1 Darcy-Weisbach pressure and flow rate relationship

For water network analysis, the Hazen-Williams approach is usually used for the head-loss relationship such as used in [144, 147, 148, 158, 159]. Since Hazen-Williams approach is only applicable in the case of water, the relationship needs to be replaced with equation suitable for other fluids. The Darcy-Weisbach pressure relationship is widely used and can replace the Hazen-Williams equation, where pressure drop can be given by;

$$\Delta P = \frac{\rho V^2 L}{2 D_h} f$$

(20)

Where, ρ = Density , V = Velocity , L = Length of pipe ,Dh = Hydraulic diameter ,f = Darcy friction factor

For Laminar flow, the friction factor can be given by,

$$f = \frac{72.92}{R_e}$$

(21)

Where Re = Reynolds number, can be given as

$$R_e = \frac{\rho D_h V}{\mu}$$

(22)

Where, ρ = density, D_h = hydraulic diameter, V = velocity, μ = viscosity

By substituting equation (*20*) & (*21*) we get,

$$f = \frac{72.92}{\frac{\rho D_h V}{\mu}} = 72.92 \times \frac{\mu}{\rho D_h V}$$

(23)

109

Friction factor can be substituted into equation (*20*)

$$\Delta P = \frac{\rho\, V^2 L}{2\, D_h} \times \frac{72.92\, \mu}{\rho\, D_h\, V}$$

$$\Delta P = \frac{72.92\, \mu\, L}{2\, D_h^2}\, V$$

$$\Delta P = \frac{72.92 \mu\, L}{2\, D_h^2}\, \frac{Q}{A}$$

$$\Delta P = K_{resistance} Q \qquad\qquad\qquad (24)$$

Units: $\text{L} = \text{m}, \text{V} = \frac{m}{s}, \text{Q} = \frac{m3}{s}, \Delta P = pascals, \mu = Pa.\text{s}$

The pressure relation applicable to different fluids have been successfully replaced in gradient algorithm. Once the resistance of each pipe is calculated, the network data will be required in order to execute the gradient algorithm. For experimental work in previous chapter, Cornish's model was used to predict permeability of a gap with different widths. However, it cannot be used in this approach as the Cornish's model predicts permeability of a gap entirely based on the shape of the gap. However the derived equation (*22*) calculates the resistance of a gap based on the geometry of the gap as well as the fluid viscosity. This will overcome the limitation of using specific fluid for the analysis.

4.2.1.2 Determining the flow rates and pressure at nodes using Global Gradient Analysis

To calculate the pressure, drop and flow rates of the pipe network shown in Figure 60**,** the following input parameters are required:

Pressure at inlet $= 1 \times 10^5\ pascals$ & Flow rate at outlet $= 1.33 \times 10^{-6}\ {m^3}/{s}$

A random initial guess of Q for each pipe and Pressure for each node is made. It has been observed that the solution is not highly affected by the initial guess of pressure, whereas the

convergence rate highly depends on an initial guess of Q'. The solution will take more iterations

to converge if the initial value of Q is far away from the final flow rate in the pipes.

K(resistance) can be calculated using the formula given in the previous section.

Node	Pressure (Initial guess)
1	30
2	35
3	45
4	60

Table 13 - Pressure guess to start the numerical model

Pipe	width (m)	height (m)	Length (m)	Initial guess of Q (m^3/s)	K (Resistance)
1	0.001	0.00022	1	5.02E-08	1.33E+15
2	0.001	0.00022	1	5.03E-08	1.33E+15
3	0.001	0.00022	0.00635	3.02E-07	8.41E+12
4	0.001	0.00022	1	1.25E-07	1.33E+15
5	0.001	0.00022	1	1.50E-07	1.33E+15
6	0.001	0.00022	0.00635	2.01E-07	8.41E+12

Table 14 - Specifications, initial flow rate guess and calculated resistance of gaps

The values can be substituted into the following equation:

$$[A]^{n \times n} \begin{bmatrix} \Delta Q \\ \Delta H \end{bmatrix} = \begin{bmatrix} -dE \\ -dq \end{bmatrix} \tag{25}$$

$$
\begin{bmatrix}
1.33E+8 & 0 & 0 & 0 & 0 & 0 & 1 & 0 & 0 & 0 \\
0 & 1.33E+8 & 0 & 0 & 0 & 0 & 0 & 1 & 0 & 0 \\
0 & 0 & 5.07E+8 & 0 & 0 & 0 & 1 & -1 & 0 & 0 \\
0 & 0 & 0 & 3.33E+8 & 0 & 0 & -1 & 0 & 1 & 0 \\
0 & 0 & 0 & 0 & 4E+8 & 0 & 0 & -1 & 0 & 1 \\
0 & 0 & 0 & 0 & 0 & 3.38E+6 & 0 & 0 & 0 & 1 \\
1 & 0 & 1 & -1 & 0 & 0 & 0 & 0 & 0 & 0 \\
0 & 1 & -1 & 0 & -1 & 0 & 0 & 0 & 0 & 0 \\
0 & 0 & 0 & 1 & 0 & 1 & 0 & 0 & 0 & 0 \\
0 & 0 & 0 & 0 & 1 & 1 & 0 & 0 & 0 & 0
\end{bmatrix}
\begin{bmatrix}
\Delta Q_1 \\ \Delta Q_2 \\ \Delta Q_3 \\ \Delta Q_4 \\ \Delta Q_5 \\ \Delta Q_6 \\ \Delta P_1 \\ \Delta P_2 \\ \Delta P_3 \\ \Delta P_4
\end{bmatrix}
=
\begin{bmatrix}
K_1|Q_1|^n + P_1 - P_{source} \\
K_2|Q_2|^n + P_2 - P_{source} \\
K_3|Q_3|^n + P_1 - P_2 \\
K_4|Q_4|^n + P_3 - P_1 \\
K_5|Q_5|^n + P_4 - P_2 \\
K_6|Q_6|^n + P_4 - P_3 \\
Q_1 + Q_3 - Q_4 - q_1 \\
Q_2 - Q_3 - Q_5 - q_2 \\
Q_4 - Q_6 - q_3 \\
Q_5 + Q_6 - q_4
\end{bmatrix}
$$

$$
\begin{bmatrix}
1.33E+8 & 0 & 0 & 0 & 0 & 0 & 1 & 0 & 0 & 0 \\
0 & 1.33E+8 & 0 & 0 & 0 & 0 & 0 & 1 & 0 & 0 \\
0 & 0 & 5.07E+8 & 0 & 0 & 0 & 1 & -1 & 0 & 0 \\
0 & 0 & 0 & 3.33E+8 & 0 & 0 & -1 & 0 & 1 & 0 \\
0 & 0 & 0 & 0 & 4E+8 & 0 & 0 & -1 & 0 & 1 \\
0 & 0 & 0 & 0 & 0 & 3.38E+6 & 0 & 0 & 0 & 1 \\
1 & 0 & 1 & -1 & 0 & 0 & 0 & 0 & 0 & 0 \\
0 & 1 & -1 & 0 & -1 & 0 & 0 & 0 & 0 & 0 \\
0 & 0 & 0 & 1 & 0 & 1 & 0 & 0 & 0 & 0 \\
0 & 0 & 0 & 0 & 1 & 1 & 0 & 0 & 0 & 0
\end{bmatrix}
\begin{bmatrix}
\Delta Q_1 \\ \Delta Q_2 \\ \Delta Q_3 \\ \Delta Q_4 \\ \Delta Q_5 \\ \Delta Q_6 \\ \Delta P_1 \\ \Delta P_2 \\ \Delta P_3 \\ \Delta P_4
\end{bmatrix}
=
\begin{bmatrix}
1.00E+05 \\
1.00E+05 \\
4.24 \\
-3.59E+01 \\
-5.51E+01 \\
-1.53E+01 \\
-2.26E-07 \\
4.02E-07 \\
1.41E-06 \\
9.78E-07
\end{bmatrix}
$$

$[\Delta Q | \Delta P]^T = [1.28E-6 \quad 1.28E-6 \quad -1.92E-7 \quad 1.31E-6 \quad 1.07E-6 \quad -9.24E-8 \mid 9.980E+4 \quad 9.79E+4 \quad 9.932E+4 \quad 9.931E+4]$

$[Q | P]^T = [1.33E-6 \quad 1.33E-6 \quad 1.09E-7 \quad 1.44E-6 \quad 1.22E-6 \quad 1.09E-7 \mid 9.983E+4 \quad 9.983E+4 \quad 9.937E+4 \quad 9.937E+4]$

For the next iteration, flow rates and pressure can be updated, exact steps are followed, and the iteration resumes until the solution is converged. The graph below shows the convergence of both pressure and flow rates in the pipe network.
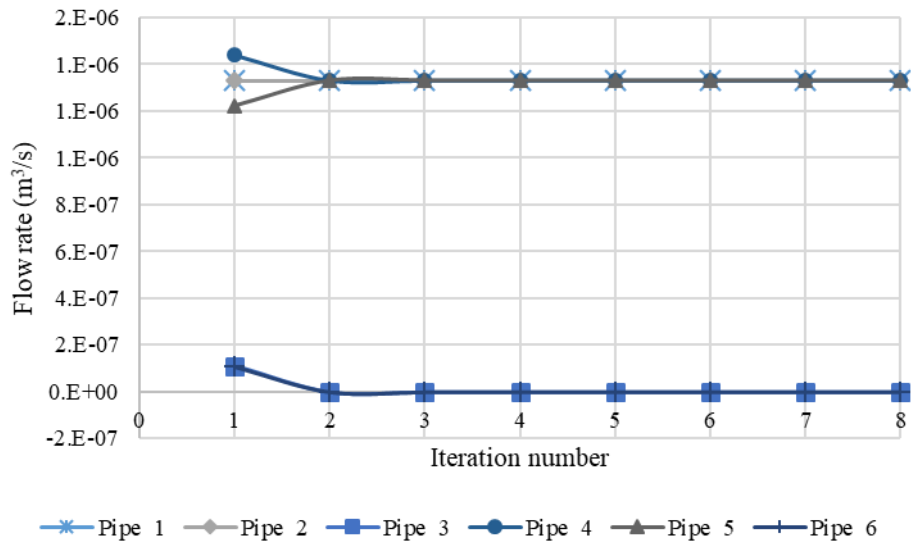

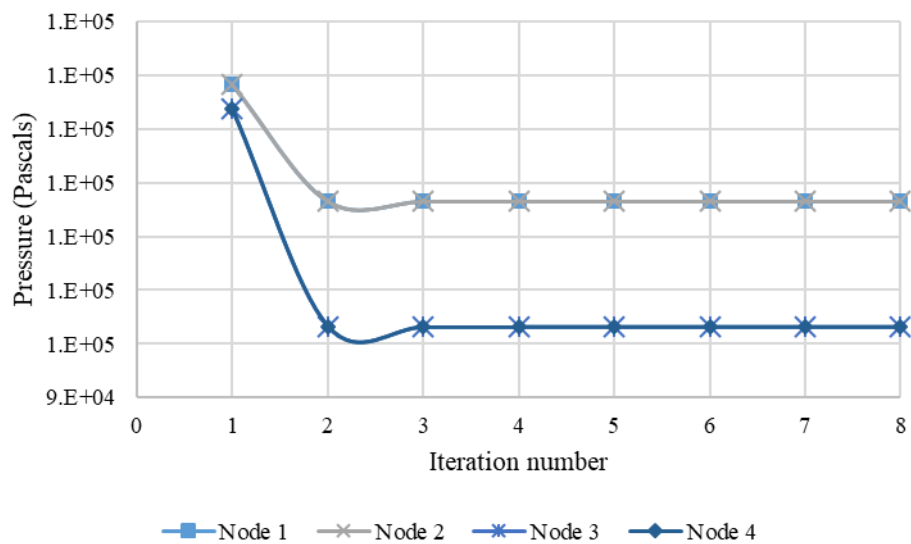Figure 61 - The flow rate (m^3/s) convergence of solution through iteration process using GGA.

Figure 62 – Nodal pressure (Pa) convergence of solution through iteration process using GGA. Nodes 1 and 3 has exact same pressure as Nodes 2 and 4.

4.2.1.3 Process Flow chart

The process flow chart shown in Figure 63 shows the input data that will be required to execute the GGA code. The network flow rate is the total flow rates in the inlet gaps, pressure at inlet, and the viscosity of fluid that is injected and max number of iterations that can be changed per simulation to minimize computational time. Once the max number of iteration is reached the code uses the latest pressure data at the inlet and outlet nodes to compute the permeability of the layer. It prints the convergence graph for the user to confirm the convergence of solution and displays the fill time and permeability of the layer.
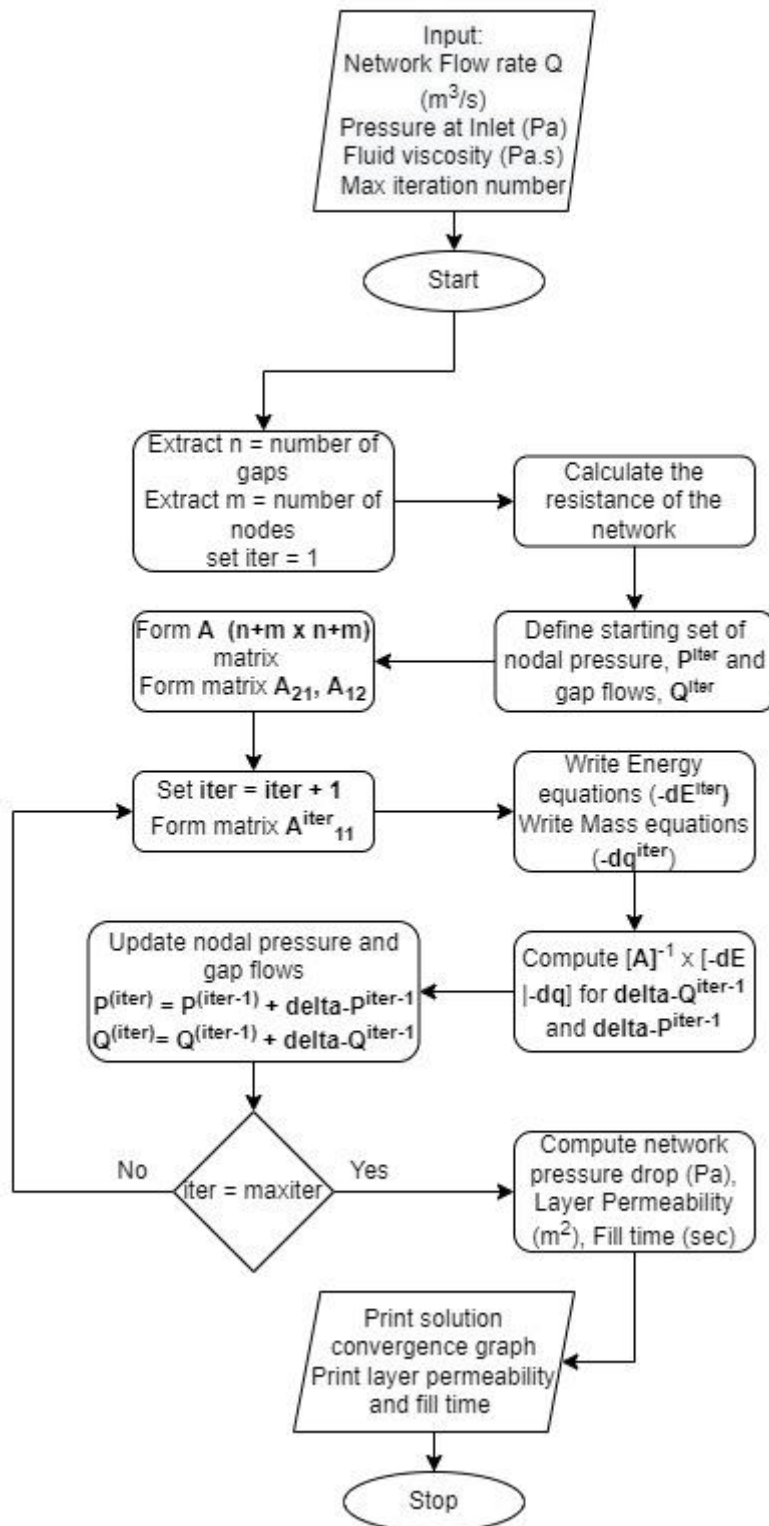
Figure 63 - Detailed flow chart of Global Gradient Analysis (GGA) algorithm

4.2.1.4 Computing layer permeability using results from GGA

Once the solution successfully converges and the flow rates in gaps and pressure at nodes are acquired using GGA method, the overall layer/preform permeability needs to be computed. To calculate the layer permeability, the following equation is used:

$$K = \frac{\mu L}{\Delta P} \frac{Q}{A} \tag{26}$$

Where, μ (Pa.s) is viscosity of the fluid, L (m) is the length of the layer/preform, Q (m^3/s) is the network flow rate, ΔP (Pa) is the pressure drop computed through GGA and A (m^2) is the cross-sectional area of the layer.

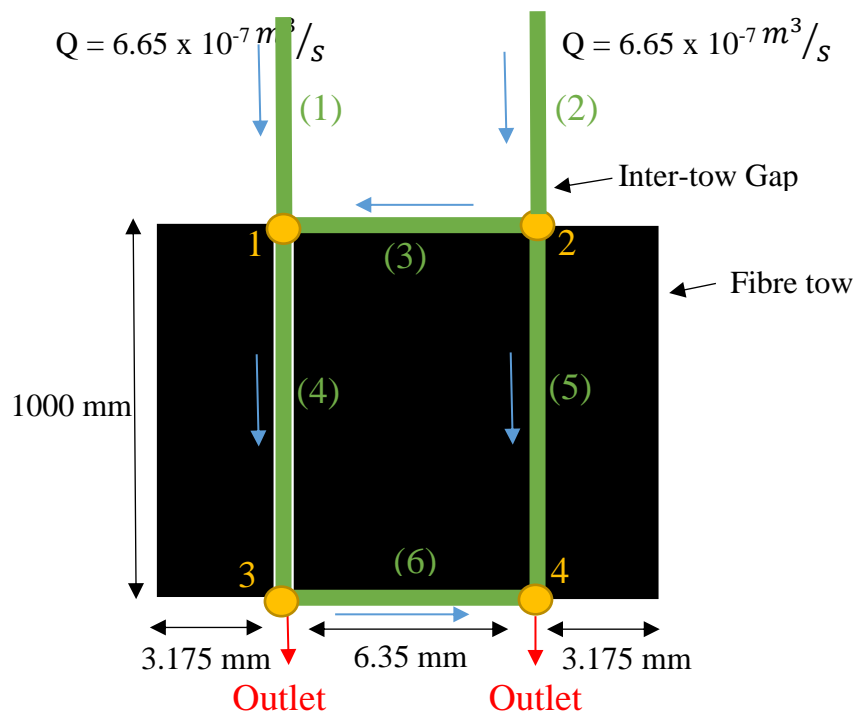
Figure 64 - Schematic and flow description of two gap network model

Network flow rate = 6.65 x 10^{-7} m^3/s + 6.65 x 10^{-7} m^3/s = 1.33 x 10^{-6} m^3/s

Cross sectional area of the layer (tow tows + two 1mm gaps) = (6.35mm +6.35mm + 2mm) × 0.22mm = 3.23 × 10^{-6} m^2

Pressure drop = 881.17 MPa

Viscosity = 1.04 Pa.s

Length = 1m

Substituting the values into the equation above:

$$K_{layer} = 2.43E\text{-}10 \ m^2$$

4.3 Code development of network formation and network analysis

A numerical code is developed to generate preform design with different gap specifications and assess their corresponding global flow behaviour. As it shown earlier that the gaps form a vascular network inside the preform. The GGA method which is also highly used in WDM will be used to assess the flow behaviour in these gaps. The numerical code is written using MATLAB R2018a. The code consists of 4 main stages: Network formation, formation of mass and energy equations, global gradient analysis and visualization of the flow behaviour in the network. Two different approaches have been adopted for network formation. The first approach automatically generates a rectilinear preform based on a few input parameters. The second approach is designed to incorporate real gap width data in the form of a CSV file. Files are generated from the physical deposition hardware and are used as input data to generate a gap network. The details and results acquired from the first approach, the automated network formation are discussed in this section.

4.3.1 Automated network formation Approach

A minimum number of inputs are used to form a network. The required inputs are the following:

Course width = distance between each gap in a layer (gap after 1 tow, 2 tow or 8 tows etc)

Length = length of the layer

Width = total width of a layer

Lay-up sequence = orientation of layer

Thickness = thickness of the layer

Based on the inputs, the gap network is calculated and the network graph can be plotted. For example, if a gap is designed after every tow for a 5 layer thick laminate with the following specifications:

Input Parameter	Value
Course-width (mm)	6.35 (gap after every tow)
Length (mm)	100
Width (mm)	12.7
Layup sequence	[45;0;-45;90]
Thickness (mm)	0.22

Table 15- Example of input parameters required to generate a rectangular preform

From these inputs, simple lines are generated for each layer using the information in the layup sequence and a graph is generated as shown in Figure 65 (left).
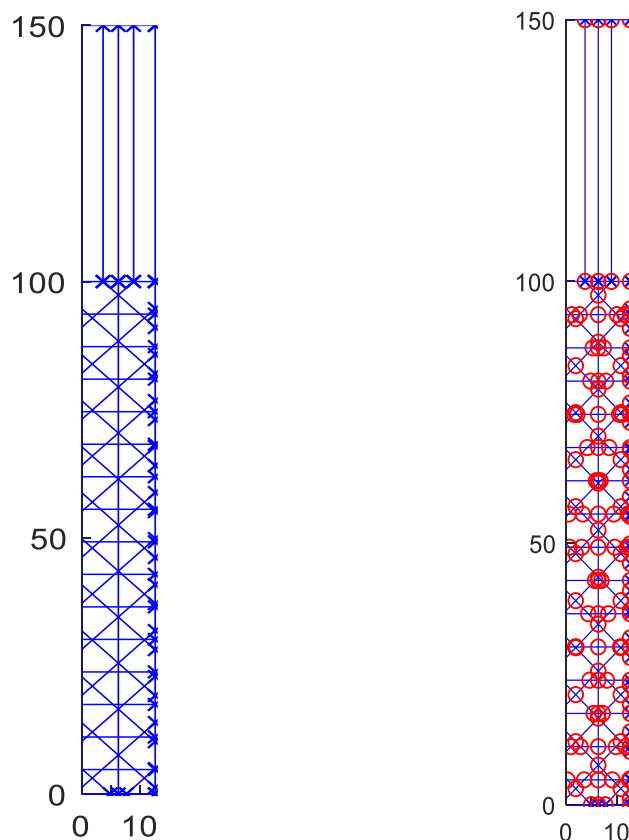

Figure 65 - Generated lines using the input parameters (left), intersection points identified in Matlab marked in red circles (Right)

Once the lines have been generated, the point of intersections for each line and its coordinates needs to be identified. This is achieved by using the polyxpoly command in Matlab [160] to identify the intersections' points and save their coordinates into a new array called coordinates. Moreover, the number of lines which are intersecting are also saved into the coordinates array. This will be used later to form a graph network. Another function in Matlab, Mapshow, is used to highlight each of these intersection points with red marker, as shown in Figure 65 (right).

To convert this line graph into a graph network, these intersection points are converted into nodes and two new arrays are formed to act as the source and target. Each coordinate is given a node number. The program then picks each coordinate in the coordinate array and loops through the rest of the array to check if similar line numbers are intersecting with any other coordinate. When it finds the similar line numbers intersecting for any other coordinates, it transfers the picked coordinate number (node) to the source array, and the identified coordinate number (node) to the target array.

At this stage, it also measures the distance between the two coordinates and updates the length of the gap and stores its thickness as well. Once the program loops through the complete coordinate array, the information is stored into five new arrays: source, target, distance, length and thickness. Each row of source and target array represent a gap in the network and the rest of the arrays represent its corresponding properties. Using the Source and Target arrays, a graph network can be produced to visualize the network formed using the designed input parameters as shown in Figure 66.
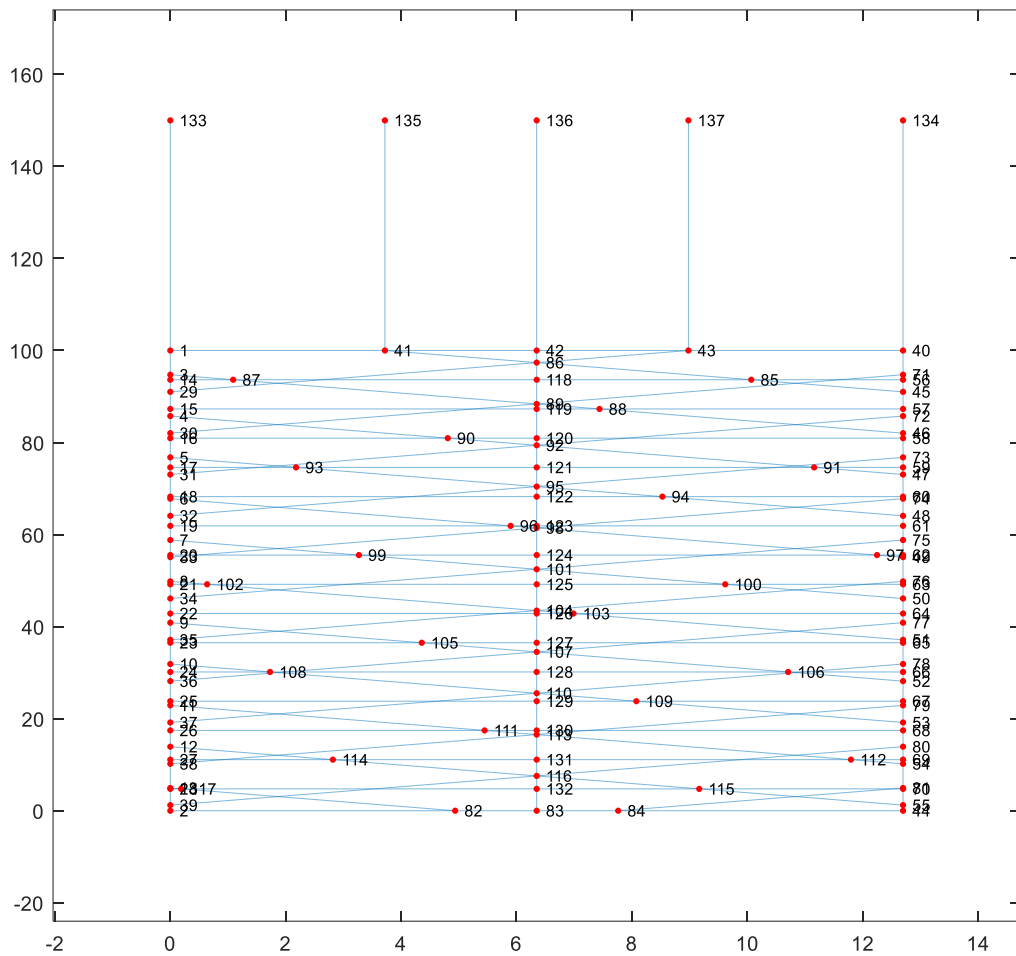
Figure 66 - Graph network generation where red dots represent the nodes/intersections and blue lines are the edges/gaps

4.3.1.1 Process flow chart

The flow chat in Figure 67 shows the each step of the network formation code. It can be observed that only 7 input parameters are required to run the code. It includes course to course width, the designed gap width, the width of the inlet gaps, standard deviation in real gap width data, the layer layup sequence and tolerance value to merge any nodes. The flow chart also exhibits the final output data that is produced by the code for the next part of model.
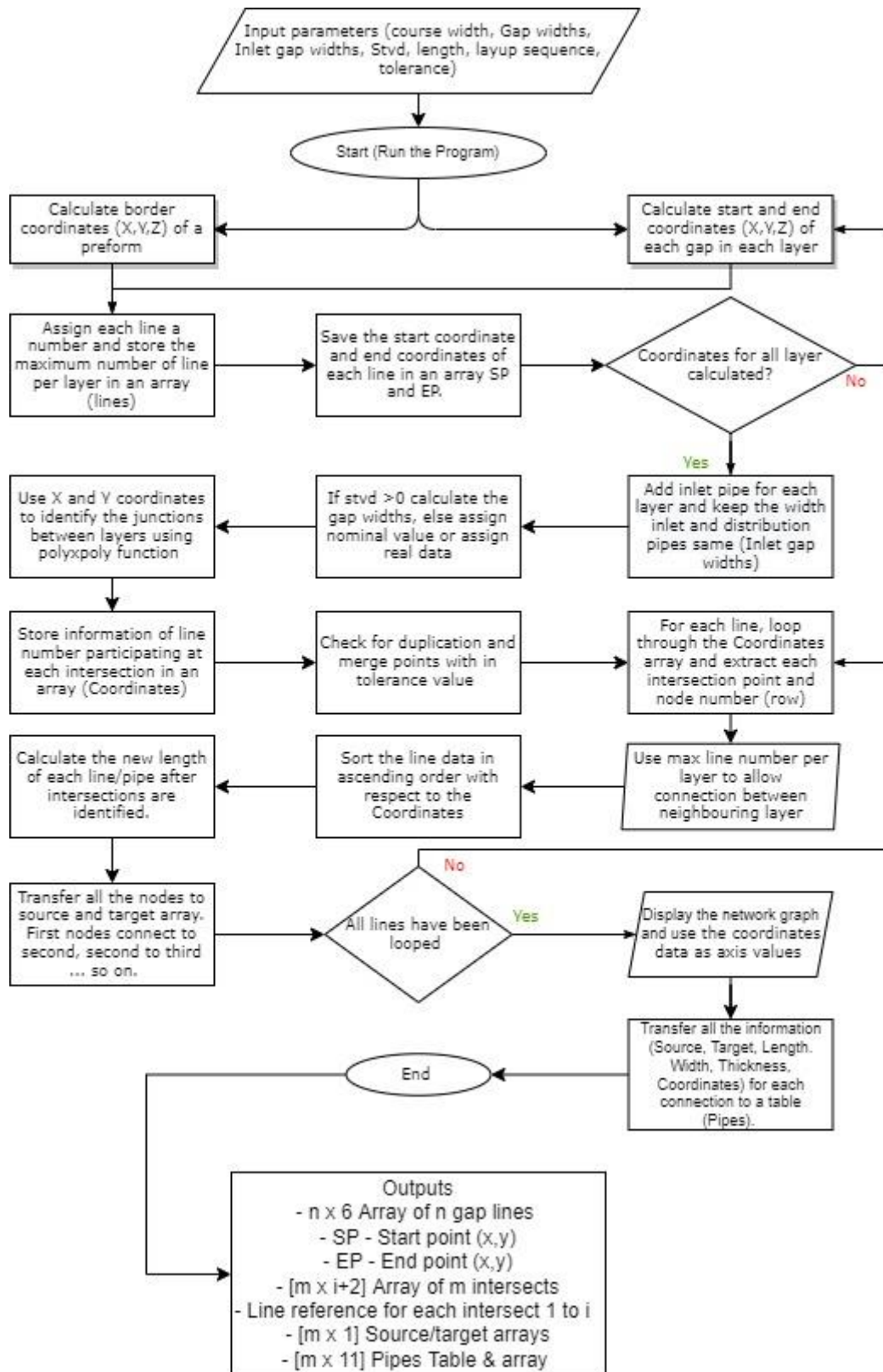
Figure 67 - Detailed flow chart of steps in network formation process

4.3.2 Formation of mass and energy equations in code

To write equation for each of the nodes and edges in the graph network, the edges in the graph are labelled for ease of identification and extracting relevant information. An algorithm known as Breadth First Search (BFS) is adopted. BFS is an algorithm for searching a tree-formatted data for a node. The BFS algorithm searches for nodes by travelling through the child nodes level by level as shown in Figure 68.
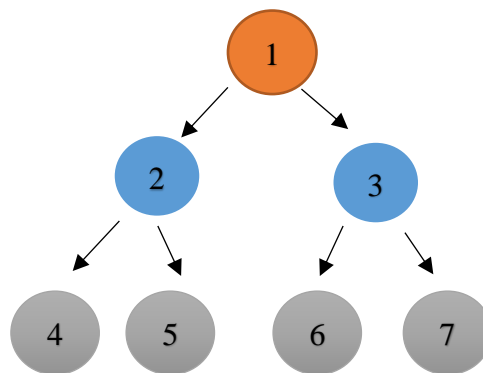

Figure 68 - Breadth First Search (BFS) algorithm method of exploring nodes

As the algorithm searches for the nodes through the edges (pipes), it labels each of the edges involved in the network. This information is stored into another array (A) representing node numbers connected by unique edge number. From this array (A) the number of edges a single node is connected to can be identified and therefore equation of continuity can be easily written. A random direction of flow can be assigned to all of the edges as long as it follows the law of continuity (sum of influx and sum of outflux = 0). The detailed flow chart (Figure 70) shows the continuity equation extraction process. At this stage, a new table is created to store all the information of each gap to access the information when required. The table contains the following information.

Source Node	Target Node	Edge Number	Length (m)	Width (m)	Thickness (m)	Gap Cross-sectional Area	Gap Parameter	Hydraulic Radius	Resistance

Table 16 - Information stored about each gap in a table (Gap properties)

At this stage, GCA is conducted by introducing a few more inputs. It requires a random guess for flow rate in each pipe. A random array is generated for flow rates during the first iteration. To keep the number of iterations required to converge the solution minimum, the random flow rates are generated using the assigned outflow from the network. Viscosity of fluid is required and finally maximum number of iteration can be assigned. Some network design can be converged in very few iterations and as long as the solution is converged, the program can be stopped. The number of iterations required depends on the complexity of the network design. Also higher number of iterations means the code will take longer to converge. The number of iterations can be adjusted before running the program as shown in Figure 69. Once all of the information is collected, the program starts formulating the GGA equations as the flow chart shows in Figure 63. After the solution converges, the pressure drop across the model is calculated and permeability is computed.
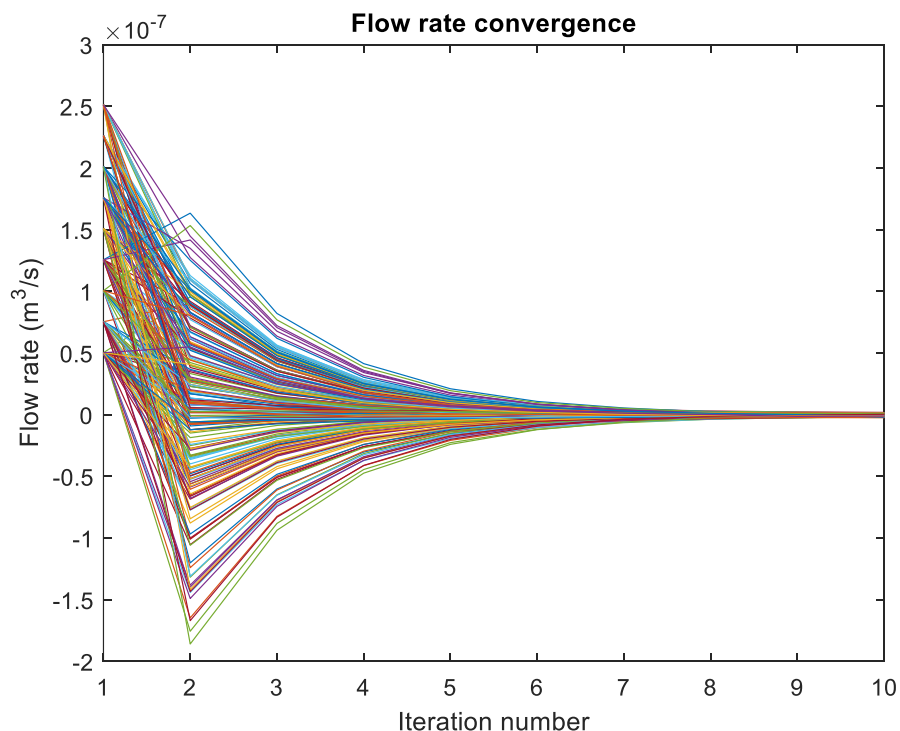
Figure 69 - Convergence graph shows the solution is converged before the 10th iteration therefore maximum number of iterations for such designs can be 10 instead of 30

4.3.2.1 Process flow chart

The steps used to successfully formulate the energy and mass equations in each iterations are shown in the Figure 70. The number and information of edges connected to each node is first gathered, random direction of flow is assigned to each edge and a check is done to ensure continuity of flow. Based on the assigned direction mass and energy equations are written for each edge and node within the network.
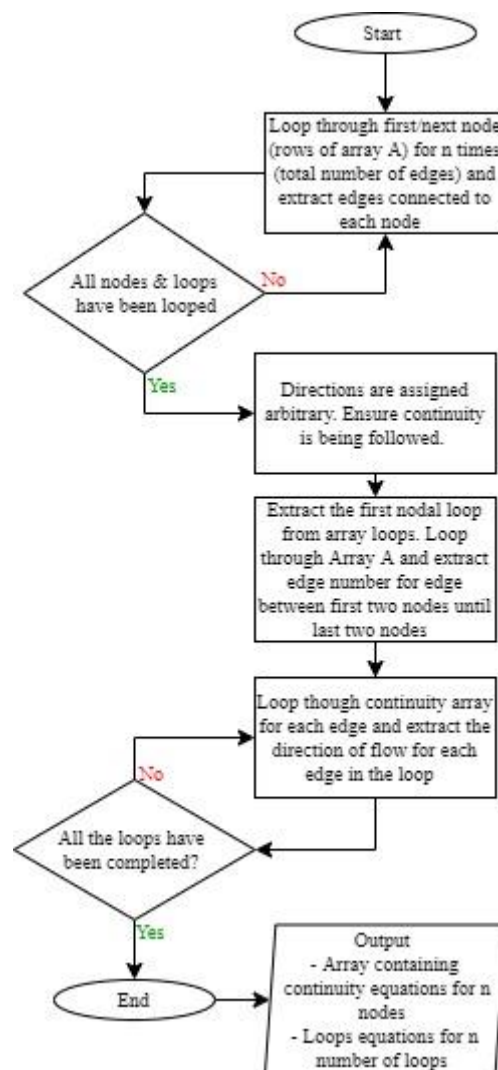

Figure 70 - Extraction of continuity equations from the graph network

125

4.3.3 Visualization of the Network

As the solution converges and the corrected flow rates are acquired, the information for flow rates in gaps and pressure at nodes is stored in relevant arrays. For a complex network, it can be difficult to understand through the numbers which area of the network is exhibiting slowest or fastest flow. To visualize the behaviour of flow in a network, different functions have been implemented:

A- Line weight representing the gap width and producing directed graph.

The weight of the line in the graph is adjusted to represent the physical gap width. This helps to visualize the variation in gap widths across the gap network. After the solution converges, the negative flow rates shows the initial assumption of flow direction was incorrect. Hence, the flow directions are corrected for all of the gaps and based on corrected flow direction a directed version of the graph can be produced showing direction of flow in gaps as shown in Figure 71.
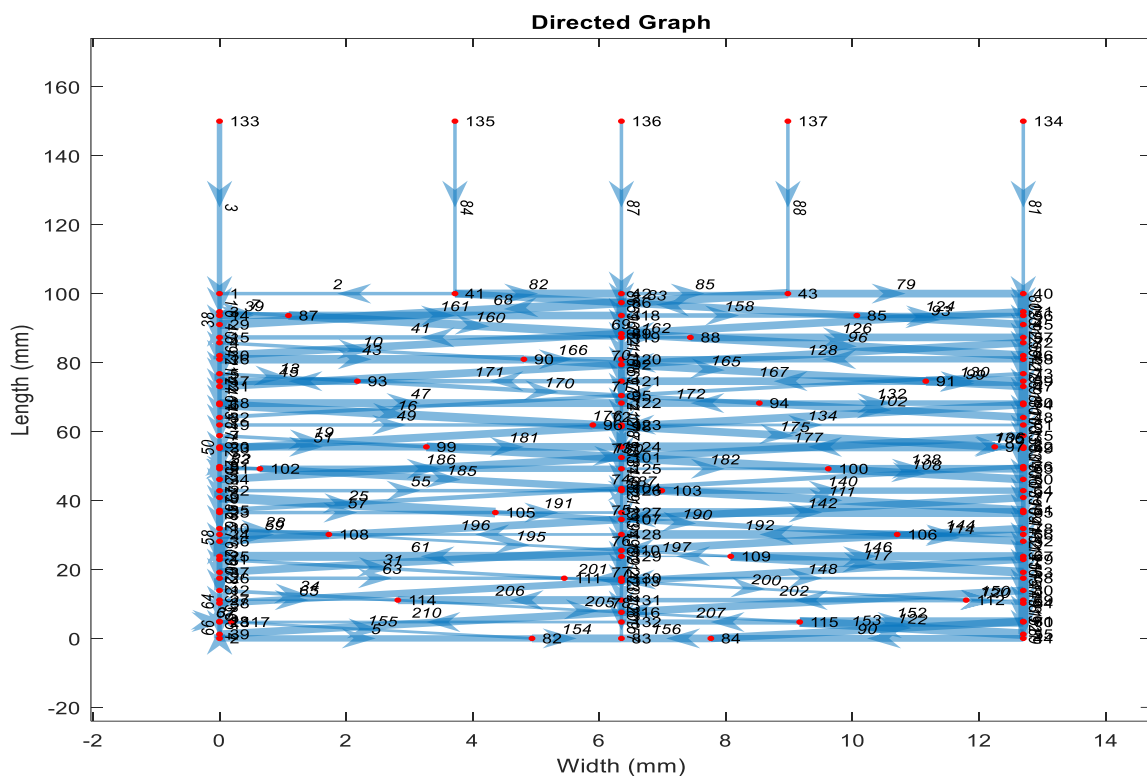

Figure 71- Directed Graph shows the direction of flow in each of the edge and with line weight reflecting the actual gap widths.

B- Colour gradient to display flow rates and pressure

Colour mapping is also implemented with the aim of enabling a user to look at the figure and easily identify the regions of highest and lowest flow rates and investigate the relevant gap properties accordingly. A similar scheme is implemented to show pressure at each node as well. Therefore, the final graph displayed at the end of the program consists of all three (line weight, directed graph and colour scheme) visualization approaches for pressure and flow rate profiles of the network as shown in Figure 72 and Figure 73.

Figure 72 - Flow rate profile of the network with constant gap width = 1mm across the network. The graph exhibits three different visualization methods implemented (line weight, direction of flow and colour mapping)
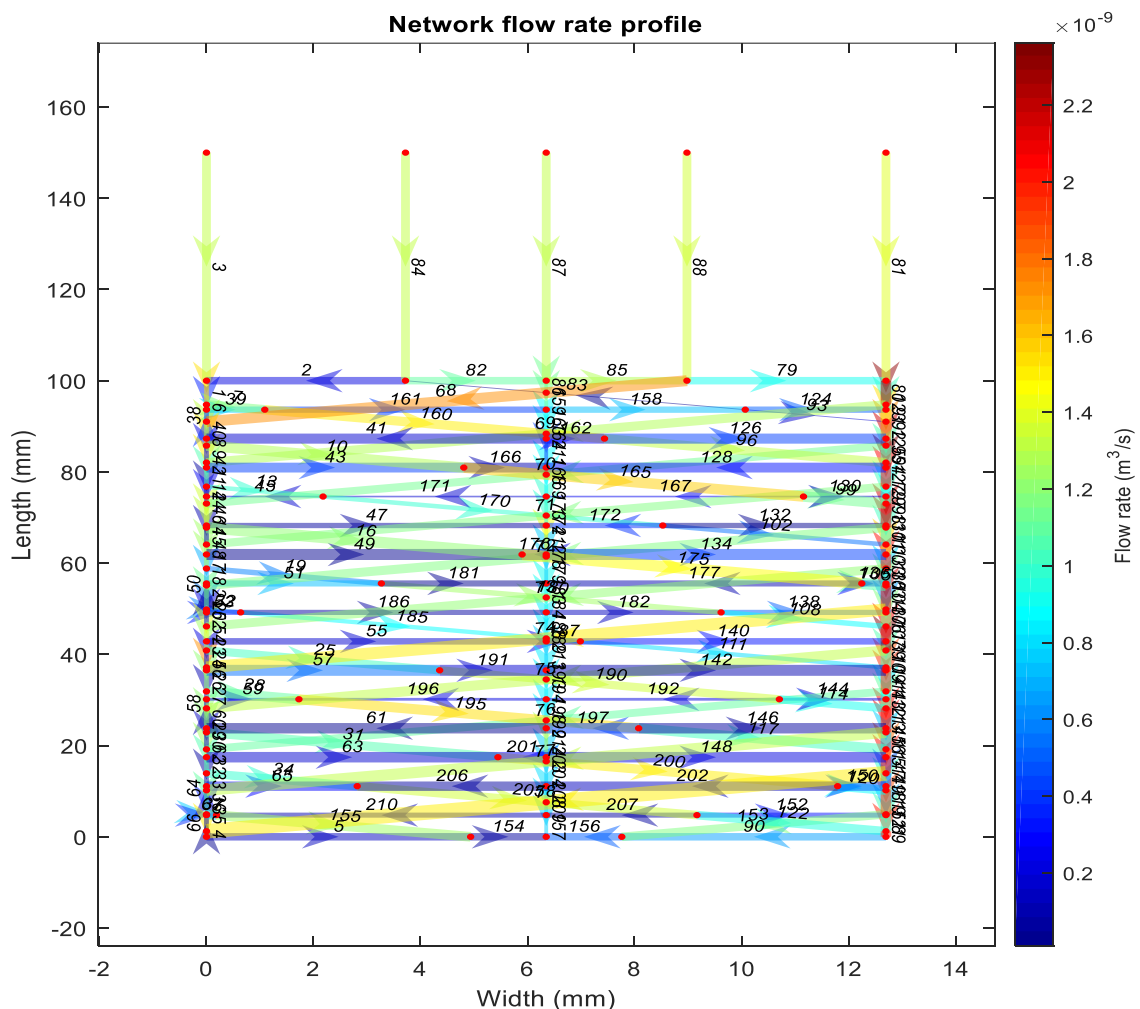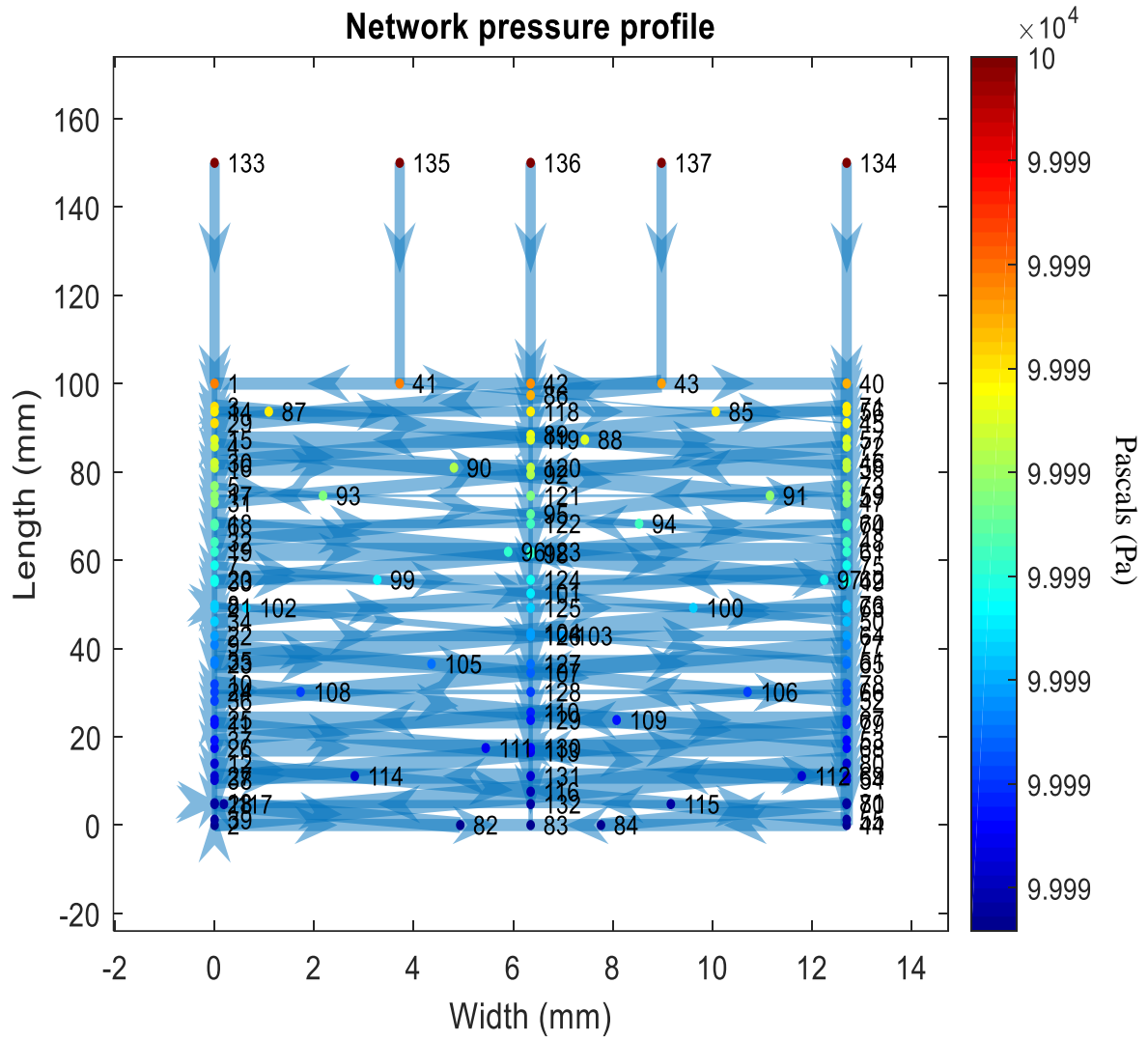
Figure 73 - Pressure profile of the network with constant gap width = 1mm across the network. The graph exhibits three different visualization methods implemented (line weight, direction of flow and colour mapping)

4.4 Results and Discussion

It has been discussed in the previous sections that global permeability highly depends on local gap widths. The developed model calculates permeability only based on gap widths in a vascular network. One can argue that this model does not include the flow in tows into the permeability predictions. Therefore, an analytical exercise is conducted to examine the magnitude of effect of flow in tow on global permeability predictions using the conventional models explained in the previous chapter. Two half tows of 3.175mm with a gap of different widths have been analysed. Two scenarios are considered for the layer shown in Figure 74 (Right), first scenario where tows are permeable and equation (*7*) is used to calculate permeability of the tow region, Equation (*8*)is used to calculate permeability of gaps with different widths (1mm to 5mm) and weighted averaging approach equation (*9*)is used to calculate homogenised layer permeability. Second scenario where tows are considered impermeable and only equation (*8*) and equation (*9*) is used to calculate layer permeability.
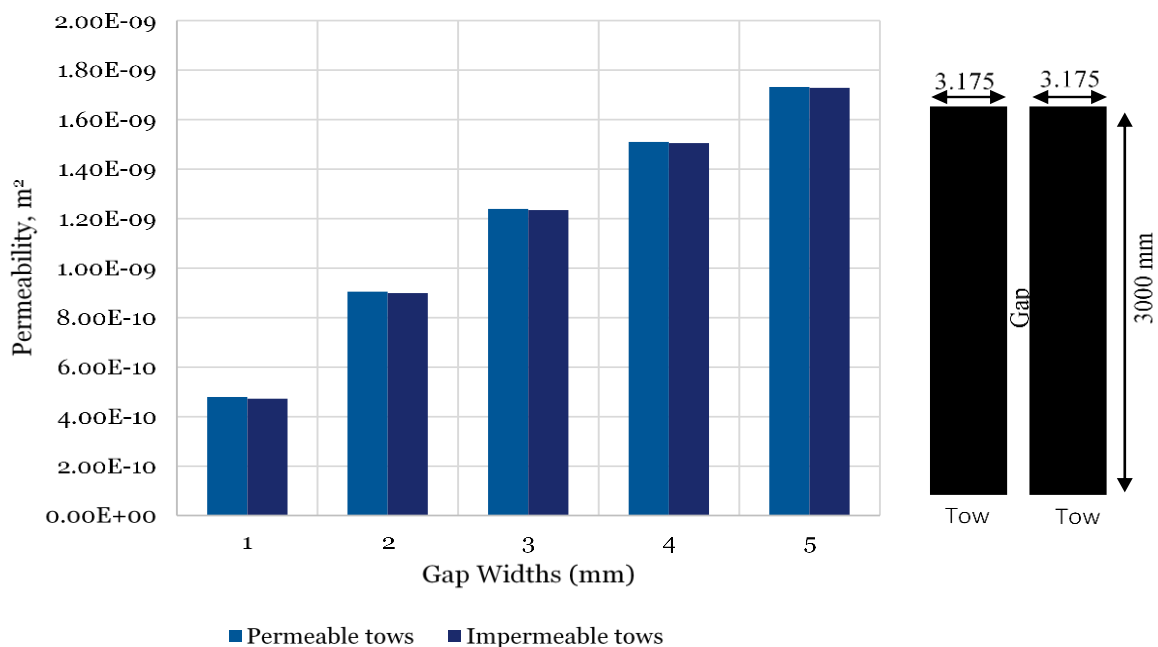

Figure 74- Global layer permeability when tows are considered permeable or impermeable shows a small difference between the tow cases (Left), schematic of layer used for the analytical investigation (Right).

The results clearly revealed that both scenarios had very little/negligible difference in all the cases with different gap widths. In presence of gap, the layer permeability is dominated by gap permeability. To check how narrow gaps can be until tow permeability significantly contributes the global permeability, layer permeability was calculated analytical for smaller gaps. Figure 75 shows a weighted average of contribution of tow and layer permeability in the layer permeability (100%). The figure shows clearly that for wider gaps widths (2mm – 5mm) tow permeability contribution is too small to be measured while for gaps width (0.3mm to 0.9mm) the tow permeability contribution to layer permeability remains below 10% and therefore can be neglected. It is only when gap widths drop below 0.2mm that tow permeability shows significant contribution. When gaps are intentionally placed after every course, widths 0.5mm or greater are sensible as any lower gap width is likely to show high variability and cause overlapping regions and change the dynamics of flow in the preform . Therefore it is concluded that tow permeability can be neglected for preforms under discussion in this work.
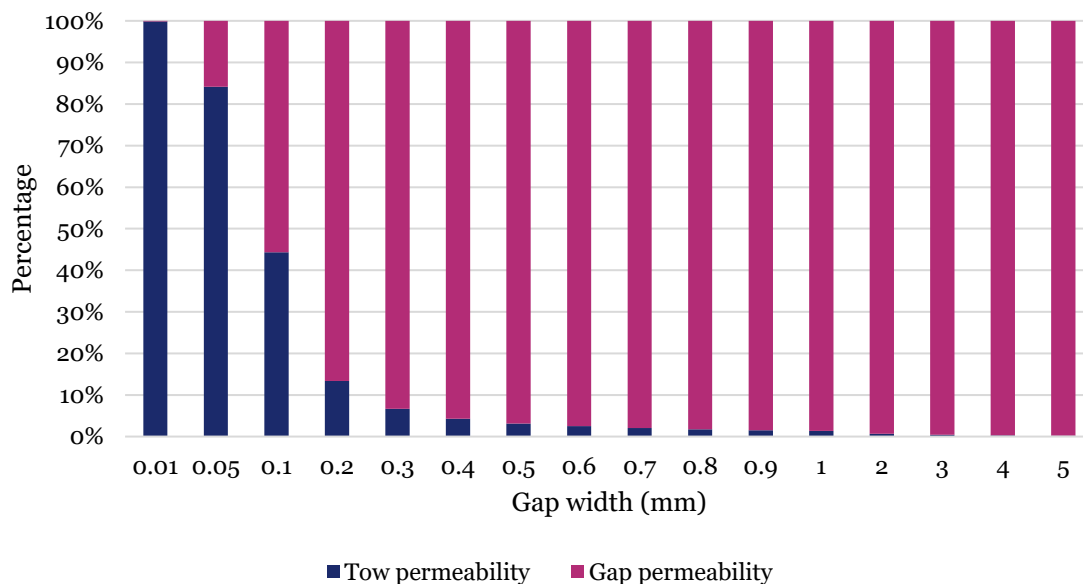
Figure 75 – A weighted averaging 100% represents layer permeability and shows contribution of sub region permeabilities (gap and tow) to overall global permeability.

4.4.1 Reconstruction of preform geometries from literature

Matveev et al. [27] & Veldnez et al. [32] investigated ADFP produced preforms with high gap volume fractions in detail. While their findings are discussed in the literature review (2.5) in detail, the data reported in their papers were used to reconstruct the preform tested as closely as possible using the network model developed in this project. In [27], Matveev et al. investigated a preform consisting of 16 layers in [0/90] direction. The nominal gap width was designed to be 1mm wide and 250mm in length. Each layer was staggered by 3.5 times the width of the tow. Therefore, the code was developed to enable staggering of layers by specified values. Figure 76 shows the reconstructed preform gap network where the connection with only neighbouring layers can be noticed. The analytical results in paper were calculated by using a nominal, an averaged, and a variable gap width data. The average value was calculated using micrographs from different sections of preform. A network model was reconstructed using both nominal and averaged values.
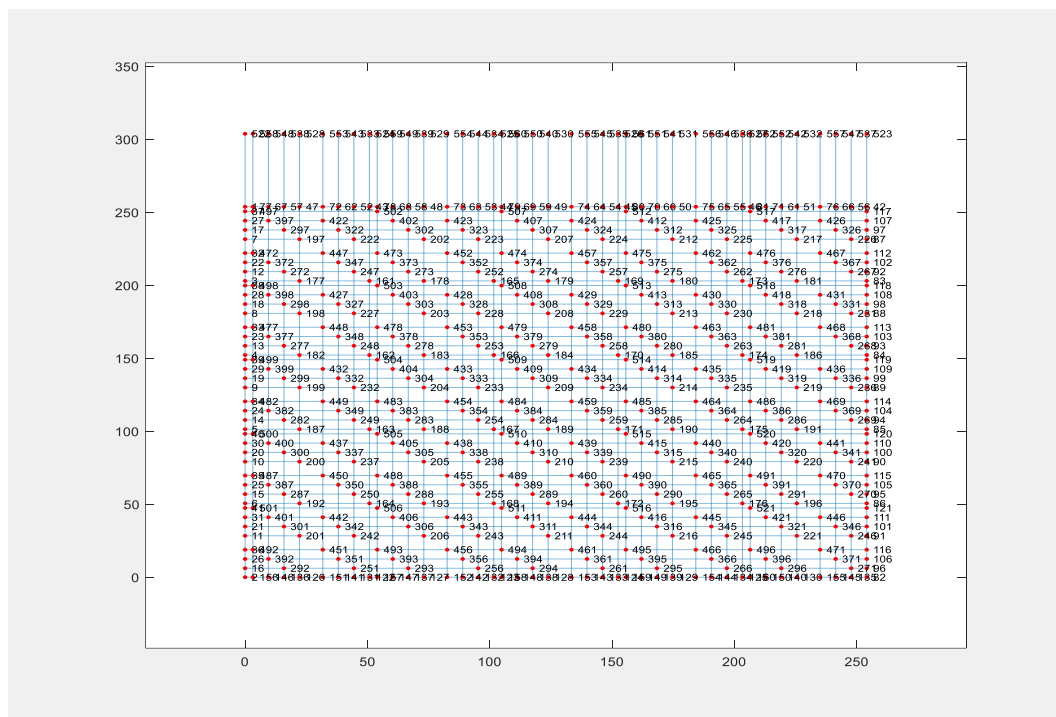

Figure 76 - Preform reconstructed by using network model based on data shared in [45]

Models	Gap width (mm)	Gap height (mm)	VGF	Permeability (In paper), 10^{-11} m^2	Permeability (Network model), 10^{-11} m^2
Designed	1.0	0.2	0.02	2.81	2.34
Averaged	0.8	0.16	0.015	1.80	1.26

Table 17- Permeability results reported by [27] and computed results by reconstructed model using network model.

Some data such as preform dimensions, exact positioning of gaps in each preform, and gap width variability data was missing in their paper. The reconstruction is likely to have some degree of difference from the original preform. The overall V_{gf} was used as a reference to the characteristics of reconstructed preform similar to the original. To incorporate the variability, standard deviation was used to generate random gap widths for the model. Therefore, the standard deviation in gap width in the model was similar to the standard deviation provided in the paper. In case of averaged gap width model, the gap widths were uniform throughout the preform. The experimental permeability was found to be $1.56 \times 10^{-11} m^2$. Table 17 shows the results from the paper and the network model. The results computed using the network model are compared with the experimental permeability. Similarly the analytical results in [27] are compared with their experimental results and Table 18 shows that even the network model was reconstructed using some estimated parameters, it yielded less difference when compared with experimental results. The designed model in paper [27] showed 80% difference while network model yielded only 49.88%. Similarly, averaged model in paper showed 15% difference while the network model showed 19.40%. This confirms that when the real preform data is used in numerical modelling, improved predictions can be expected.

	Paper [27]	Network model
Designed	80.13%	49.88%
Averaged	15.38%	19.40%

Table 18 – Percentage difference of analytical & network model results from preform tested in [27] where designed gap width was 1mm and averaged gap width was 0.8mm
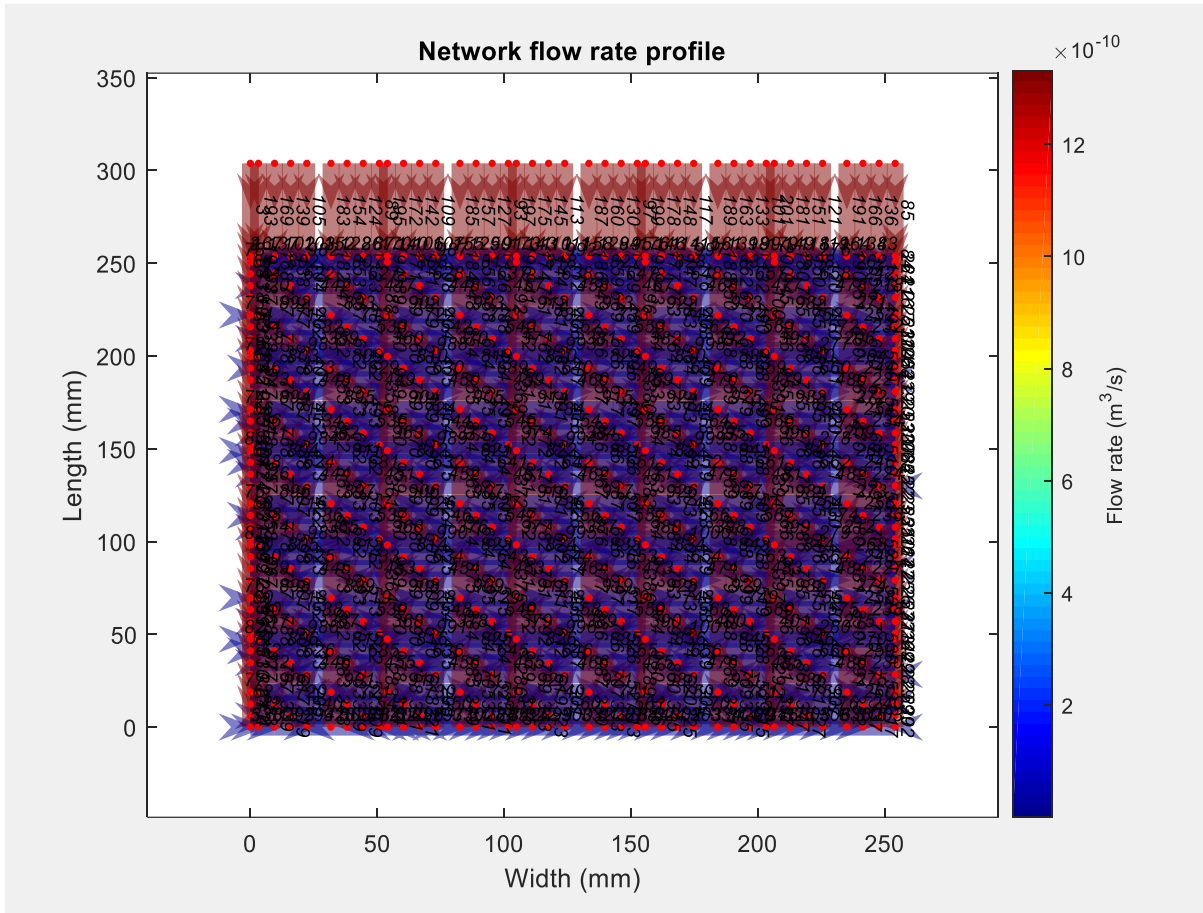
Figure 77- Flow rate profile obtained using network model of reconstructed preform

The Figure 77 shows regions of high (red) and low (blue) flow rates are formed across the network. The pressure profile is given in appendix B. Similar ADFP produced preform was investigated experimentally in [32]. A more complex preform with a layup of [(-45,+45,0,90)s,0,(-45,+45,0,90)]s was produced where every layer was staggered by 3.5 times the tow width. The details of this paper are discussed in the literature review **(sections ref)**. Significantly, it was concluded that gaps of different widths (1, 2, 4mm) have no effect on

preform permeability. This preform was reconstructed using the network model as shown in the Figure 78.

Figure 78 – Reconstructed network model from[32] (Top). Connections with neighbouring layers enabling through thickness flow can be observed (Bottom)

Figure 79 – Results acquired by the developed network model by reconstructing the preform tested in [32] shows increase in permeability when gap widths and gap volume fraction are increased (Figure 21 shows the results from the paper).

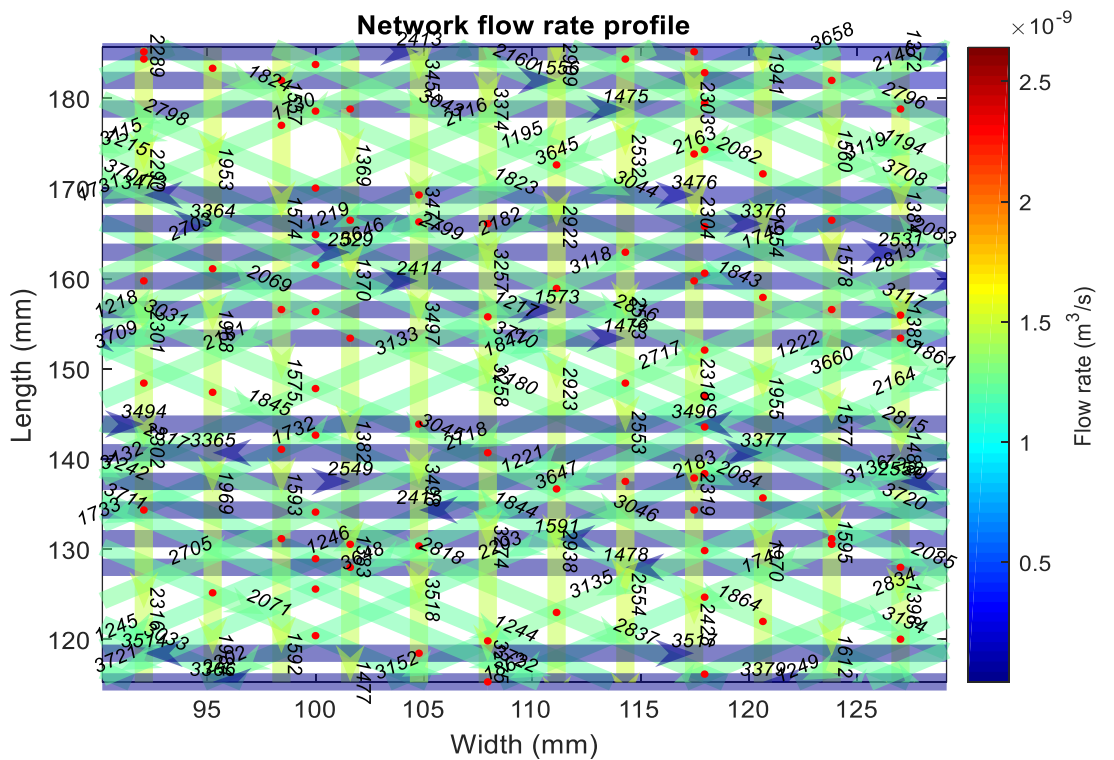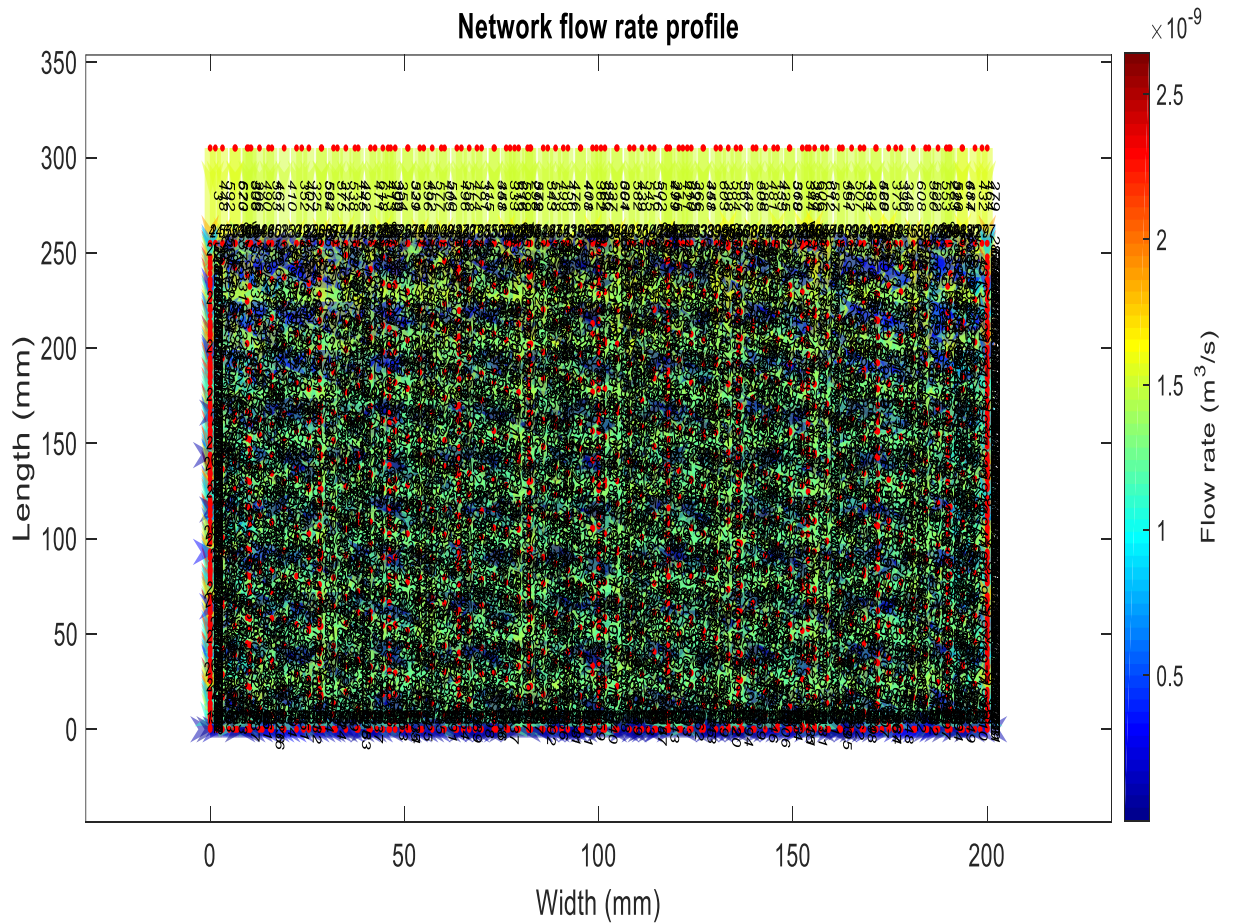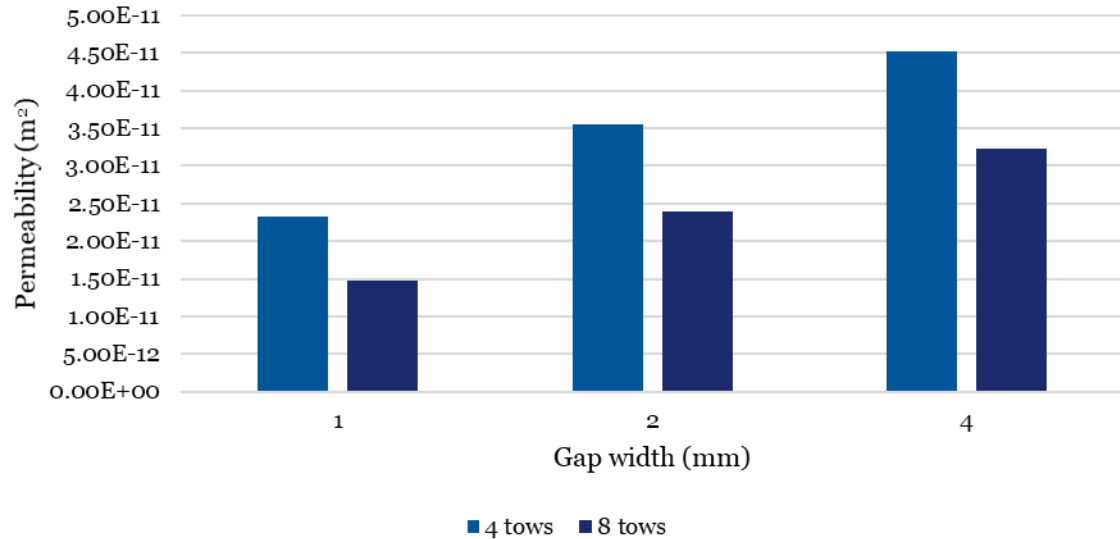The complexity of preforms can be observed in the Figure 78, when gaps are placed after each course consisting of either 4 tows (25.4mm) or 8 tows (50.8mm) with the layers in different orientations. The advantage of the model is evident at this point as it successfully generates a model with high complexity, ensures layers are connected to neighbouring layers only and runs the flow simulation while requiring only a few input parameters and offering run times under 10 minutes. Moreover, the directed graph network shows the colour gradient of flow rate across the network; where layers in 90° orientation exhibits the lowest flow rate, layers in ±45° orientation exhibits medium, and layers in 0° exhibits the highest flow rate. In the paper, experimental results were reported in graph only and ranged from 5.0E-11 m^2 to 2.0E-10 m^2. Since the results from different preform configurations were scattered across the range in the graph, it concluded that gaps have no significant effect on preform permeability. On the other hand, Figure 79 shows contradicting results where permeability is increased (58% in preform with 1mm gaps, 48% in preform with 2mm gaps and 40% in preform with 4mm gaps) when course width is decreased from 8 tows (50.8mm) wide to 4 tows (25.4mm) wide. It also shows the permeability increases as the gap width is increased from 1mm to 4mm. Only nominal gap

widths were applied in network model as no further data was available in the paper and fundamentally, permeability should be expected to increase by increasing the V_{gf}.

It is worth noting that the results by network model showed lower error for reconstructed preform by [27], this should be further tested as all of the input parameters were not known for both papers [27, 32]. But the fact that the results are close as shown in Table 18 and, showed that network model is working as expected. Also the interlayer flow is neglected in the homogenization approach used in the paper [27] and only two representative layers from a 16 layer thick preform were used to take the gap width measurements. In the case of [32], limited data was available therefore only nominal parameters were used, which makes the direct comparison difficult but results under nominal conditions were calculated. This shows the necessity of easily accessible preform data which can be used to quickly to characterize the preform flow behaviour.

4.4.2 Statistical analysis of a layer to predict averaged layer permeability

In this section, the preforms produced and investigated in the previous section (3.3.4) is used to measure the gap width variability and calculate the mean and standard deviation of the data. The standard deviation is than applied to the network model to replicate real conditions and measure averaged permeability of a preform.

Preform	Number of plies	Nominal Gap Width (mm)	Mean (mm)	Standard deviation
1	9	0.5	0.188	0.21
1a	18	0.5	0.766	0.38
2	9	1	1.595	0.31
2a	18	1	1.620	0.1

Table 19 – Gap width variability data from industrial grade preforms

A model with 500mm length was produced with gap after every tow up to maximum of 100 gaps. 1mm gap width was selected as nominal gap width and the standard deviation (0.1, 0.2, 0.3, and 0.4) was selected from the Table 19 and used to generate random gap widths with

respect to nominal gap width and applied to the network model. A total of 600 runs of model were completed for each standard deviation value given above. Figure 80 below shows the frequency plot of gap widths generated over 600 model runs by applying 0.2mm standard deviation. Similar plots were produced for each standard deviation and can be found in appendix B.
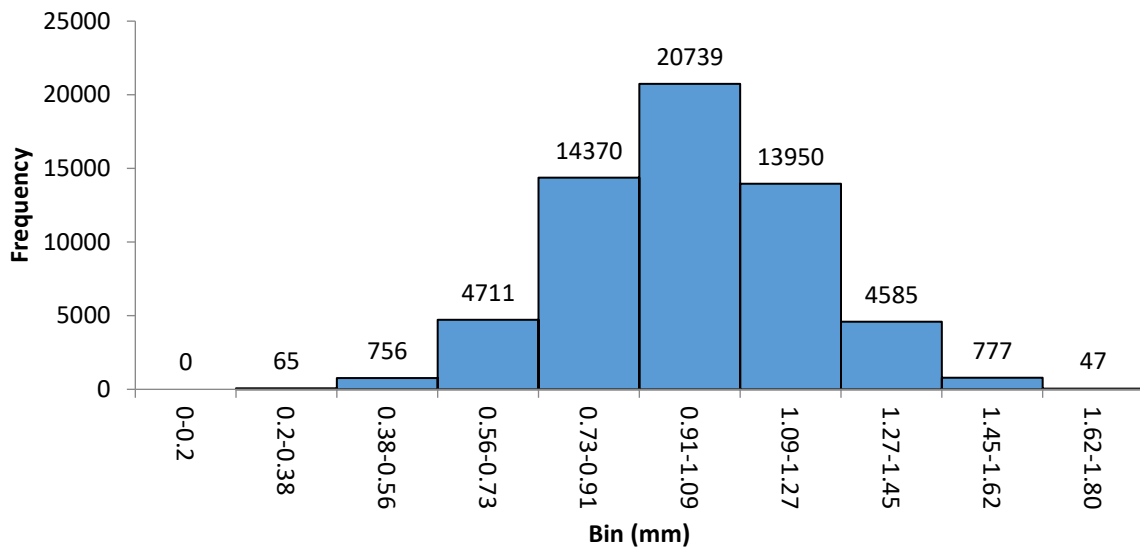
Figure 80 – Gap widths frequency plot when 0.2mm standard deviation was used to generate the gap width data.

An averaged layer permeability can be calculated using the 600 model runs. Each of this run assigns random gap widths to the model generated by using the standard deviation. The model calculated permeability of layer for each of these runs and stored in an array. Permeability for each run is calculated by equation (**26**). From run 2 onwards, an averaged layer permeability is calculated by adding the permeability values from run 1 and run 2 and diving it by run number. From run three onwards the averaged permeability is calculated by taking the previous averaged permeability value (permeability (n-1) in this case) and permeability value produced by the model for current run and dividing it by the run number. The solution will converge after a few run and the final converged value will be the average permeability that can be expected

from a preform with defined standard deviation in the gap data. An average layer permeability

for each run (n) is calculated by the following equation:

$$\text{Averaged permeability (n)} = \frac{\text{Averaged permeability (1:n−1)} + Permeability(m)}{n} \qquad (27)$$

Where, n = run number, permeability (m) = permeability produced by the model for latest run.

The change in permeability for each run can be calculated by,

$$Percentage\ change\ (\%) = \frac{Avg\ Layer\ K_n -\ Avg\ Layer\ K_{n-1}}{Avg\ Layer\ K_n} \qquad (28)$$

It is also worth looking at the difference of averaged permeability from the nominal model. It

will demonstrate the overall difference in permeability to be expected in a real preform in

comparison with nominal prediction. The percentage difference from nominal K for each run

(n) can be calculated by:

$$\frac{Avg\ Layer\ K_n - Nominal\ K}{Nominal\ K} \qquad (29)$$

The results acquired from Equation (*28*) & (*29*) are plotted against the number of runs in Figure

80. Similar graphs were plotted for each of the standard deviation selected which can be found

in the appendix. It can be seen in the figure below that the average permeability converges after

only 100 runs of the model. A similar trend was found in all other cases with different standard

deviations. In a full preform, number of gap will be higher and this will required more model

runs to converge the average, hence the number of runs are likely to increase. The difference

from the nominal model line shows that minimum negative 1.5% - 2.0% difference from

nominal K under as designed layer configuration should be expected when the gap width data

shows 0.2mm standard deviation. Similarly, the difference from the nominal K increases as

standard deviation is increased and found as high as 6% in case of 0.4mm standard deviation.

In this section variability in gap widths was successfully assigned into the network model and the model was developed to be able to run for assigned number of times to generate different gap width specifications across the network using the standard deviation from real data. All this requires the user to assign inputs to the network model only once and an averaged permeability of preform under specific standard deviation will be predicted.
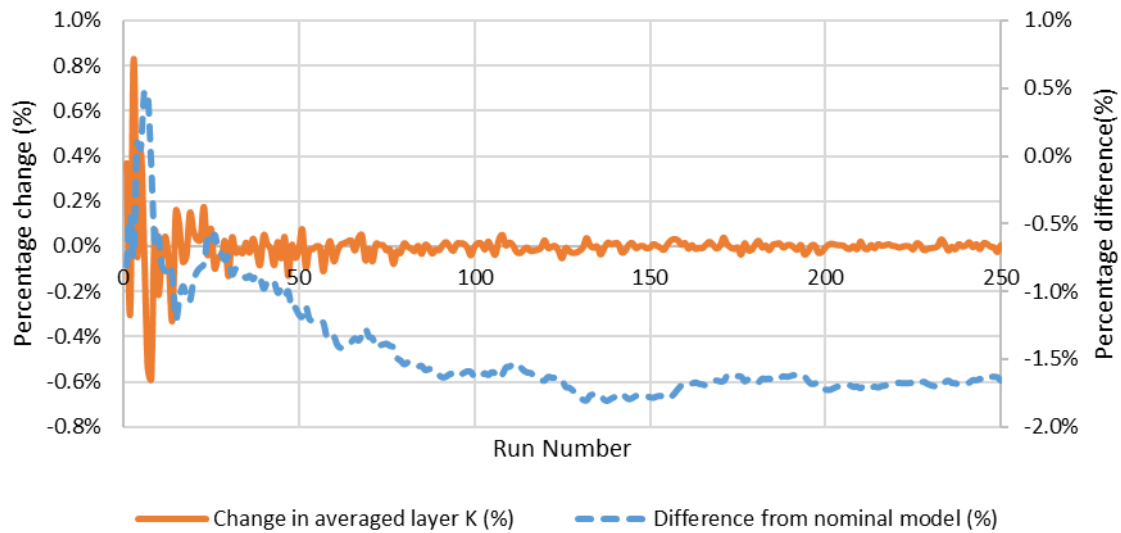
Figure 81 – Percentage change of layer K from previous run shows the K converges after 100 runs. The percentage difference from nominal layer K shows the level of difference to be expected under given stand deviation

4.5 Conclusions

The analytical investigation of contribution of tow permeability and gap permeability to layer permeability clearly showed that the difference between models with permeable and impermeable tows for wide gap is insignificant (Figure 74). This justifies the use of a network type method. Figure 75 exhibits that the tow permeability contributions for gaps ≥ 0.3mm widths is below 10% and only becomes significant for $\leq 0.2mm$. The statistical exercise showed that even if standard deviation of 0.4mm is assigned to the model, very few gaps $\leq$ 0.27mm were generated. One may think at this stage, tow permeability contribution should not be neglected as shown in Figure 75. But most gaps assigned in the network have greater widths

overcomes the contribution from tow permeability. Therefore, tow permeability can be disregarded at this stage of network modelling.

Due to complexity of the preform and limitation of conventional simulation methods, in [27] simulation was only conducted for 6 gap. However, the network model successfully generated the geometry of full 16 layer thick preform and conducted a flow simulation. The preform designs $[0/90]_8$ and $[(-45,+45,0,90)s,0,(-45,+45,0,90)]_s$ can be produced straightforwardly using a ADFP machine, however their geometries can be extremely complex to reconstruct for reliable flow simulations. It will require hours of skilled user time to generate a fully connected 3D mesh and >13 hours for a 10cm element size with 600,000 elements to run a conventional flow simulation show in Figure 58. Meanwhile, the network model was able to generate the network and run the GGA analysis in under 10 minutes for both cases and generate the coloured flow rate and pressure profiles of the networks. A user would be required to start from the scratch if any changes (e.g., gap width variability) were required to be made in the model. Hence, the reconstruction of preforms from literature [27, 32] exhibited the advantages of network model. Moreover, the network model enables the user to change any gap widths' specification across the network before running the GGA section. For example, A network can be generated by running the first part of code which identifies the intersections of lines across the graph. A new node is added at the coordinate of each junction and the nodes are then connected to neighbouring layers. The lengths are calculated by calculating distances between the coordinates of nodes and the undirected graph network is generated. At this stage any changes required to the gap data can be made user can proceed to run the GGA code. If the user wishes to make any changes to the gap widths on similar network, the data can be assigned and GGA code can be executed directly. This further saves the computational time required to reconstruct the same model with different gap width data.

Despite a few unknown parameters, the results from the reconstruction produced some sensible ADFP preform permeability values when compared with the values given in literature. The results acquired from reconstruction of preform tested in [32] directly contradicted with the conclusion made in the paper by exhibiting preform permeability increases with increasing gap width and V_{gf} . This means the real preform data should have been investigated in depth to understand what caused the difference in permeability of all preforms. But the process to investigate the preform data post infusion can be expensive in terms of time and cost. Therefore, the most economical way to access the data which can enable rapid flow characterisation in preform is to record it during the deposition process.

The statistical averaging technique enables using a standard deviation value based on real data acquired from industrial grade preforms and predicting the average preform permeability by running 600 runs of the model under different gap widths configuration across the network. This shows the convergence of the averaged permeability and maximum runs required to minimize computational time in future. Moreover, it shows magnitude of difference from nominal model that can be expected due to variability induced in preform.

The network model development completed for this chapter has overcome the main challenges in comparison to conventional flow simulations. It successfully enables a user to generate a complex gap network using very few input parameters, joins the neighbouring layers at gap junctions only and enables through thickness flow in the preform, perform a flow simulation based on data acquired directly from the preform and generates a directed graph displaying gaps with highest to lowest flow rates.

At this stage the model verification was done by only using the results from the reconstruction of preforms using limited data provided in the literature. The main reason behind the lack of model verification at this stage is that the developed model cannot be validated using the data

142

acquired through conventional methods such as XCT scan or microscopy. Limited data can be accessed through such methods as they are time and cost expensive and the data is collected post infusion/consolidation. To validate the network model the pre-infusion data of each gap within the preform is required. Therefore, ADFP machine equipped with laser scanning technology is required to excess the full preform data at layup/pre-infusion stage.

The developed numerical model can predict the preform permeability based on nominal gap width, averaged gap width, or assumed standard deviation of gap width data. The numerical model produces a 2D directed graph and shows flow rates in edges, but it does not display the flow behaviour globally. The model is based on steady state flow therefore it does not incorporate any sink effect of fluid flowing transversely into the fibre tows. However, it was also observed from the results in this chapter that the overall effect of fibre permeability is very low in preforms with high gap volume fractions therefore it is safe to neglect this. Further development is required which can enable a user to display local and global flow regions in a ADFP preform without requiring high time investment. This will be addressed in detail in the next chapter.

4.6 Appendix B
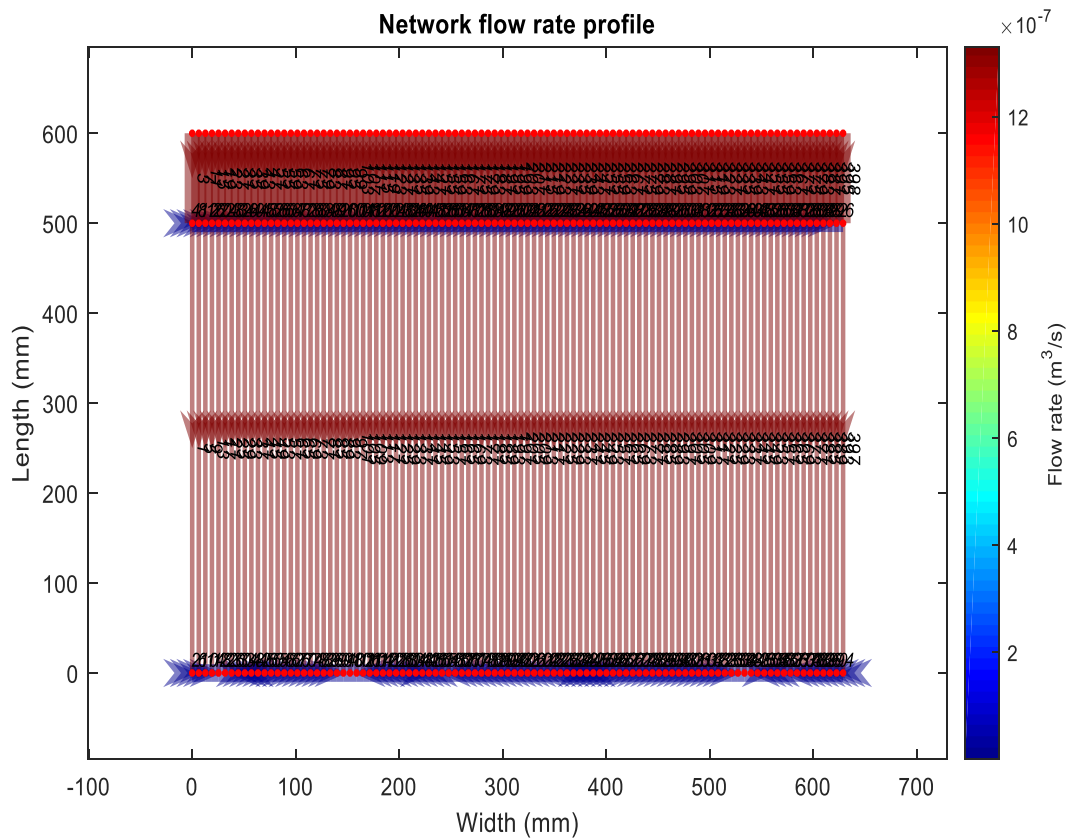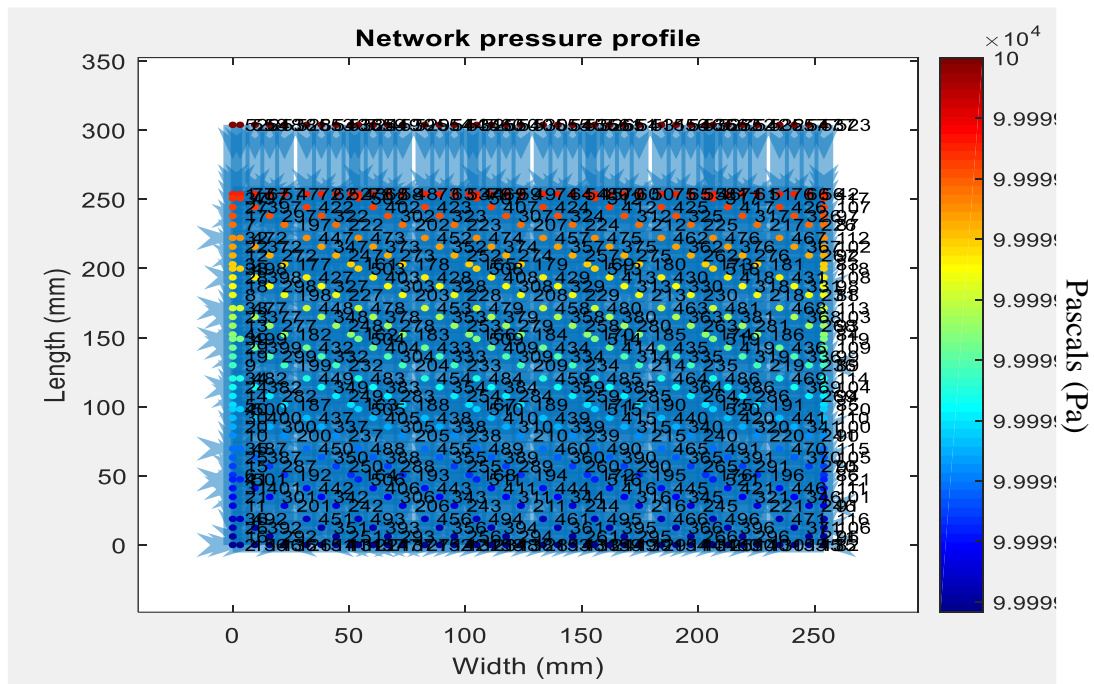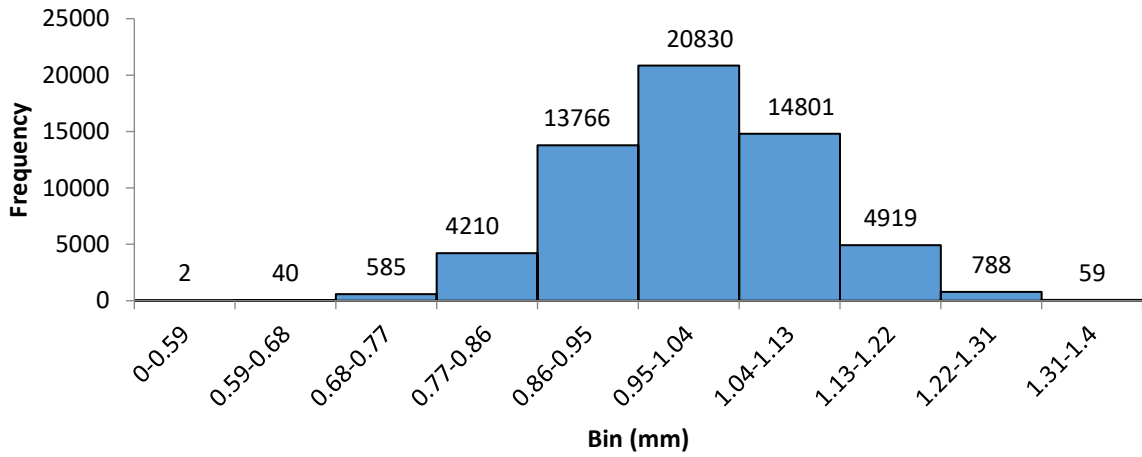
Frequency of gap widths generated using standard deviation - 0.1mm
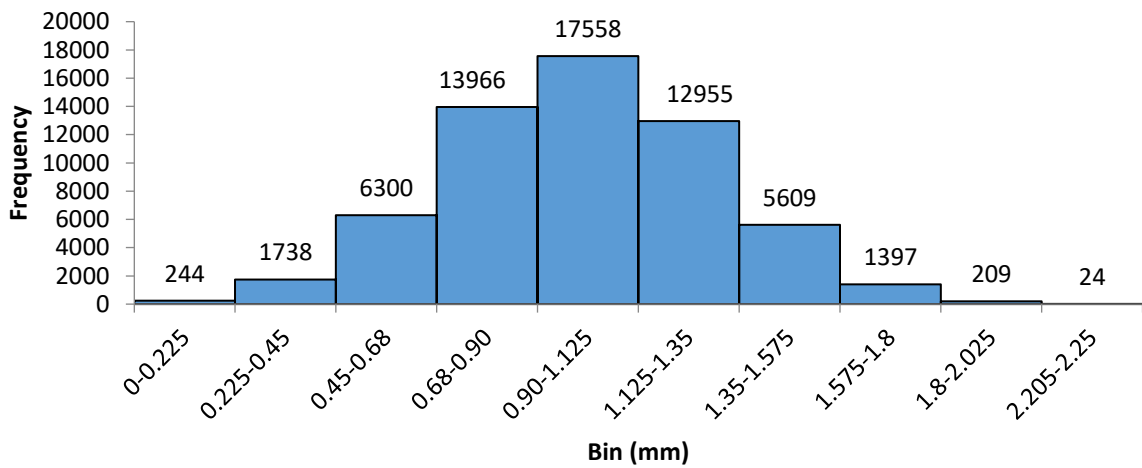
Frequency of gap widths generated using standard deviation - 0.3mm

Standard deviation - 0.4mm
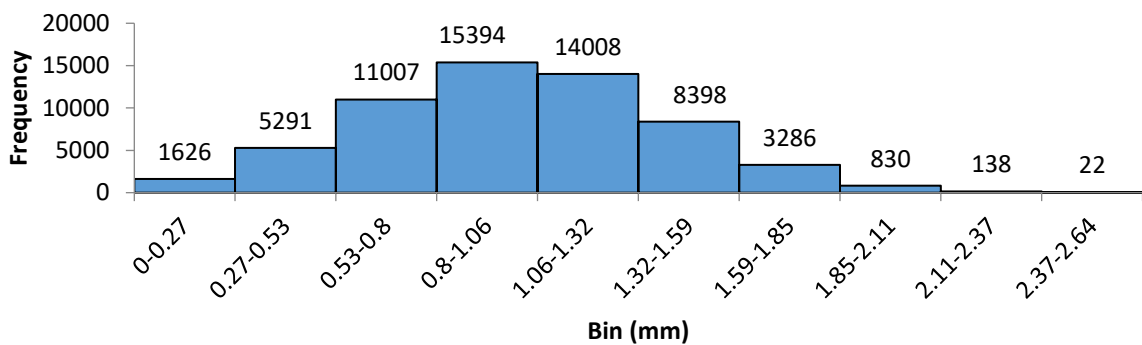
Frequency of gap widths generated using standard deviation - 0.4mm
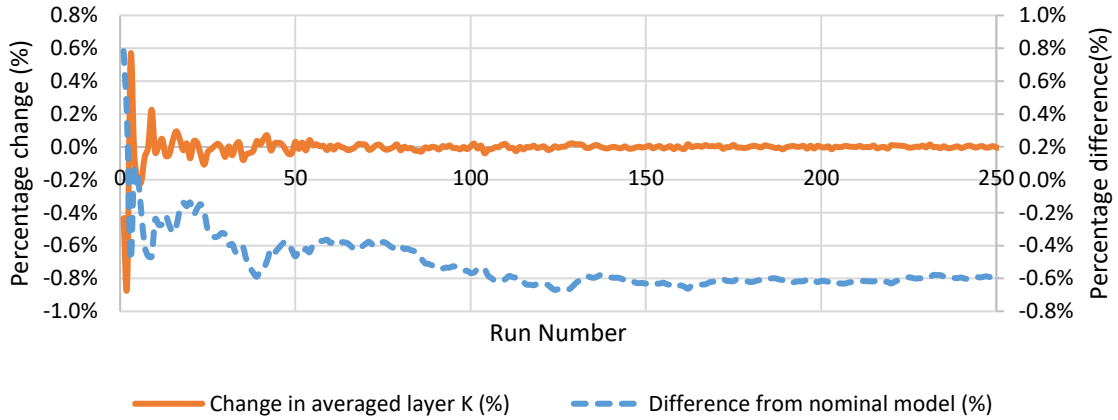
Percentage change of layer K from previous run shows the K converges after 100 runs. The percentage difference from nominal layer K shows the level of difference to be expected under given stand deviation (0.1mm STDEV)
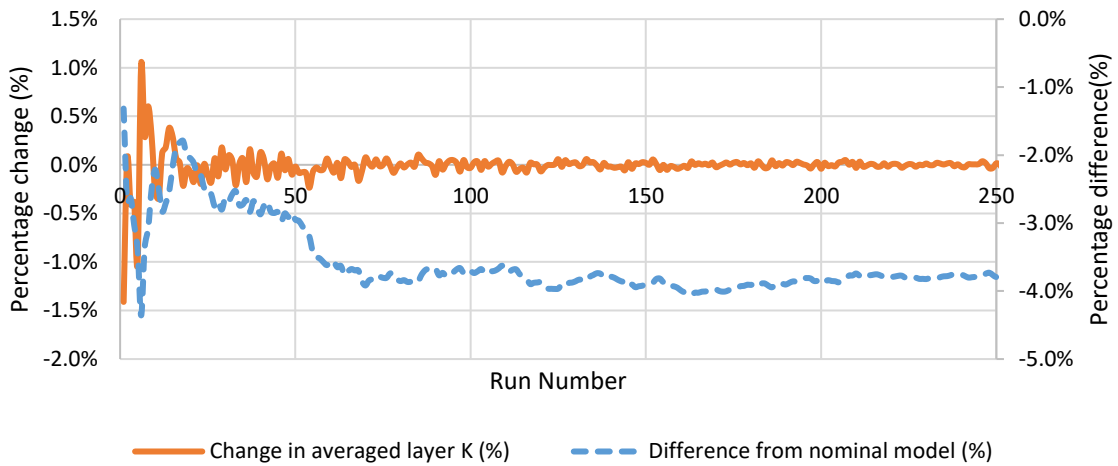
Percentage change of layer K from previous run shows the K converges after 100 runs. The percentage difference from nominal layer K shows the level of difference to be expected under given stand deviation (0.3mm STDEV)
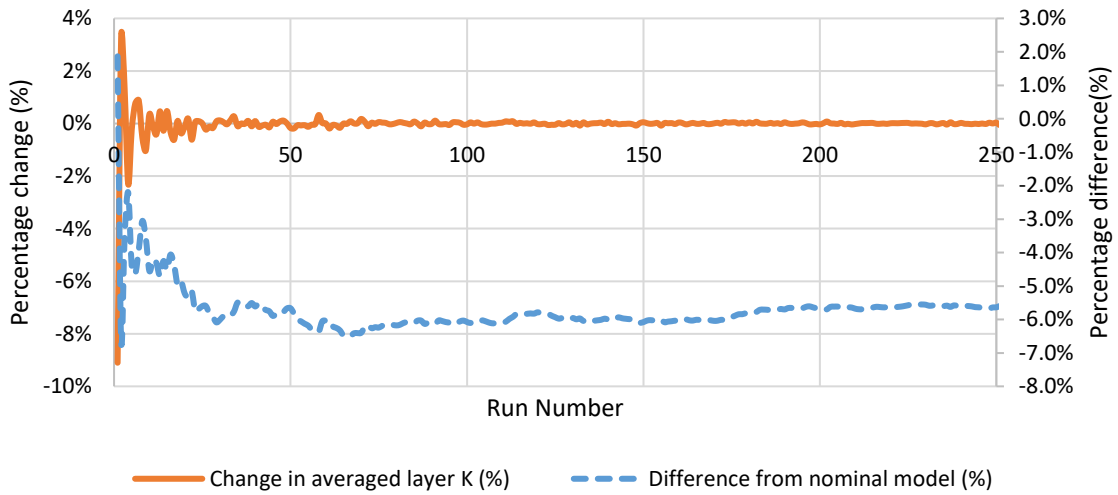
Percentage change of layer K from previous run shows the K converges after 100 runs. The percentage difference from nominal layer K shows the level of difference to be expected under given stand deviation (0.4mm STDEV)

Chapter 5 Flow characterization by mapping local and global velocity in cells across the gap networks generated by real data

5.1 Introduction

The numerical model developed in the previous chapter enabled the characterization of the flow rates across complex gap networks and measurement of the permeability of a preform. This aim of developing such a model was to overcome the limitations in conventional simulation software and enable rapid flow assessment of an ADFP produced preform. Flow front progression over time is a main advantage of conducting a flow simulation by using any conventional flow simulation software as it can display low permeability regions and propensity to void formation under specified parameters as shown in Figure 82. While the numerical model developed in the previous chapter significantly decreases the network formation time and flow simulation run time, it is not capable of displaying flow front progression. Therefore, the numerical model is further developed to enable a user to identify local and global regions of high or low flow by mapping the homogenised velocity in specified cell size across the preform and produce local and global colour maps.

Moreover, the code is able to incorporate the real data acquired from laser profilometry during deposition process but requires either a nominal value, averaged or a standard deviation value to assign gap widths in the gap network. This requires the user to process the real data separately each time a preform is produced. The aim of this model is to be able to characterize the flow characteristics of an ADFP produced preform based of real preform data acquired from the deposition rig. To achieve this aim, the model is further developed in this chapter so the code can be commenced as soon as real data file is delivered from the deposition rig without requiring too many input parameters. The 2D visualization shows connection to neighbouring layers, but the difficulty to find the specific gap information increases as the preform becomes

complex due to various gaps. Therefore, the visualization will also be developed in this chapter to demonstrate the connection with neighbouring layers more clearly.
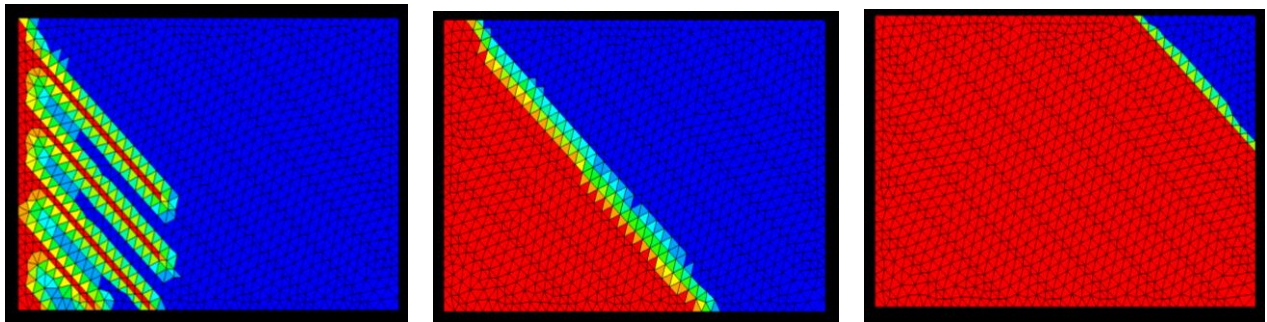
Figure 82 – Flow progression simulated in PAM-RTM in a 45° layer in the presence of gaps after every 6.35mm wide tow.

5.2 Methodology

The code developed in the previous chapter has enabled the generation of rectangular preform geometry and gap network based on the input parameters and conducts GGA on the network. In this chapter, the first part (Formation) of the code is developed to form a network based on real data acquired from the deposition rig. Furthermore, the code is developed after the GGA is conducted to perform a cell by cell analysis to calculate the local and global homogenised cell velocity. In this section, details of the above mentioned process will be discussed.

5.2.1 Incorporation of real preform data into the network model

The ADFP deposition rig records data points by using laser profilometry. It generates a CSV. File which contains start and end coordinates for each gap placed in the preform. It rearranges the data as required for the code to run, add the inlet pipes for each layer and finds the junctions between the neighbouring layers.

5.2.1.1 Process flow chart

Figure 83 shows the flow chart of developed code, the initial flow chart is shown earlier in

Figure 67. The code imports the file generated by ADFP rig during online deposition. The

code identifies the total number of layers in a preform, stores each gap into the relevant layer

and generates a network following the same steps described for Figure 69.
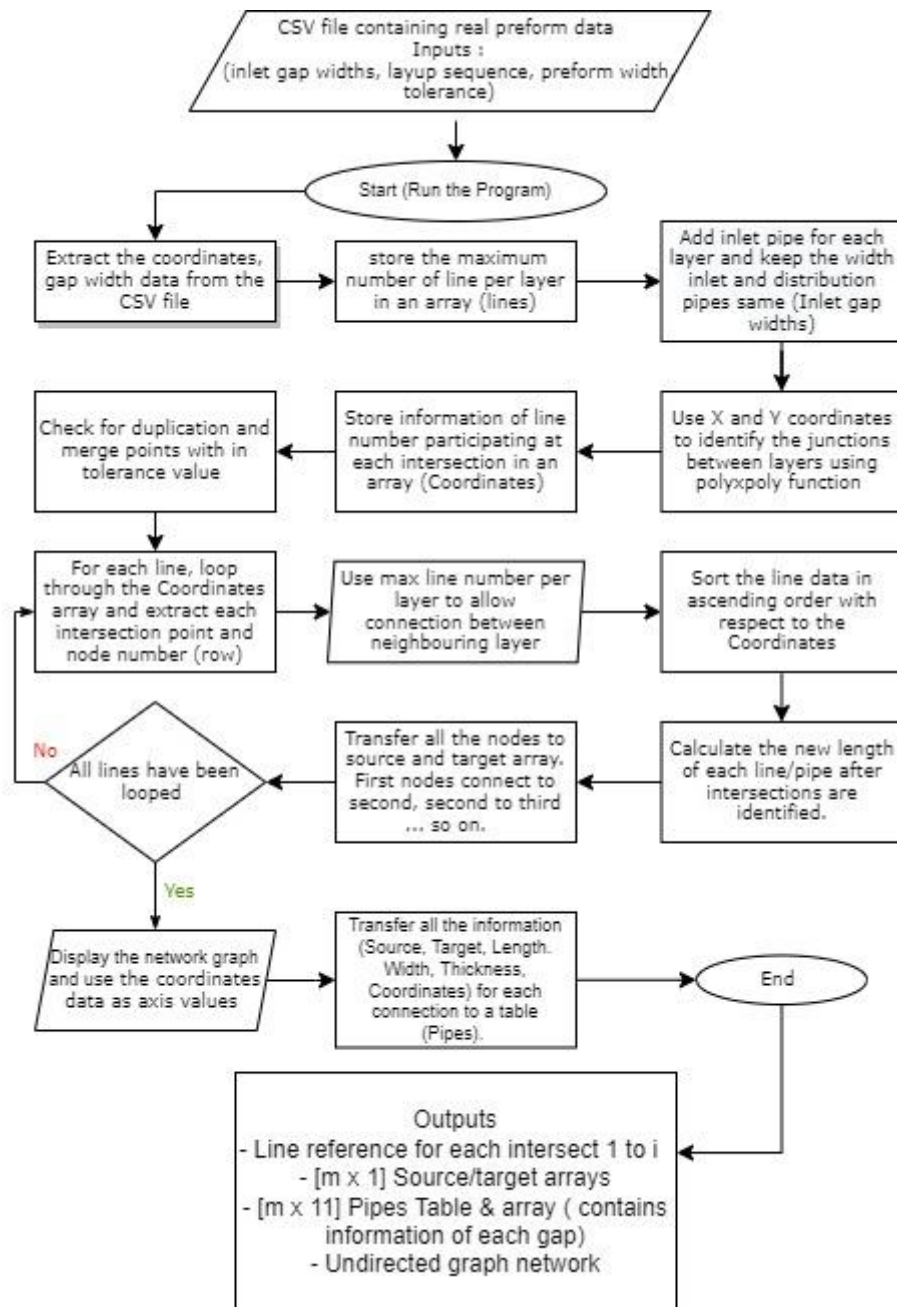
Figure 83 – The detailed flow chart of formation of graph network using the real data
acquired from the ADFP rig

5.2.2 3D visualization of the graph network

As the preform becomes complex, the 2D graph network shows the junctions but the difficulty rises to understand the junctions/connections only from observing the figure. A graph network demonstration is necessarily flat but the geometry of a preform is in three dimensions. Hence the 2D graph network doesn't necessarily represent the real geometry. Therefore, the layer number is used to assign a Z-coordinate to each of the gap in the network. Additional inlet pipes are added to demonstrate inlets of each layer. A line graph was produced which plotted each gap as a line in a loop. It also applied a colour gradient to shows gap with lowest and highest flow rates from yellow to red.
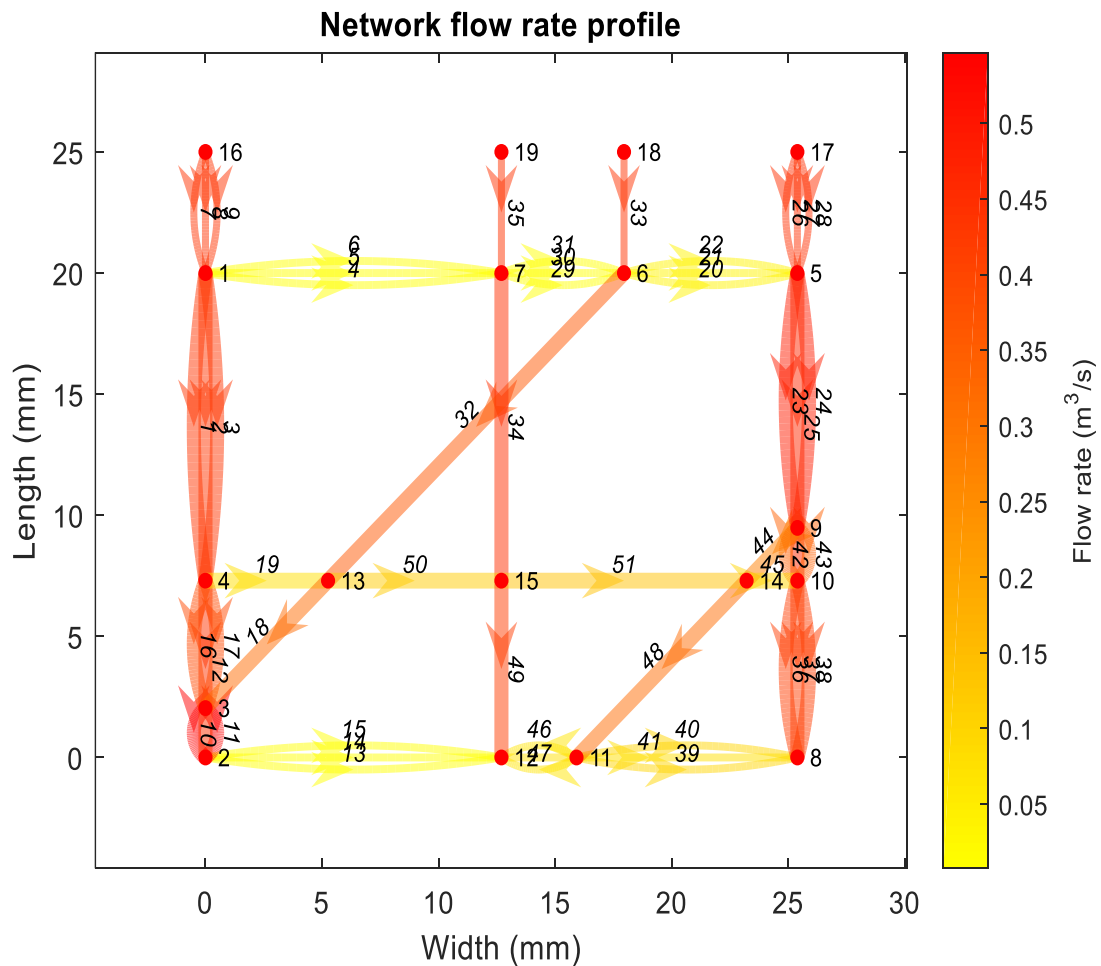
Figure 84- 2D representation of an example graph network produced for a [0/90/45] layup

3D representation of the gap network
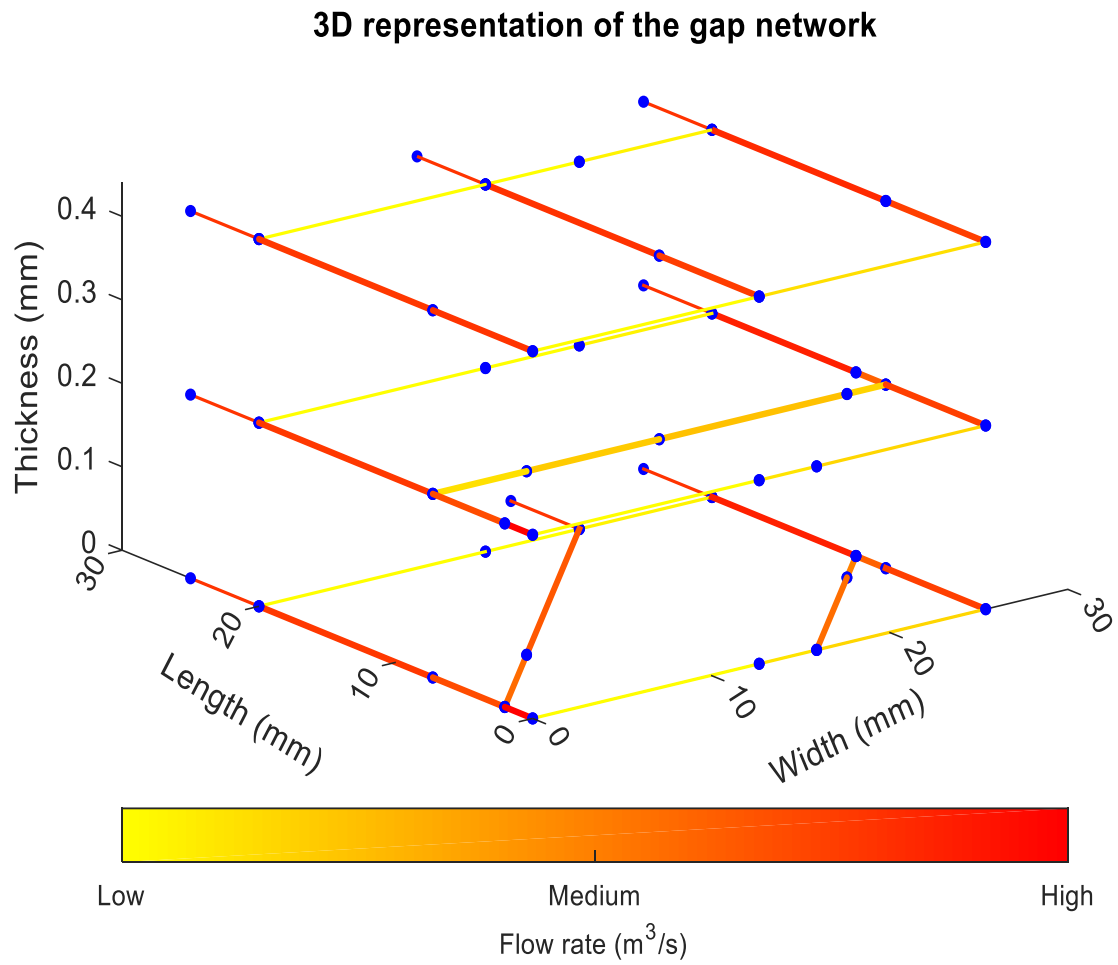
Figure 85 - 3D representation of graph network in Figure 84 with [45/90/0] layup shows the layer in 45° orientation and 0° orientation is only connected to middle layer in 90° orientation. The connection are highlighted with blue dots.

5.3 Homogenised cell flow velocity mapping (local and global) using cell-edge method.

The aim of this chapter is to develop the network model to enable a display of flow behaviour in each layer and a combined global effect. To be able identify such regions in a preform, a cell-edge method is adopted. In this method, a cell with a specified boundary will be produced which loops through each layer of preform and identifies the edges/gaps and their properties that resides inside the cell. These properties will be used compute the homogenised velocity of each layer in a cell. Once the velocities are computed, the results are then used to produce a local and global colour maps. The detail of the process in discussed in the following two sections.

5.3.1 Cell-edge detection method and computation of cell velocities

To be able identity regions of poor flow in the produced preform, a cell method is adopted. The numerical model will be initiated by an Hcell and Vcell values, by which the preform length and width will be divided and the cell size will be specified. For example, if a gap network is generated for a 25mm x 25mm preform with [90/0] layup and a gap after every tow. The user will require five cells at length and three cells on the width. The cell size will be determined as per Equation (*30*)

Hcell = 5

Vcell = 3

$$\text{Cell size} \ = \ (\text{length/Vcell}) \ * \ (\text{width/Hcell})$$

$$\text{Cell area} = 5 * 8.466 = 42.33 \ \text{mm}^2$$

(30)

Once the cell size is measured, the model loops through the network. The first cell boundary as shown in Figure 86 is used to search the gaps inside layer by layer. An example of cell 1 is shown in detail below.
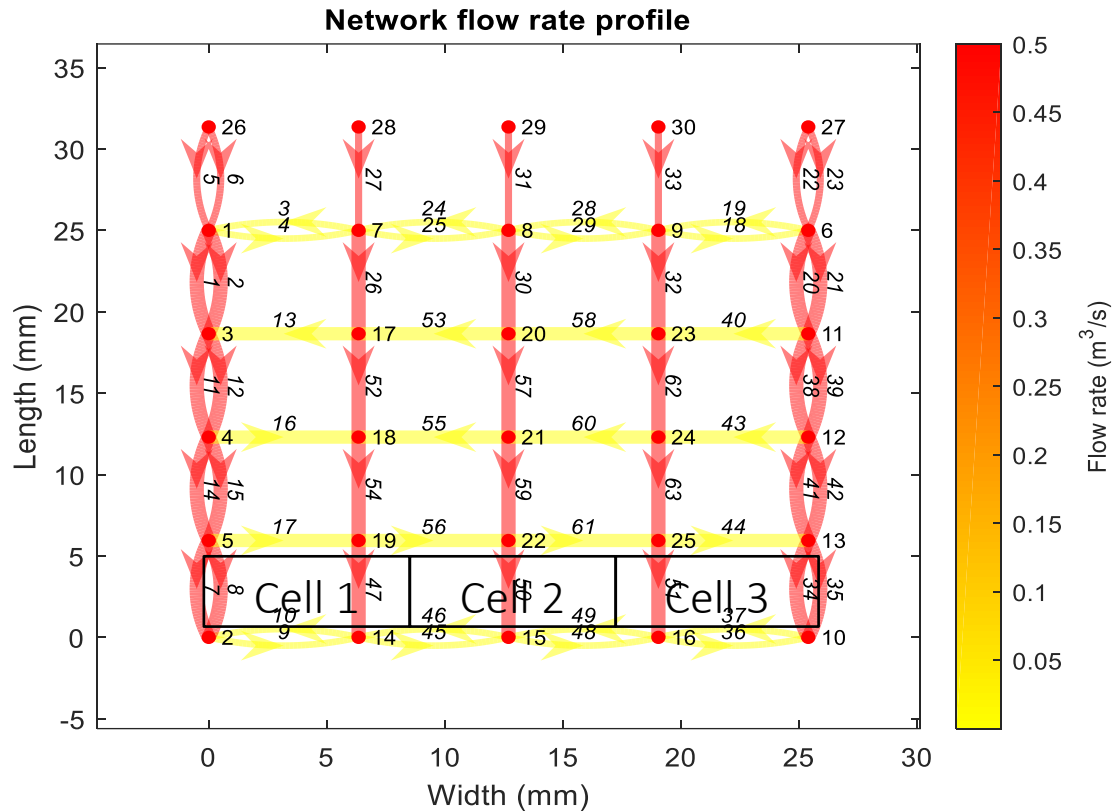
Figure 86 - Cell search to identify gaps in the boundary

In cell 1, the first layer one is checked for the gaps inside the boundary. It can be seen in Figure 86 that there are three boundary gaps (7, 9, and 45) and no primary layer gap. The model then checks gap in layer two that exists inside the boundary of cell 1 which are given in Table 20.

Cell	Layer	Gap numbers			
Cell -1	1	7	9	45	
	2	8	10	46	47

Table 20 – Step 1: Gaps identified within the boundary of cell -1 for a 2 layered preform in [90/0] orientation

Once the gaps in the cell are identified, the model tracks the coordinates of the gap and measures the length of the gap that lies within the cell boundary by taking the difference of cell boundary and outside coordinates. If the gap coordinates are similar to one of the boundary lines of the cell, the width of gap will be divided by two. If the gap lies within the cell, the full width of gap will be saved into another array. It stores the information and calculates the gap

154

volume fraction of each gap in the relevant cell (cell 1 in this case) as shown in Table 21. V_{gf}/cell is the sum of gap volume fraction for each layer.

	Layer	Gap	Length (mm)	Width (mm)	Gap Area (mm^2)	V_{gf}	V_{gf}/cell
Cell 1	Layer 1	7	5	1	5.0	0.1181	0.218
		9	6.35	0.5	3.2	0.0750	
		45	2.1167	0.5	1.1	0.0250	
	Layer 2	8	5	1	5.0	0.1181	0.336
		10	6.35	0.5	3.2	0.0750	
		46	2.1167	0.5	1.1	0.0250	
		47	5	1	5.0	0.1181	

Table 21 – Step 2: Using the length and width data for each gap that is inside the cell, V_{gf} of each gap is calculated

Once V_{gf} for each gap is computed, flow rates that are calculated by GGA are retrieved and velocity is calculated for all the gaps in the network. The direction of the flow was initially assigned manually and later corrected by GGA using the inlet and outlet information. A weighted averaging approach is used to measure gap velocity in the cell as shown in Equation (*31*). And an absolute computed velocity values are used to exhibit the overall flow behaviour across the preform using colour maps.

$$\textit{Gap velocity in cell} \, \boldsymbol{V_c} = \textit{Velocity} \times V_{gf} \tag{31}$$

And finally, a homogenised cell velocity for each cell and each layer is calculated by equation (*32*),

$$V_{layer\,1} = \sum \boldsymbol{V_{c7}} + \boldsymbol{V_{c9}} + \boldsymbol{V_{c45}}$$

$$\mathbf{V}_{layer\,2} = \sum \boldsymbol{V_{c8}} + \boldsymbol{V_{c10}} + \boldsymbol{V_{c46}} + \boldsymbol{V_{c47}} \tag{32}$$

	Layer	Gap	Vgf	Velocity (m/s)	Gap Velocity in cell (V_c)	Homogenised velocity (m/s) - V_{layer}
Cell 1	Layer 1	7	0.118	0.005791	0.000684	0.000943
		9	0.075	0.003119	0.000234	
		45	0.025	0.00102	2.55E-05	
	Layer 2	8	0.118	0.005791	0.000684	0.001695
		10	0.075	0.003119	0.000234	
		46	0.025	0.00102	2.55E-05	
		47	0.118	0.006365	0.000752	

Table 22 - Step 3: calculating homogenised cell velocity for each layer in a cell

This way the cell loops through the graph network and each time checks each layer in the preform to identify the gaps that are inside their boundary. The figures are generated from Matlab code and given in appendix C, where it shows how each gap within the cell is marked in a red circle. For improve the code speed, these figures are usually not generated, and a user can enable it again it any checks are required. Information about each cell, gap inside, their V_{gf}, and homogenised velocity is stored to be retrieved when required.

5.3.1.1 Process flow chart

The Figure 87 shows a flow chart of the code for two orientation (0 & 90). A limit values are set based on total number of cells assigned in horizontal and vertical direction. Polyxpoly function in Matlab is used to generate the limit cell and to identify the junction point for each line intersecting at two ends of the rectangle. Information about corresponding line is than stored and the intersecting length is calculated based on intersection data provided by the function Polyxpoly. Once all the gaps have been checked, the next cell is generated based on limit value.
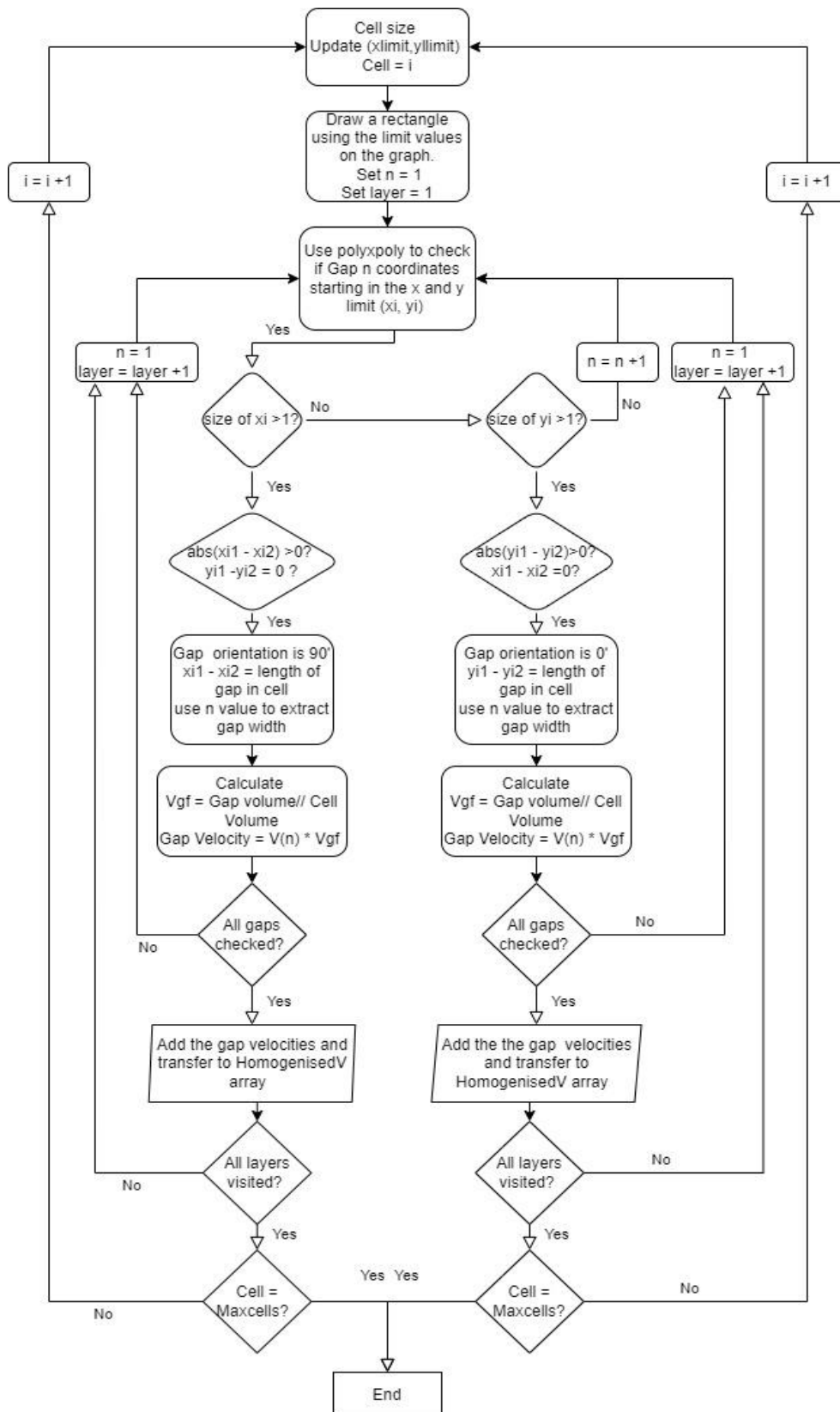
Figure 87 - Detailed flow chart of velocity homogenization using network model data for layers in 0° or 90° orientation

5.3.2 Local and global colour mapping of homogenised velocities

The maximum and minimum values from the local homogenised velocities are than used to generate RGB values for heat colour map. The colour map starts from yellow for the minimum value and ends at red for the highest value. Same process is done for the global homogenised velocities. Each of the cell boundaries are plotted by using a built in funtiopn in MATLAB (function reference: Mapshow [161]).

5.3.2.1 Local homogenised velocity profile

Figure 88 shows an example of local velocity colour map produced for the network shown in Figure 86. As the preform is simple and consists of two layers only, two local velocity profiles are created, one for each layer. It can be observed in the figure below that layer 1 which is in 90° orientation Figure 88 (Top) shows the lowest velocity in the middle and medium at the boundaries. The reason for higher velocity at boundary is the boundary gaps for each layer are in 0° orientation and encouraged the velocity is the corresponding regions. Similarly for 2nd layer in 0° orientation Figure 88 (Bottom) each of the cell consists of at least one gap and the corner cells consist of one additional boundary gaps. Therefore the corner cell exhibits the highest velocity.
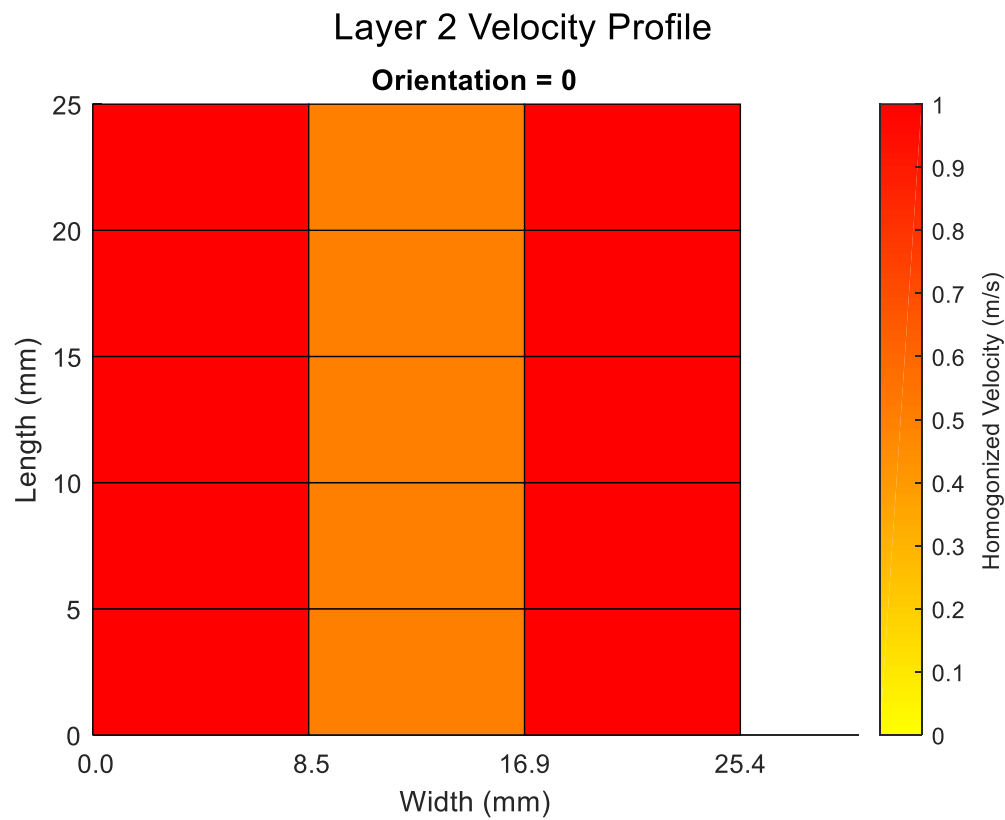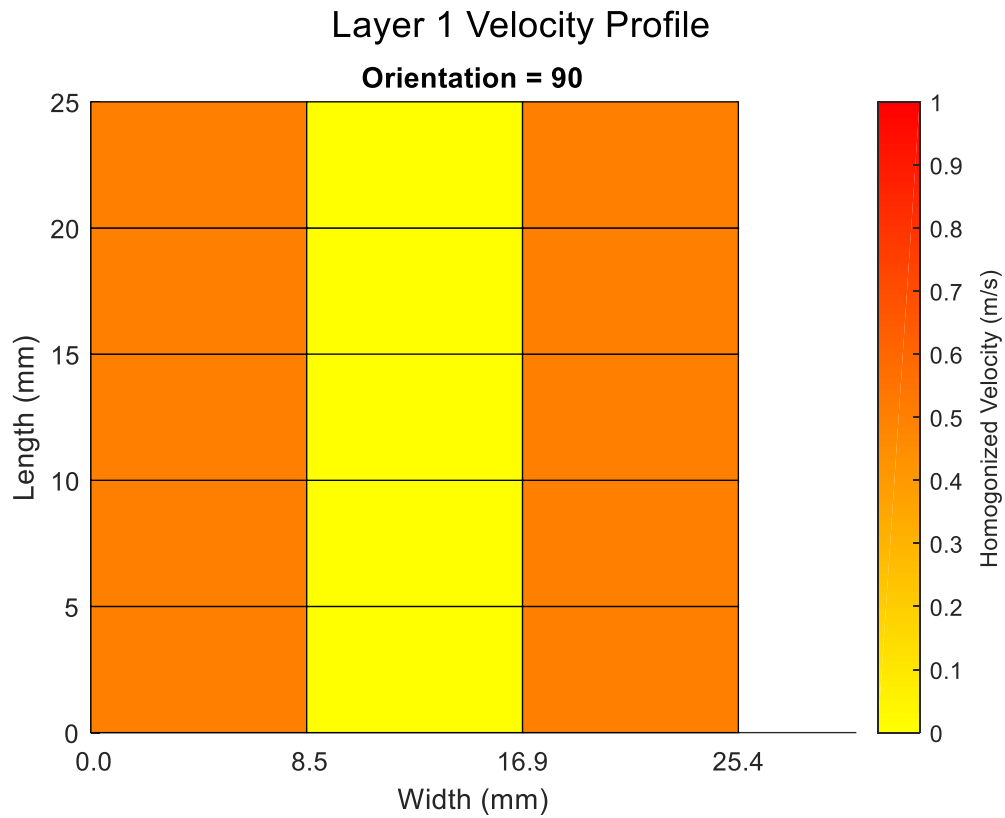
Figure 88 - Local velocity profiles for graph network in Figure 86 shows separate maps produced for each layer and shows area of low and high velocities.

5.3.2.2 Global homogenised velocity profile

To enable a display of effect all layers combined in a single plot, a new set of RGB values are generated based on maximum and minimum values from global homogenised results for each cell as shown in Table 22. The colour map produced in Figure 89 shows a global behaviour of the flow for a non-complex network in Figure 86. The map shows the regions of low and high velocity. Once a large and complex preforms are analysed, cell size will be decreased and each of the cell will consist of multiple gaps. This will result in a colour map demonstrating a global flow behaviour in a preform based on real data.
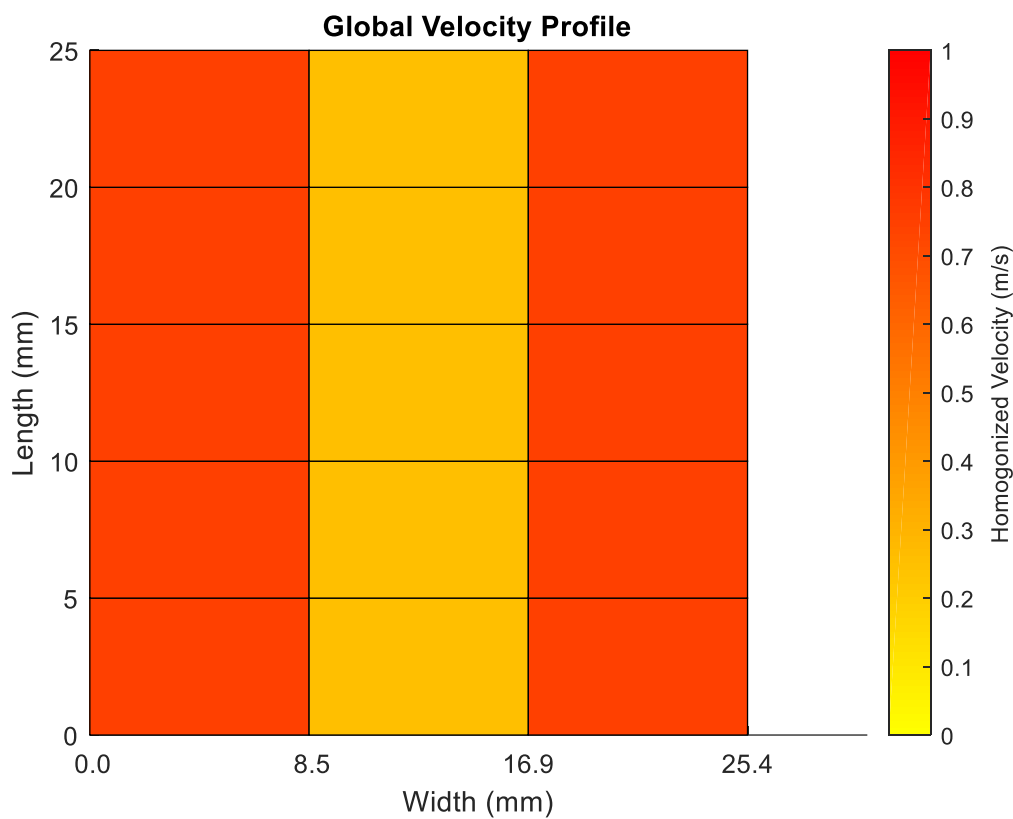
Figure 89- Global homogenised velocity profile of graph network shown in Figure 86 - Cell search to identify gaps in the boundaryFigure 86 shows the regions of low and high velocities.

5.4 Results and discussions

The target gap width was 1mm after every course. The numerical model is divided into three sub-codes:

1 – Network formation

2 – Flow simulation (GGA method)

3 – Velocity mapping (Cell-edge method)

First a single layer analysis is presented here to demonstrate the velocity map on a larger scale. A 1-meter layer data is exported from the CSV. file into the model. There were 578 gaps in the imported data and the three sub-codes were completed in 61 seconds only. The Figure 90 shows the network graph generate displays the flow rates of gaps, represent the widths and direction of the flow.
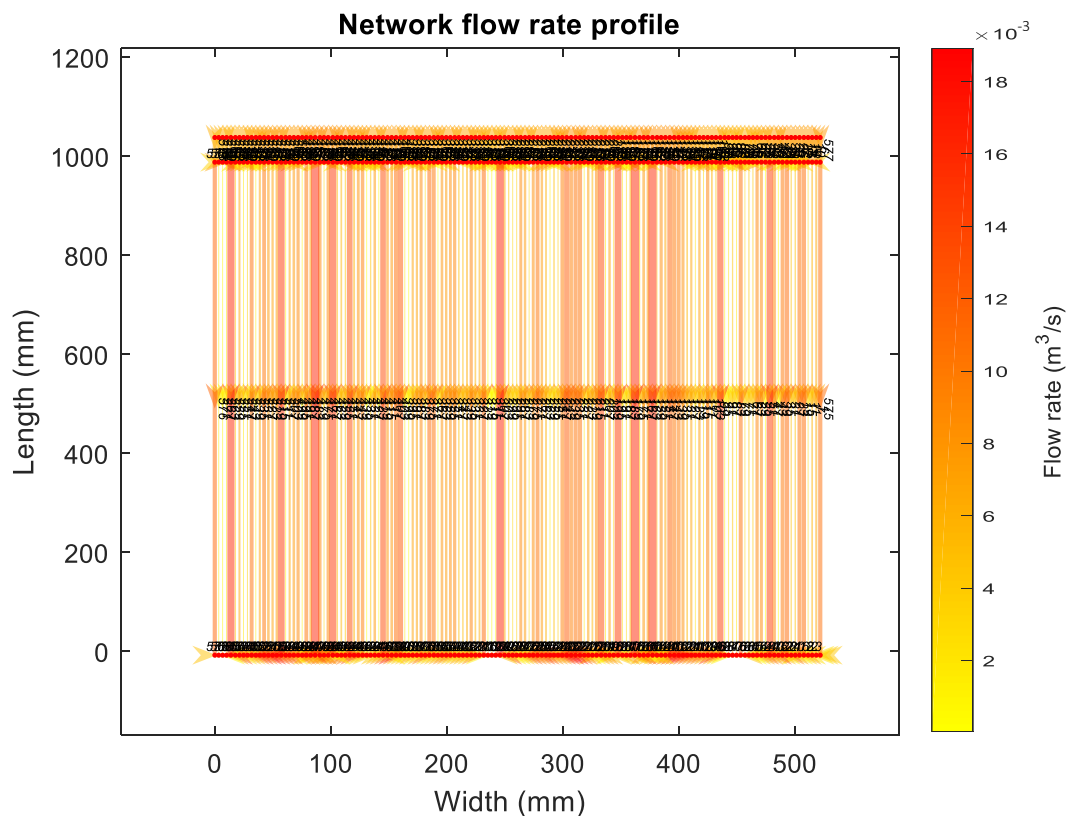
Figure 90 – A 1m x 1m layer analysis completed in 61 seconds using the network model.

One of the main parameter for visualizing the homogenised flow velocity is the cell size. The cell size will control the trade-off   between presenting the homogenised velocity colour map with too less detail (also referred as over-smoothing) and too much detail (also referred as under-smoothing) [162]. Sturges' rule was the first rule given in literature and still widely used today that gives a formula to compute number of cells [163].

$$Total\ number\ of\ cells = 1 + 3.322 \log(N) \qquad (33)$$

Where, N is the total number of observations.

The layer shown in Figure 90 consisted of a total of 578 gaps and using that in equation gives 8.36. The results is rounded to closest whole number and total of 9 cells will be used to display the velocity map.
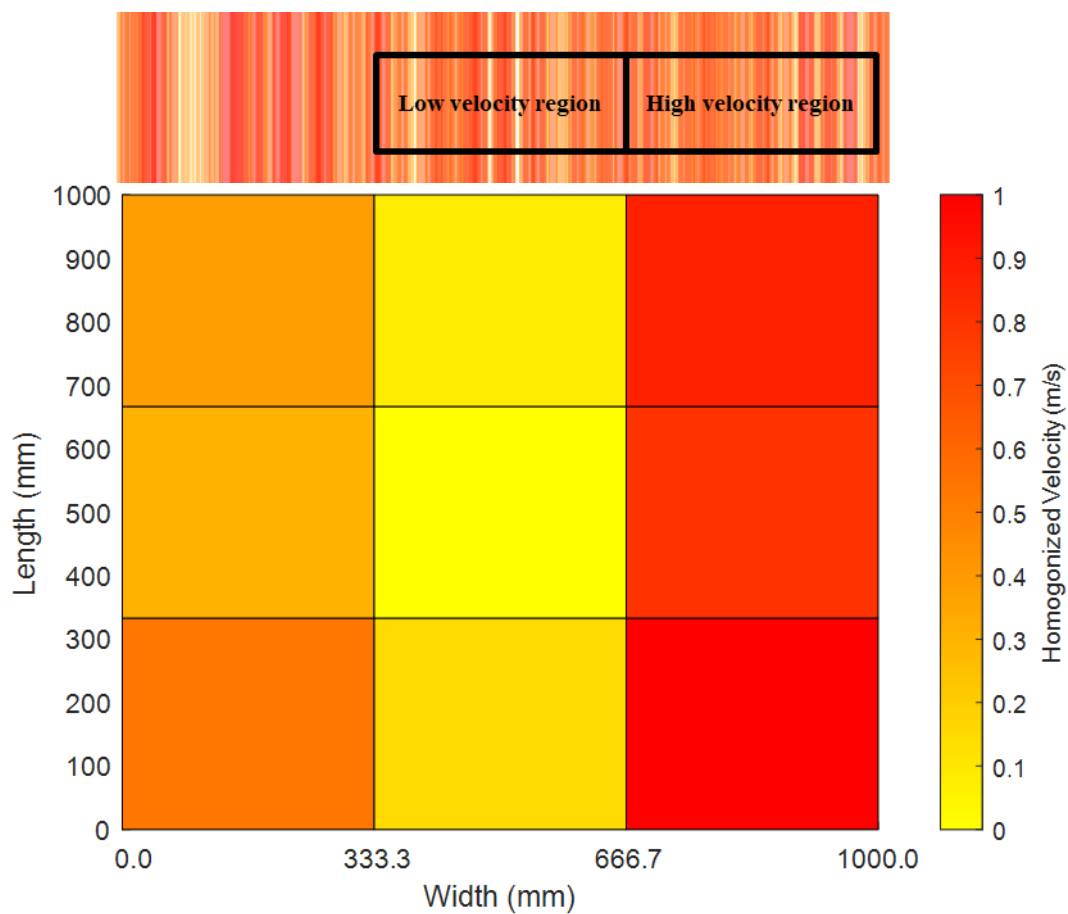
Figure 91 - Velocity map of a 1m x 1m layer based on real data shows the region of poor velocity

The velocity map in Figure 91 shows the regions of high and low velocity in a single layer. The code successfully shows the region (333.3mm-666.7mm) of lowest velocity in the layer. A screen shot of the flow rates is shown in the Figure 91, where it can be clearly observes the high flow region from the velocity map contains more gaps with high flow rates than the low velocity region.

5.4.1 Computational time

The main purpose of this network model approach is to enable a user to execute a flow simulation in short period of time. The Figure 58 showed the expected time to run a 3D simulation. The simulations were done in PAM-RTM. The graph in the Figure 58 shows that a 3D simulation with 600,000 elements of 10cm in size were simulated in 13.33 hours. For the preforms with high gap volume fraction, a much finer mesh with smaller elements will be required to be able to produce a reliable simulation. Similarly, a simulation was completed for a 2D models with element size of 20mm in 20 minutes (Figure 59). The gap size in the network model much smaller(<2mm) than 20mm therefore much finer mesh will be required to for a 2D simulation. Moreover, 2D simulation will only provide limited information such as fill time, homogenised permeability etc. To be able to simulate preforms with high gap volume fraction, fine mesh is required which will result into higher computational time. Additional time is spent to produce a mesh geometry for 2D and 3D simulations.

On the other hand, the network model computational is given below in Figure 92. The network model was able to process data from 4300 gaps in under 6 minutes. This graph is a combined computational time for network formation, flow simulation and velocity mapping codes.
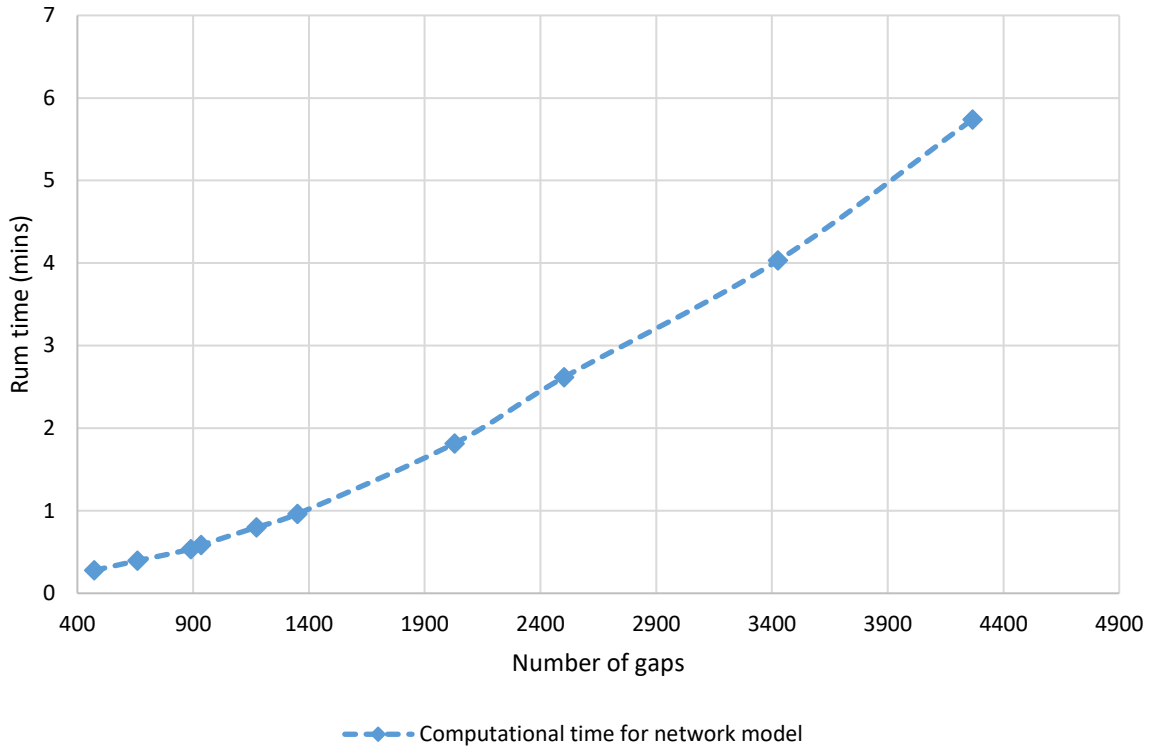
Figure 92 – Combined computation time to the three sub-codes (network formation, flow simulation, velocity mapping) of the numerical model shows up-to 4300 gap can be processed under 6 minutes

The network can be reconstructed for each preform produced in that time frame. Whereas, for a 3D or 2D model, user will be required to reconstruct the mesh for reliable simulation and reconstruction of mesh is not practical if there are 4300 individual gap regions present in the preform. On the other hand, network model will be created for each preform without requiring the user to start from the CAD geometry file again and produce a working mesh.

5.4.2 Local and global velocity maps

To demonstrate the complexity that can be received in a CSV. file from the rig, a simple preform of 150mm x 150mm with target gap width 1mm after every tow has been designed and data is imported from the CSV file.

The 3D network is shown below in the Figure 93 where all the blue marks present the nodes added at the intersection points of inter layer gaps. The network is made of 2675 gaps and 15782 nodes. The magnitude to inter layer junctions shows that unlike in [27] through thickness flow cannot be neglected or assumed insignificant in preforms with high gap volume fractions. This also demonstrates the complexity level that can be expected from ADFP preforms designed with gaps for flow enhancement. The 2D graph is given in appendix C.
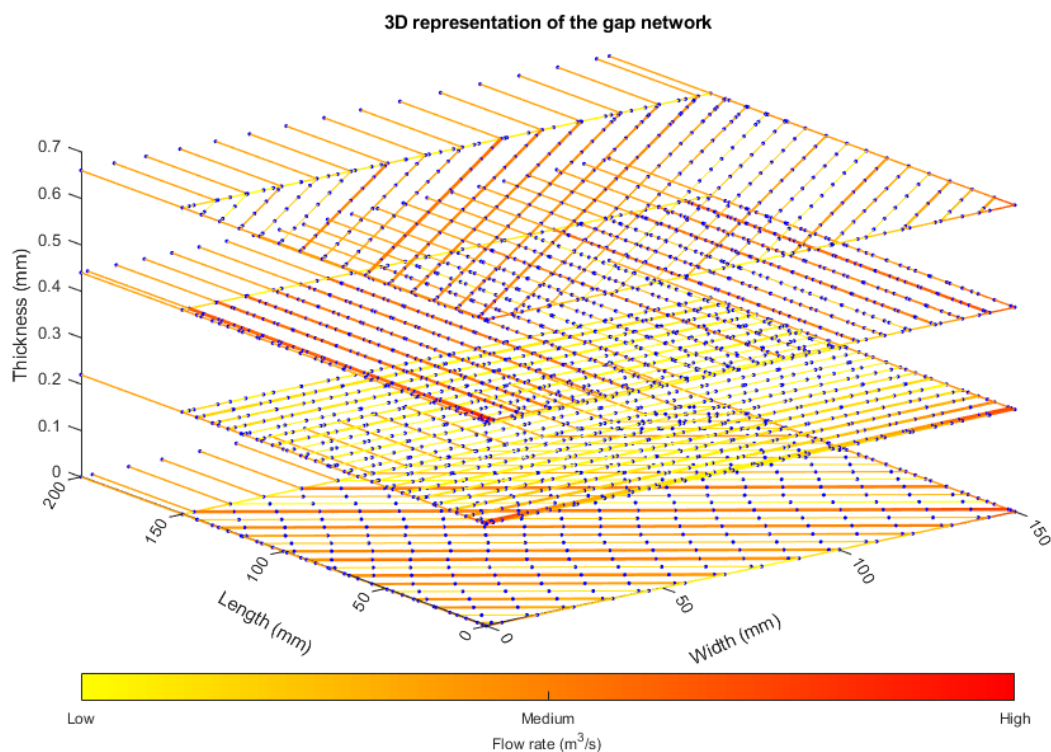
Figure 93- 3D gap network produced using real data from CSV. file

12 number of cells are calculated using Sturge's equation. The colour maps are generated for each layer to exhibit local layer behaviour which are given below in Figure 94.
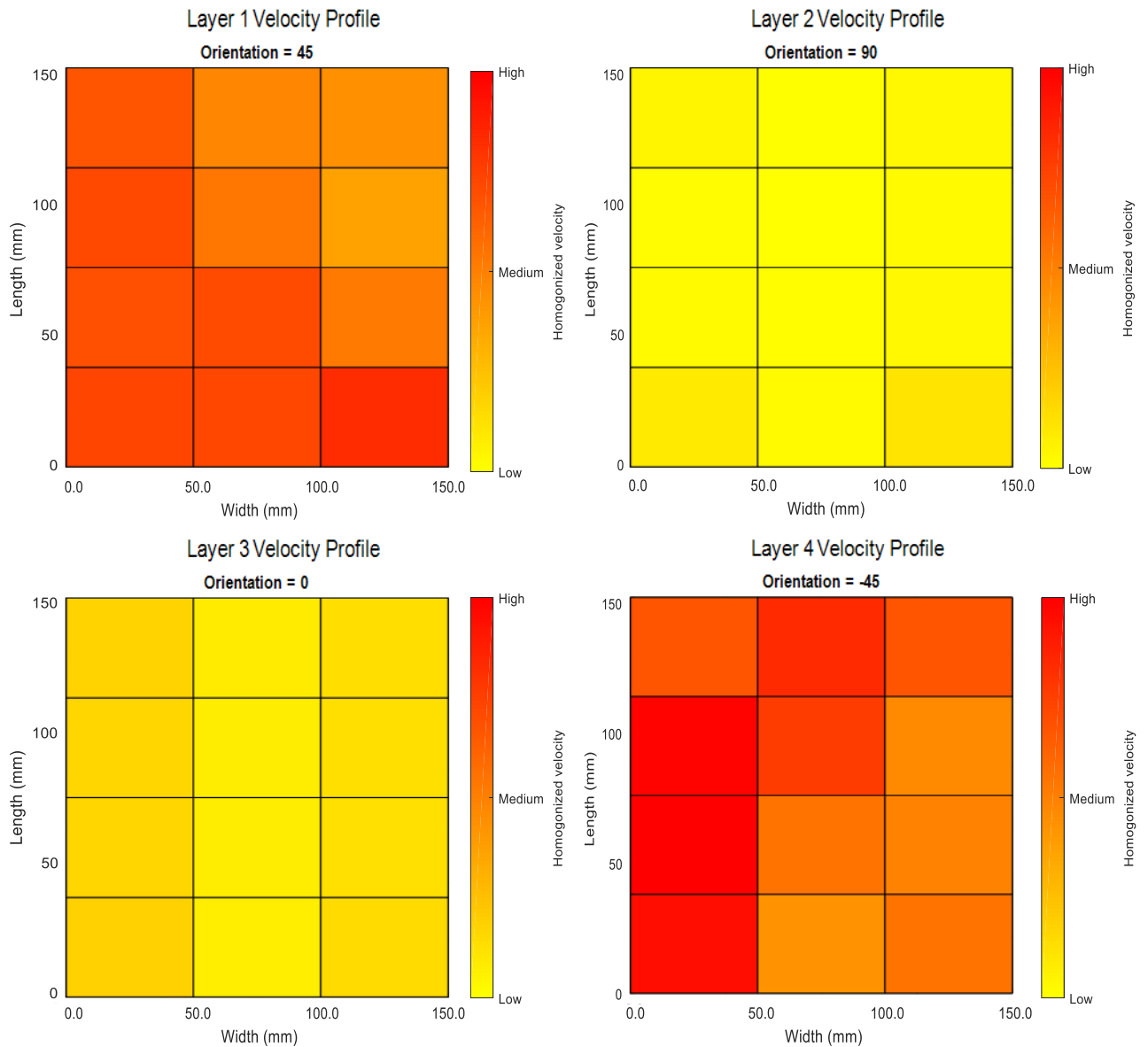
Figure 94 - Local layer homogenised velocity can be enabled in the code if required to observe local behaviour in any layer.

Although highest flow velocity should be expected from gaps in 0° orientation, this is where the cell size calculated by Sturge's shows its importance. A total 7 gap in 0° orientation are in each cell. Whereas 9 gaps in ±45° orientation exists within boundary of the cell. This can be that total 7 gaps are in 90° orientation as well, but since the gaps are perpendicular to the outlets, the have the lowest flow rates. This can be confirmed from Figure 95. Also, the RGB values are generated based on minimum and maximum from all the preform layers. Therefore 1st and 4th layer shows the highest flow velocity.
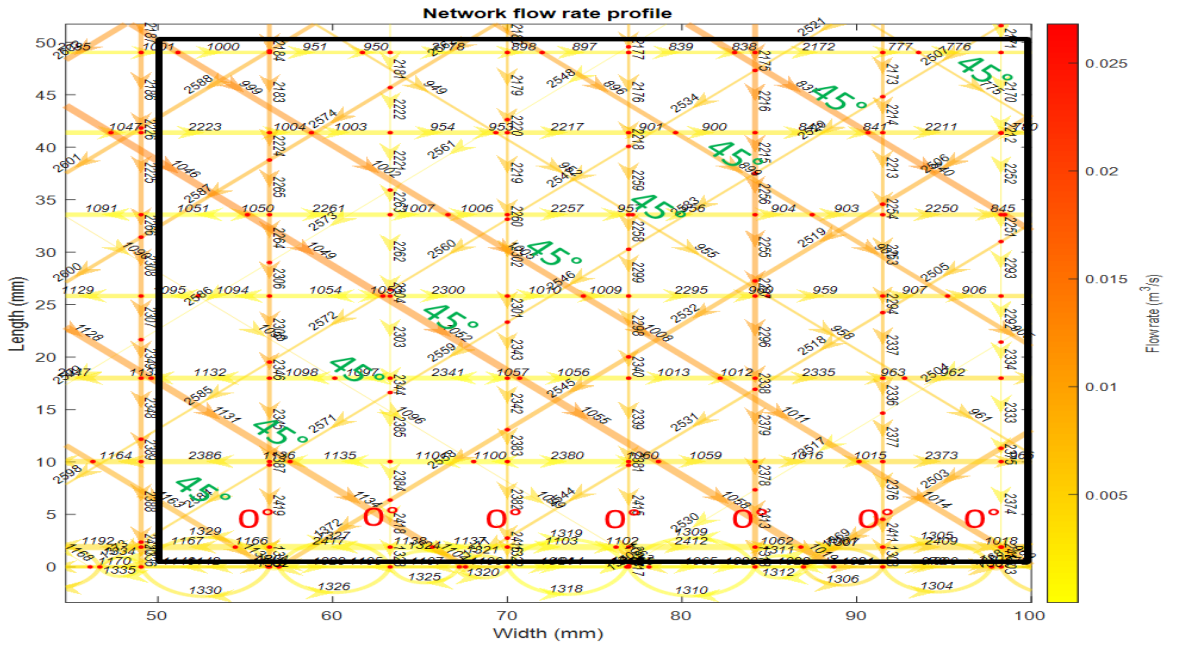
Figure 95 - The number of gaps in the cell can be followed by colour markers (0° - Red, 45° - Green)
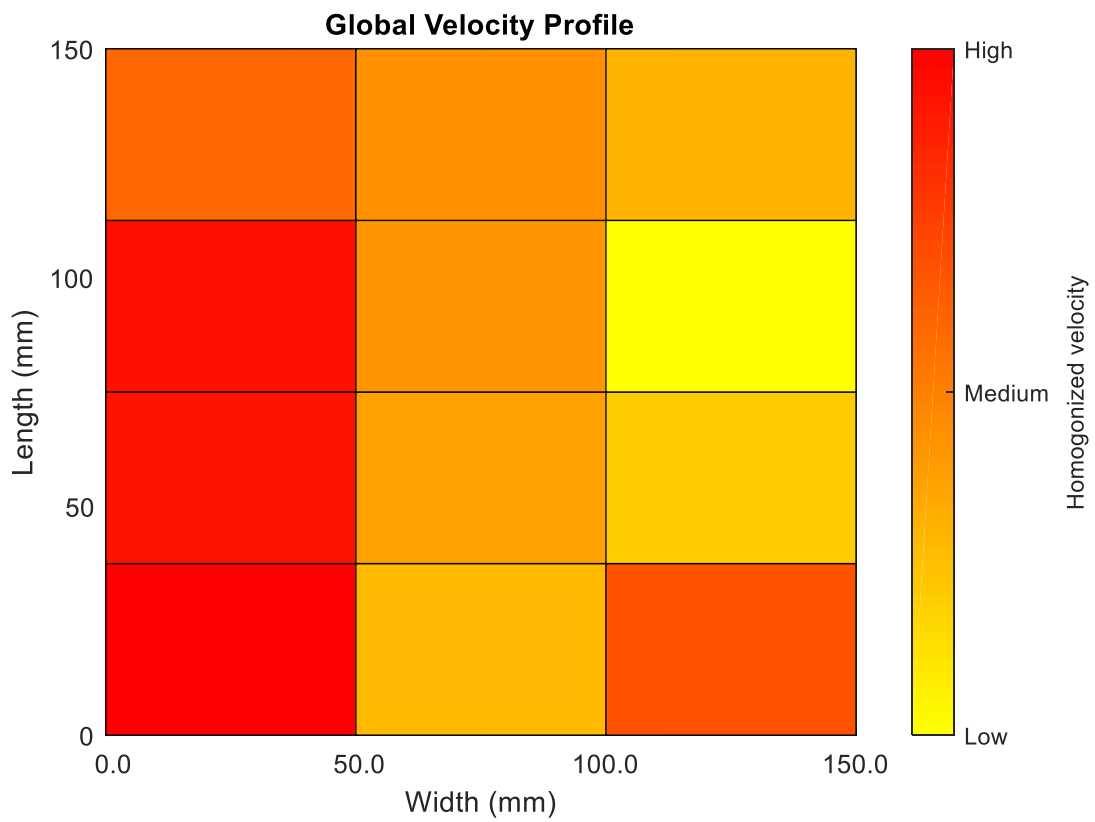
Figure 96 – Global flow behaviour generated by real data of 4-layer laminate

The RGB values for global velocity profile are based on minimum and maximum from global homogenised velocities of the cells. The Figure 96 above shows the global homogenised velocity profile of the preform in Figure 93. This successfully shows the region where lowest flow should be expected during infusion. Especially modern out of autoclave methods and automated layup that targets low manufacturing time and cost tends to exhibit higher voids in the final part [164]. Therefore, the velocity mapping approach enables the designer to make relevant changes to ensure complete impregnation of the preform.

5.5 Conclusion

Preform data imported from a CSV. file was successfully used to generate the gap network. This enables the user to generate gap networks based on real data for each preform produced without requiring any time consuming and costly methods such as XCT and microscopy as used by [27, 31, 32]. The real preform data was used to generate a network with 4300 gaps in under ten minutes. This demonstrates the advantage over conventional 3D simulation which requires a fully connected mesh that will be non-practical to produce for 4300 gap regions in a preform.

The cell edge method is implemented to identify gaps within each cell and calculate their corresponding homogenised velocity. The homogenised velocity is calculated for each cell in a layer and a velocity map is produced for each layer in a preform. This shows the local layer flow behaviour. The global velocity map showed regions of different velocities and shows where the lowest velocity should be expected during infusion. This model was developed for this project to demonstrate the potential of the network approach and further developments will be required prior to industrial application.

The three sub codes enable a user to generate the gap network for each preform without requiring any user time such as required to produce a mesh for 2D or 3D simulation.

Furthermore, a flow simulation provides the flow rates and pressure drop across the network without requiring the user to assign permeabilities in each zone as required in conventional models. Lastly a homogenised flow velocity map is produced which doesn't require high computational times such as in PAM-RTM to demonstrates different regions with high and low velocity. This means the developed numerical model can significantly reduce user time required for reliable flow simulation by eliminating the need of post infusion analysis to access limited preform data, production of mesh for each part and executing time-step based flow simulation expenses. Moreover, the ability of the model to incorporate real preform data for each simulation will lead to reliable predictions of parameters.

In terms of limitations of this approach, it has been highlighted in the earlier chapter that this model is based on steady state flow. During the saturation of a preform, the flow from gaps is absorbed by the neighbouring tows in transverse direction, this phenomenon was neglected at this stage of model development based on the analytical results that showed flow is dominant in the gap regions and fibre tow permeability contributions are negligible for when preform contains high V_{gf}. However analytical results are computed using weighted averaging approach and extensive research is required to understand the intensity of the sink effect during impregnation of ADFP preform with high V_{gf}. Once the sink effect is incorporated into the models, the next limitation will be the representation of transverse flow. The current representation takes the flow rates within the gaps of each layer and calculates a weighted average to exhibit the homogenized velocity of a cell, however a different approach may be required to incorporate the transverse flow results into the colour maps.

The perform data was generated using a code provided by the rig designer. This raw data was generated as the real preform data will be produced once the ADFP machine is equipped with the laser scanner. The experimental validation of this model was not done at this stage of model development. The model validation requires a real preform produced by ADFP machine

equipped with laser scanner to produce local gap data. The preform flow behaviour can be compared with the colour maps and regions of high and low velocity can be compared.

5.6 Appendix C

3D representation of the gap network

A 3D representation of graph network shown in 5.3.1
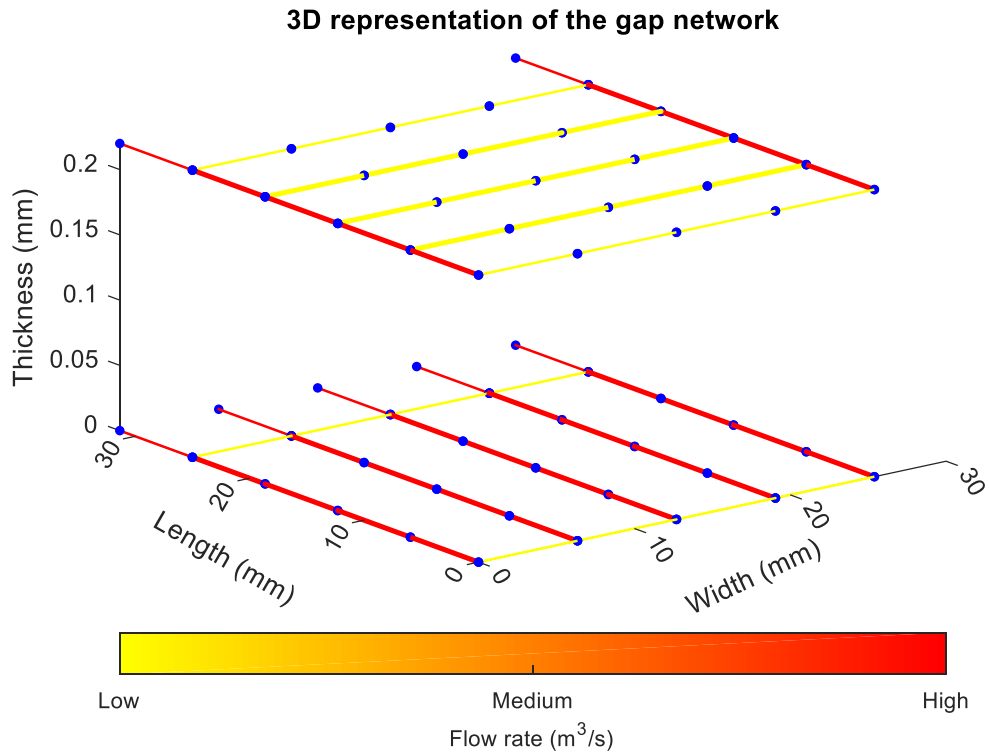
3D representation of the gap network
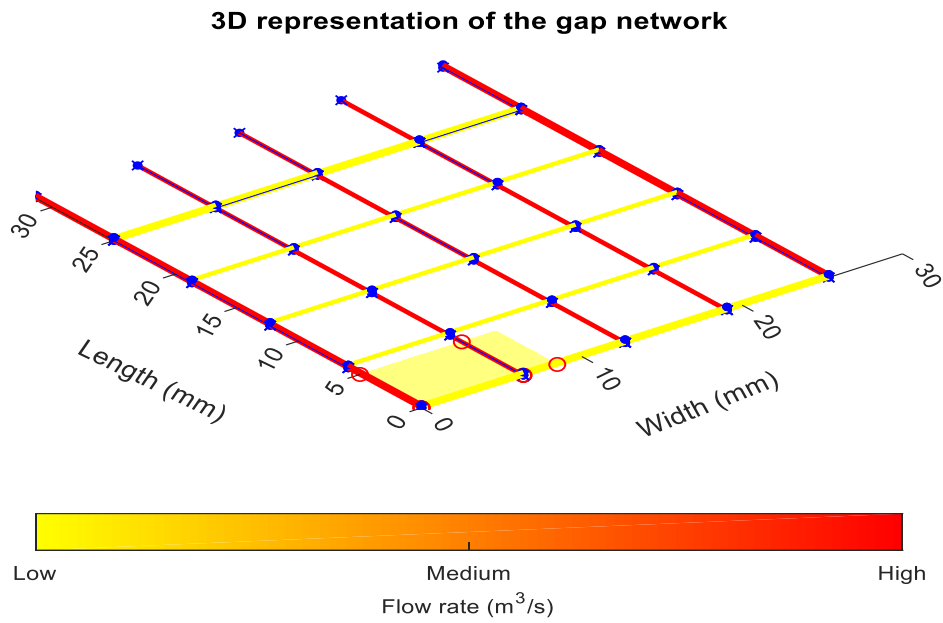
Gap search in a defined cell boundary step 1where the yellow box is formed and identifies the gap that are found and saves calculates the corresponding properties

3D representation of the gap network
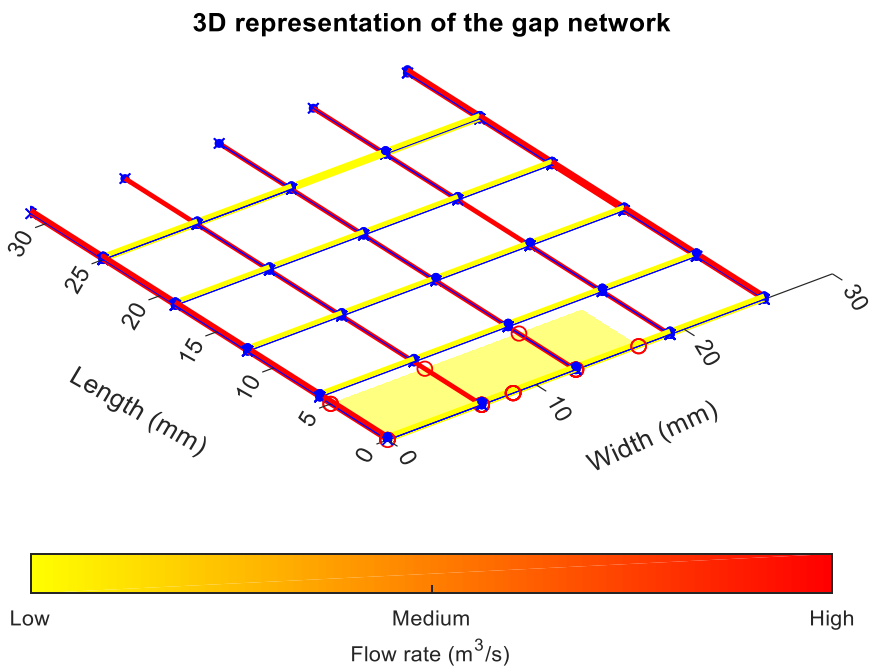
Gap search in defined cell boundary step 2 – Once all the gap are checked in the first cell. The next cell is formed and the process is reputed

3D representation of the gap network
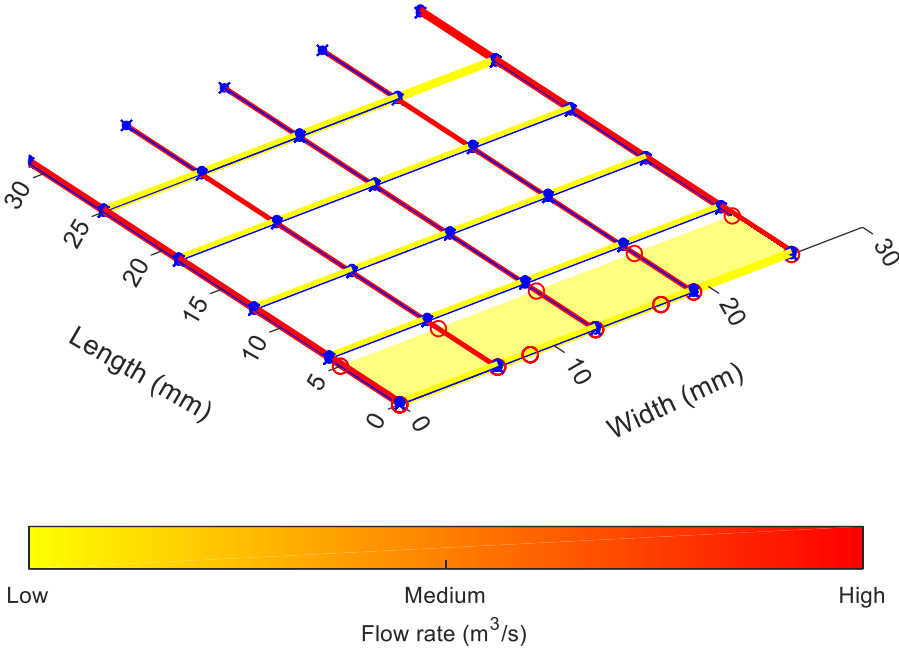
Gap search in defined cell boundary step 3

3D representation of the gap network
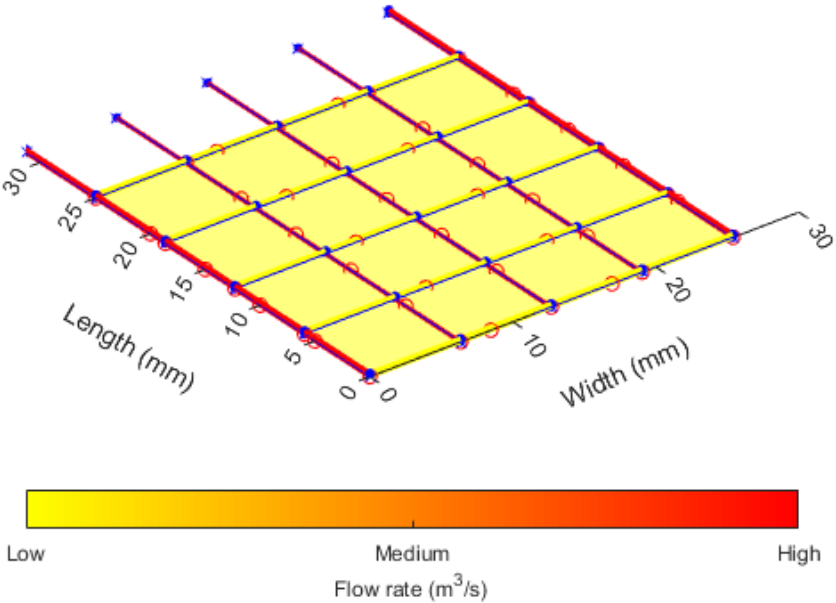
Once all the gaps are checked across the width of preform, the next cell is formed. The next cell is formed, and the process is repeated along the length of the preform.
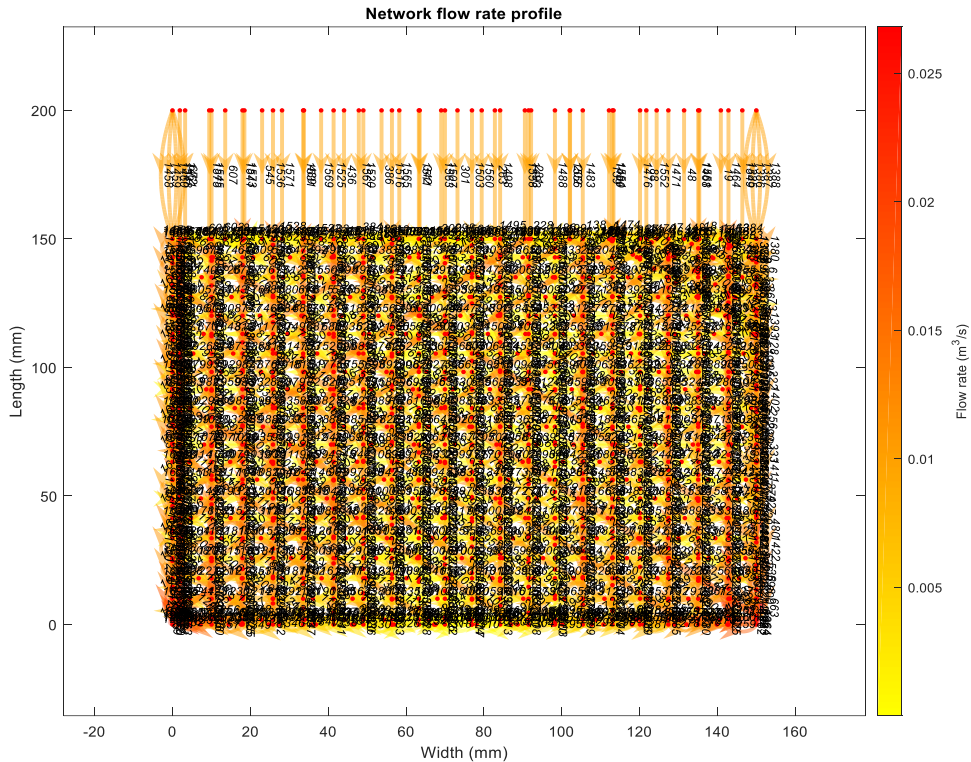
For a 4 layer laminate with [45;90;0;-45] layup processed is section 5.4

Chapter 6 Conclusions

The goal of this thesis was to exploit the fact that the resin preferentially flows in the preform gaps and to develop a new modelling approach based on this phenomenon. The limitations in the conventional approaches were identified through detailed review of literature. The aim of the developed numerical model was to overcome the limitations and enable rapid assessment to flow behaviour in ADFP preforms.

Experimental and analytical permeability - The meso-scale and macro-scale experimental work has demonstrated the complexity of measuring the permeability of tow level, layer and performs at high gap volume fractions. Gap widths of 0.25mm, 0.5mm, 1mm and 2mm were investigated. Employing different methods of computing (Direct and K_{sff}) and flow front positions (fastest point and slowest point) showed the sensitivity of overall permeability results

to such input parameters. The K_{sff} and fastest point was employed to process the overall results as it takes any local changes in flow behaviour into account. The conventional analytical models (Gebart's models for fabric region and Cornish's model for gap region) were used to measure the analytical permeability of corresponding specifications. The results showed 45% difference between experimental and analytical results in the case of single tow and gaps. The analytical model assumes the tapes and gaps are perfectly rectangular and the tapes are dry. These assumptions are not true under experimental conditions. Therefore results into higher differences between the results.

The difference between the results was increased to 60% in the case of two tows and a gap, 123% in the case of layer level (single layer with inter tow gaps) and 165% in a results of 44/44/12 preform with 1mm and 0.5mm designed gap width. In case of preform, wet patches across the preform were identified. Some of the patches were well ahead of visible flow front in the top layer. This demonstrated the gaps inside the preforms are behaving as a network. This network offers channels for resin with less resistance compared to the densely packed fibre regions. Therefore, the resin travel within the network cannot be observed from the top layer and impregnates the preform. The analytical models used as-designed gap widths and neglected any through thickness flow. This resulted into higher difference between analytical and experimental results comparing to tow land layer level results. This shows the difference between the results will increase as the number of gaps in a preform increases and produce unreliable permeability.

Therefore, the early chapters identified that an accurate analytical solution requires real gap width data to give accurate predictions. This is usually incorporated into the models by accessing local preform data post consolidation for instance, by micro-CT measurements. This can only provide reliable permeability results of the preform which is already manufactured. Each ADFP produced preform contains variability which leads to irreproducible flow

behaviour and permeability measurements. Due to the nature of variability in preforms, it was required to propose a new method to allow characterizations of flow in such preforms.

Numerical modelling - The gap network is a formed model based on real data. The gap network can be formed for preforms with layers in any orientation. The approach enables formation of network for each preform produced using the data file directly in shorter time (<10 minutes). This eliminates the time and cost associated with the extra steps required (XCT, microscopy etc.) post consolidation to access preform data which was done previously. Moreover, this approach also eliminates the user time required to build a fully connected 3D mesh to execute a conventional simulation. For example, the model forms a network consisting of 43000 gaps in a multi-layered preform in under 6 minutes. Also, the model can be rebuilt in similar time when a new preform is manufactured and contains different gap width specifications. On the other hand, for conventional simulation, a 3D mesh will be required to be reproduced again based on CAD data. While a 2D simulation model homogenises regions of different permeabilities. In case of complex preform, such as a preform with 4300 gaps, the exact number of zone will need to be assigned in a 2D model and the homogenization will neglect the through thickness flow and predict permeability based on weighted average. Therefore, the simulation software have their own negative effect on accuracy. This demonstrates a clear advantage of the numerical model for formation of gap network based on real data over conventional approaches to access preform data and producing 3D mesh.

Flow characterization– For flow characterization in the network model, a global gradient algorithm is executed where a set of energy and continuity equations are formed and the solution for flow rates and pressures in network model are computed by successive iterations. The results from the GGA and real data are issued to display a 2D network. These are where the line widths are representative of actual gap widths and a colour gradient is applied to the network to display gaps with high and low flow rates. The models were used to reconstruct the

preform networks using the data from literature [27, 32]. The results acquired by network model showed less difference from experimental results than the analytical approach solution employed by Matveev et al. [27]. The network approach allowed reconstruction of a complex preform [(-45,+45,0,90)s,0,(-45,+45,0,90)]s used in [32] and demonstrated the ability of model to handle complex preform designs.

The network model is also designed for users without access to ADFP rigs with laser technology that capture real preform data. In that case, the user will access the data through other conventional methods such as microscopy. The network model is regenerated under different gap specifications, assigned using the standard deviation as a limit. Permeability is calculated for each network model and used to predict an averaged permeability for the preform. The reliability results from this approach will depend on number of gap width measurements taken by the user. In conventional analytical solutions, permeability of preform is calculated under only one specification gaps in preform, by assigning one averaged gap width globally. On the other hand, the network model will predict much realistic permeability as it regenerates the model for different gap width specifications using standard deviation until the averaged permeability is converged.

Local and global velocity mapping – In a conventional 2D or 3D simulation model, flow front progression can be observed in a time-step based method. The computational time for producing this simulation depends on the number of elements in the mesh. Finer mesh will produce detailed flow behaviour but increase the computational time significantly. Therefore, this network model is developed to a user to visualize flow behaviour on a local (layer) level and globally without requiring excessive computational times, a cell method was employed to visualise the gaps within a cell boundary and calculate the homogenised cell properties. A homogenised value for each cell in a layer (locally) is used to measure a single resultant flow velocity for all layers (global) in a cell. This is used to plot a colour map for each layer in a

176

preform and a global velocity profile. It successfully shows the regions of high and low velocity and potential void regions. Moreover does not require excessive computational time for instance, map of preform with 4300 gaps are generated in under 1 minute.

This numerical tool has used the pipe network modelling approach and successfully implemented for ADFP preforms, moreover it use the results from GGA one step further and shows the flow behaviour through colour maps. It is important to highlight that this is first version of the numerical tool and does have its own limitations. Some limitations are highlighted in previous chapters such it neglects the flow in the fibre tows, this can be important as the complexity of gap network increases. The other highlighted limitation is that once the transverse flow is incorporated the visualization technique will not be valid to exhibit a homogenised velocity of a cell using all regions (gap and fibre tows) within the cell. Moreover, in order to successfully run the numerical tool to predict the flow behaviour based on real preform data, the deposition head of ADFP machine must be equipped with laser technology and produce a CSV. file that can be used to generate the gap network. These important limitation will needed to be resolved before using the numerical tool.

A major gap in the flow characterization of ADFP performs with high V_{gf} was identified in literature review. The current limitations in numerical prediction of reliable permeability for such preforms were identified. It was established through experimental results that conventional analytical methods based on as-designed preform parameters are not sufficient to predict reliable permeability of preforms with high V_{gf}. Therefore, a numerical model was developed that addresses the limitations identified from literature. The model, incorporates data about ADFP lay-up inaccuracy, overcomes the simulation limitations and produces colour maps of local and global flow behaviour. This enables a user to execute a quick preform simulation based on real data as soon as the preform is manufactured.

6.1 Potential future work

Observations were made throughout this project that would benefit from further study:

- A preform should be manufactured using ADFP rig equipped with laser scanning technology to provide real data. Then this numerical model can be experimentally validated by conducting LCM and compare the regions of low and high velocity identified by the numerical model. A step-by-step validation should be done starting at single layer level, single layer in different orientations, a multilayer unidirectional preform and finally a complex preforms with layers in different orientations

- The model does not incorporate the variability in the material and the permeability predicted by the network model is based on steady state flow. The saturated permeability can be lower comparing to the unsaturated permeability as the local variability in the material (twists, lose fibres, excessive binder, microscale gaps) may affect the local flow behaviour. The data from the rig should be further analysed using a sub-code and regions of any microscale variability in tow regions should be marked and compared with experimental flow behaviour to understand the magnitude of effect on flow behaviour due to corresponding material variability.

- Further understanding of phenomena at gap and fibre interface is required. The fibre tow sinks some flow from the gap region during the impregnation called as flow in y-direction. This phenomenon can be incorporated into the model to account for fluid that dissipates into the permeable neighbouring regions. Furthermore, flow direction of each layer can be incorporated into the model. One way of achieving this is through the product of rotational matrix, orientation of each layer and the principal permeability of each gap.

- The model requires the formation of a large matrix for GGA, the size of matrix increases as the number of gaps are increased in the model. This requires high computer memory. This matrix could be divided into sub matrices to enable execution of larger simulation on normal computers. Potential numerical model can be re-written in a better language than MATLAB to enable simulation of industrial size preforms.

- The model can be developed further to establish guidelines for gap placement in ADFP. This can be achieved by analysing preform with different gap volume fractions and placement strategies and search the optimum gap placement strategy for reduced infusion times.

- The ADFP preform permeability can be enhanced due to high gap volume fractions but because these gaps are also resin rich areas which behave as crack initiating zones. The effect of different gap volume fractions on mechanical properties (tensile, compression, bending etc.) of the preforms should be investigated in detail. This will lead towards establishing guidelines for optimum gap volume fractions to achieve lowest fill time without adversely affecting mechanical properties.

References

1. Vasiliev, Valery V. and Evgeny V. Morozov, *Chapter 1 - Introduction*, in *Advanced Mechanics of Composite Materials (Third Edition)*, V.V. Vasiliev and E.V. Morozov, Editors. 2013, Elsevier: Boston. p. 1-27.
2. Chamis, C., *Mechanics of Composite Materials: Past, Present, and Future.* Journal of Composites, Technology and Research, 1989. **11**(1): p. 3-14.
3. Andersson, Frida, et al., *Design for Manufacturing of Composite Structures for Commercial Aircraft – The Development of a DFM Strategy at SAAB Aerostructures.* Procedia CIRP, 2014. **17**: p. 362-367.
4. Soutis, C., *Carbon fiber reinforced plastics in aircraft construction.* Materials Science and Engineering: A, 2005. **412**(1): p. 171-176.
5. Mangalgiri, P. D., *Composite materials for aerospace applications.* Bulletin of Materials Science, 1999. **22**(3): p. 657-664.
6. Knight, M., Curliss, D., *Composite Materials*, in *Encyclopedia of Physical Science and Technology (Third Edition)*. 2003.
7. Robinson, Mark, *6.20 - Applications in Trains and Railways*, in *Comprehensive Composite Materials*, A. Kelly and C. Zweben, Editors. 2000, Pergamon: Oxford. p. 395-428.
8. Grzesik, Wit, *Chapter Thirteen - Machinability of Engineering Materials*, in *Advanced Machining Processes of Metallic Materials (Second Edition)*, W. Grzesik, Editor. 2017, Elsevier. p. 241-264.
9. M'Saoubi, Rachid, et al., *High performance cutting of advanced aerospace alloys and composite materials.* CIRP Annals, 2015. **64**(2): p. 557-580.
10. Jerome, PORA. *Composite materials in the airbus A380-from history to future*. in *Beijing: Proceedings 13th International Conference on Composite Materials (ICCM-13)*. 2001.
11. Bauer, Patricia. *Encyclopedia Britannica*. 2018 [cited 2019; Available from: h[ttps://www.britannica.com/technology/Boeing-707](https://www.britannica.com/technology/Boeing-707)
12. B., Rowan O., *Lightning protection system for conductive composite material structure*. 1986: USA.
13. Alemour, Belal, Omar Badran, and Mohd Roshdi Hassan, *A review of using conductive composite materials in solving lightening strike and ice accumulation problems in aviation.* Journal of Aerospace Technology and Management, 2019. **11**.
14. Lukaszewicz, Dirk H. , Carwyn Ward, and Kevin D. Potter, *The engineering aspects of automated prepreg layup: History, present and future.* Composites Part B: Engineering, 2012. **43**(3): p. 997-1009.
15. Stuart Dutton, Donal Kelly, Alan Baker, *Composite Materials for Aircraft Structures*. 2004: American Institute of Aeronautics and Astronautics, Inc.
16. Lubin, George, *Handbook of Composites*. 1 ed. 1982, Boston, MA: Springer. XI, 786.
17. Rajan, G., Prusty, B. G., *Structural health monitoring of composite structures using fiber optic methods*. 2016: CRC press.
18. Oromiehie, Ebrahim, et al., *Automated fibre placement based composite structures: Review on the defects, impacts and inspections techniques.* Composite Structures, 2019. **224**: p. 110987.
19. R., Chris. [cited 2022 01/08]; Available from: h[ttps://www.compositesworld.com/articles/sampe-europe-highlights-composites-face-challenges-in-next-commercial-airframes.](https://www.compositesworld.com/articles/sampe-europe-highlights-composites-face-challenges-in-next-commercial-airframes.)^01/08
20. Barile, M, et al. *Advanced AFP applications on multifunctional composites*. in *The Second International Symposium on Automated Composites Manufacturing. April*. 2015.
21. Nithin, J., Sadik, O,. Mihalis, K., *Novel multi-zone self-heated composites tool for out-of-autoclave aerospace components manufacturing.* Science and Engineering of Composite Materials, 2020. **27**(1): p. 325-334.
22. Mouritz, Adrian P, *Introduction to aerospace materials*. 2012: Elsevier.

23. Rimmel, O., D. Becker, and P. Mitschang, *Maximizing the out-of-plane-permeability of preforms manufactured by dry fiber placement.* Advanced Manufacturing: Polymer & Composites Science, 2016. **2**(3-4): p. 93-102.
24. Arbter, R., et al., *Experimental determination of the permeability of textiles: A benchmark exercise.* Composites Part A: Applied Science and Manufacturing, 2011. **42**(9): p. 1157-1168.
25. Gauvin, R., et al., *Permeability measurement and flow simulation through fiber reinforcement.* Polymer Composites, 1996. **17**(1): p. 34-42.
26. Belhaj, M., et al., *Dry fiber automated placement of carbon fibrous preforms.* Composites Part B: Engineering, 2013. **50**: p. 107-111.
27. Matveev, MY, et al., *Uncertainty in geometry of fibre preforms manufactured with Automated Dry Fibre Placement and its effects on permeability.* Journal of Composite Materials, 2017. **0**(0): p. 0021998317741951.
28. Yun, Minyoung, et al., *Characterization of 3D fabric permeability with skew terms.* Composites Part A: Applied Science and Manufacturing, 2017. **97**: p. 51-59.
29. Becker, David, et al., *An evaluation of the reproducibility of ultrasonic sensor-based out-of-plane permeability measurements: a benchmarking study.* Advanced Manufacturing: Polymer & Composites Science, 2016. **2**(1): p. 34-45.
30. Becker, D., J. Broser, and P. Mitschang, *An experimental study of the influence of process parameters on the textile reaction to transverse impregnation.* Polymer Composites, 2016. **37**(9): p. 2820-2831.
31. Aziz, A. R., et al., *Transverse permeability of dry fiber preforms manufactured by automated fiber placement.* Composites Science and Technology, 2017. **152**: p. 57-67.
32. Veldnez, L., Astwood, S., Giddings, P., Kim, B.C., Potter, K. , *INFUSION CHARACTERISTICS OF PREFORMS MANUFACTURED BY AUTOMATED DRY FIBRE PLACEMENT*, in *SAMPE Europe Conference 2017 Stuttgart - Germany*. 2017.
33. Croft, Kaven, et al., *Experimental study of the effect of automated fiber placement induced defects on performance of composite laminates.* Composites Part A: Applied Science and Manufacturing, 2011. **42**(5): p. 484-491.
34. Gebart, B.R., *Permeability of Unidirectional Reinforcements for RTM.* Journal of Composite Materials, 1992. **26**(8): p. 1100-1133.
35. Tamayol, Ali and Majid Bahrami, *Transverse permeability of fibrous porous media.* Physical Review E, 2011. **83**(4): p. 046314.
36. Berdichevsky, Alexander L and Zhong Cai, *Preform permeability predictions by self-consistent method and finite element simulation.* Polymer Composites, 1993. **14**(2): p. 132-143.
37. Tamayol, A and M Bahrami, *Analytical determination of viscous permeability of fibrous porous media.* International Journal of Heat and Mass Transfer, 2009. **52**(9-10): p. 2407-2414.
38. Cai, Z and AL Berdichevsky, *An improved self-consistent method for estimating the permeability of a fiber assembly.* Polymer composites, 1993. **14**(4): p. 314-323.
39. Endruweit, A, F Gommer, and AC Long, *Stochastic analysis of fibre volume fraction and permeability in fibre bundles with random filament arrangement.* Composites Part A: Applied Science and Manufacturing, 2013. **49**: p. 109-118.
40. Bechtold, Georg and Lin Ye, *Influence of fibre distribution on the transverse flow permeability in fibre bundles.* Composites Science and Technology, 2003. **63**(14): p. 2069-2079.
41. Chamsri, Kannanut and Lynn S Bennethum, *Permeability of fluid flow through a periodic array of cylinders.* Applied Mathematical Modelling, 2015. **39**(1): p. 244-254.
42. Papathanasiou, TD, *On the effective permeability of square arrays of permeable fiber tows.* International journal of multiphase flow, 1997. **23**(1): p. 81-92.
43. Um, MK and WI Lee, *A study on permeability of unidirectional fiber beds.* Journal of reinforced plastics and composites, 1997. **16**(17): p. 1575-1590.

44. Cornish, R. J., Edward A. M. , *Flow in a pipe of rectangular cross-section.* Proceedings of the Royal Society of London. Series A, Containing Papers of a Mathematical and Physical Character, 1928. **120**(786): p. 691-700.

45. Endruweit, A., et al., *Effect of yarn cross-sectional shape on resin flow through inter-yarn gaps in textile reinforcements.* Composites Part A: Applied Science and Manufacturing, 2018. **104**: p. 139-150.

46. F. Zarandi, M. A., Pillai, K. M., *Spontaneous imbibition of liquid in glass fiber wicks, Part II: Validation of a diffuse-front model.* AIChE Journal, 2018. **64**(1): p. 306-315.

47. Soltani, P., Johari, M. S., Zarrebini, M., *Effect of 3D fiber orientation on permeability of realistic fibrous porous networks.* Powder Technology, 2014. **254**: p. 44-56.

48. McKeen, Laurence W., *12 - Effect of Radiation on the Properties of Laminates and Composites*, in *The Effect of Radiation on Properties of Polymers*, L.W. McKeen, Editor. 2020, William Andrew Publishing. p. 393-408.

49. Blass, D., Kreling, S., Dilger, K., *The impact of prepreg aging on its processability and the postcure mechanical properties of epoxy-based carbon-fiber reinforced plastics.* Proceedings of the Institution of Mechanical Engineers, Part L: Journal of Materials: Design and Applications, 2016. **231**(1-2): p. 62-72.

50. Jabbar, M., Nasreen, A., *Composite fabrication and joining*, in *Composite Solutions for Ballistics*, Y. Nawab, S.M. Sapuan, and K. Shaker, Editors. 2021, Woodhead Publishing. p. 177-197.

51. Schlimbach, J., Ogale, A., *Out-of-autoclave curing process in polymer matrix composites*, in *Manufacturing Techniques for Polymer Matrix Composites (PMCs)*, S.G. Advani and K.-T. Hsiao, Editors. 2012, Woodhead Publishing. p. 435-480.

52. Meredith, J., Bilson, E., Powe, R., Collings, E., Kirwan, K., *A performance versus cost analysis of prepreg carbon fibre epoxy energy absorption structures.* Composite Structures, 2015. **124**: p. 206-213.

53. Composites, Easy. *Carbon Fiber Tow*. Available from: h[ttps://www.hexcel.com/Products/Carbon-Fiber/](https://www.hexcel.com/Products/Carbon-Fiber/)

54. Hexcel. *Carbon Fibre Roll*. Available from: h[ttps://www.easycomposites.co.uk/?_escaped_fragment_=/fabric-and-reinforcement/carbon-fibre-reinforcement/woven-carbon-cloth-over-400gsm/heavyweight-carbon-fibre-cloth-22-twill-650gsm-12k-1m.html](https://www.easycomposites.co.uk/?_escaped_fragment_=/fabric-and-reinforcement/carbon-fibre-reinforcement/woven-carbon-cloth-over-400gsm/heavyweight-carbon-fibre-cloth-22-twill-650gsm-12k-1m.html)

55. Technotes, Boeing Environmental, *Composite Recycling and Disposal An Environmental R&D Issue.* Boeing Environmental Technotes, 2003. **8**: p. 1-4.

56. Lomov, S. V., *Non-crimp fabric composites: manufacturing, properties and applications.* 2011.

57. Raji, Marya, et al., *3 - Prediction of the cyclic durability of woven-hybrid composites*, in *Durability and Life Prediction in Biocomposites, Fibre-Reinforced Composites and Hybrid Composites*, M. Jawaid, M. Thariq, and N. Saba, Editors. 2019, Woodhead Publishing. p. 27-62.

58. Jamir, M., Majid, M., Khasri, A., *Natural lightweight hybrid composites for aircraft structural applications*, in *Sustainable Composites for Aerospace Applications*, M. Jawaid and M. Thariq, Editors. 2018, Woodhead Publishing. p. 155-170.

59. Balasubramanian, K., Sultan, M., Rajeswari, N., *Manufacturing techniques of composites for aerospace applications*, in *Sustainable Composites for Aerospace Applications*, M. Jawaid and M. Thariq, Editors. 2018, Woodhead Publishing. p. 55-67.

60. Sidwell, D. R., *Hand Lay-Up and Bag Molding*, in *Handbook of Composites*, S.T. Peters, Editor. 1998, Springer US: Boston, MA. p. 352-377.

61. Elkington, M., et al., *Hand layup: understanding the manual process.* Advanced Manufacturing: Polymer & Composites Science, 2015. **1**(3): p. 138-151.

62. Grone, R., Grimshaw, M., *Composite tape laying machine with pivoting presser member*. 1986, Google Patents.

63. Hardesty, E, Goldsworthy, W., Karlson, H., *Geodesic path length compensator for composite-tape placement head*. 1974, Google Patents.

64. Smith, F., Grant, C., *Automated processes for composite aircraft structure.* Industrial Robot: An International Journal, 2006.

65. Crosky, A., et al., *4 - Fibre placement processes for composites manufacture A2 - Boisse, Philippe*, in *Advances in Composites Manufacturing and Process Design*. 2015, Woodhead Publishing. p. 79-92.

66. Campbell, F. C., *Chapter 5 - Ply Collation: A Major Cost Driver*, in *Manufacturing Processes for Advanced Composites*, F.C. Campbell, Editor. 2004, Elsevier Science: Amsterdam. p. 131-173.

67. Thomas, J., *The A380 programme - the big task for Europe's aerospace industry.* Air & Space Europe, 2001. **3**(3): p. 35-39.

68. Carson, R., et al. *Advanced materials technology '87; Proceedings of the Thirty-second International SAMPE Symposium and Exhibition, Anaheim, CA, Apr. 6-9, 1987*. 1987. United States: Society for the Advancement of Material and Process Engineering,Covina, CA.

69. Hinrichsen, J., Bautista, C., *The challenge of reducing both airframe weight and manufacturing cost.* Air & Space Europe, 2001. **3**(3): p. 119-121.

70. Goel, Anjali, *Economics of composite material manufacturing equipment*, in *Dept. of Mechanical Engineering.* 1978, Massachusetts Institute of Technology. .

71. Astrom, B., *Manufacturing of polymer composites*. 1997: CRC press.

72. Izco, Luis, J. Istúriz, and Ma.-J. Motilva. *High Speed Tow Placement System for Complex Surfaces with Cut / Clamp / & Restart Capabilities at 85 m/min (3350 IPM)*. 2006.

73. Grove, S. M., *Thermal modelling of tape laying with continuous carbon fibre-reinforced thermoplastic.* Composites, 1988. **19**(5): p. 367-375.

74. *humm3® - intelligent heat for composites*. [cited 2019; Available from: https://www.heraeus.com/en/hng/products_and_solutions/arc_and_flash_lamps/humm3/humm3.html

75. Evans, A. Turner, T., Endruweit, A., *Development of Automated Dry Fibre Placement for High Rate Deposition.* 2019.

76. Devlieg, R., Jeffries, K., Vogeli, P., *High-Speed Fiber Placement on Large Complex Structures.* 2007.

77. Béland, S., *High performance thermoplastic resins and their composites*. 1990: William Andrew.

78. August, Z., Ostrander, G., Michasiow, J., Hauber, D., *Recent developments in automated fiber placement of thermoplastic composites.* SAMPE J, 2014. **50**(2): p. 30-37.

79. Jonsson, M, et al. *Automated manufacturing of an integrated pre-preg structure*. in *The Second International Symposium on Automated Composites Manufacturing. April*. 2015.

80. Schmidt-Eisenlohr, C., *INTRODUCTION OF AUTOMATED 3D VACUUM BUILDUP IN THE COMPOSITE MANUFACTURING CHAIN.* 2015.

81. Di Francesco, M, P Giddings, and K Potter. *On the layup of convex corners using Automated Fibre Placement: an evaluation method*. in *Proceedings of ACM2– International Symposium on Automated Composites Manufacturing, Montreal, CA*. 2015.

82. Solvay. *ADFP machine* [cited 2018 July 28]; Available from: http://cytec.com/prism/.^July 28

83. SOLANO, J., *OAK Aerocomposit chooses innovative solutions to build the MS-21 composite wing: AEROSPACE.* JEC composites, 2012(72): p. 44-46.

84. Ginger, G. *Resin infused MS-21 wings and wingbox*. 2014 [cited 2018 03]; Available from: https://www.compositesworld.com/articles/resin-infused-ms-21-wings-and-wingbox.^03

85. Halley, P. , *Rheology of thermosets: the use of chemorheology to characterise and model thermoset flow behaviour*, in *Thermosets*, Q. Guo, Editor. 2012, Woodhead Publishing. p. 92-117.

86. Eckold, Geoff, *6 - Manufacture*, in *Design and Manufacture of Composite Structures*, G. Eckold, Editor. 1994, Woodhead Publishing. p. 251-304.

87. Karbhari, V. M., *2 - Fabrication, quality and service-life issues for composites in civil engineering*, in *Durability of Composites for Civil Structural Applications*, V.M. Karbhari, Editor. 2007, Woodhead Publishing. p. 13-30.

88. Centea, T., Grunenfelder, L., Nutt, S., *A review of out-of-autoclave prepregs – Material properties, process phenomena, and manufacturing considerations.* Composites Part A: Applied Science and Manufacturing, 2015. **70**: p. 132-154.

89. Drakonakis, V., Seferis, J., Doumanidis, C., *Curing pressure influence of out-of-autoclave processing on structural composites for commercial aviation.* Advances in Materials Science and Engineering, 2013. **2013**.

90. Li, P., Chen, P., Su, JZ., Liu, WP., *The recent development of advanced liquid composite molding technique and its application in aviation.* FRP/CM, 2016. **8**: p. 99-104.

91. Wei, J., Zhang, Y., Guo, W., *Development of vacuum assisted resin infusion (VARI).* Development and application of materials, 2010. **3**.

92. Advani S. , Sozer E., *Process Modeling in Composties Manufactuing* ed. M. DEkker. 2003, New York.

93. *RTM*. 24/06/2018 [cited 2018 24 June]; Available from: h[ttp://nptel.ac.in/courses/112107085/module5/lecture10/lecture10.pdf.](http://nptel.ac.in/courses/112107085/module5/lecture10/lecture10.pdf.)^24 June

94. Klunker, F., Danzi, M., Ermanni, P., *Fiber deformation as a result of fluid injection: modeling and validation in the case of saturated permeability measurements in through thickness direction.* Journal of Composite Materials, 2014. **49**(9): p. 1091-1105.

95. Linganiso, Z. and Anandjiwala, D., *4 - Fibre-reinforced laminates in aerospace engineering*, in *Advanced Composite Materials for Aerospace Engineering*, S. Rana and R. Fangueiro, Editors. 2016, Woodhead Publishing. p. 101-127.

96. Liu, Ya-Nan, et al., *Study on the resin infusion process based on automated fiber placement fabricated dry fiber preform.* Scientific Reports, 2019. **9**(1): p. 7440.

97. Khani, A., Abdalla, MM., Gürdal, Z., Sinke, J., Buitenhuis, A., Van Tooren, MJL., *Design, manufacturing and testing of a fibre steered panel with a large cut-out.* Composite Structures, 2017. **180**: p. 821-830.

98. Han, Z., Wang, ZY., Bian, DY., *A review on advances in defect formation mechanism of automated fiber placement components.* Fiber composites, 2014. **4**: p. 3-7.

99. Chiu, Tzu-Heng, et al., *Estimation of local permeability/porosity ratio in resin transfer molding.* Journal of the Taiwan Institute of Chemical Engineers.

100. Darcy, H., *Les Fontaines Publiques de la Ville de Dijon*. 1856: Victor, Dalmont, Paris.

101. Endruweit, A. and P. Ermanni, *Influence of Fixation Structures on the In-Plane Permeability of Unidirectional Glass Fiber Tapes.* Journal of Composite Materials, 2002. **36**(16): p. 1993-2010.

102. Okonkwo, K., et al., *Characterization of 3D fiber preform permeability tensor in radial flow using an inverse algorithm based on sensors and simulation.* Composites Part A: Applied Science and Manufacturing, 2011. **42**(10): p. 1283-1292.

103. Dungan, F. and A. Sastry, *Saturated and Unsaturated Polymer Flows: Microphenomena and Modeling.* Journal of Composite Materials, 2002. **36**(13): p. 1581-1603.

104. Pillai, Krishna M., *Modeling the Unsaturated Flow in Liquid Composite Molding Processes: A Review and Some Thoughts.* Journal of Composite Materials, 2004. **38**(23): p. 2097-2118.

105. Naik, N., M. Sirisha, and A. Inani, *Permeability characterization of polymer matrix composites by RTM/VARTM.* Progress in Aerospace Sciences, 2014. **65**: p. 22-40.

106. Di Fratta, C., et al., *Characterization of textile permeability as a function of fiber volume content with a single unidirectional injection experiment.* Composites Part A: Applied Science and Manufacturing, 2015. **77**: p. 238-247.

107. Wang, J., H. Wu, and J. Lee, *In‑plane permeability measurement and analysis in liquid composite molding.* Polymer Composites, 1994. **15**(4): p. 278-288.

108. Woerdeman, D., F. Phelan, and R. Parnas, *Interpretation of 3‑D permeability measurements for RTM modeling.* Polymer Composites, 1995. **16**(6): p. 470-480.
109. Yun, M., et al., *Stochastic modeling of through the thickness permeability variation in a fabric and its effect on void formation during Vacuum Assisted Resin Transfer Molding.* Composites Science and Technology, 2017. **149**: p. 100-107.
110. Liu, B., S. Bickerton, and S. Advani, *Modelling and simulation of resin transfer moulding (RTM)—gate control, venting and dry spot prediction.* Composites Part A: Applied Science and Manufacturing, 1996. **27**(2): p. 135-141.
111. Correia, N. C., et al., *Use of Resin Transfer Molding Simulation to Predict Flow, Saturation, and Compaction in the VARTM Process.* Journal of Fluids Engineering, 2004. **126**(2): p. 210-215.
112. L., Maarten, *Permeability Measurements - In Plane and Through the Thickness.*
113. Han, K. , C. Lee, and B. Rice, *Measurements of the permeability of fiber preforms and applications.* Composites Science and Technology, 2000. **60**(12): p. 2435-2441.
114. Becker, David and Peter Mitschang, *Influence of preforming technology on the out-of-plane impregnation behavior of textiles.* Composites Part A: Applied Science and Manufacturing, 2015. **77**: p. 248-256.
115. Drapier, S., et al., *Characterization of transient through-thickness permeabilities of Non Crimp New Concept (NC2) multiaxial fabrics.* Composites Part A: Applied Science and Manufacturing, 2005. **36**(7): p. 877-892.
116. Li, Min, et al., *Evaluation of through-thickness permeability and the capillary effect in vacuum assisted liquid molding process.* Composites Science and Technology, 2012. **72**(8): p. 873-878.
117. Vernet, N., et al., *Experimental determination of the permeability of engineering textiles: Benchmark II.* Composites Part A: Applied Science and Manufacturing, 2014. **61**: p. 172-184.
118. Alms, Justin, et al., *Experimental procedures to run longitudinal injections to measure unsaturated permeability of LCM reinforcements*. 2010.
119. Lawrence, Jeffrey M., et al., *Characterization of preform permeability in the presence of race tracking.* Composites Part A: Applied Science and Manufacturing, 2004. **35**(12): p. 1393-1405.
120. Nedanov, B. and S. Advani, *A Method to Determine 3D Permeability of Fibrous Reinforcements.* Journal of Composite Materials, 2002. **36**(2): p. 241-254.
121. Ahn, S., W. Lee, and S. Springer, *Measurement of the Three-Dimensional Permeability of Fiber Preforms Using Embedded Fiber Optic Sensors.* Journal of Composite Materials, 1995. **29**(6): p. 714-733.
122. Hoes, Kris, et al., *New set-up for measurement of permeability properties of fibrous reinforcements for RTM.* Composites Part A: Applied Science and Manufacturing, 2002. **33**(7): p. 959-969.
123. Scholz, S., W. Gillespie, and D. Heider, *Measurement of transverse permeability using gaseous and liquid flow.* Composites Part A: Applied Science and Manufacturing, 2007. **38**(9): p. 2034-2040.
124. Ouagne, P. and J. Bréard, *Continuous transverse permeability of fibrous media.* Composites Part A: Applied Science and Manufacturing, 2010. **41**(1): p. 22-28.
125. Sas, S., et al., *Effect of relative ply orientation on the through-thickness permeability of unidirectional fabrics.* Composites Science and Technology, 2014. **96**: p. 116-121.
126. Guin, W., R. Jackson, and M. Bosley, *Effects of tow-to-tow gaps in composite laminates fabricated via automated fiber placement.* Composites Part A: Applied Science and Manufacturing, 2018. **115**: p. 66-75.
127. Lan, Marine, et al., *Microstructure and tensile properties of carbon–epoxy laminates produced by automated fibre placement: Influence of a caul plate on the effects of gap and overlap embedded defects.* Composites Part A: Applied Science and Manufacturing, 2015. **78**: p. 124-134.

128. Rimmel, O., Mack, J., Becker, D., Mitschang, P., *Automated Direct Fibre Placement with Online Binder Application.* Lightweight Design worldwide, 2017. **10**(2): p. 48-53.

129. Drapier, S., et all.,, *Influence of the stitching density on the transvese permeability of non-crimped new concept (NC2) muliaxial reinforcements.* Composites Science and Technology 2002. **62**

130. Vallons, K, et al., *The influence of the stitching pattern on the internal geometry, quasi-static and fatigue mechanical properties of glass fibre non-crimp fabric composites.* Composites Part A: Applied Science and Manufacturing, 2014. **56**: p. 272-279.

131. Zarandi, M. Amin F., Salvador Arroyo, and Krishna M. Pillai, *Longitudinal and transverse flows in fiber tows: Evaluation of theoretical permeability models through numerical predictions and experimental measurements.* Composites Part A: Applied Science and Manufacturing, 2019. **119**: p. 73-87.

132. Nedanov, B., Advani, S., *Numerical computation of the fiber preform permeability tensor by the homogenization method.* Polymer Composites, 2002. **23**(5): p. 758-770.

133. Silva, L., Coupez, T., Digonnet, H., *Massively parallel mesh adaptation and linear system solution for multiphase flows.* International Journal of Computational Fluid Dynamics, 2016. **30**(6): p. 431-436.

134. Shojaei, Akbar, *Numerical simulation of three-dimensional flow and analysis of filling process in compression resin transfer moulding.* Composites Part A: Applied Science and Manufacturing, 2006. **37**(9): p. 1434-1450.

135. Park, CH, *Numerical simulation of flow processes in composites manufacturing*, in *Advances in Composites Manufacturing and Process Design*. 2015, Elsevier. p. 317-378.

136. Lebel-Lavacry, Aurelie, Chung Hae Park, and Abdelghani Saouab. *Air entrapment simulation in the resin transfer molding of industrial applications*. in *Advanced Materials Research*. 2013. Trans Tech Publ.

137. Trochu, F., Boudreault, F., Gao, M., Gauvin, R., *Three-Dimensional Flow Simulations for the Resin Transfer Molding Process.* Materials and Manufacturing Processes, 1995. **10**(1): p. 21-26.

138. Ansar, Mahmood, Wang Xinwei, and Zhou Chouwei, *Modeling strategies of 3D woven composites: A review.* Composite Structures, 2011. **93**(8): p. 1947-1963.

139. ESI-GROUP. *PAM-RTM*. [cited 2019 02 May]; Available from: h[ttps://www.esi.com.au/software/pamrtm/.](https://www.esi.com.au/software/pamrtm/.)^02 May

140. Grössing, H., Stadlmajer, N., et al., *Flow front advancement during composite processing: predictions from numerical filling simulation tools in comparison with real-world experiments.* Polymer Composites, 2016. **37**(9): p. 2782-2793.

141. Walski, Thomas, Zheng Wu, and Wayne Hartell, *Performance of Automated Calibration for Water Distribution Systems*, in *Critical Transitions in Water and Environmental Resources Management*. 2004. p. 1-10.

142. Wood, D. Charles, C., *Hydraulics network analysisusing linear theory.* ASCE, 1972. **98**(7): p. 1157-1170.

143. Gupta, Rajiv and T. D. Prasad, *Extended Use of Linear Graph Theory for Analysis of Pipe Networks.* Journal of Hydraulic Engineering, 2000. **126**(1): p. 56-62.

144. Ayad, A., H. Awad, and A. Yassin, *Developed hydraulic simulation model for water pipeline networks.* Alexandria Engineering Journal, 2013. **52**(1): p. 43-49.

145. Michaud, V., *14 - Permeability properties of reinforcements in composites A2 - Boisse, Philippe*, in *Composite Reinforcements for Optimum Performance*. 2011, Woodhead Publishing. p. 431-457.

146. Hamam, Y. and A. Brameller. *Hybrid method for the solution of piping networks*. 1971.

147. Todini, E. Pilati, S., *A gradient algorithm for the analysis of pipe networks*, in *Computer applications in water supply: vol. 1---systems analysis and simulation*. 1988. p. 1-20.

148. Menapace, A., Avesani, D. , *Global Gradient Algorithm Extension to Distributed Pressure Driven Pipe Demand Model.* Water Resources Management, 2019. **33**(5): p. 1717-1736.
149. Rossman, LA, *EPANET 2 Users Manual, EPA/600/R-00/057.* National Risk Management Laboratory, Office of Research and Development, US Environmental Protection Agency, Cincinnati, OH, 2000.
150. Rossman, Lewis A, *EPANET 2 users manual, water supply and water resources division.* National Risk Management Research Laboratory, US Environmental Protection Agency, Cincinnati, Ohio, 2000.
151. FM., White, *Fluid mechanics* 3rd ed. 1994: McGraw Hill.
152. Endruweit, A. and A. C. Long, *A model for the in-plane permeability of triaxially braided reinforcements.* Composites Part A: Applied Science and Manufacturing, 2011. **42**(2): p. 165-172.
153. Lundström, T. Staffan, Vilnis Frishfelds, and Andris Jakovics, *A Statistical Approach to Permeability of Clustered Fibre Reinforcements.* Journal of Composite Materials, 2004. **38**(13): p. 1137-1149.
154. Mogavero, Jeffrey and Suresh G. Advani, *Experimental investigation of flow through multi-layered preforms.* Polymer Composites, 1997. **18**(5): p. 649-655.
155. Yu, Boming and L. James Lee, *A simplified in-plane permeability model for textile fabrics.* Polymer Composites, 2000. **21**(5): p. 660-685.
156. Caglar, Baris, et al., *In-plane permeability distribution mapping of isotropic mats using flow front detection.* Composites Part A: Applied Science and Manufacturing, 2018. **113**: p. 275-286.
157. HexFlow. *RTM6 180°C Mono-component epoxy system*. 20/11/2019; Available from: h[ttps://www.hexcel.com/user_area/content_media/raw/RTM6_DataSheetPDF.pdf](https://www.hexcel.com/user_area/content_media/raw/RTM6_DataSheetPDF.pdf)
158. Dake, J M.K., *Essentials of engineering hydraulics*. 1983: MacMillan Press Ltd. 440.
159. Li, S. C., Z. H. Xu, and G. W. Ma, *A Graph-theoretic Pipe Network Method for water flow simulation in discrete fracture networks: GPNM.* Tunnelling and Underground Space Technology, 2014. **42**: p. 247-263.
160. Matlab R2018a. *polyxpoly*. 2018 Feburary, 2020]; Available from: h[ttps://uk.mathworks.com/help/map/ref/polyxpoly.html.](https://uk.mathworks.com/help/map/ref/polyxpoly.html.)^Feburary, 2020
161. *Mapshow*. [cited 2022 22/03/2022]; Available from: https://uk.mathworks.com/help/map/ref/mapshow.html.^22/03/2022
162. Wand, M. P., *Data-Based Choice of Histogram Bin Width.* The American Statistician, 1997. **51**(1): p. 59-64.
163. Scott, David W., *Sturges' rule.* WIREs Comput. Stat., 2009. **1**(3): p. 303–306.
164. Mehdikhani, Mahoor, et al., *Voids in fiber-reinforced polymer composites: A review on their formation, characteristics, and effects on mechanical performance.* Journal of Composite Materials, 2019. **53**(12): p. 1579-1669.